Space Weather and Interactions with Spacecraft

Final Report of

Study of plasma and energetic electron environment and effects
ESTEC/Contract No.11974/96/NL/JG(SC)

H. Koskinen[1,5], L. Eliasson[2], B. Holback[3], L. Andersson[2], A. Eriksson[3], A. Mälkki[1], O. Norberg[2], T. Pulkkinen[1], A. Viljanen[1], J.-E. Wahlund[3], J.-G. Wu[4,6]

1) Finnish Meteorological Institute, Geophysical Research, P.O.Box 503, FIN-00101 Helsinki, Finland
2) Swedish Institute of Space Physics, P.O. Box 812, SE-98128 Kiruna, Sweden
3) Swedish Institute of Space Physics, Uppsala Division, SE-75591 Uppsala, Sweden
4) Swedish Institute of Space Physics, Solar-Terrestrial Physics Division, Scheelevägen 17, SE-22370 Lund, Sweden
5) Also at: University of Helsinki, Department of Physics, P.O. Box 9, FIN-00014 Helsinki University, Finland
6) Now at: Danish Meteorological Institute, Lyngbyvej 100, DK-2100 Copenhagen O, Denmark

ESA Technical Officer:

A. Hilgers
D/TOS Space Environments and Effects Analysis Section (TOS-EMA)

ESA Technology Research Programme
Space Environments and Effects Major Axis

Page left intentionally empty

Document status

1. Document Title:
   Space Weather and its Interactions with Spacecraft
   Summary report of
   Study of plasma and energetic electron environment and effects (SPEE)
   SPEE-FR-2.0
2. Issue: 2
3. Revision: 0
4. Date: 20.08.1999

Document change record

Issue	Date	Comments	Modified parts
0.1	15.12.1997	PM4, outline	
0.2	22.03.1998	PM5	Introduction, Section 4
0.3	18.05.1998	PM6	All
1.0	29.05.1998	All chapters included (Ch. 4 incomplete) Conclusions to be revised	
1.1	18.06.1998	Submitted for approval	
1.2	18.05.1999	Revised, after revisions of all WP documents	
2.0	20.08.1999	Approved by A. Hilgers, 14.06.1999	

PREFACE

This document is the final report of the ESTEC/Contract No.11974/96/NL/JG(SC) "Study of plasma and energetic electron environment and effects (SPEE)". The document summarises the results of the project in a self-contained manner. In addition to this document the different work packages produced Technical Notes and URD/SRD listed below which are available upon request from ESTEC and at the WWW-server of this project: http://www.geo.fmi.fi/spee/docs/

The goals of the present study were to

– gain better understanding of spacecraft charging phenomena
– investigate the forecasting of satellite anomalies based on anomaly database
– summarise the European capabilities in the fields related to space weather and determine requirements for establishing a European space weather programme.

The study was organised under the leadership of the prime Contractor, the Finnish Meteorological Institute, Geophysical Research (FMI/GEO), with two units of the Swedish Institute of Space Physics, Uppsala (IRF-U) and Kiruna (IRF-K) as Subcontractors. In addition to the overall management, FMI/GEO was responsible for the third of the items above. IRF-U took care of the first item (section 4) and IRF-K the second item. The Technical Officer at ESTEC was A. Hilgers. The Project Manager was H. Koskinen from FMI/GEO and the University of Helsinki.

Relevant documents from individual work packages:

WP-110-TN: Charging events identification and case study of a subset of them
WP-120-TN: Modelling of Freja observations by spacecraft charging codes
WP-130-TN: Analysis of Freja charging events/Statistical occurrence of charging events
WP-210-TN: Spacecraft anomaly forecasting using local environment data
WP-220-TN: Spacecraft anomaly forecasting using non-local environment data
WP-230-TN: Spacecraft anomaly forecasting using heterogeneous environment data
WP-310-TN: State of the art of space weather modelling and proposed ESA strategy
WP-320-URD/SRD: Requirements for modelling tools for space weather programme
WP-330: WWW-server: http://www.geo.fmi.fi/spee

ACKNOWLEDGEMENTS

In this kind of a project it is always difficult to give proper credit to all people and organisations who have contributed to its successful execution.

We are deeply indebted to Dr. D. Cooke (US Air Force Research Laboratory) for the provision of the latest version of the POLAR code as well as for instructions and discussions on its use. Without it one of the most important parts of this study would have suffered considerably. Another crucial contribution was the Tele-X anomaly set provided by the satellite owner (Nordiska Satellitaktiebolaget, NSAB). Jonny Järnmark at the Swedish Space Corporation in Kiruna made this possible. Comments and opinions of two members of the Tele-X operational team G. Töyrä and H. Kling were very much appreciated. The Swedish Space Corporation (SSC) contributed substantially by providing the material information of the Freja satellite, for which we are indebted to P. Rathsman. Of course, SSC's excellent management was essential to make this small satellite project successful.

Great number of scientists has given important input to our project. Among the most important were R. Behnke (NSF), D. Boscher (ONERA-CERT), T. Clark (British Geological Survey), C. R. C. Clauer (NSF and University of Michigan), E. Friis-Christensen (DSRI), A. Johnstone (MSSL), J. Lemaire (IASB), D. Rodgers (DERA), R. Schwenn (MPAe), H. Singer (NOAA/SEC), G. Wrenn (T S Space Systems). Furthermore, we wish to thank all those scientists who have contributed to the several space weather-related sessions at various scientific meetings where our team members have participated.

Several of our colleagues at FMI and IRF have contributed in many ways to this project. We wish to give our special thanks to O. Aulamo, P. Janhunen, H. Laakso, R. Pirjola, P. Toivanen, and W. Schmidt from FMI/GEO; I.Sandahl from IRF-Kiruna; T. Carozzi, E. Dackborn, and L. Wedin from IRF-Uppsala; L. Liszka, from IRF-Umeå; H. Lundstedt and P. Wintoft, from IRF-Lund; R. Moses and J. Waldemark, from Umeå University. We also thank each of these institutes for providing their facilities and infrastructure to our project.

Last but not least we wish to thank the ESA TOS-EMA for initiating this project and their interest throughout its completion. Special thanks belong to the ESTEC Technical Officer Dr. A. Hilgers and to Dr E. Daly whose comments were particularly useful. Furthermore, the preliminary study by U. Svensson who was a stagiare at ESTEC was very useful for us.

ABSTRACT

Space weather is a new concept addressing the electromagnetic and charged particle environments of the Earth and their effects on space-borne and ground-based technological systems. In this investigation spacecraft charging phenomena on high-inclination low Earth orbit (PEO/LEO), satellite anomalies on geostationary orbit (GEO), and global space weather modelling have been investigated.

The PEO charging was studied using the database of the Swedish-German Freja satellite. While the spacecraft was successfully designed to be electromagnetically clean and highly conductive, it, nevertheless, experienced charging events of negative potential when it crossed the auroral electron beam. The largest potentials were estimated to exceed –2000 V. Most, but not all, charging events took place in eclipse. Furthermore, all charging events took place during winter months. Several severe payload operation problems occurred during charging, and the high charging levels are large enough to cause arcing effects. This suggests that auroral induced charging may be of concern for future spacecraft operation and design.

Several of the Freja charging events were modelled using charging codes. Even after careful modelling of the spacecraft shape and surface materials as well as the observed electron spectra it was found that the charging levels could not be modelled well, especially the large charging levels caused by intense 10-keV electron precipitation were not possible to achieve. This study gives useful hints for further development of the charging codes to account for auroral plasma environment.

The satellite anomalies on GEO were analysed using anomaly databases from the European meteorological satellite Meteosat-3 and the Swedish telecommunication satellite Tele-X.

Meteosat-3 carried an instrument for local observations of electrons in the range 43–300 keV. These observations were used to study how well neural networks could be trained to predict observed satellite anomalies. After treating the particle data with principal component analysis the networks were found to train well. Requesting that non-existence of anomalies during next 24 hours had to be predicted at least at 80% accuracy about 50% of anomalies were possible to predict based on the local input data.

Tele-X, as most GEO satellites, did not carry instruments to study the local space weather conditions. Both Meteosat-3 and Tele-X anomalies were studied using non-local data including energetic particles (E > 2 MeV) from geostationary GOES-6, GOES-7, and GOES-8 spacecraft and ground-based magnetic activity indices Kp and Dst. In this study several variations of neural networks were tested. It was found that the best predictions were obtained using the Kp index, the best predictions for Meteosat reaching about 80% for both anomalies and non-anomalies. The Dst showed to be a less successful predictor. The non-local electron data was not found as useful, especially due to its lower accuracy to predict non-anomalies.

Both local and non-local input data were combined in a study to search for a satellite anomaly index. It was found that combining the non-local and local observations reasonably good anomaly indices can be constructed. However, the index used by satel-

lite operators must be adjusted for each satellite individually. In addition to local measurements of high-energy electrons, simple lower-energy detectors in the 10-keV range are expected to be useful.

State of art of space weather modelling capabilities worldwide and in Europe were investigated. While it is clear that in the US space weather activities are farther ahead than in Europe there are certain fields where Europe is strong and it is possible and even desirable to formulate a European space weather programme built on these strengths.

The European solar-terrestrial physics community has strong scientific competence in the fields relevant to space weather modelling and forecasting. On the technological side Europe has good expertise in modelling of the effects of space environment. However, the cross-fertilisation between scientists and engineers is much weaker in Europe than in the US.

In the field of space weather modelling Europe has already established impressive activities in the modelling of energetic particles and their effects in the ring current and radiation belt regions of the inner magnetosphere. Also in the field of applying modern analysis methods, such as neural networks, Europeans are at high international level. Furthermore, the Solar and Heliospheric observatory (SOHO) has given European scientists leading position in the studies of the solar origins of space weather. Joining the European expertise in global magnetospheric dynamics, it is quite feasible that competitive global magnetohydrodynamics (MHD)-based modelling activity could be initiated in Europe.

User and software requirements for a physics-based space weather modelling tool capable of specifying the conditions in the inner magnetosphere were investigated in the form of User and Software Requirements Document. The most visible output of the project is an open World Wide Web space weather server installed at the Finnish Meteorological Institute and at ESTEC (http://www.geo.fmi.fi/spee).

A specific weakness in Europe is that the resources are scattered and it is unlikely that any single group or country could form a significant independent space weather activity. It is suggested that

1) The ESA Science Programme should take space weather on its agenda

2) A formal Science/Technology Interdisciplinary Space Weather Programme that should report to SPC/SSWG and IPC should be initiated

3) ESA should initiate work to establish a European Space Weather Data and Model Centre (either centralised or distributed with a central core). This Centre should have as its goal to become a European Data, Model, and Specification Centre, and it should look for a workable solution for a full-scale European Space Weather Centre.

Table of Contents

1. INTRODUCTION

The plasma environment, especially energetic electrons in the upper atmosphere and in the magnetosphere surrounding the Earth form a hazardous environment to man-made Earth-orbiting satellites. As more and more everyday functions rely on satellite operations, knowledge of the plasma and energetic particle effects on technological systems, including reliable modelling and forecasting methods, has become increasingly important. This has led to a number of initiatives world-wide toward more coherent and goal-oriented programmes often referred to as Space Weather programmes.

For both spacecraft engineering and operations, a key question is when, where, and why satellite charging and other environment-related anomalies occur, and how hazardous these phenomena may be. Although much work has been devoted to the understanding of the charging and other anomalous phenomena, and to protection against them, they still take place, sometimes with serious consequences. The development of smaller and more sensitive electronics and, most likely, the increasing use of spacecraft in the most hazardous orbits crossing high latitudes and radiation belts point out the necessity for intensified effort to understand both the origin and effects of these events.

In the present project the recently acquired database from the Swedish Freja mission has been extensively used for studies of charging phenomena. Although Freja was electromagnetically very clean, it experienced a relatively large amount of charging events. Because the spacecraft was specifically designed to study the electromagnetic environment with a several electric probes and particle detectors, its data set allows for both detailed single event studies and statistical considerations. It is also important that Freja's inclination of 63 degrees brought it above the auroral zone from where we have much less experience of charging effects than from geostationary orbit. This together with the altitude range of the Freja orbit (600–1700 km) make this particular study especially relevant for future high-inclination spacecraft. When the Freja charging events were studied with the help of charging codes NASCAP and POLAR, it was found that the high-latitude charging phenomena pose considerable challenge for understanding and, consequently, further development of modelling tools for charging is needed.

Before global "physics-based" models with satisfactory advance prediction, i.e., forecasting, capability will be usable, and most likely also thereafter, an alternative approach to predict the occurrence probability of satellite anomalies is to use information on past anomalies and conditions under which they took place. The commercial spacecraft operators are often reluctant to release their anomaly data bases, but for this study the Meteosat-3 and Tele-X anomaly data were made available. The anomaly data were related both with the local observations onboard the spacecraft in question and/or with non-local data specifying global solar-terrestrial conditions. In this study these data sets were thoroughly analysed using modern neural network techniques. The results were encouraging showing that it is possible to develop a spacecraft anomaly predictor for such phenomena that depend on the state of the magnetospheric plasma. Unfortunately,

a large number of anomalies are related to cosmic rays whose appearance is not predictable in the same way.

However, without extensive further development of tools for global modelling of the geospace dynamics, the only way of avoiding hazards due to space environment effects is to build space weather-proof spacecraft which in many cases would require extensive over-design with associated costs. During past few years the development of useful models has advanced significantly due to rapidly increasing computer resources and improved large-scale models for the interactions between the upper atmosphere, the ionosphere, the magnetosphere, and the solar wind. Especially, in the United States a considerable effort has been focused to the creation of truly global space environmental modelling with forecasting capability within the framework of the National Space Weather Program. Although Europe has good resources in this field both in terms of intellectual capacity and computer facilities, the resources are scattered and there evidently is a need for a more concentrated European effort. European resources and opportunities were studied as a part of the present project.

Last but not least, it is important that the widely scattered space community interested in the information of this study gets an easy access to its results. As a visible outcome of this project, a public World Wide Web (WWW) server has been developed and installed at ESTEC with a mirror server at the Finnish Meteorological Institute. The public parts of the server contain detailed information of European space weather resources, links to the relevant Web servers world-wide, samples of relevant data sets, and means of retrieving data from various data bases. WWW is a continuously evolving structure where links change and become obsolete. This particular is planned to be maintained and updated over several years to come.

2. SPACE WEATHER

2.1. What is space weather?

Space weather is a relatively new concept and as such its content and meaning are still under evolution. Quite generally it is understood as the time-variable conditions in space environment that may damage space-borne or ground-based technological systems and, in the worst case, endanger human health or life. While this definition is quite negative, the physical phenomena relevant for space weather are extremely interesting and under active basic research, and also include positive effects such as the beautiful auroral displays in the polar regions. The most important social and economical aspects of space weather aim at avoiding the consequences of space weather events either by system design or by efficient warning and prediction systems allowing for preventive measures to be taken.

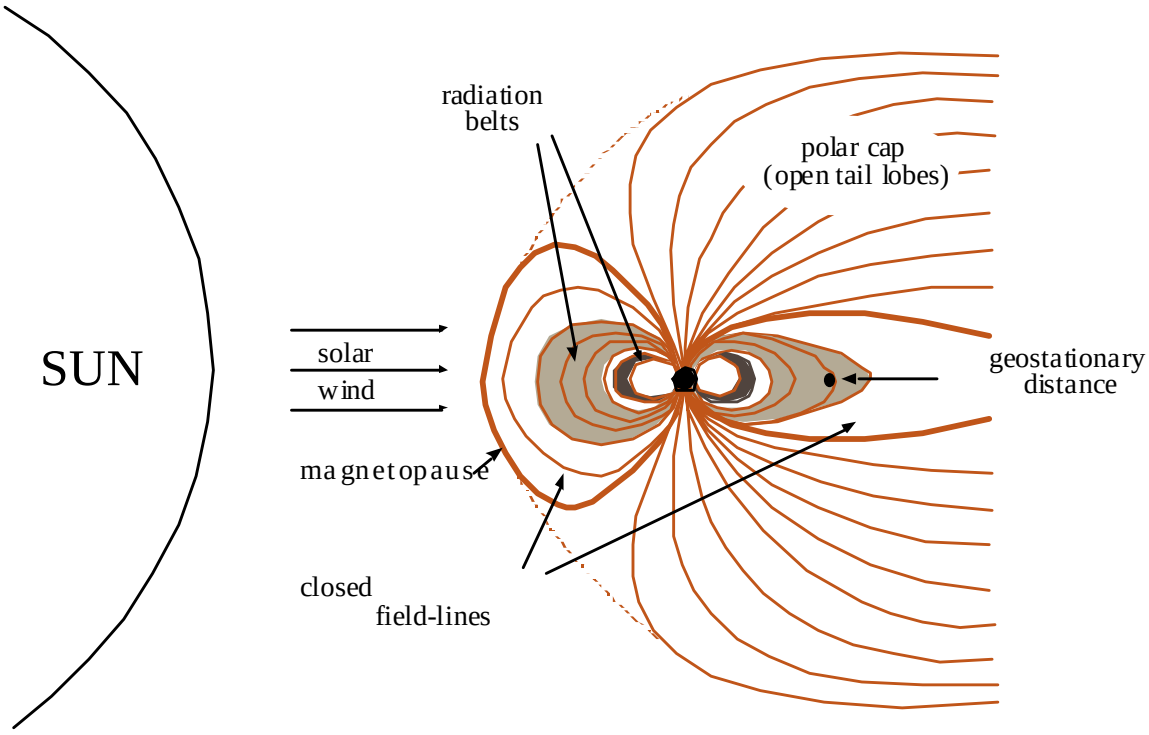

Figure 2.1. Main physical domains of space weather

The ultimate source of most space weather phenomena is the Sun and a control of space weather effects requires thorough understanding of Solar-Terrestrial Physics (STP), the physics of the intercoupled plasma environments of the solar wind, the magnetosphere, the ionosphere, and the atmosphere. Although closely linked, the distinction between space weather and STP is the more practical flavour of space weather research. Thus, if needed, a distinction between these concepts can be made: Basic research in the field of STP is necessary to deal with space weather, whereas space weather research is an ap-

plication-oriented discipline stimulating research of various problems in STP. This distinction has been implicitly assumed in the preparation of this Report, although we do not claim that it would be fully adapted by all parties in the space weather field. However, any space weather activity must ultimately address the needs of the applications community, e.g., engineers and operators. Identification of user needs is paramount but, as yet, one of the most unclear parts of the activity.

2.2. What are space weather activities?

Space weather has many similarities with atmospheric weather; thus the design of future space weather activities will, to a large extent, utilise the experience from meteorological services. This is already now a fact at Space Environment Center (SEC) of NOAA, and the 55th Space Weather Squadron of the US Air Force, both in Colorado, USA.

However, there are important differences between the atmospheric and space weather systems:

1) While many meteorological processes are localised and it is possible to make good limited-area weather forecasts, space weather is always global in the planetary scale. This arises from the large spatial scale-sizes of the solar-terrestrial plasma systems and the long correlation times of these plasmas. The most important and most dramatic effects originating from the Sun disturb the Earth's plasma environment, the magnetosphere, which responds to these disturbances globally.
2) Space weather events occur over a wide range of time scales: the entire magnetosphere responds to the solar-originated disturbances within only a few minutes, global reconfiguration takes a few tens of minutes, and sometimes extreme conditions may remain for much longer periods. The fastest signal in the global magnetospheric system is associated to the so-called Storm Sudden Commencement (SSC): ground-based magnetometers react immediately to a significant change in the magnetopause current system when a strong solar wind disturbance hits the magnetosphere. At the slowest end the enhanced fluxes of energetic particles in the radiation belts decay in time scales of days, months, or even years.
3) Our means to monitor the space weather are much more limited than our ability to install weather stations on the Earth's surface: Our prediction schemes must be capable of functioning with input from only a few isolated measurement points in the upstream solar wind conditions and magnetospheric parameters. These aspects are discussed in more detail below in the section dealing with the physics requirements for space weather modelling. As a consequence of these properties, successful space weather activities are performed on a global scale, merging space-borne and ground-based observational capabilities.

There is no doubt that at present the US is further ahead in space weather activities than other countries: They have the largest number of spacecraft, their scientific STP community is the largest, and they already have some operational space weather activities. This is demonstrated by the documentation of the National Space Weather Program (NSWP), which is a result of an initiative from the American space science community in 1993. The Strategic Plan of the NSWP was published in 1995 and the Implementation Plan in 1997.

The European activities and capabilities for an extended European approach are analysed in Chapter 6 below. At present, while Europe has a strong scientific community in the field of STP, there are only few attempts toward space weather, and the resources are scattered to relatively small groups in different countries. Furthermore, Europe is not as independent in space-borne facilities as the US is. The US STP community has always maintained synergies with the applications community. Space physicists often act as consultants on space environment issues for aerospace companies and military organisations. This kind of ties are much weaker in Europe.

As space weather is a global phenomenon, it is not clear that Europe should aim at full autonomy in this field. Actually, although the US NSWP has a strong national flavour, there is a general understanding that the programme must be widened to become international. Most of the present space weather activities are driven by the scientific community and the awareness of the users is only beginning to emerge. When the user awareness increases and more space weather tools and products are developed, the needs to protect national (or e.g., ESA) technological assets and commercial interests move also the space weather modelling away from the scientific openness. This is one reason why ESA should have a clear space weather policy to support the European space weather activities in their integration to the international space weather community.

On the truly international level there actually already exists an organisation that covers most of the world, The International Space Environment Service (ISES) (see: http://www.sel.bldrdoc.gov/ises/ises.html). ISES is a joint service of URSI, IAU and IUGG and a permanent service of the Federation of Astronomical and Geophysical Data Services (FAGS). There are ten Regional Warning Centres (RWC) scattered around the globe. These centres are located in Beijing (China), Boulder (USA), Moscow (Russia), Paris (France), New Delhi (India), Ottawa (Canada), Prague (Czech Republic), Tokyo (Japan), Sydney (Australia), and Warsaw (Poland). A data exchange schedule operates with each centre providing and relaying data to the other centres. The centre in Boulder plays a special role as "World Warning Agency", acting as a hub for data exchange and forecasts. For some reason the awareness of ISES among the present day space weather activists has remained smaller than expected, regardless of the fact that ISES has organised well-attended Solar Prediction Workshops, the latest one in Japan 1996.

Of the European ISES Centres the centre in Paris is the most active in space-based applications, in particular providing services for spacecraft orbits, altimetry, as well as launch and re-entry calculations (see: http://previ.obsem.fr/previ).

2.3. What is a space weather product?

A way of categorising space weather can be based on the warning time allowed for users to react to the possible hazard.

Space weather "forecasts", like their atmospheric weather counterpart, cover a variety of time scales and levels of accuracy. The long-range solar cycle forecasts are based on models of solar activity, but lack accuracy in timing of actual events. Shorter term forecasts may cover a period from several hours to a few days, and are based on solar and solar wind observations, in-situ magnetospheric data, and modelling.

"Warnings" are needed for events that have the potential to harm satellites, equipment, and humans in near-Earth space environment and on the ground. The warnings are based on solar observations and modelling techniques for prediction of geomagnetic activity, and are given less than 24 hours in advance, often only minutes in advance.

"Nowcasts" are based on in-situ real-time data assimilation techniques and models capable of running in real time. They provide global information about the state of the magnetosphere based on measurements in different regions of space.

"Post-event analysis" is used to assess the possible factors that may have caused operational anomalies. Post-event analysis utilises all available information of a given event to gain an accurate understanding of the sequence of events. This is valuable both for assessing damage and for future improvements of spacecraft design.

2.4. Who are the users?

The identification of users of space weather products or space weather modelling is one of the most critical issues for the development of space weather activities. This is partly related to the fact that until useful products become available, there will be no well-defined market for them. Most likely the awareness of the potential users will develop in parallel with the developing space weather services. Both sides of the development, i.e., products and the market, gain if the space weather community gives a high priority to education and public outreach. Also in this field the US space weather community is far ahead Europe. NOAA/SEC organises regular user conferences where their needs and the development of scientific models to applications are discussed.

The needs of the various users, actual or potential, are very variable, and, for the time being, rather poorly specified. Perhaps the most clear end-users of present space weather products are spacecraft engineers and spacecraft operators. The spacecraft development is based on accumulated knowledge of space environment and its effects. It is important that both non-critical and, particularly, hazardous satellite anomalies are

carefully analysed using the best available modelling tools. Spacecraft operators need information to avoid critical manoeuvres during critical conditions. Spacecraft launches may be postponed due to bad space weather conditions and the re-entry of Space Shuttle depends on the atmospheric drag conditions.

Other users are telecommunication operators, users of the global positioning system (GPS), electric power industry, etc. Commercial airlines must be careful not only with the radiation doses on their crew and passengers but also consider the potential radiation damages to the increasingly miniaturised electronic components. Often the end-user is just interested in receiving useful information from a space weather service provider. There is, however, a large group of users who wish to get pre-processed data for further modelling work. For example, a spacecraft engineer may want to analyse a spacecraft failure by varying the input parameters around the state of the radiation belts specified by a space weather centre. Also the scientific community sees themselves often as users because efficient data dissemination and modelling services are useful for them in one of the most tedious steps of scientific analysis, namely rapid access to data and model results.

With all hazards the insurance questions are important. With society's increasing dependence of space technology the insurance industry is becoming an increasingly important customer of space weather services. Due to the very high unit price of spacecraft the correct risk analysis is important for the insurance companies as well as their customers.

Another contributing factor is that the space weather models are of very variable size and level of sophistication, and will remain so. The most extensive physics-based models will always be run in supercomputers, and the most advanced models will follow the most advanced computer evolution. On the other hand, there are a great number of simpler models that can be used locally by the users themselves. Examples of these are various artificial intelligence systems, such as neural networks or non-linear filters. The users can run these models given that suitable interfaces and input data bases are developed.

3. IMPACT OF SPACE WEATHER EFFECTS ON TECHNOLOGICAL SYSTEMS IN SPACE AND ON GROUND

Space weather effects change the Earth's plasma environment on time scales varying from minutes to days and weeks. Dynamic magnetospheric processes may enhance the existing energetic particle populations to levels that are hazardous to the electronics onboard Earth-orbiting satellites. Solar activity and particle acceleration through cosmic processes create very energetic ions that can enter through the magnetospheric shield, again posing a hazard to both humans and technological systems in space.

Space weather effects are by no means limited to space-borne systems. The strong currents in the auroral region induce large Geomagnetically Induced Currents (GIC) in the long power lines. The increased and irregular plasma density in the ionosphere disturbs high-frequency (HF) and very-high-frequency (VHF) communications, the future satellite telephone communications, and satellite-based positioning systems (e.g., GPS). Furthermore, increased radiation doses on electronics and human beings on high-altitude flights, especially over polar regions can reach harmful levels.

3.1. Examples of hazardous space weather events

3.1.1. Historical examples

The first space weather events reported to harm technological systems took place around 1850 when electric telegraph communications were disturbed and in some cases completely stopped during strong auroral activations (Prescott, 1860). For a long time the telegraph and later the telephone communications were the most susceptible technological systems for space weather problems. The first reported effect on power systems took place on March 24, 1940 (Davidson, 1940). A great geomagnetic storm caused voltage dips, large swings in reactive power, and tripping of transformer banks in the US and Canada. During the same event 80% of all long-distance telephone connections out of Minneapolis, Minnesota, were out of operation.

A widely-known event took place on March 13, 1989, when a severe geomagnetic storm caused the failure of a complete electric distribution system in Quebec, Canada. Several million people lost their electric power for up to 9 hours and the estimated peak power lost exceeded 20 GW. The effect spread throughout the network very rapidly, from the first signs of problems to the system collapse in about 90 seconds. At the same time HF communications were blocked world-wide, whereas VHF signals propagated unusually far creating interference problems. A Japanese communication satellite lost half of its redundant communication circuitry, a NASA satellite dropped about 5 km in altitude due to increased atmospheric drag, and several other satellites experienced various types of upsets.

3.1.2. Recent satellite failures

As a consequence of a high-speed solar wind stream impacting the Earth's magnetosphere on January 20, 1994, at 1735 UT, the Anik E-1 spacecraft at geostationary orbit suffered an operational anomaly causing a loss of attitude control. Telesat Canada operators were able to finally switch to the backup momentum wheel controller and resume reasonably normal operations. The Anik E-2 satellite also experienced failure of its momentum wheel control circuitry at 0210 UT the following day. Anik E-2's backup circuitry was found to be non-functional, and therefore normal operational control of the spacecraft was lost. TV, radio, telephone, and scientific operations within the American continent were affected for hours to days by these spacecraft anomalies: The news, weather, and entertainment programming were affected, daily newspapers' information gathering systems were inoperative, and telephone services were interrupted in Canada (Baker, 1996).

During an extended (about two weeks) period of greatly enhanced electron fluxes present in the outer trapping region, the same Anik E-1 communication satellite suffered a severe operational problem on 26 March 1996. The satellite lost all power from its south solar panel array when the array was effectively disconnected from the satellite payload at 2047 UT. The 50% power loss reduced the spacecraft's capacity significantly. The lost communication capability affected a broad range of video, voice, and data services throughout North America. Service to Telesat Canada customers was restored after about six hours by link switches to other spacecraft and by using backup systems such as fibre optics ground links. During the same period, several other spacecraft operators also reported problems. Direct measurements showed that the operational anomalies were due to deep dielectric charging caused by elevated fluxes of very high-energy electrons (Baker et al., 1996).

A coronal mass ejection emerging from the Sun formed a magnetic cloud, which impacted the Earth on January 10, 1997. On early morning of January 11, 1997, AT&T lost contact with its Telstar 401 satellite. Telstar 401, one of the two Skynet satellites, was fully functioning before the incident. The other, Telstar 402R, took re-routed network signals right away following 401's difficulties. Satellites like the Telstars transpond TV programmes, telephone calls, and computer data. The magnetic cloud caused an exceptionally strong enhancement of relativistic electron fluxes in the Earth's magnetosphere detected both by geostationary and low-altitude polar-orbiting satellites. These electrons remained within the radiation belts for over a week after the incident. Evidence suggests that the increased levels in the radiation environment were connected to the malfunction of the AT&T Telstar satellite although it has remained unclear what the immediate cause of the failure was.
(see http://www-istp.gsfc.nasa.gov/istp/cloud_jan97/event.html)

3.1.3. Other effects on spacecraft

Interference and other hazards (SEUs, problems with star tracking, etc.) are much more common than the most publicised examples discussed above. Examples of space weather related problems on European satellites include radiometer stops of Meteosat, SEUs on most satellites (ISO, Hipparcos, ERS, SOHO, etc.), ISO experienced problems in its star tracker, and so on. Exact information on anomalies is difficult to get. The commercial companies consider this information confidential but even inside space organisations there is reluctance to admit problems. Another problem is that there are no standards how to collect anomaly information. At the beginning of a spacecraft mission the operators report on all anomalies but when more experience of the spacecraft behaviour has been gained, the less harmful anomalies are not always recorded. However, when anomaly information has been available, various effects have been traced directly to space weather events, thus it would be useful to organise homogeneous procedures to gather and report on all anomalies. In Chapter 5 below we discuss the determination of empirical anomaly indices based on extensive anomaly databases from two operational spacecraft Meteosat-3 and Tele-X. Another useful reference is Wrenn and Smith (1996) that includes a table of reported anomalies due to electrostatic discharges (ESD) from 47 spacecraft.

3.2. Spacecraft charging and satellite anomalies

Spacecraft charging and satellite anomalies are closely linked to each other. While spacecraft charging is a general physical phenomenon that cannot be totally avoided, it does not necessarily lead to anomalous behaviour of the spacecraft. On the other hand, damaging anomalies can be due to excessive charging.

Satellite anomaly is here defined as a change in spacecraft behaviour for which the spacecraft was not designed and which is not caused by an operational error. This can be anything from a bit flip to a total malfunction of the spacecraft. In the early days of space activities, some anomalies on geostationary (GEO) spacecraft were linked to the photoemission of the sunlit surfaces. With this knowledge new design recommendations for spacecraft were made. In plasmas where the local Debye length is larger than the spacecraft dimensions (such as in GEO) the main recommendations are proper grounding of the satellite and use of conductive surface materials. These recommendations can minimise or prevent accumulation of charges, which can generate a potential difference between the sunlit and the shaded side of the spacecraft (Frezet et al., 1989).

3.2.1. Spacecraft charging

The accumulation of charges on a spacecraft depends on the charge transport (currents) to and from a surface (including charge transport in the structure). Low energy particles from the plasma are stopped on the surface (photo emission, ionospheric plasma), high

energy particles penetrate the surface and can create secondary particles that can deposit charges somewhere else in the spacecraft system. Internal charging takes place when high energy particles penetrate the spacecraft and deposit charges inside the spacecraft. Dielectric charging occurs when a potential has been built up in a dielectric material. Surface charging refers to the surface of the spacecraft and interacts with the surrounding plasma. If one wants to monitor the low energy plasma surrounding the spacecraft these measurements are affected by surface charging which can lead to either shielding off or acceleration into the spacecraft of the low-energy charged particles.

Motion of a body across a magnetic field induces an electric field $\mathbf{E} = -\mathbf{V} \times \mathbf{B}$ (where **V** is the velocity and **B** is the magnetic field). If the body has low conductivity, this can create a potential difference between two positions on the spacecraft. This effect implies that large objects in strong magnetic field never can have the same potential at all points on the spacecraft without active potential control.

When the accumulation of charges at a location is more rapid than its diffusion, discharges can occur. This can take place between two points on the spacecraft or between spacecraft and space. At a threshold where the discharges occur charges will move between the two points giving rise to a current, followed by an electromagnetic disturbance. The acceleration of particles (a current peak during a short time interval) can cause an anomaly that may damage the spacecraft. Light flashes, such as arcs on solar arrays (between interconnections and space) are commonly observed discharge phenomena. Small discharges cannot be detected when the spacecraft is in space but during the Meteosat-1 ground tests small discharges on the spacecraft surface were observed as frequently as one discharge per second (Hoge, 1980). One problem with the discharges is that they may drain current from the spacecraft system and cause current spikes on the electronics bus. The discharges do not only damage the electronics in different ways but they also damage parts by sputtering the surface material to space and thus change the material properties. Discharges can also lead to degradation, to loss of solar strings, to loss of electronic components, and to changed thermal properties. Discharges may stop after a while in space due to changes in the material caused by the discharges.

Energetic radiation also affects the spacecraft material in different ways, depending on energy and material properties. Radiation on a material causes ageing, changes in thermal and resistive properties, darkening of glass etc. The effects shorten the mission lifetime depending on the total dose the spacecraft is exposed to. These environmental effects on the material have to be taken into account in spacecraft design.

3.2.2. Satellite anomalies

In the months immediately following the launch of a new spacecraft numerous anomalies are usually reported. Later, as knowledge on the spacecraft behaviour improves, the number of reported anomalies drops dramatically (Wrenn, 1995), leaving a significant number of spacecraft anomalies associated with charged particles in the magnetosphere. Possible regions and environmental effects, which may affect spacecraft, are: the neutral

thermosphere drag, plasma particles, meteoroids and spacecraft debris, solar radiation, cosmic rays and geomagnetic phenomena. These are often related to each other and determining the cause of a given event is often difficult (James et al., 1994). Spacecraft charging, high-energy particles and debris are the three main causes of anomalies.

When an anomaly occurs it is important to determine if it is caused by a command from the ground or by interference aboard the spacecraft. Sometimes failures occur when two parts of a system interact in a way that cannot be seen when they are operated separately. During 1993-95 twenty environmentally induced anomalies onboard NASA Goddard spacecraft were reported (Goddard Space Flight Center, 1994; Remez and McLeod, 1996; Walter, 1995). While many more anomalies occur during the first few months of spacecraft operation, the more ”interesting” (for this type of study), and possibly more damaging, cases occur once the educational process is completed and the spacecraft is in normal operation. For the Goddard spacecraft more than 400 anomalies occurred in the 3 years of operation but most of these could be identified either as part of the process of learning to control and use the spacecraft or as single event upsets (SEUs) from single high energy particles. Sometimes anomalies can occur due to the RF environment (Leach and Alexander, 1995). For example, NOAA-11 had phantom commands due to a noisy VHF-communication with the spacecraft. On NOAA-12 phantom commands occurred when the vehicle flew over commercial VHF-disturbances in Europe.

NASA maintains a spacecraft anomaly data base (Wilkinson, 1994). NASA’s environment data can be accessed through GOIN and NASDA. On internet anomaly data can be found at http://envnet.gsfc.nasa.gov/. IASB in Belgium provides information about environmental effects on spacecraft as a part of an ESTEC Contract (http://www.spenvis.oma.be).

3.2.3. Causes of spacecraft anomalies

Spacecraft anomalies can have different origins. A short description of some of them is given below.

The vacuum environment

When a spacecraft is launched significant outgassing is taking place that can give rise to anomalies. UV-degradation of different materials can also take place above the atmosphere. We do not further deal with these effects.

The neutral environment (chemical and drag)

The neutral environment extends far outside the Earth's magnetosphere. However, the effects of chemical (mainly atomic oxygen) interaction with spacecraft material and drag forces occur mainly at low heights (below 150 km), where the particle densities are high enough. The neutral environment is not considered in this study.

Plasma interactions

Charges accumulated on spacecraft surfaces (e.g., Garrett, 1981; Garrett and Whittlesey, 1996) can cause potential differences that can impact spacecraft systems through arcing. A discharge can occur between the surface and the surrounding space plasma, between different parts on the surface, or inside materials of the satellite. A current spike, during discharge, can generate electromagnetic radiation that can penetrate the spacecraft and/or damage the surface and electronics directly. Discharges at the edges of solar cells are common (Tribble, 1995).

Potentials can be generated by the **V** x **B** effect, depending on the spacecraft size and the local plasma density and temperature. Other sources for are currents to and from the spacecraft such as photoelectron emission, auroral electron beams, hot plasma injections during magnetic storms or substorms. Charges mainly accumulate at sharp edges and the amount of chargind depends on the surface properties.

On low-altitude orbits outside the auroral region the level of surface charging is usually small and voltages between different surfaces on a spacecraft are usually less than 10 V (See Chapter 4). On auroral field lines the charging may become 100 V or more and voltages above 1000 V may occur (Garrett and Whittlesey, 1996) due to, e.g., the auroral electron beams (Stevens and Jones, 1995; Chapter 4, below).

There is a strong seasonal variation in spacecraft charging. This may be associated to the orientation Earth's magnetotail with respect to the plane of the geostationary orbit, or to the known seasonal dependence of substorm activity, or both. One of the phenomena associated with spacecraft discharges are phantom commands. In the GOES spacecraft practically all phantom commands occurred between 23:00 and 08:00 local time. They peaked in spring and autumn.

Radiation (internal)

High-energy particles can penetrate the surface, interact with the material, and deposit their energy in the interior of the spacecraft. How the energy is deposited and what kind of interactions that takes place depends on the radiation type (photon, electron, ion, or neutral particle), the energy of particles and the material where the energy is deposited. The energy lost by the particle per unit length is referred to as its stop power or its linear energy transfer (LET) (Robinson et al., 1994). The LET depends on the number of interactions the penetrating particle makes with the target material. Secondary particles can cause lattice damages. The charged secondary particles can increase the charge on different surfaces and inside materials.

If charges are built up inside capacitors, which have a slow decay time, radiation induced dielectric charging can occur (Frederickson, 1980). High energy radiation can charge dielectric material to the electric field breakdown level.

Radiation through semiconductors causes electron and hole pairs along the path of the penetrating particle. The extra charges in the semiconductor can cause the component to fail. The generic name for events following a single high-energy particle impact is single event phenomenon (SEP) or single event effect (SEE). There are three classes of SEPs: single event upset (SEU), single event latch-up and single event burn-

out (SEB) (Hastings, 1995). A single event upset is a change in state of a digital circuit due to a high energy particle. A single event latch-up occurs when, instead of a bit flip, the circuit hangs and a reset has to be made. A single event burnout occurs when the circuit fails permanently due to the high energy particle.

Single event upsets (SEUs) on LEO satellites often occur in or near the South Atlantic Anomaly (SAA). SEUs are anti-correlated with solar activity except for strong solar events, but some of the more intense solar events generate high energy particles, making it more complicating to predict SEUs. The SEU probability is also related to the sensitive area (Lauriente and Vampola, 1996) and to the types of electronic devices.

The high-energy particles from cosmic rays can be predicted statistically but individual impacts are random (later seen as SEUs). Solar outburst effects can be predicted a few hours or days ahead, if adequate data and modelling are available which also can cause SEUs.

Dust and debris interaction

At geostationary distances the main debris are of natural origin. In low-earth orbit the population of man-made micrometer debris are comparable to natural particles. Depending on density, relative velocity and size debris can contaminate spacecraft, puncture insulators or even completely demolish satellites. Small debris can puncture the surface without directly damaging the spacecraft. Small-sized particles impacting on surfaces charged by plasma interactions can initiate a discharge.

Meteor showers can cause problem to satellite operation. Not necessarily a meteoroid making a hole in the satellite, but rather, from the creation of a plasma, or free electric charge on the spacecraft. The discharge can cause damage to sensitive electronic circuits on board the spacecraft, and ultimately cause the spacecraft to fail. The first assumed case of a satellite being lost by a meteoroid came in 1993. The Olympus communications satellite was reported being damaged by a meteor strike (1993 Perseid meteor shower) and was lost as a result of an electrical failure. The ESA press release from 26 August tells. "As indicated in the [earlier] press release of 17 August, 1993, service from the Agency's experimental OLYMPUS satellite was interrupted during the night of 11/12 August when, for reasons which are not yet understood, the satellite lost earth pointing attitude and began spinning. This event, and the subsequent recovery actions, used the last few kilograms of fuel remaining on the satellite. An assessment of the situation indicated that it would be impossible to re-establish service. It has therefore been decided that the Olympus mission should be terminated and the satellite removed from the geostationary orbital ring."

3.2.4. Anomalies and orbits

The types of anomalies vary with orbit (Vampola, 1994), but because the space is not in a steady state, the environment may also change considerably on the same orbit as a function of time, or in different places along the orbit. For example a solar proton event can create a radiation belt at 2 R_E lasting for several months (Daly et al., 1994). During

the high solar activity during the coming years we may expect several of these proton events which will effect all spacecraft.

On geostationary orbits surface charging occurs near midnight whereas thick dielectric charging occurs often in early afternoon. SEUs mainly occur if a solar proton event is in progress and due to cosmic rays. The transition between shadow and sunlight can cause surface charging due to photoemission.

On low-altitude polar orbits the most pronounced SEUs occur in the auroral oval and at the South Atlantic Anomaly. Surface charging is usually associated with the auroral oval.

Anomalies are not only reported from satellites orbiting the Earth. For the Voyager spacecraft, during close passes of Jupiter, internal electrostatic discharges occurred. These discharges appear to have resulted from high-energy electron flux with a rather good correlation with electrons of greater than 10 MeV energy. The Pioneer spacecraft encountered severe space weather conditions in the Jovian radiation belts, which nearly destroyed some on-board systems.

Independent of orbit, solar proton events can degrade the solar panels of satellites simultaneously causing reduction in the power output. Intense events can cause sensor failure or loss of the satellite control.

Examples of anomalies that have occurred on spacecraft at different locations and times are given in Table 3.1. The anomalies range from harmless SEU to total loss of spacecraft. The orbits of the satellites range from low-earth orbit to geostationary, but also interplanetary missions are included.

3.2.5. Spacecraft Design

Most spacecraft are designed to have the interior shielded from the surrounding plasma and a wide variety of protections against anomalies. These include shunt diodes for protecting solar cells, filters and diodes to prevent discharges from influencing internal and components and circuits which are SEU and discharge resistant (Kalweit, 1981) and/or constructed with error corrections and latch-up protection.

To avoid potential differences conducting materials are used. If dielectric materials are on the outside they are usually coated with e.g., indium tin oxide (Garrett, 1981). In some scientific experiments active control of potential is established using ion or electron gun.

Spacecraft have been launched with a smaller spacecraft attached by a fibre. These tethered spacecraft are designed to interact with the plasma environment for current generation or thrust, in some cases simply to probe the properties of the plasma.

Spacecraft	**Time**	**Comment**	**Reference**
DSP		Anomalies associated with >1.2 MeV electrons	Vampola, 1994
SCATHA		Internal discharges associated with outer radiation belt	Garrett and Whittlesey, 1996
ATS 5 and ATS 6		Charged to 10 kV in eclipse at GEO	SMASS Report
NOAA spacecraft	from 1971	Contains 2779 events from 1971to 1988	Wilkinson, 1994
Goddard space-craft	1993-1995	More than 400 anomalies	Remez and McLeod, 1996; Walter, 1995
Voyager 1		Power-on resets	Leung et al., 1986
Pioneer		Severe space weather near Jupiter	SMASS Report
GPS		Clock shift, false commands	James et al., 1994
Intelsat 3 and 4		Spin up	James et al., 1994
GOES 2			Lauriente et al., , 1996, 1998
GOES 3		Upsets	
GOES 4	Nov 26, 1982	Instrument failed on arrival of 110-500 MeV protons	Vampola 1994
Intelsat K	Jan 20 1994	Loss of attitude control in GEO	Baker et al. 1994
ANIK E1 and ANIK E2	Jan 20-21 1994	Loss of attitude control due to high energy electrons	Baker et al. 1996
ANIK E1	Mar 26 1996	Array of solar power panels disconnected	ISTP Newsletter, Vol 6, no 2, 1996.
DRA-delta		Phantom commands	Wrenn and Sims, 1996
CTS		Short circuit	James et al., 1994
DSCS II		Spin up, amplifier gain	James et al., 1994
DMSP 7		Charged to 300 V in less than a second- associated with a sharp drop in ion density	Stevens and Jones, 1995
GOES 5	July 22 1984	Failure during high energetic electron fluxes	Baker
DMSP F13		Problems while passing through an aurora	Anderson and Koons, 1996
Hispasat 1A and 1B	Sep 1992 and July 1993		Selding, 1998
Telstar 401	Jan 11 1997	Failure probably due to coronal mass ejection	Anselmo, 1997
Telstar 402		Spacecraft charging	Lanzerotti et al., 1996
Topex/Poseidon		Failures due to electrostatic discharges and SEUs caused by high energy protons	Lauriente and Vampola 1996
Intelsat 511	Oct 7 1995	Lost Earth lock	http://www.astro.lu.se/~henrik/spacew4b.html
GOES 8	Feb 14 1995	Attitude control difficulty	http://www.astro.lu.se/~henrik/spacew4b.html
TDRSS 1	1988-1991	SEUs anticorrelated with solar cycle	Wilkinson 1994
CRRES	1990	674 reported anomalies	Violet & Frederickson 1993
Tempo 2	11 Apr 1997	Temporary power fluctuations.	http://www.seds.org/spaceviews/970515/tech.html
Olympus	11/12 Aug 1993	Affected by the 1993 Perseid meteor shower?	See 2.1.5 above

Table 3.1. Some reported spacecraft anomalies

3.3. Space physics background of charging and anomalies

3.3.1. Trapped radiation belt particles

The quasi-dipolar magnetic field of the Earth is capable of confining and trapping large fluxes of energetic electrons and ions, which bounce back and forth between magnetic mirror points in northern and southern hemisphere and drift around the Earth. As negative charges drift eastward, and positive westward, this motion produces a westward current encircling the Earth. In the dipolar region, particles can be stably trapped for extended periods, even years, as was demonstrated in connection with atmospheric nuclear tests. The inner Van Allen radiation belt consists mainly of energetic protons, whereas the outer belt hosts mostly energetic electrons. While the inner belt is quite stable, the outer belt can be quite variable both in intensity and radial extent. The energetic (tens of keV to many MeV) electron and ion populations, at variable intensity levels, are always present in the near-Earth space environment.

The most obvious effect on Earth-orbiting spacecraft is the radiation dose on satellites traversing the trapped radiation belts. The almost stable inner radiation zones have been extensively modelled in the past (e.g., the NASA AE8 and AP8 models although there are well-known shortcomings in these models). The environment obviously is a major contributor to operational problems, but evaluation of the risk is possible (see, Chapter 5). Although many problems could traditionally be accounted for by radiation hardening of the spacecraft components, there is a drive to use advanced components that are more sensitive to radiation effects. The radiation also causes interference in sensors that cannot always be shielded against radiation. In addition, radiation effects to the growing astronaut population have to be very carefully monitored.

Intense long-term exposure to high-energy proton fluxes, particularly in the inner radiation belt, produces crystal-lattice structure damage in solid state devices, which can become completely inoperative after a certain integrated dose. The effects of heavily ionising radiation on electronics have been extensively investigated, and models for the damage as a function of fluence are available.

3.3.2. Magnetospheric substorms

Magnetospheric substorms are large-scale dynamic events in the magnetosphere, which lead to injections of energetic (tens to hundreds of keV) electrons and ions into the inner magnetosphere as well as to a global reconfiguration of the magnetospheric magnetic field. Substorms are well correlated with the orientation of the interplanetary magnetic field; they are known to occur after a period of southward interplanetary magnetic field (IMF) when part of the solar wind energy has been loaded into the magnetosphere. Under average conditions there are several isolated substorm events per day. The energetic particle populations created during substorms obviously constitute a quasi-continuous hazard for the spacecraft. Furthermore, substorms are associated with strong ionospheric

currents at auroral latitudes, which in turn can cause problems to the high-latitude power lines and communication systems.

During magnetospheric substorms the plasma density around a geostationary satellite may drop several orders of magnitude. The energetic electrons can then charge insulated surfaces negatively to several kV, especially in eclipse. Negative charging can also become a problem when the spacecraft is immersed within an auroral electron beam, which cannot be compensated by photoelectrons. This is a problem especially in eclipse. The risk for this effect is also strongly enhanced during substorm activity when the electron beams are strongest and most frequent. These kind of charging events are discussed in Chapter 4 below.

Magnetospheric substorms and storms create significant fluxes of field-aligned energetic (tens of keV) particles (mainly electrons), which precipitate into the auroral regions encircling the magnetic poles. At the same time the ionospheric currents in the auroral region enhance and may exhibit strong temporal variations. Transformers in the high-voltage electric transmission lines can be saturated by the current induced by the changes in the local magnetic field caused by ionospheric currents. The saturation can lead to overloading, overheating, or false relay tripping in the transformers, or disturbances in the reactive power balance of the transmission lines. This is a risk mostly in Fenno-Scandia and Canada, but the effects can reach lower latitudes during strong disturbances. Also the increasingly complicated interconnectivity of the power distribution systems increases the risk of propagation of the effects in the network.

Oil or natural gas pipelines are also affected by the changing geomagnetic conditions, as currents induced between the pipe and earth cause corrosion. To protect the pipes, they are kept at a potential lower than that of the surrounding earth in order to prevent current flow from the pipe to earth.

3.3.3. Coronal mass ejections and geomagnetic storms

Large, non-recurrent geomagnetic storms develop as a consequence of aperiodic solar disturbances, such as coronal mass ejections (CME). These are large expulsions of material from the Sun, usually associated with solar prominences and flares. Fast CMEs can be thought of as large plasma blobs moving rapidly outward from the Sun. The rapid motion through the ambient solar wind leads to a forward shock wave in front of the CME. The interplanetary magnetic field is draped over the CME, which creates a strong northward or southward magnetic fields ahead of the CME. A strong southward IMF, combined with the high velocity of the structure, constitute an efficient driver for magnetospheric activity.

Major geomagnetic storms cause strong distortion of the geomagnetic field as well as hours or days of hot plasma enhancements in the outer trapping region. These injected particles strongly enhance the ring current encircling the Earth. The ring current intensity can be monitored by ground-based magnetometers at low-latitudes: The Dst index composed of data from several stations around the world is an approximate measure of the total ring current energy content. It has been shown that the ring current usu-

ally decays in a time scale of 2–10 hours. Radiation belt particles can also be monitored by low-altitude, polar-orbiting satellites equipped with energetic particle sensors. These have shown that storm-generated populations can last for weeks or even months.

Large interplanetary shock waves driven by CMEs can also have pronounced effects in the inner magnetosphere, causing strong particle acceleration on a time scale of minutes. Note that the acceleration during storms typically reaches higher energies than during substorms. The compression and relaxation of the Earth's magnetic field caused by the arrival of the shock can lead to strong, highly time-variable electric fields, which can efficiently accelerate electrons in the outer trapping region.

Geomagnetic storms are most frequent before and after solar cycle maxima, and typically occur much more infrequently during quiet solar conditions.

3.3.4. High-speed solar wind streams and recurrent storms

Fast solar wind streams, when they interact with the Earth's magnetosphere, cause acceleration of energetic electrons: The lower-energy (below hundreds of keV) particle fluxes are well-correlated with solar wind velocity variations. These electrons appear as a product of magnetospheric substorm activity driven by the high-speed solar wind.

The highest energy electrons (several MeV) show a strong recurrence tendency at the 27-day rotation period of the Sun. These electrons are produced during geomagnetic storms driven by recurrent high-speed solar wind streams, which occur most often during times when the coronal holes extend to low latitudes during the declining phase of the solar cycle. The acceleration mechanism of the MeV electrons in the magnetosphere is still unknown, the substorm activity may play a role but the acceleration processes are most likely more complicated than the injections at substorm onset (Blake et al., 1997).

The strong driving of the solar wind during storms can cause the magnetospheric boundary to move inside the geostationary orbit. In such cases geostationary satellites on the dayside lose the shielding the magnetosphere provides against solar wind particles as well as the guidance of the magnetic field possibly used by orientation magnetometers. Furthermore, storms include a series of repetitive and often intense substorms, posing similar hazards as discussed above.

The very high energy electrons created by storms and especially by the interactions with the high-speed solar wind streams can cause deep dielectric charging of internal spacecraft components. In this process, the high energy electrons bury themselves in dielectric materials (such as coaxial cables), giving rise to high electric fields (potential differences of several kilovolts) in their vicinity until an intense breakdown occurs.

The high-energy (>1 MeV) electron population in the radiation belts intensified by the storm and high-speed stream-associated activity constitute a primary integrated dose problem for operation of spacecraft within the inner magnetosphere. They also interfere with sensors, e.g., as flashes in glass and impacts on detectors.

3.3.5. Solar particle events

Coronal mass ejections and flares often accelerate particles to very high energies. If there is a magnetic connection between the disturbance site on the solar surface and the Earth, the energetic solar protons travelling at speeds close to the speed of light can enter the near-Earth space within tens of minutes, and the peak flux can reach the Earth in a few hours. These particles constitute the largest risk for missions outside the magnetosphere, e.g., Moon and the planets. These very energetic protons also have an access to the polar cap regions and the outer magnetosphere where the shielding effect of the geomagnetic field is weakest.

Solar energetic particle events (SEPE) may have important effects on passengers, crew, and electronics onboard polar-crossing aircraft and manned spacecraft. Furthermore, the planned orbit of the International Space Station is such that it will be influenced by solar proton events. The damaging aspects of solar energetic particles on spacecraft come from fluence effects. Energetic protons and other ions (tens to hundreds of MeV) are highly penetrating, and one large event can be as damaging as years of operation in the normal near-Earth environment. Particularly vulnerable are systems and human beings outside the magnetosphere, e.g., on interplanetary flights or on the future Moon base. An astronaut has less than 20 min to seek cover after an event is observed on the surface of the Sun.

Solar protons can also penetrate directly into spacecraft sensor systems. The energy deposition by the protons may cause malfunction in the instruments at times when the fluxes are sufficiently high. A variety of proton-induced disruptions have been directly traced to solar energetic particles.

3.3.6. Galactic cosmic rays

The galactic cosmic ray population consists mostly of protons and alpha particles, but it also contains significant levels of heavier ions. A specific component in the galactic radiation are the so-called anomalous cosmic rays which are singly- or doubly-ionised heavy ions picked-up from the interstellar neutral matter by the solar wind. These ions enter the inner solar system after being accelerated at the heliospheric termination shock. The galactic cosmic ray energy spectrum near the Earth peaks in the energy per mass range 1-10 GeV/nucleon but the tail of the distribution contains ions of much higher energies. The integral intensity of galactic cosmic ray particles shows a 5–10% modulation with the solar cycle.

Galactic cosmic rays are shielded from directly reaching the low-altitude magnetosphere by the terrestrial magnetic field and the Earth's surface by the thick neutral atmosphere. However, the galactic cosmic rays have a direct access to the polar regions through the polar cusp and can be transported from there to high equatorial altitudes in the magnetosphere (e.g., to geostationary orbit).

Ground-based systems at polar latitudes and low-altitude polar-orbiting spacecraft can be strongly affected by galactic cosmic rays. Humans in polar-transiting aero-

planes or on long-duration spaceflights can be subjected to strong galactic cosmic ray influence. The most hazardous part of the cosmic rays is the highly ionising and relatively abundant Fe nuclei. These heavy ions can cause severe tissue damage in humans and major single event upsets in space electronics.

3.4. Outlook for effects

The future society will increasingly rely on space systems. Various positioning applications are already now based on GPS and these applications are continuously expanding. The same happens with communications. Today's geostationary communication systems will be completed by low-altitude polar telecommunications spacecraft networks of which the Iridium of the Motorola company was the first to be deployed with more than 70 satellites. Even larger new type of telecommunications services, based on hundreds of satellites, are expected to take care of wide-band multimedia applications (e.g., Celestri of Motorola and Teledesic of Microsoft). Polar orbiting or high-inclination geosynchronous satellites cross the low-altitude ends of the radiation belts and auroral regions several times every day and thus encounter hazardous conditions more regularly than geostationary spacecraft.

In the field of commercial air traffic only the crew and passengers were until recently considered to be threatened by radiation damages. This, of course, remains a concern, e.g., the airline companies have to take into account the new EU directive concerning radiation doses to workers. In addition, the development toward smaller electronic devices increases the risks as consequence of single event upsets. These effects become even more serious if the long-haul flights move to higher altitudes.

With the building of the International Space Station the human presence in space will grow. The orbit of the space station will routinely cross high fluxes of radiation belt particles. Space weather events are particularly serious during extravehicular activity (EVA). In planning of EVAs the space weather forecasts are needed and there must be effective systems to rapidly warn the astronauts of unexpected SEPEs. The precautions for SEPEs are of course critical for any long-duration activities outside the magnetosphere, be they a trip to Mars or work outside a future lunar base.

4. ANALYSIS OF FREJA CHARGING EVENTS

4.1. Background

4.1.1. Why are spacecraft charging studies important ?

The discipline of spacecraft-environment interaction has developed in the past as a series of specific engineering responses to various space environment effects as they were discovered. The variation in current flows to/from a spacecraft in different space environments can cause charge accumulation on the spacecraft surface(s). This charge, in turn, can produce potential gradients between electrically isolated surfaces as well as the spacecraft ground and surrounding space plasma. Spacecraft potentials of several tens of thousands of volts have been reported from several spacecraft (e.g. ATS, DMSP, SCATHA) since their first detection (DeForest, 1972). Such potential buildup can give rise to destructive arc discharges or microarcs that generate electromagnetic noise and erode surfaces. For example, arcing on highly biased solar arrays are so severe that it destroys the array in a short time. The arcing associated with high amplitude surface charging by the magnetospheric plasma is believed to have caused the loss of at least one spacecraft (Shaw et al., 1976) and possibly several more, but also anomalies on several GEO satellites (Rosen, 1976; Leach and Alexander, 1995). This started numerous efforts to understand and mitigate charge accumulation on surfaces in space. The study of charging processes on the Freja satellite is one more such effort.

The natural space environment depends, of course, on exactly where in space the spacecraft traverses. Over the years, several different regions have been identified where high amplitude spacecraft charging is more prone to arise. One such environment is the Polar Earth Orbit (PEO), which traverses the high-latitude auroral plasma regions. Other common charging environments are the Low Earth Orbit (LEO) of cold, dense ionospheric plasma, and the Geostationary Earth Orbit (GEO) immersed in the hot (high-energy) plasmasheet. Charging effects in all of these regions are heavily dependent on the magnetospheric substorm activity level, and therefore on space weather. There are also many (inter-)planetary regions (explored and un-explored) which are known to cause environmental disturbances, especially the magnetospheres of other planets. The Freja measurements, reported here, add further to the knowledge on spacecraft surface charging in a Polar Earth Orbit (PEO). Only very few studies have been devoted to spacecraft charging in PEO (see below), with the exception of the DMSP (Defence Meteorological Satellite Program), which presented an extensive set of surface charging occasions from a lower altitude (840 km).

Modern spacecraft often carry increasingly more complex, sensitive, and expensive payloads, which are affected by the space environment (natural or self-induced). Many instruments have in the past experienced operation problems due to the plasma electrostatic environment, and the interpretation of data from measurements depend critically on the knowledge of spacecraft charging effects. For instance, any shift in potential relative to the spacecraft ground or the space plasma can affect instruments

designed to collect or emit charged particles, but the spacecraft environment may also be a source of instrumental noise in general. Beside destructive arcing effects on surfaces, charge buildup on a spacecraft can in itself attract charge contaminants to sensitive surfaces. This contamination, in turn, can alter the properties of the surface, e.g. changing its conductivity, thermal properties, or optical properties in the case of lenses or mirrors. The study of Freja charging events identifies several problematic payload disturbances, which need to be addressed by instrument designers in the future to assure accurate and scientifically valid data extraction and/or analysis.

4.1.2 Goals of the study of Freja charging events

This chapter summarises the work packages of this project related to the study of charging of the Freja satellite. A detailed analysis of 10 charging events detected by Freja was conducted in order to identify the precise mechanisms behind the charging processes that operate at Freja altitudes (1000–1800 km). The presented events aim at being a representation of different types of charging processes found in the Freja data set. The analysis is complemented with precise electron and ion energy/pitch angle distributions, sunlight/eclipse characteristics, geomagnetic location and auroral activity conditions, as well as cold plasma information.

Five of these events were modelled by the POLAR charging code in order to identify the exact mechanisms behind charging onboard Freja. This analysis also provides a detailed description of the Freja structure and its surface materials. Some recommendations are also given for improvements of the existing charging software tools.

Spacecraft charging was analysed statistically from using all data the Freja spacecraft sampled within the time period October, 1992, to April, 1994 during declining solar activity conditions. This analysis was used to establish the occurrence and intensity characteristics of surface charging events from this polar (high-latitude) orbiting spacecraft in the altitude range 1000–1800 km. The statistics is complemented with information on the environmental characteristics during the charging events, such as cold plasma density, energetic electron and ion distributions, lightning conditions, and geomagnetic location as well as geomagnetic activity.

The detailed database of the Freja charging events is accessible through the SPEE WWW server (http://www.geo.fmi.fi/spee). The database includes all 291 charging events found in the Freja dataset. This database can be used for further studies of surface charging on the Freja spacecraft, but its primary aim is to provide an easy accessible database on environmental statistics for spacecraft charging.

4.2. The Freja satellite and its payload

4.2.1. The Freja mission

The Freja* spacecraft was launched on October 6, 1992, and ended its operations in October, 1996, two years after its planned operation time. Freja was a spin-stabilized sun-pointing spacecraft with a spin period of 6 seconds. The Freja mission objective was to study the polar (high-latitude) auroral processes and the spacecraft was therefore equipped with a highly advanced plasma payload package and the spacecraft itself was designed to be as electrically clean as possible. Such a payload package is, of course, also suitable for spacecraft charging studies. Numerous surface charging events did indeed occur with negative charging levels as large as –2000 V. No damagne were apparently associated to the charging, probably because of the high conductivity of the surface materials (see section 4.5. below). Surface charging should, however, be of concern for low-altitude hihg-inclination spacecraft design.

This study is limited to the time period October, 1992, to May, 1994, when most on-board plasma instruments provided good measurements. This time period covered a declining phase of the solar cycle from medium solar activity to minimum solar activity. The Freja spacecraft orbited Earth with a 63° inclination, with the apogee in the northern hemisphere of 1756 km, and the perigee in the southern hemisphere of 601 km. Freja therefore passed along the auroral region almost tangentially on each orbit, and can therefore be considered to be a Polar Earth Orbit (PEO) spacecraft. Only low-resolution survey data exist from below the altitude of 1000 km.

4.2.2. The Freja payload

The Freja project was designed to give high temporal/spatial resolution measurements of the auroral plasma characteristics and contained 73 kg of state-of-the-art plasma diagnostic experiments. A detailed description of all experiments onboard Freja can be found in a special Freja instrumentation issue of *Space Science Reviews* (Lundin et al., 1994). Here we just note that we have made most use of the F3H, F4, and the F7 instrumentations. The instruments are summarised below.

---

*) ***Freja***, *the goddess of fertility in Nordic mythology, was not a gentle "Afrodite of the north". She was the empress of Folkvang, the estate of the Nordic Gods, and she stood close to Odin, the almighty. She is a female warrior like Pallas Athena in Greek mythology. Her power encompassed life and death, love and battle, fertility and black magic. Half of the heroes killed in battle were her toll, sent to her for her amusement.*

MATE

The MAgnetic imaging Two-dimensional Electron spectrometer (MATE) measured electron energy and angular distributions in the energy range 0.1-100 keV. MATE consisted of a 360° field-of-view sector magnet energy analyser with 90° deflection angle for simultaneous energy and pitch-angle determination. The sampling rate for the full energy range was 10 ms, and a collimator system enabled measurements of the energy spectrum at 16 energies (with resolution $\Delta E/E = 30$ %) and 30 angular sectors.

Unfortunately, the MATE instrument was not deployed completely and was to 1/3 blocked by the Freja spacecraft itself and only every 4th angular sector provided data. Furthermore, the instrument did work properly up to orbits around 1600 only, whereafter only the integrated flux of the high energy electrons (with some pitch-angle information) could be obtained. This instrument was otherwise the only instrument onboard Freja that could give accurate information on the high-energy electrons.

TESP

The Two-dimensional Electron SPectrometer (TESP) on Freja consisted of a "top-hat" style sweeping electrostatic analyzer. The energy range of 20 eV-25 keV was covered by 32 sectors to complete a spectrum. Depending on instrument mode, 16 or 32 spectra were returned each second (31.25 ms resolution). The angular field-of-view was the full 360° and electrons were counted in 32 equally spaced bins, yielding an angular resolution of 11°. The entrance aperture of TESP also contained a set of electrostatic deflectors which allows the plane of acceptance to be "warped" into a cone.

The TESP experiment started working around orbit 720, when the instrument software were sent to the spacecraft after the launch. TESP data cover energies up to 25 keV, but give nontheless important information regarding the high energy electrons. Since low-energy electrons may cause an excess emission of secondary electrons (and thereby stabilize charging), the information from this experiment is very usefull.

TICS

The Three-dimensional Ion Composition Spectrometer (TICS) measured the positive ion distributions in the energy range 0.5 eV/q–5 keV/q. TICS carried out measurements perpendicular to the spacecraft spin plane and thus gave 3D ion measurements every 3 s. TICS consisted of a spherical "top-hat" electrostatic analyser with 16 or 32 energy steps sampled each 10 ms. This means that one 16 step energy sweep took 160 ms + 40 ms for adjusting the high voltage. TICS also gave limited ion composition information in the range 1–40 amu/q. This instrument gave us the best measurement of the degree of negative charging, since the whole ion population was accelerated toward the spacecraft and the whole ion population could be detected at energies corresponding to the potential of the spacecraft. Even as small negative potentials as –5 V can be seen in the TICS data.

Langmuir probes

Freja carried 4 spherical probes (P3-P6), which could be operated in the Langmuir mode, situated on wire booms, and a cylindrical Langmuir probe (CYLP). The CYLP was almost always available, but the operation of the spherical probes depended on measurement mode for the orbit in question. The spherical LPs were 6 cm in diameter and coated with graphite (Dag 213). They were situated 5.5 m (P5 and P6) and 10.5 m (P3 and P4) from the spacecraft respectively. The CYLP is 57 cm long and 1 cm in diameter, and was made of carbon fibre. It was mounted on the DC magnetometer stiff boom (2 m from the spacecraft) parallel to the spin axis. As the spin axis was "sun-pointing" within 30°, this minimised the projected surface area and thus the photoelectron emission.

A Langmuir probe samples all current contributions in a plasma at a certain bias potential, with respect to the spacecraft floating ground, according to its current-voltage characteristics. Therefore, a LP yields a direct measurement of the charge state of the probe (and spacecraft). Most often this measurement gives information on the density and electron temperature of the ambient thermal plasma, since the sampled probe current is directly proportional to $n_e / \sqrt{T_e}$ and since the ambient thermal electron current usually dominates the current collection. However, when the spacecraft (and probe) attains a large negative potential (i.e. a large negative charge) with respect to the surrounding plasma, the thermal electrons start to become repelled from the LP. If the negative potential becomes much larger than the average energy of the thermal electrons (typically below 2 eV), a majority of these electrons cannot easily reach the negatively charged LP, and the probe current drops sharply to very low values more characteristic for the collected ion thermal current. A LP current below $5 \cdot 10^{-8}$ A therefore either indicates a negative charging event of at least a few V negative or a very low electron density below 10^7 m^{-3}. The sampled LP current is therefore a very sensitive measurement for spacecraft charging, even though it does only give a threshold value for the negative potential during charging events.

Plasma wave instruments

The plasma wave experiments (F4) measured in three frequency ranges, LF (5–2000 Hz), MF (5 Hz–16 kHz) and HF (10 kHz–4 MHz). The LF measurements most often consisted of 4 simultaneously sampled waveform components of several possible types and the MF consisted most often of 2 simultaneous waveform components. All wave measurements were normally made in snapshots of various lengths and duty cycle, dependent on sampling rate, telemetry allocations, etc. There were 3 pairs of spherical probes, P12 (21 m), P34 (21 m), and P56 (11 m) mounted on three wire boom pairs in the satellite spin plane. Four of the probes (P3, P4, P5, and P6) could be used for either electric field measurements (potential mode) or plasma density measurements (current mode). Probes P1 and P2 were only used for electric field measurements. The HF measurements were made either with the P12 probe pair or a special short (1.2 m) antenna probe pair (PAB) mounted on one of the magnetometer booms. Freja carried also a Search Coil Magnetometer (SCM) assembly consisting of three identical coils which were mounted orthogonally, one parallel to the spin axis and the other two in the spin

plane. All signals were transmitted to the ground as waveforms and there was no onboard treatment except filtering, A/D conversion and intermediate storage.

During a charging event the LF and MF electric field measurement became strongly disturbed up to rather large frequencies due to large negative potentials of the probes. This is due to the fact that the potential between the spacecraft and each of the probes were measured separately and the total potential between the probes is just the difference between these results. Unfortunately the work point of these measurements only allow for a +/–50 V change, which obviously was exceeded during charging events. The HF measurements on the other hand make use of the short PAB booms and measure the relative difference in potential between these probes directly. Therefore no large disturbances occurred on the HF measurements during charging events.

Magnetometer

The FluxGate Magnetometer (FGM) was mounted on a 2 m long boom, and gave the full 3D vector measurements of the DC geomagnetic field as well as magnetic variations with 128 samples/s. The magnetic fluctuation level was often a good measure of the auroral activity, and the magnetic measurements seemed not to be affected by charging events in any way.

Experiment	***Measurement***	***Principal Investigator***
F1 Electric Fields	3 pair of wire booms (< 3 kHz)	Göran Marklund
F2 Magnetic Fields	3-axis fluxgate magnetometers (< 64 Hz)	Lawrence Zanetti
F3H Hot Plasma	2D electron spectrometer (MATE, 0.1-115 keV) 2D ion composition spectrometer (TICS, 1 eV-10 keV)	Lars Eliasson
F3C Cold Plasma	3D ion/electron distr. (<300 eV)	Brian Whalen
F4 Plasma Waves	3 wire boom pairs, 3-axis search coil magnetometers, HF booms (E, B, dn/n, 1 Hz-4 MHz)	Bength Holback
F5 Auroral Imager	2 UV CCD Cameras	John S. Murphee
F6 Electron Beam	3 electron guns (3D of E-field)	Götz Paschmann
F7 Electron Spectrometer	2D electron spectrometer (TESP, 0.01-20 keV)	Manfred Boehm

4.3. Examples of Freja charging events

4.3.1. Methodology

Several selection criteria are necessary for identification of charging events on the Freja spacecraft in order to distinguish these events from naturally occuring plasma processes

(e.g. transverse ion heating events in connection with plasma density cavities). One very sensitive indicator for negative charging events is that the Langmuir probe (LP) current drops to values below about $5 \cdot 10^{-8}$ A, because very few thermal electrons can reach the negatively charged probe. A strong negative potential of the spacecraft also causes the surrounding ion populations to accelerate toward the spacecraft. The ion spectrometers onboard Freja (e.g. TICS) detected a general increase in energy of all ion components when this happened. This general increase has a different appearance in the data compared to naturally occuring ion heating events, in that a "string" of enhanced flux is detected at all pitch-angles rather than showing conic characteristics. Unfortunately, ion heating events and spacecraft charging events occured simultaneously at times. A third indicator is that the low-frequency electric field measurements became strongly disturbed.

We employ the following methodology when identifying surface charging events on the Freja spacecraft:

1) The sampled Langmuir probe currents of the spherical probes (P3, P4, P5, P6) as well as the cylindrical (CYLP) probe are below $2 \cdot 10^{-8}$ A. This either means that the plasma density is extremly low or the probes are negatively charged to a few V.

2) The narrowband Langmuir emission (in the HF) indicates a larger density than the Langmuir probe currents would indicate. During charging events the narrowband HF emission is often unaffected, while the LP currents drops to very low values, thus suggesting that the density remains larger than the LP current would indicate.

3) The TICS data show a clear lift in energy of the whole ion population at least 5 eV, and the ion distribution characteristics show a well-defined energy "strip" at most pitch angles. If the ion distributions have characteristics similar to transverse ion heating events (ion conics), they are only kept as suspected charging events if there is a clear miss-match between the density inferred from the Langmuir probes and the HF narrowband emissions.

4) The events should show disturbances in the LF and MF electric field data. This is not a requirement for identifying a charging event, though.

4.3.2. Determination of plasma density

The HF measurements of narrowband Langmuir waves, and/or the upper cutoff of electrostatic whistler type waves, give us the best estimate for the electron density from

$$f_{pe} = \frac{1}{2\pi}\sqrt{\frac{n_e e^2}{\varepsilon_0 m_e}} \quad \Leftrightarrow \quad n_e = \frac{\varepsilon_0 m_e}{e^2}\left(2\pi f_{pe}\right)^2$$

The electron density inferred in this way varies most of the time almost exactly as the probe current measured by the LPs. This correlation strongly supports the interpretation

that both the narrow-band HF signals and the probe current give the plasma density. However, during surface charging events the sampled LP current drops to very low values and cannot longer be a good estimate for the plasma density. In such cases the narrowband Langmuir emission (if existing) is a very useful tool for determining the electron density (about 10 % accuracy).

The conversion factors between plasma density and sampled LP currents are based on calibrations against the HF plasma frequency emissions for a statistically significant dataset. The following conversion factors have been obtained (Carlson, 1994):

Probe	**[m^{-3}/A] in Eclipse**	**[m^{-3}/A] in Sunlight**
Spherical Probes	$1.2 \cdot 10^{15}$	$7.5 \cdot 10^{14}$
CYLP	$8.8 \cdot 10^{15}$	$2.1 \cdot 10^{15}$

These conversion factors are accurate to within 95 % confidence.

Another check of plasma density can be gained from the lower frequency cutoff of whistler waves belonging to the dispersion surface connected to the lower hybrid waves. This cutoff usually occurs around a few kHz. During a charging event the MF electric field measurements are strongly disturbed, but the weak magnetic component of the whistler emission (as measured by the SCM) is often sufficient to determine this cutoff. The cutoff occurs near the lower hybrid frequency, given by

$$f_{LH} = \frac{f_{pi}}{\sqrt{1 + f_{pe}^2 / f_{ce}^2}}$$

and is therefore dependent on the ion composition. This cutoff thus gives a rough estimate of the plasma density.

4.3.3. Orbit 790, a typical charging event

Orbit 790 is famous in the Freja community because a well-developed substorm took place during this orbit and several papers have been written about it. However, no one has addressed the charging event that seems to have taken place in the middle of the auroral activity and transverse ion heating. Figure 4.3-1 displays the overview particle data.

Between 0233:00 UT and 0243:00 UT a large auroral disturbance occurred with large fluxes of high-energy electrons as measured by both the TESP instrument (panel 7) and the MATE instrument (panel 5). The ion population was uplifted in energy in the time interval 0234:00–0239:00 UT. Most of this particular time interval occurred during sunlight conditions (panel 4), and only the later part of the event was in eclipse, where most Freja charging events yook place. The first part of the auroral event between 0233:00–0236:00 UT was most probably related to transverse ion heating, since there was no dropout in the LP current during this period. The later part is presented in more detail in Figures 4.3-2 and 4.3-3.

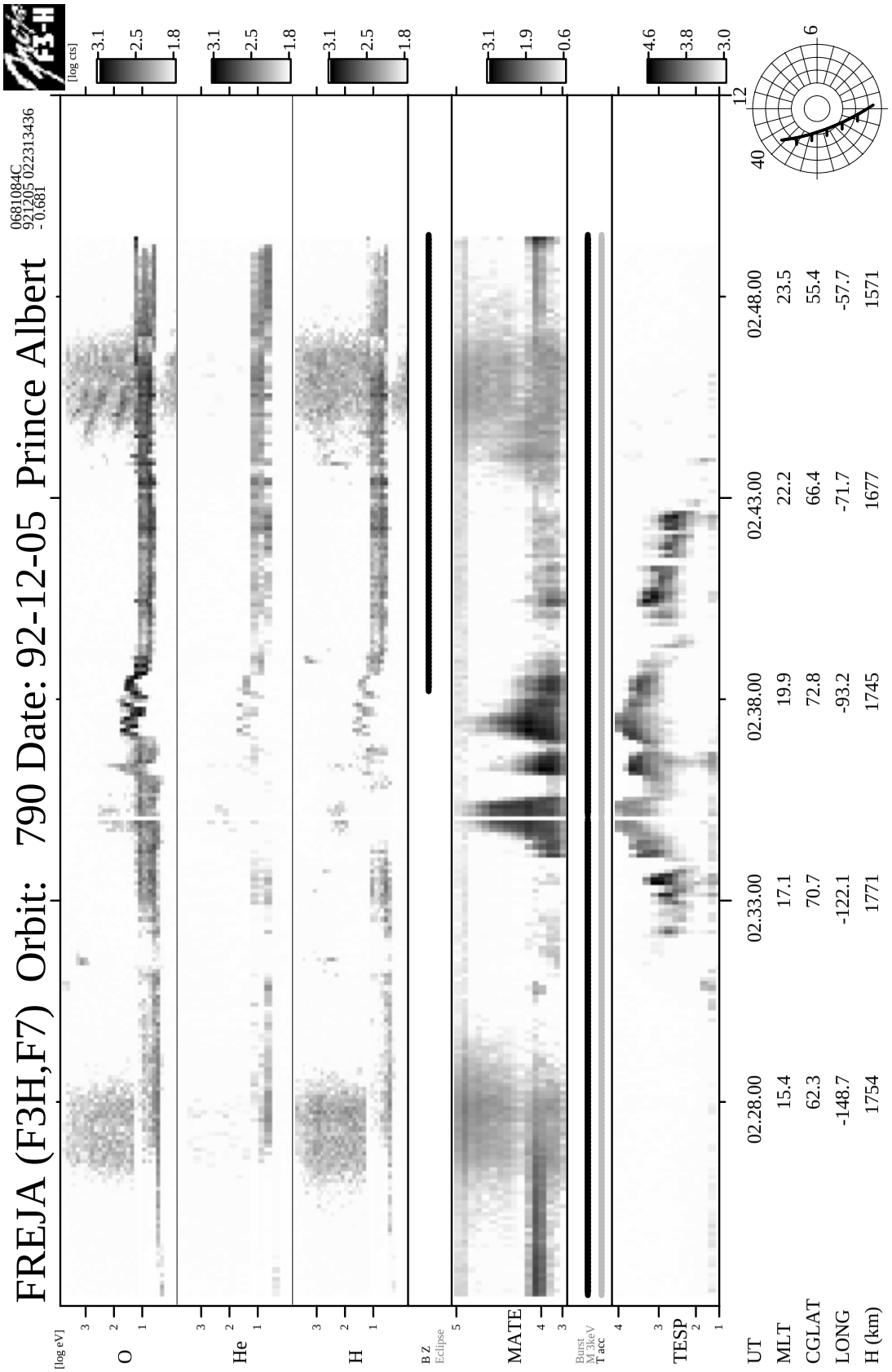

Figure 4.3-1. Overview of orbit 790 particle data. The charging event took place near the terminator at 0238:00 UT.

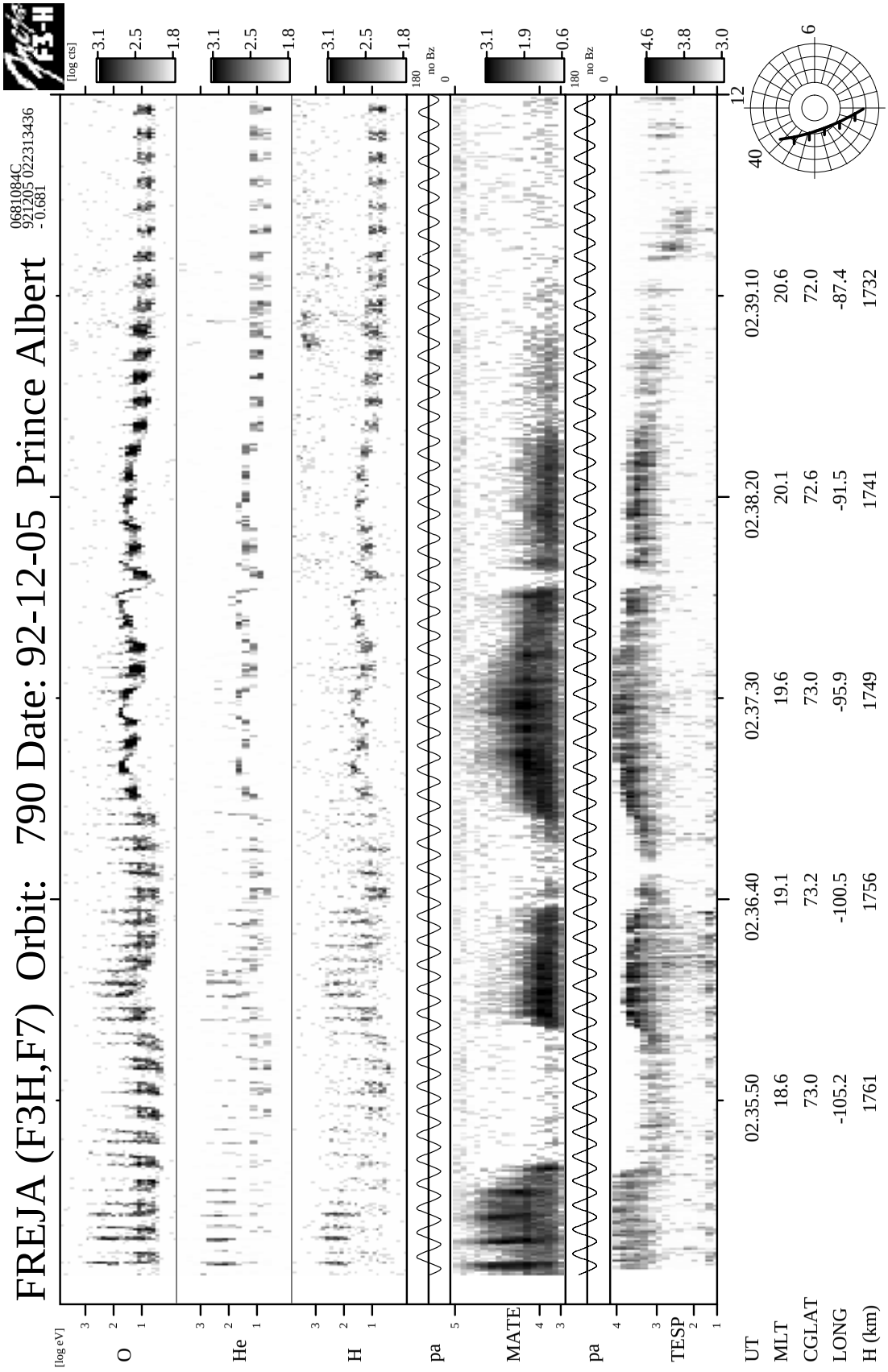

Figure 4.3-2. Orbit 790: A blowup of the particle data. A one-to-one correspondence exist between the intensity and energy of the inverted-V peak and the charging level (as detected by the uplifted energy of the ions).

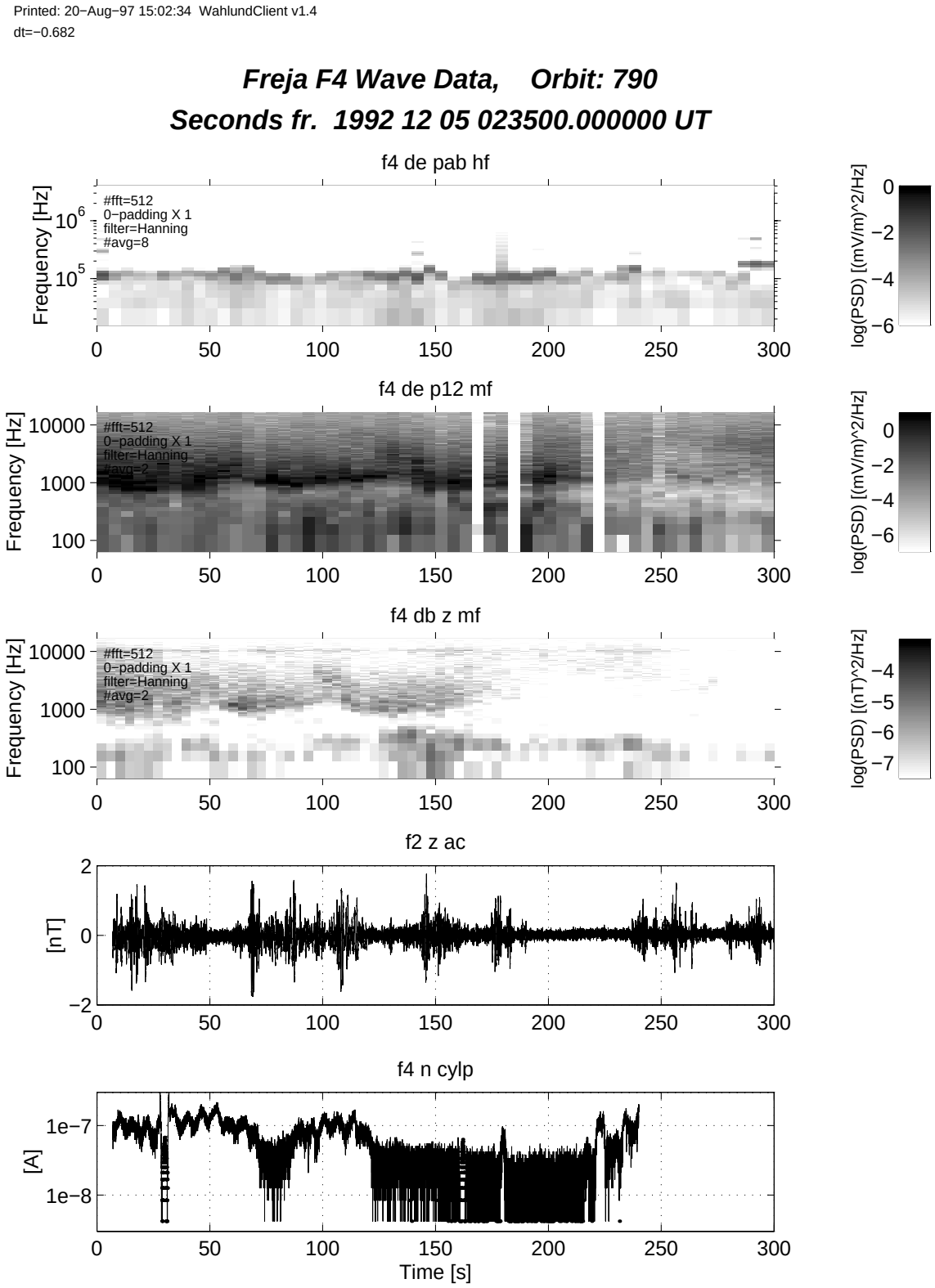

Figure 4.3-3. Orbit 790: Plasma wave data corresponding to the particle data in Figure 4.3-2. From top to bottom; HF electric data, MF electric data, MF search coil data, FGM time series, and Langmuir probe current (CYLP).

The estimated density from the HF narrowband emissions (Figure 4.3-3, panel 1) was rather constant for the whole displayed interval and attained values close to $1.2–2.8 \cdot 10^8$ m^{-3}, while the CYLP current (panel 5) occasionally dropped to very low values. Spacecraft charging is therefore suggested during the current drops. The ions were uplifted in energy to almost 100 eV (Figure 4.3-2, panels 1-3) during the CYLP current dropouts, and enhanced fluxes of high energy electrons (panels 5 and 7) correlated well in both flux intensity and maximum energy. We interpret these results that the electron flux and peak energy are major factors determining the charging level for a given plasma density.

A series of TESP are presented in Figures 4.3-4a –c, which together cover the time period 0236:40–0238:10 UT. For corresponding MATE spectra see WP-110-TN. Note how the spectra evolved with time when the charging event started, reached its maximum, and then relaxed. The maximum of the inverted-V peak reached large energies up to 10 keV during maximum charging, where also the largest electron fluxes at the highest energies occurred. The precipitating electron fluxes were close to isotropic and belonged to an inverted-V event. Thus, during the charging event the maximum flux of energetic electrons at the peak moved above the crossover energies of ITOC (2.5–3 keV) and the thermal blanket (just below 4 keV, see section 4.5. below). This suggests that the flux of the emitted secondary electrons could no longer balance the incident energetic electron flux, and in this way caused the observed negative charging. Also, the flux levels in the high energy tail up to 60 keV increased with about an order of magnitude, which further contributed to the excess charge accumulation.

Ion distributions around maximum charging are displayed in Figure 4.3-5a. They show the typical energy-lifted all-pitch-angle distribution of a charging event up to –65 V. Some indications of simultaneously occurring ion conics can be seen around 90° pitch-angle. For comparison, ion distributions from the ion conic event preceeding the charging event, are presented in Figure 4.3-5b, where clear ion conics with energies up to 1.5 keV can be seen.

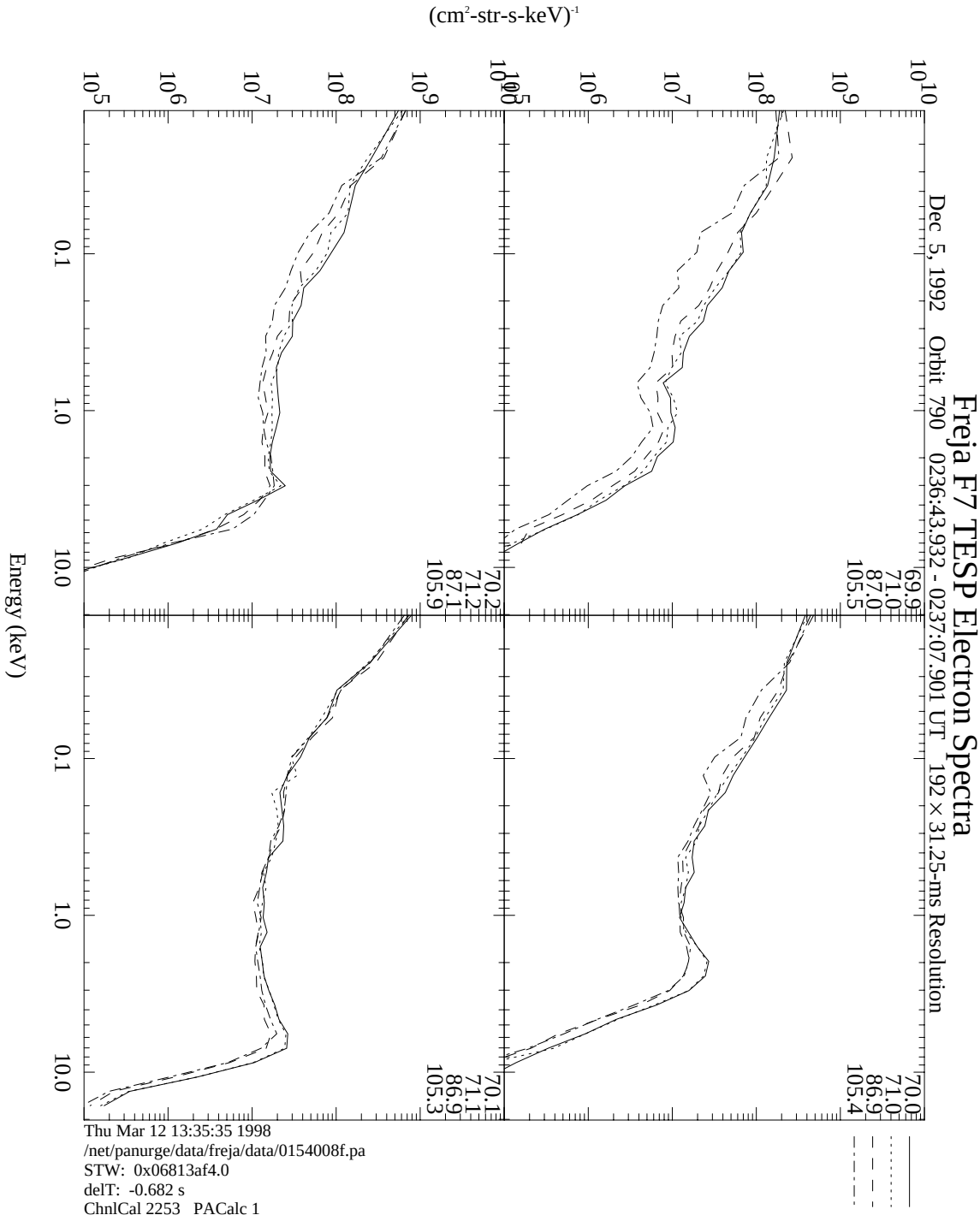

Figure 4.3-4a. Orbit 790: TESP electron spectra. Significant charging started to occur at a time corresponding to panel 4, when the inverted-V peak energy have risen above a few keV.

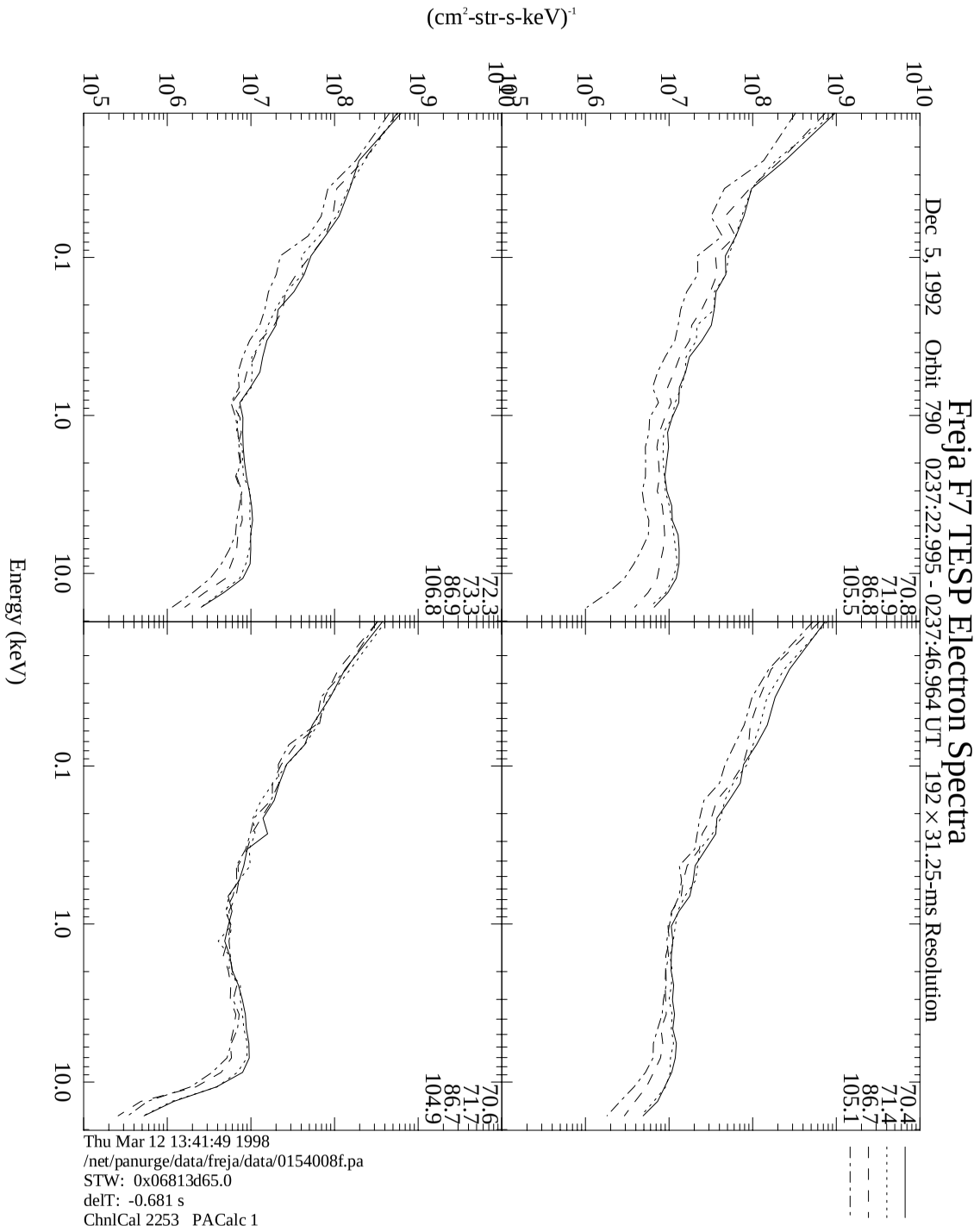

Figure 4.3-4b. Orbit 790: TESP electron spectra from a charging event.

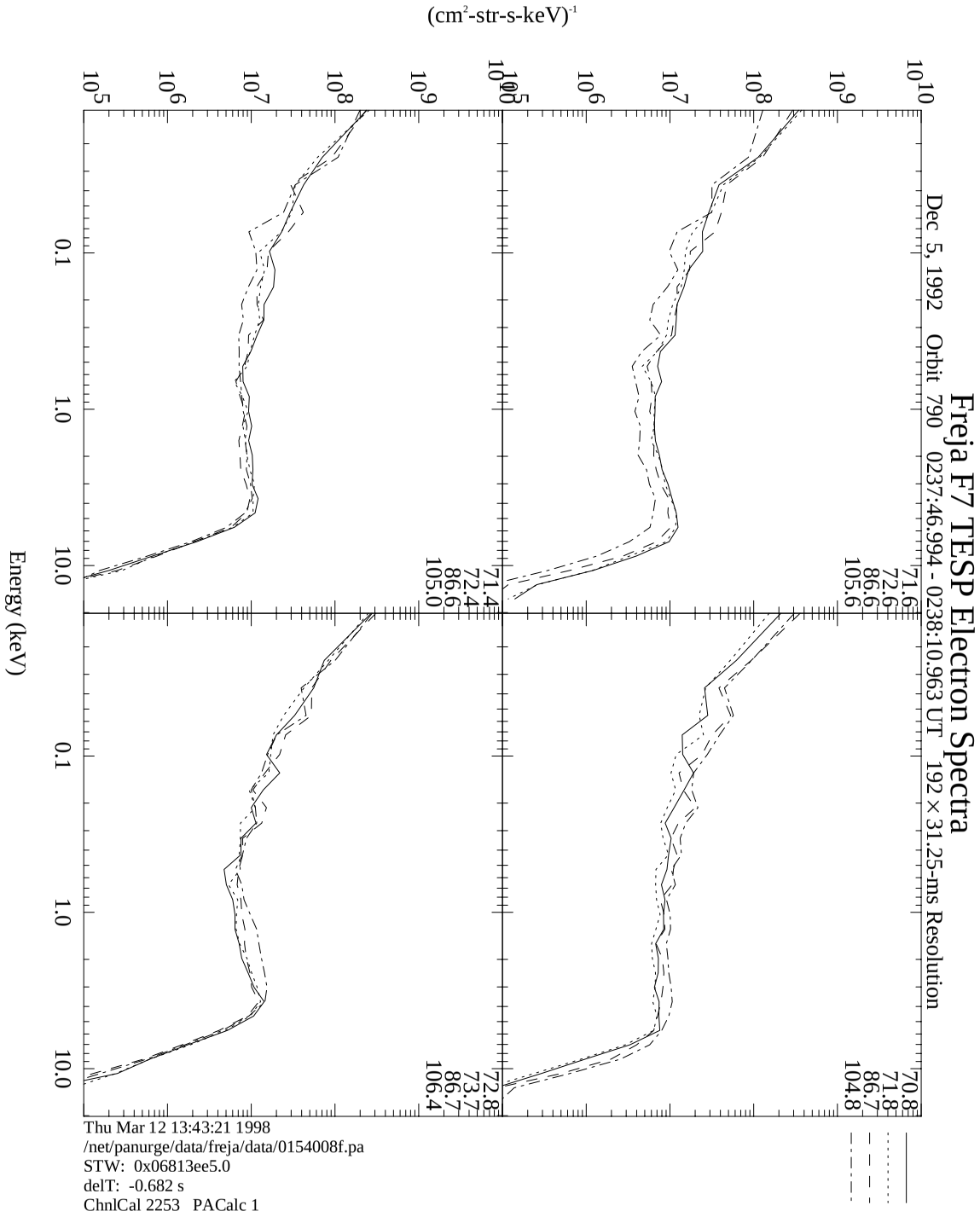

Figure 4.3-4c. Orbit 790: TESP electron spectra from a charging event.

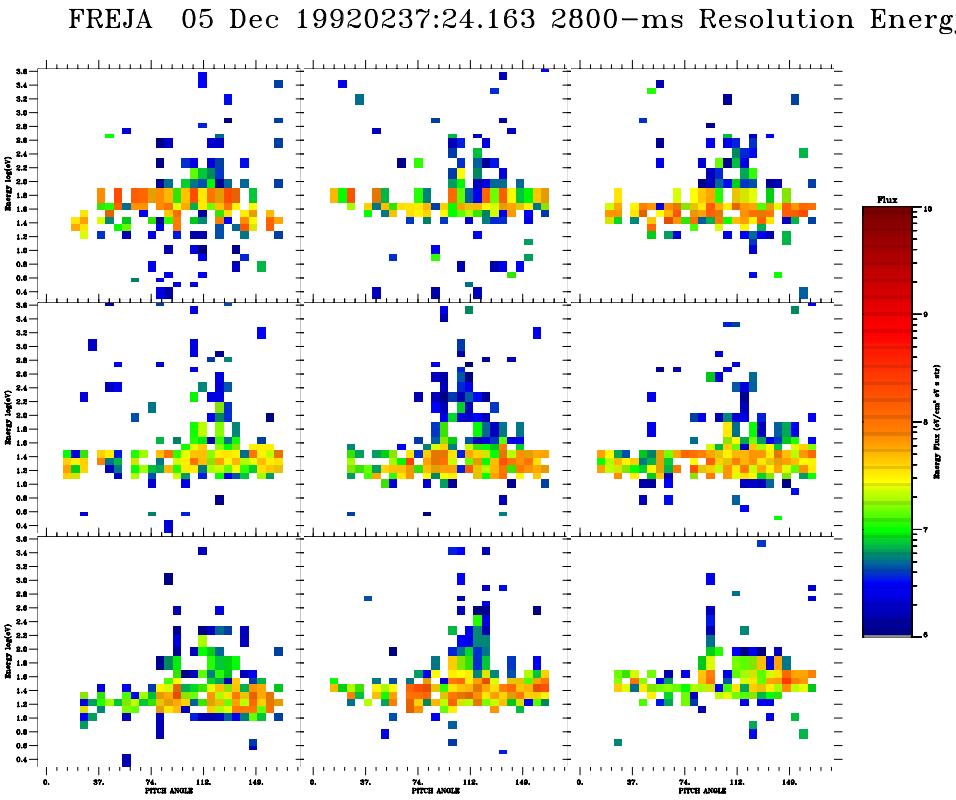

Figure 4.3-5a. Orbit 790: Ion distributions around maximum charging. They show the typical energy lifted all-pitch-angle distribution of a charging events up to –65 V.

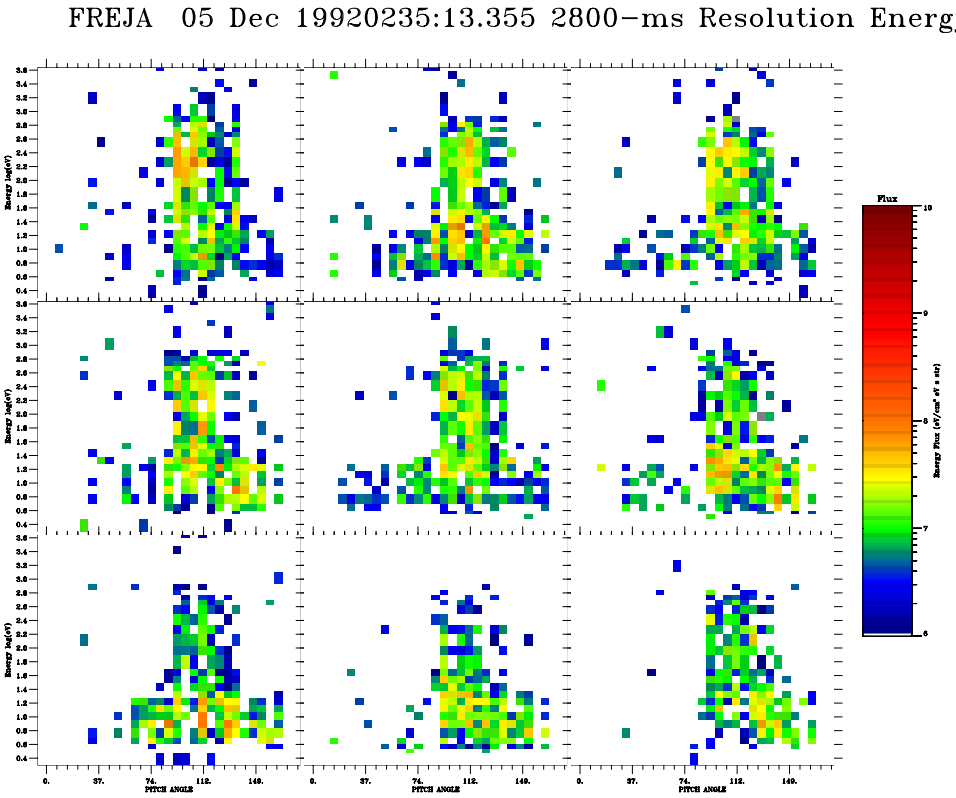

Figure 4.3-5b. Orbit 790: Ion distributions from the ion conic event preceeding the charging event. 4.3.4. Orbit 1666, one of the largest charging potentials

4.3.4. Orbit 1666, one of the largest charging potentials

The overview data for the particle measurements from orbit 1666 are presented in Figure 4.3-6. This event represents one of the largest observed charging levels observed in the Freja dataset. The ions are lifted in energy between 0916:00–0919:00 UT (panels 1-3). The event is associated with enhanced fluxes of high energy electrons which are part of an inverted-V (panel 7). The whole event occurred during eclipse (panel 4). The MATE measured only the integrated flux during this orbit.

Figures 4.3-7 and 4.3-8 display the blowup of the particle and plasma wave data around the uplifted ion event. Densities during the charging event varied between 1-$2 \cdot 10^8$ m^{-3} according to the upper cutoff of the HF emissions (panel 1, Figure 4.3-8). In this case the thermal plasma density indeed did decrease when the charging event appeared, which was not the usual case during other charging events in the Freja dataset. The ion energy attained values up to about –2000 V near 0918:00 UT (panel 1, Figure 4.3-7), a time when the energetic electron fluxes became as most intense and the peak energy rose to its largest value (panels 5 and 7, Figure 4.3-7).

Detailed TESP spectra during the event are displayed in Figures 4.3-9a and 4.3-9b. The inverted-V peak became displaced upward in energy during maximum charging, and the peak energy was probably even above maximum measured energy (25 keV). The peak flux, on the other hand, stayed rather constant during the event. The last panel in Figure 4.3-9b, which is from the time after the charging, shows evidence of field-aligned suprathermal electron bursts in the energy range 30–1000 eV.

4.3.5. Conclusions of the detailed study of Freja charging events

More details of these and the other 8 events studied in this investigation can be found in the Technical note SPEE-WP110-TN, which is available through the www-server http://www.geo.fmi.fi/spee/docs/

The following observational conclusions can be made from the detailed study regarding surface charging on the Freja spacecraft:

- All detected charging events were related to the presence of auroral inverted-V energetic electrons, at least down to time scales of the order of 1 s.
- Charging levels up to –2000 V have been observed in eclipse although the main coating material, Indium Tin Oxide (ITO), is known to have high secondary electron emission properties.
- There is a clear proportionality between charging level and the rise of the energetic electron peak energy (and the electron flux is most often enhanced an order of magnitude at the peak energy). The highest level charging events have the highest energy peaks and fluxes.
- A high energy tail up to at least 80 keV is observed during the charging events. In some cases large fluxes of MeV electrons occurred simultaneously as inferred from the contamination of the ion measurements. Such MeV electron population

only appears during the most extreme charging events and most probably is an extension of the enhanced high energy tail. MeV electrons could penetrate the upper surface layers and possibly cause internal charging.

- A threshold energy for the inverted-V peak of about 5 keV is inferred, while no charging developed below this value. Even the low level charging events of just a few volts negative were associated with energetic electrons above this threshold.
- Most charging events occurred during eclipse, but a few took place during sunlight conditions. The peak energy threshold was larger (> 10–15 keV) during sunlight conditions.
- There is only weak indication that low energy suprathermal electron bursts below 1 keV could have inhibited charging on Freja.
- The thermal plasma density did not usually change significantly when Freja encountered a charging event as compared to the surrounding densities. Also, there is only weak indication (from orbit 736) that the thermal plasma density affected the charging levels significantly.
- Thermal plasma density was rather low ($< 10^9$ m^{-3}) during charging events.
- Several of the plasma instruments showed serious operation disturbances during high level charging events (above a few tens of volts negative). The Langmuir probe currents dropped to almost zero current due to the fact that few thermal electrons reached the probes. The same effect made the LF and MF plasma wave measurements impossible, and the TICS instrument showed almost ring distributed ions due to the fact that the ions were accelerated toward the spacecraft. In some events some plasma instruments just stopped working properly after a high-level charging event.
- Transverse ion heating show similar characteristics in the ion spectrometer data (TICS) as those during a charging event. Only careful analysis or a trained eye can easily differ between the two interpretations.
- No arcing or EMC problems have been identified during the charging events presumably because most of the spacecraft was very conductive.

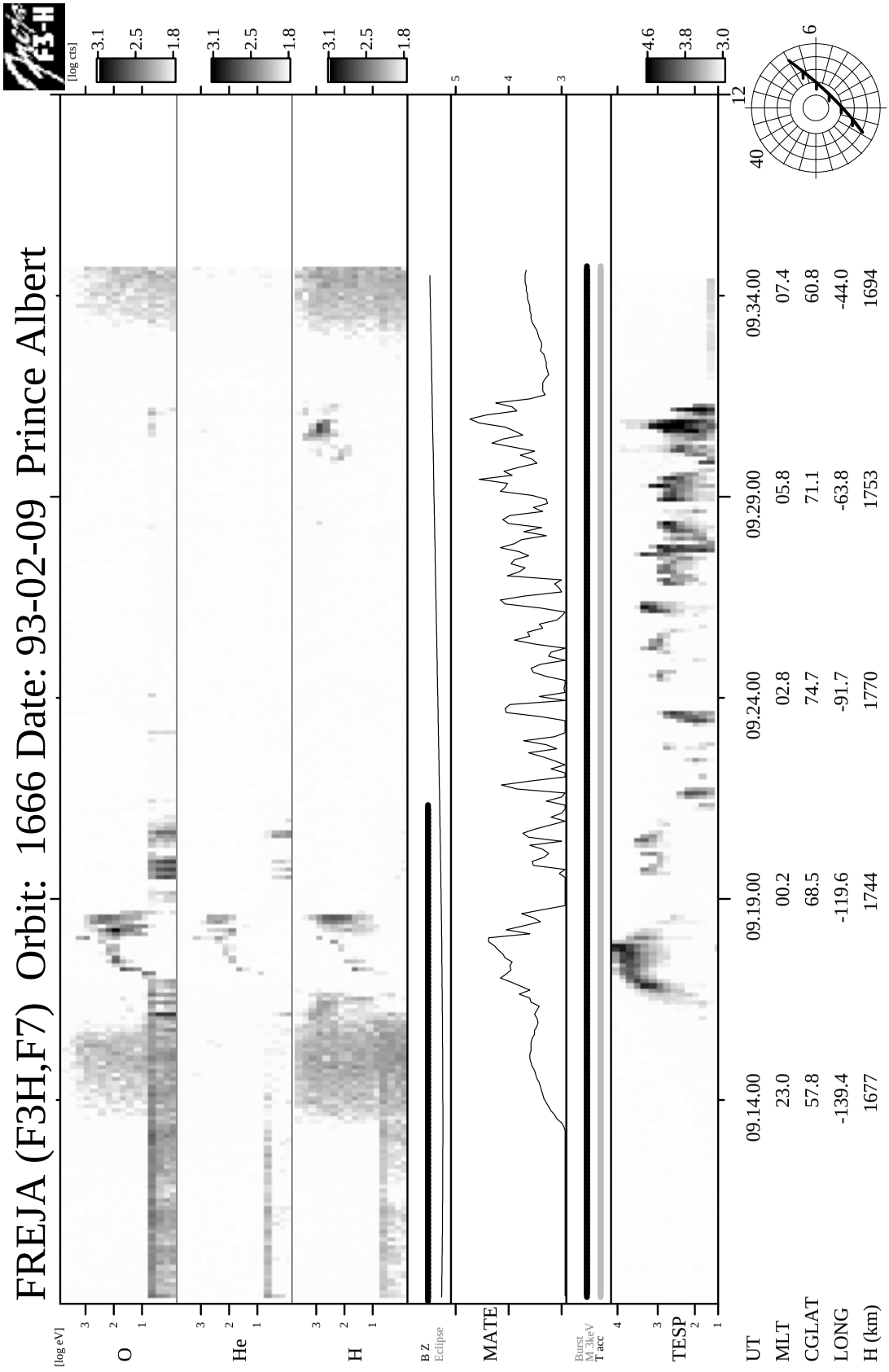

Figure 4.3-6. Overview of orbit 1666 particle data. This event represents one of the largest observed charging levels in the Freja dataset. It occurred during an intense auroral inverted-V event.

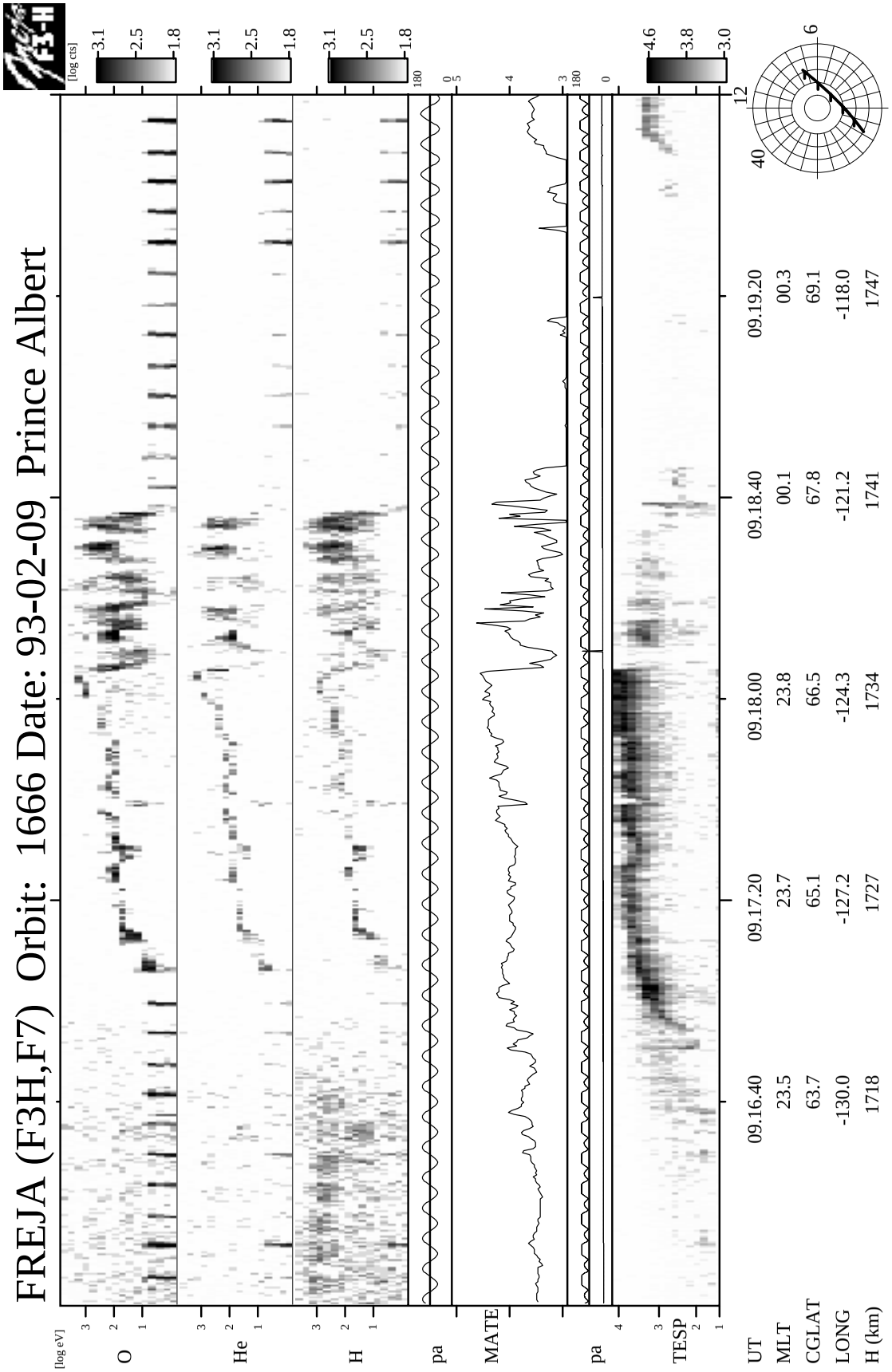

Figure 4.3-7. Orbit 1666: A blowup of the particle data. A trained eye can sort out the difference in the TICS ion data between the charging event (around 0917:00–0918:00 UT) and the later on occuring transverse ion heating event.

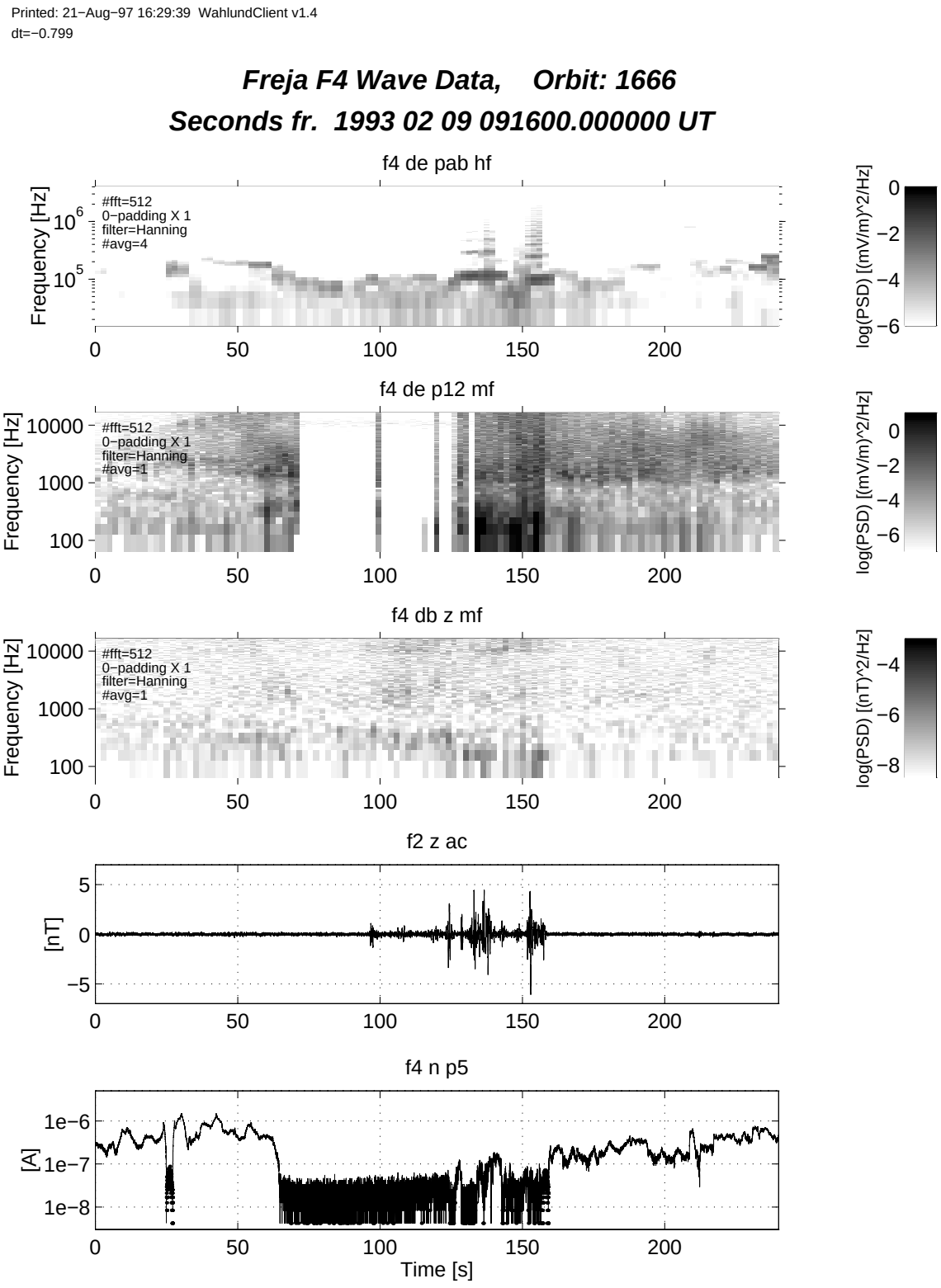

Figure 4.3-8. Orbit 1666: Plasma wave data corresponding to the particle data in Figure 4.3-7.

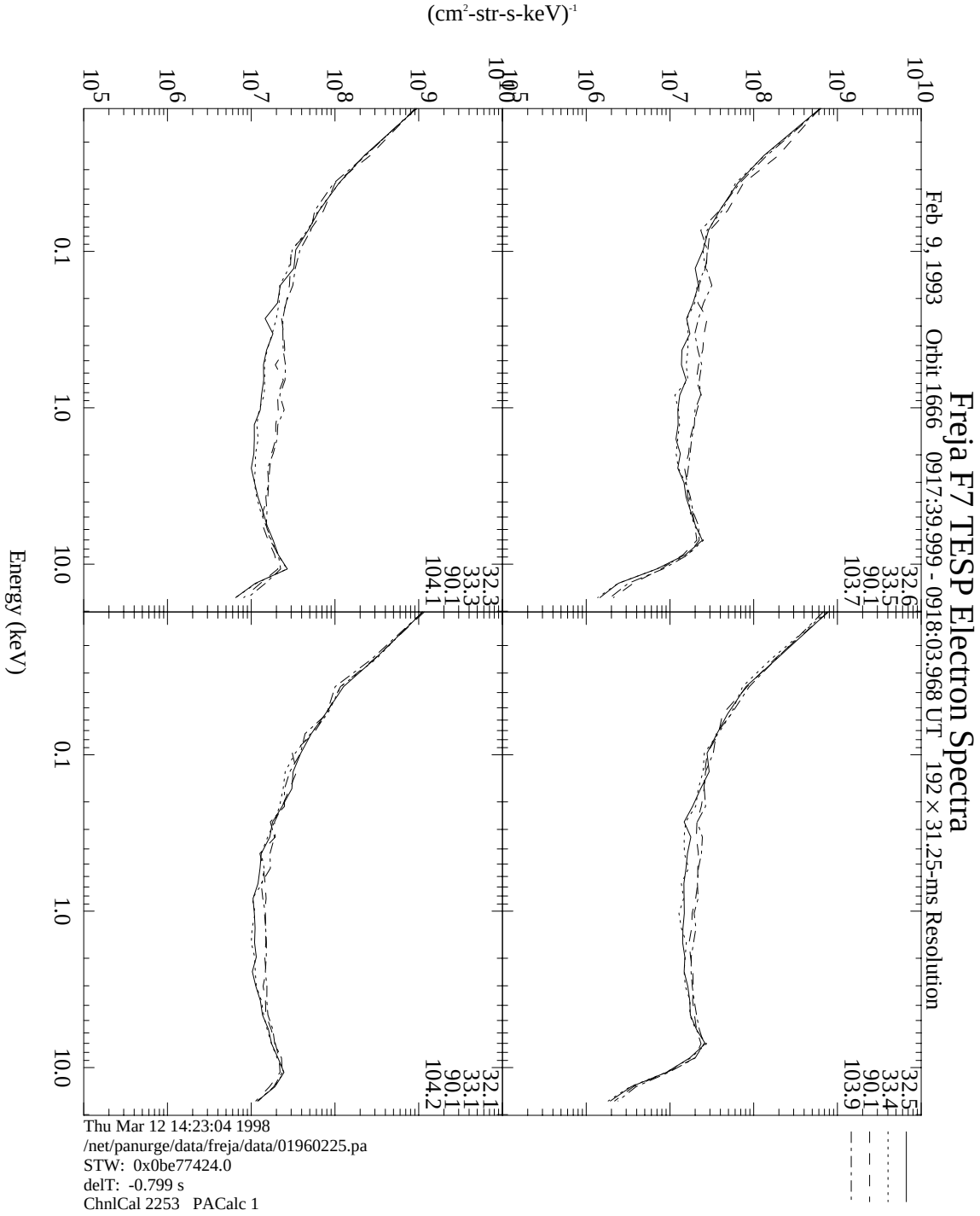

Figure 4.3-9a. Orbit 1666: Detailed TESP spectra during the charging event. The inverted-V peak becomes displaced upward in energy during maximum charging.

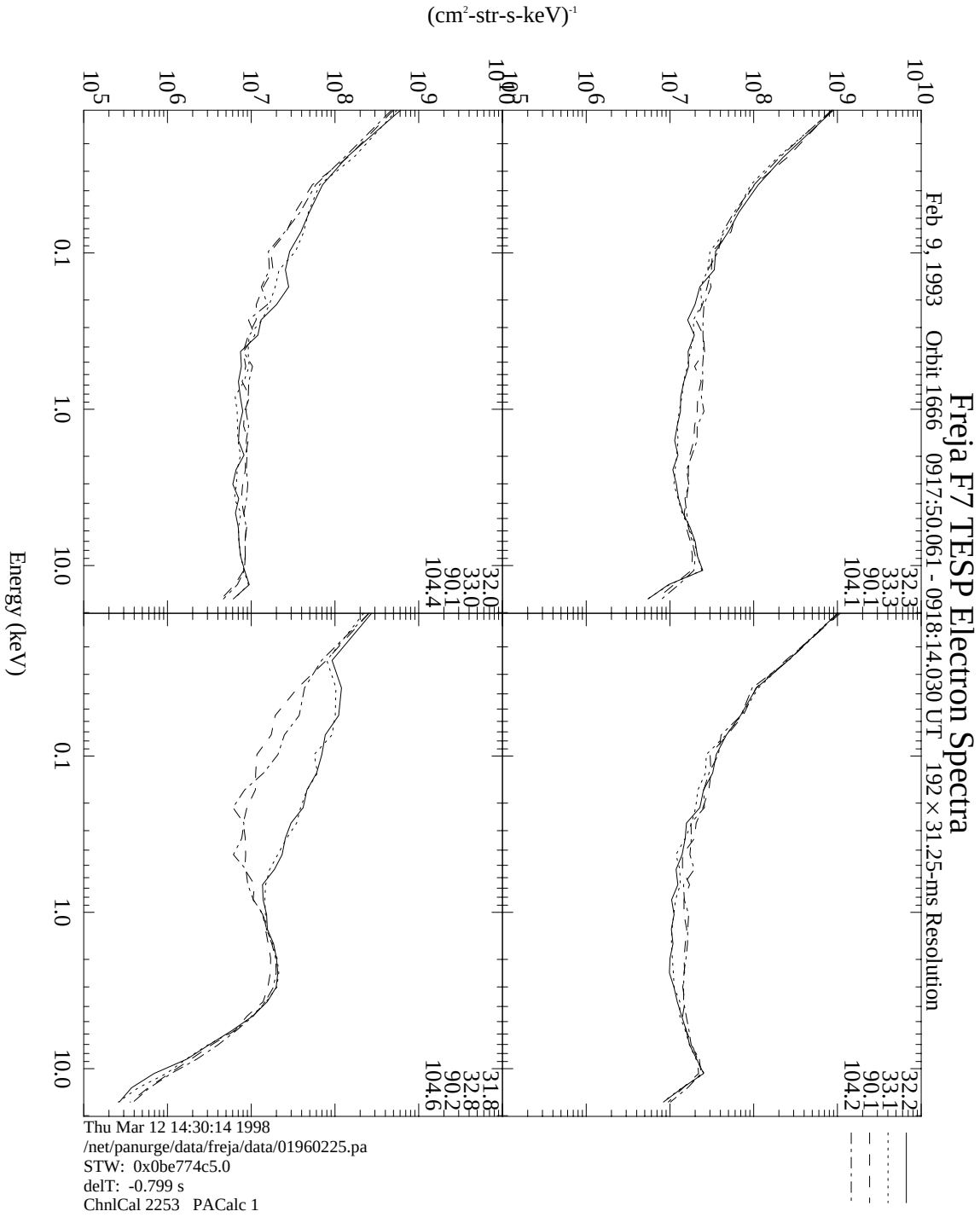

Figure 4.3-9b: Orbit 1666: A continuation of Figure 4.3-9a.

4.4. Statistics of Freja charging events

4.4.1 Amount of data and charging characteristics

This statistical study includes 291 charging events found in the time period October, 1992, to May, 1994. All ephemerid data up to orbit 10,000 were used for normalisation of the statistical data presented below. Five evenly distributed occasions were selected

from each orbit for which orbit number, date, altitude, corrected geomagnetic latitude (CGLAT), magnetic local time (MLT), longitude and universal time (UT) were extracted. Only occasions where real data existed were kept for the normalization.

Most of the charging events were low level charging events, i.e. peak charging below 10 V (Figure 4.4-1). However, a few of the Freja charging events reached larger potentials than –2000 V. The duration of the main part of the Freja charging events (Figure 4.4-2) were shorter than one minute, but a few lasted several minutes.

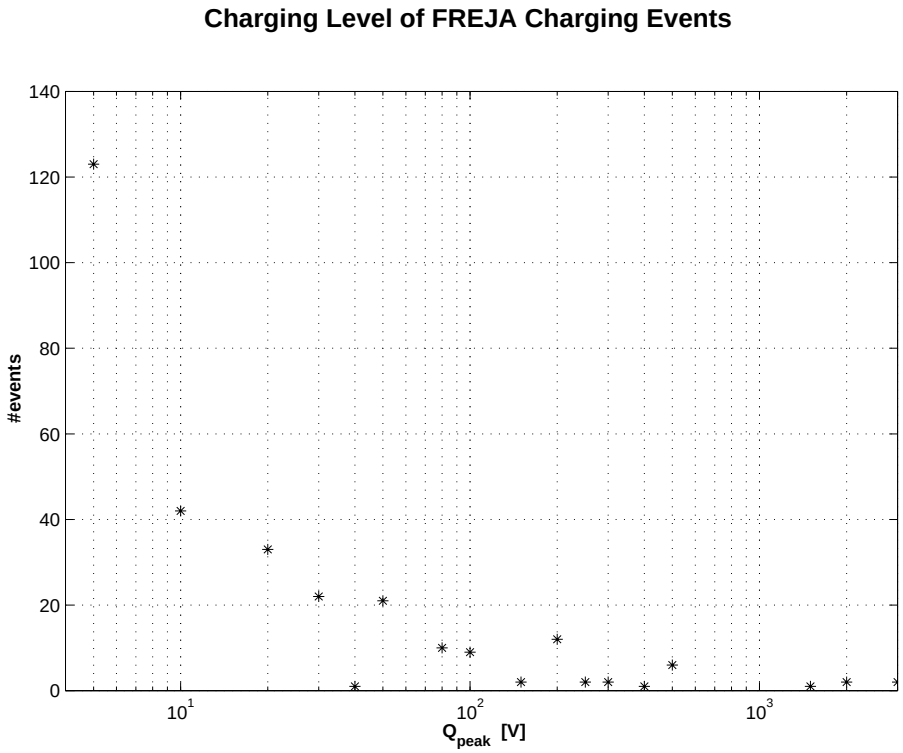

Figure 4.4-1: The charging level distribution.

The charging levels were 2–3 times larger than those reported from the DMSP F6 and F7 satellites traversing an altitude of 840 km (see e.g. Gussenhoven et al., 1985; Stevens and Jones, 1995). This is somewhat remarkable, because the Freja was designed to be as conductive as possible and therefore should be much harder to become charged. On the other hand, Freja traversed higher altitudes and therefore lower plasma density regions, a physical parameter that has been suggested to be of importance for surface charging (Frooninckx and Sojka, 1992). Also, the Freja charging levels were well below the maximum charging levels detected on spacecraft in GEO, such as the ATS-5, ATS-6 and the SCATHA (P78-2) satellites (e.g. Mullen et al., 1986; Olsen, 1983), where charging levels of several thousand volts are achieved.

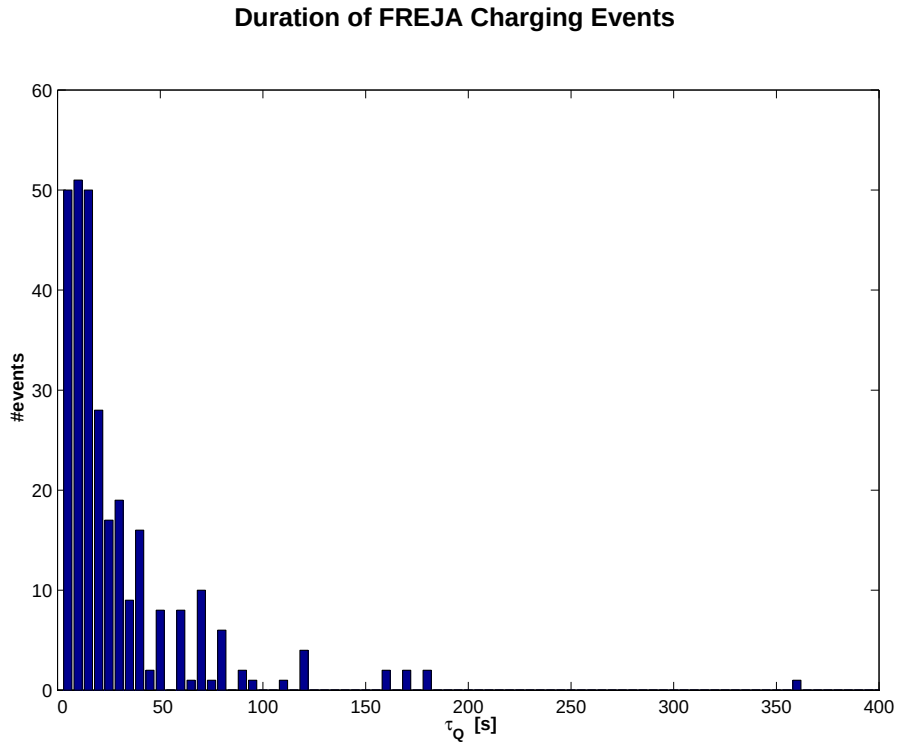

Figure 4.4-2: Duration of charging events.

4.4.2. Variation with sunlight conditions

The Freja charging events were distributed with respect to sunlight conditions according to the following:

- 32 events occurred during sunlight
- 236 events occurred during eclipse
- 23 events occurred close to the terminator

Most Freja charging events occurred during the dark winter months as can be seen in Figure 4.4-3, where the periods between November and February host most of the Freja charging events. The sunlight events (dark portion at bottom of bars) were possibly more spread out over the year, but no events were detected during the summer months.

4.4.3. Variation with geomagnetic location

The variation in Magnetic Local Time is presented in Figure 4.4-4. Freja charging events occurred clearly during nightime hours with an event peak around 22:00–23:00 MLT. Almost no charging events were found between 06:00 and 18:00 MLT. Thus most charging events occurred in the absence of the photoelectron emission from the spacecraft. We want to stress that this is not an effect due to the fact that charging events only occur in certain latitude or longitude regions because all MLT zones were covered rather evenly by the Freja orbits.

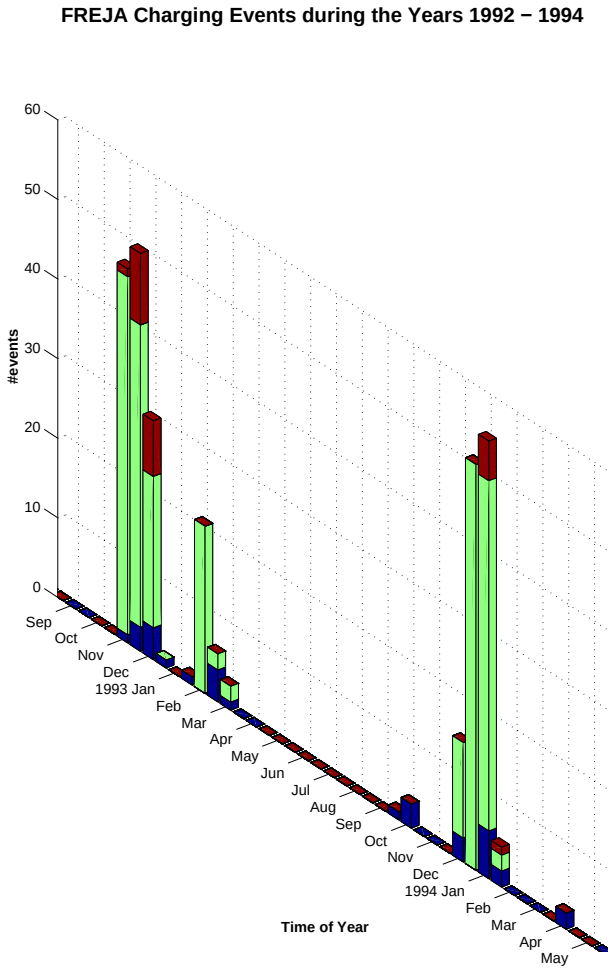

Figure 4.4-3: Seasonal dependence.

The variation in Corrected Geomagnetic Latitude is presented in Figure 4.4-5. Freja charging events were restricted to latitudes above 60°. The charging event frequency seems to decrease at geomagnetic latitudes above 70°. Clearly, all Freja charging events occurred within the auroral zone.

The variation in Longitude is presented in Figure 4.4-6. Except for the two events near –155°, the distribution is contained to –140° to –30° longitude. This is just due to a latitudinal effect, since large enough latitudes was only reached inside this longitude range. Of course, very active conditions (large Kp index) and keV electron precipitation is expected within the auroral zone as will be further shown below.

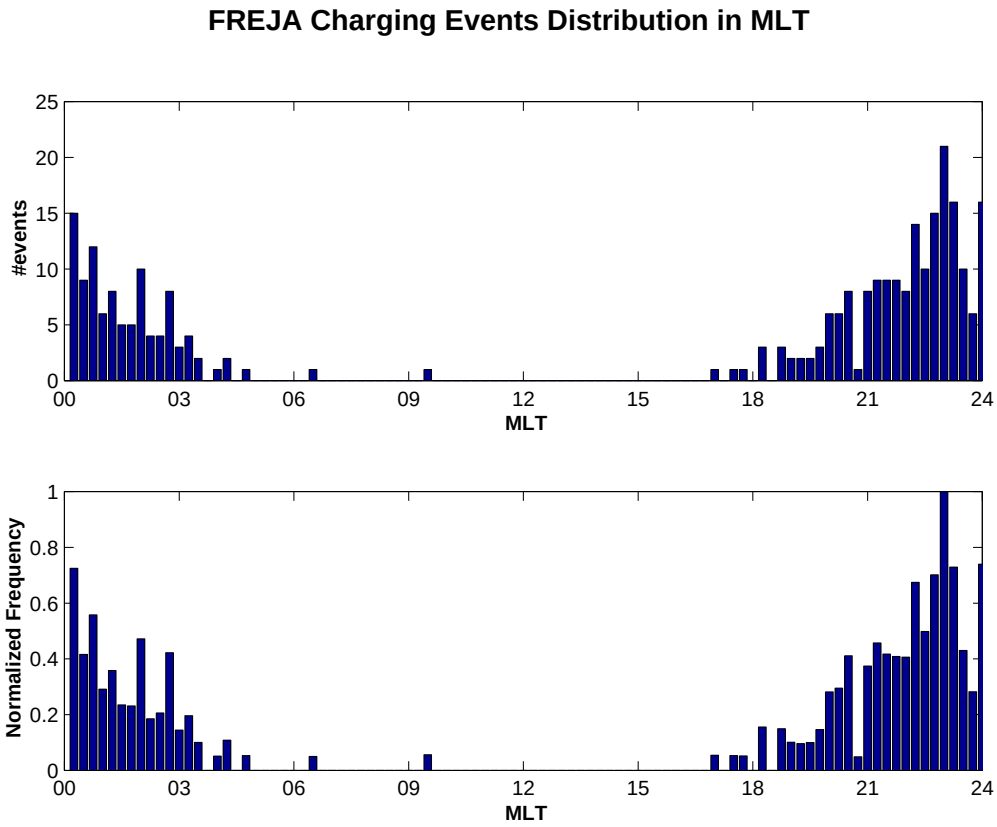

Figure 4.4-4: Variation in MLT.

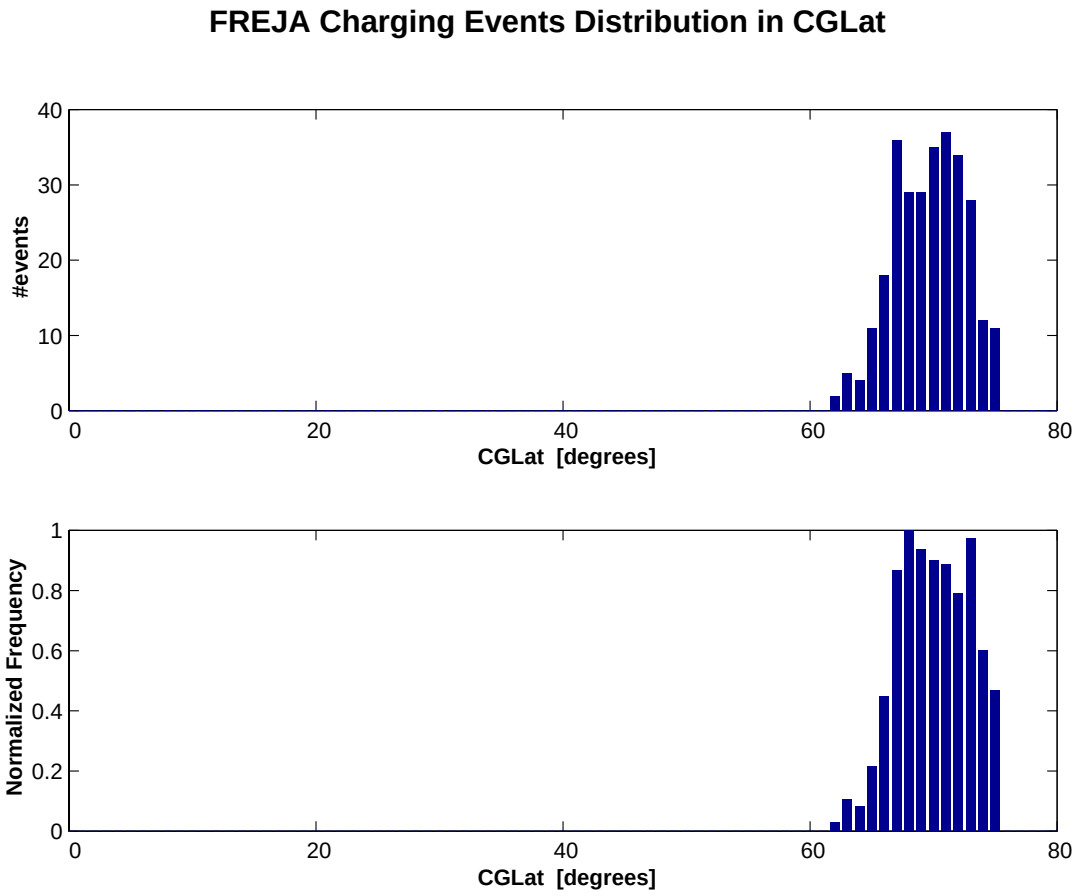

Figure 4.4-5: Variation in CGLAT. Freja covers latitudes down to 40°.

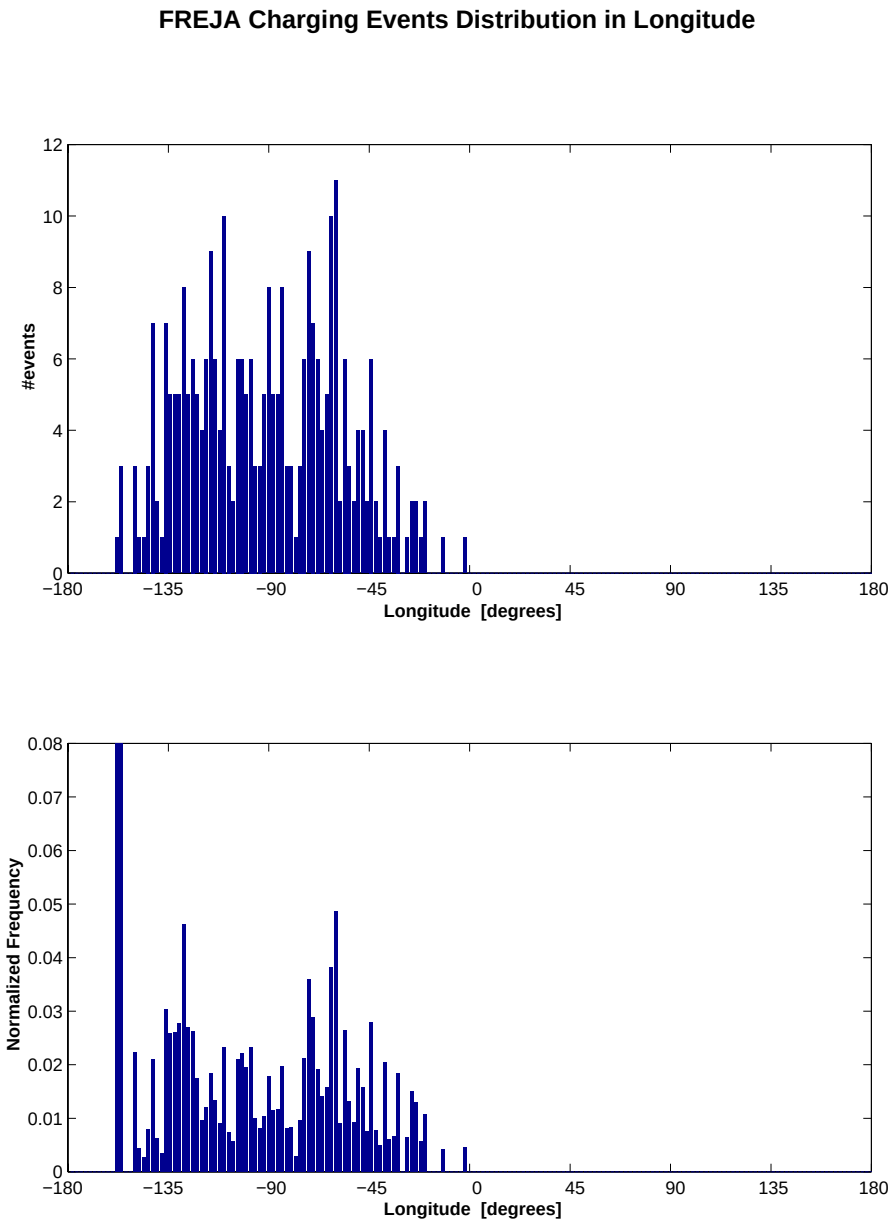

Figure 4.4-6: Variation in longitude.

4.4.4. Variation with geomagnetic activity

The Freja charging events have been binned to fit the 3-hour averages of the global Kp index, an indicator for geomagnetic activity. The bottom panel of Figure 4.4-7 shows the normalisation used for the Freja time period, the middle panel shows the normalised results for the Freja charging events. We can note that

- there is a weak increasing tendency with increasing Kp index
- the probability of charging becomes large for Kp > 3+.

These results agree fairly well with the results of Mullen et al. (1986), based on geostationary SCATHA data, while only a weak correlation was obtained with the DMSP satellites in LEO orbit (Frooninckx and Sojka, 1992).

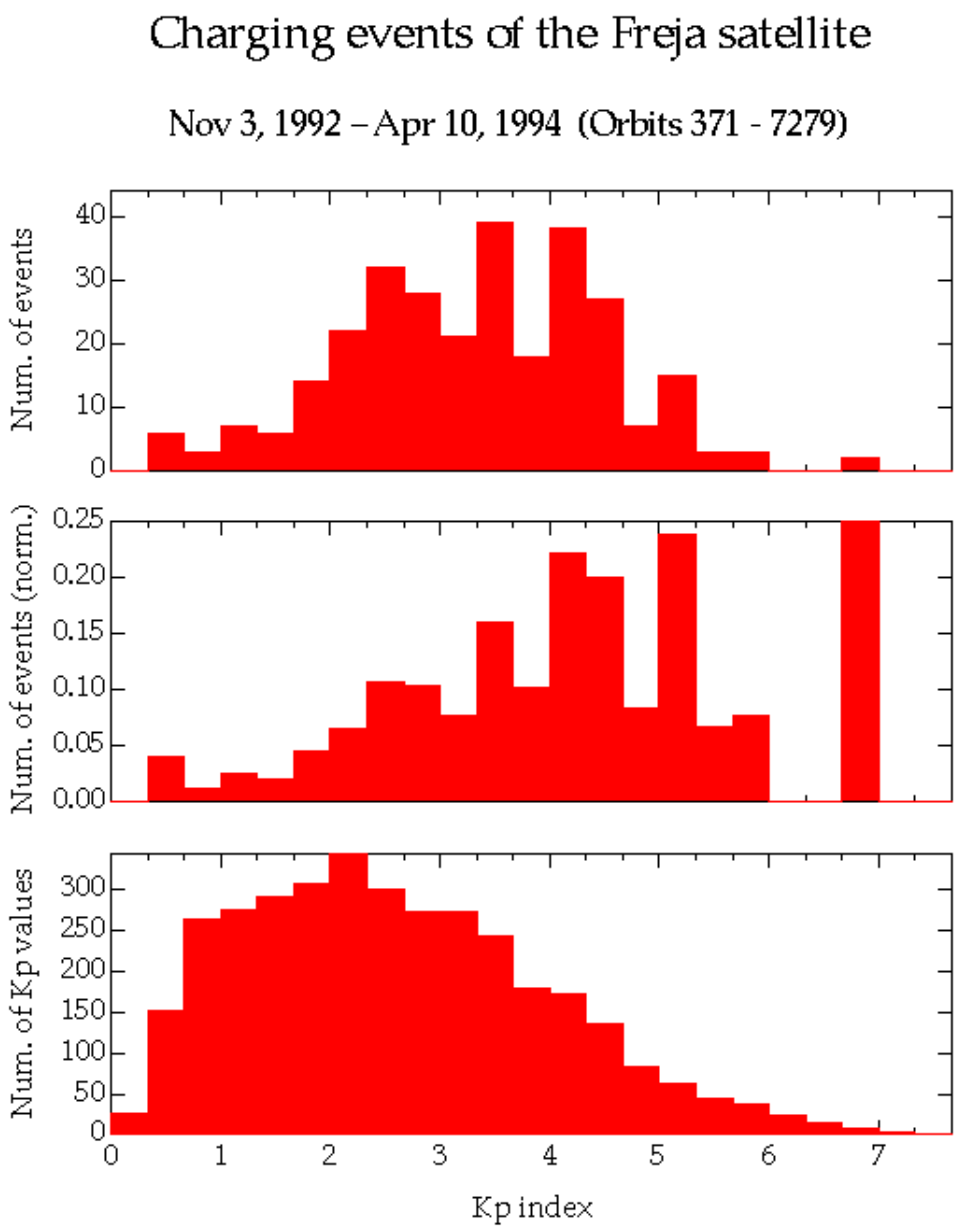

Figure 4.4-7: Variation in geomagnetic activity level (Kp).

Figure 4.4-8 shows the charging events were distributed in Kp for different MLT, altitude, and sunlight conditions. The data points in the eclipse index have been shifted randomly in order to highlight the distribution of events with sunlight conditions better. We can note that

- low Kp events tended to occur in a narrow local time sector near local midnight (panel a)
- high Kp events happened within a broader local time sector on the nightside, although the Freja spacecraft did not need be in shadow (panel a compared to panel b)
- low Kp events occurred only during eclipse (panel c)
- no obvious dependence with altitude is found

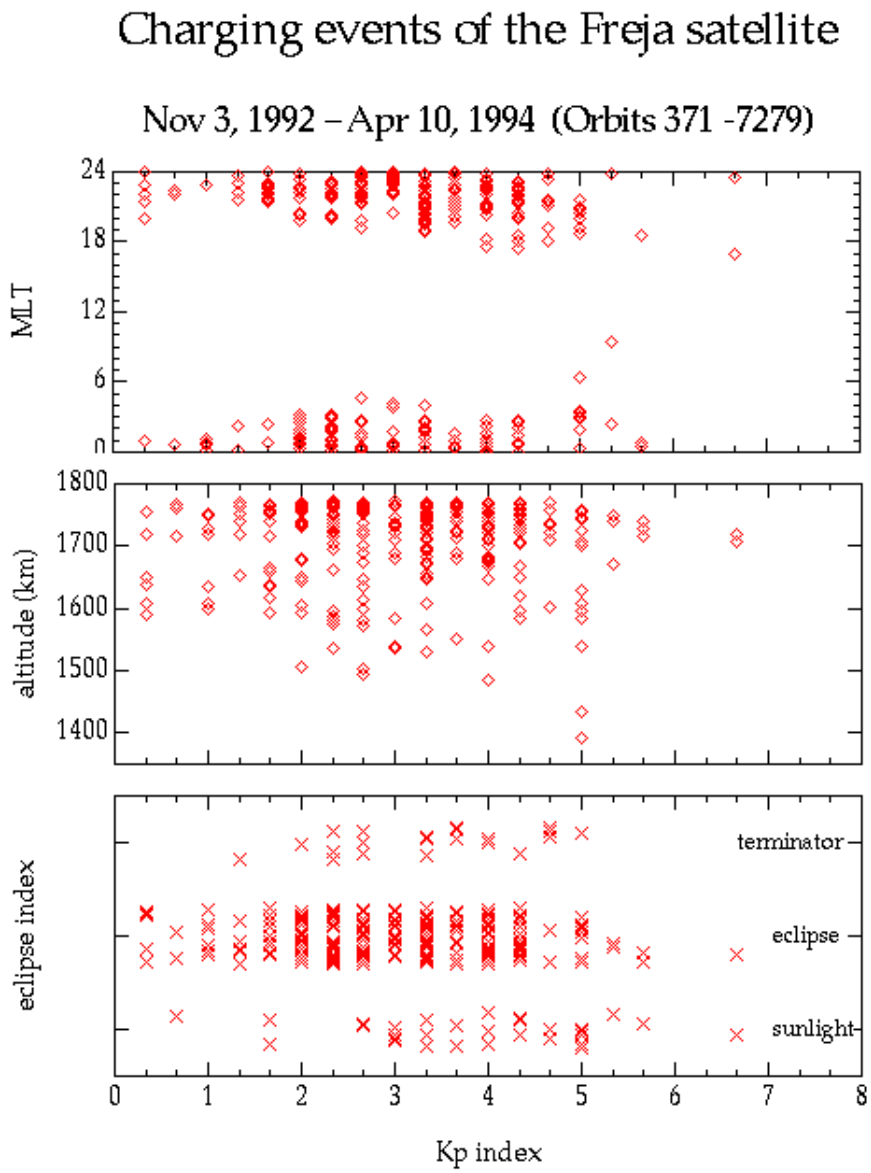

Figure 4.4-8: Variation of Kp with respect to MLT, altitude, and sunlight conditions.

4.4.5. Variation with cold plasma characteristics

Figure 4.4-9 (panel a) shows the peak charge variation with electron density. Here, the peak charge values have been slightly randomised (10 %) to highlight the dependence better. Unfortunately, no clear relationship is obvious. However, there is an upper threshold value of $2 \cdot 10^9$ m^{-3} for the cold plasma density, since it is well known that the cold plasma density often reach above this value in the Freja data. The thermal plasma density seldom decreases below 10^8 m^{-3} in the Freja dataset.

This result can be compared with the results obtained by Frooninckx and Sojka (1992), who found a similar electron density threshold value of 10^{10} m^{-3} for the DMSP satellites. Since the DMSP satellites traversed lower altitudes (840 km) and therefore larger thermal plasma densities, this result confirms that the Freja spacecraft was indeed

better designed with conductive surface coatings for electrical cleanliness. Despite this fact, Freja nevertheless charged more than 2000 Volts negative.

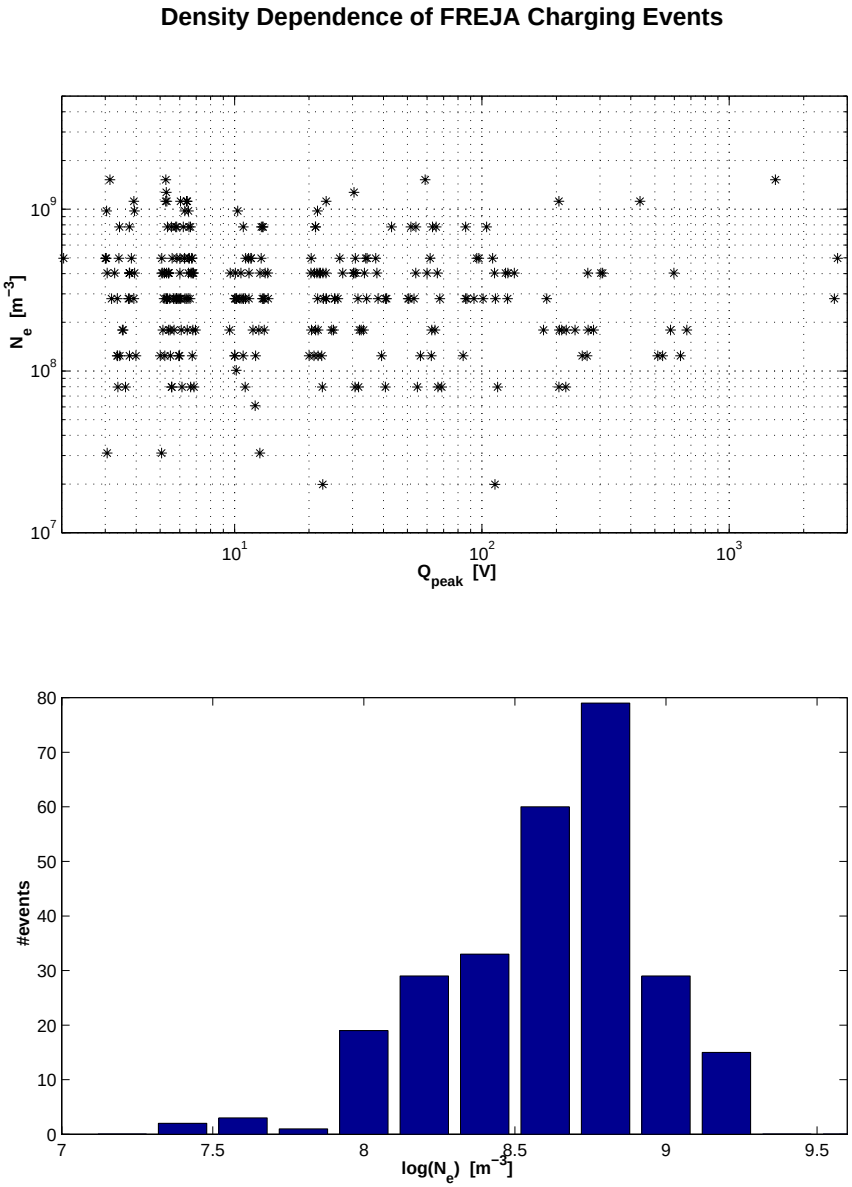

Figure 4.4-9: Variation in the cold ambient plasma density.

4.4.6. Variation with energetic particle characteristics

By far the most common type of Freja charging events was associated with energetic electron precipitation in association with inverted-V events. It is fair to conclude that the energetic electrons with energies above a few keV were the direct cause for most Freja charging events. Figure 4.4-10 shows an avaraged electron spectrum for all Freja charging events, where a clear inverted-V electron population with a peak energy of few keV and an extended power-law type high-energy tail extending to several tens of keV can be seen. Typical flux levels at the inverted-V energy peak during charging events reached 5×10^{11}–10^{13} $(m^2\text{-s-str})^{-1}$ for single charging events.

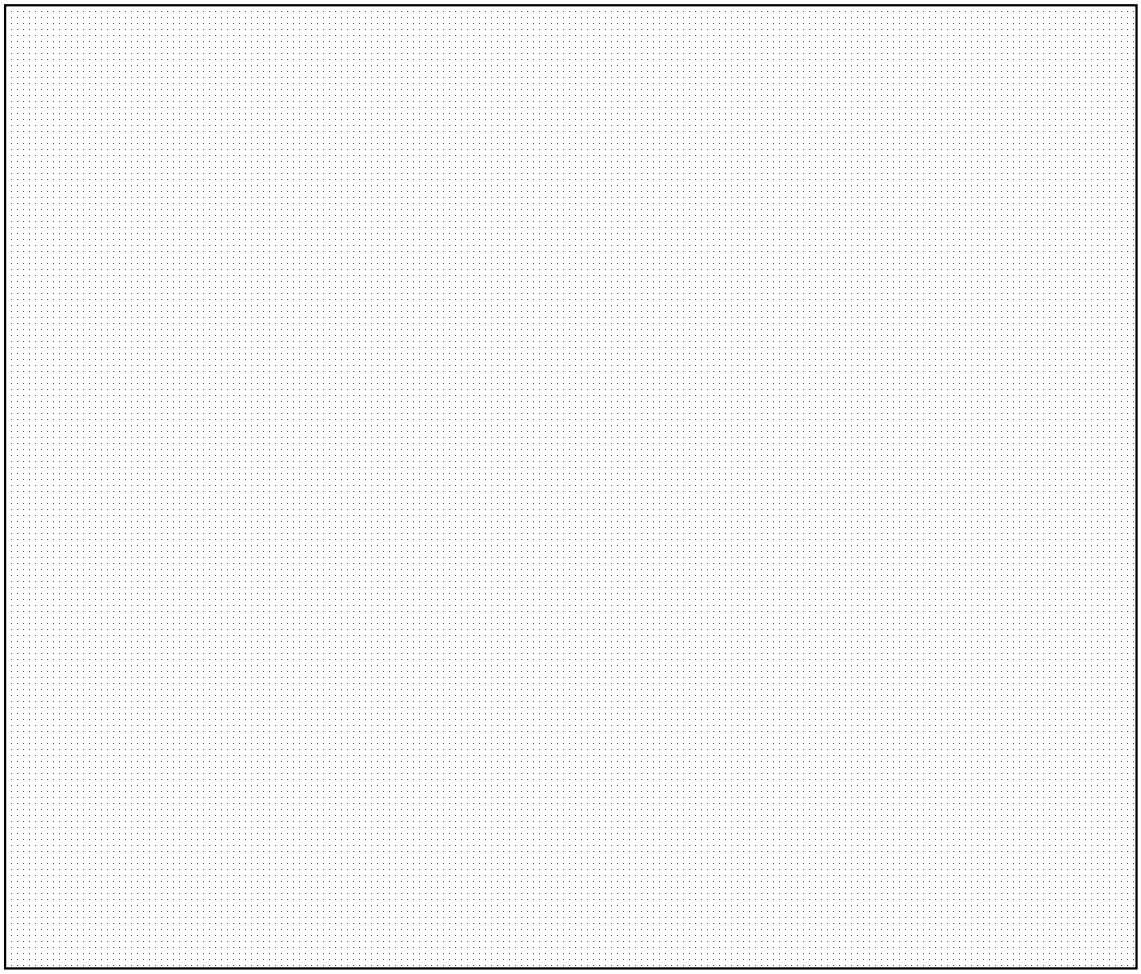

Figure 4.4-10: Averaged electron spectra for all Freja charging events.

The relationship of spacecraft charging can be further demonstrated by looking at the averaged electron spectra for different charging levels (Figure 4.4-11). It is clear from Figure 4.4-11 that both the inverted-V peak energy and flux as well as the high energy tail flux were increased for higher charging levels. A second peak seemed to exist between 10–100 keV, which becomes more pronounced at larger charging levels. Note also that no significant electron fluxes are seen at lower energies (< 1 keV). Such electrons would increase the secondary yield and inhibit charging on Freja, because ITOC is the main surface coating on Freja and because ITOC has a break-even point with respect to secondary electrons near 2.5–3 keV. The second most common surface material is the thermal blanket, which has the break-even point just below 4 keV. The results are therefore in qualitative agreement with normal surface charging theory (e.g. Garrett, 1981; Hastings, 1995; Hastings and Garrett, 1996).

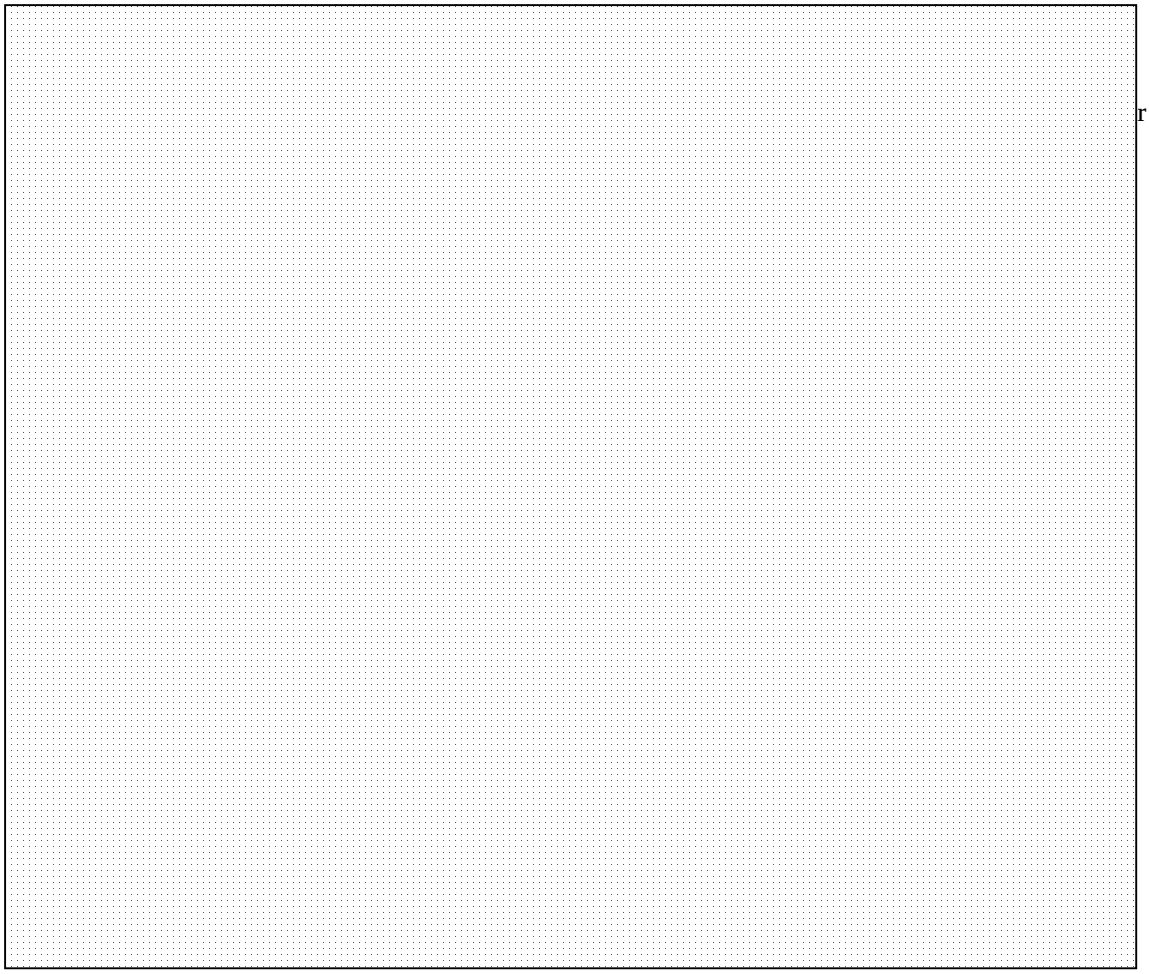

Figure 4.4-11: Variation in electron spectra with respect to different charging levels.

Frooninckx and Sojka (1992) showed that the thermal plasma density is one of the major factors determining the charging level of the DMSP spacecraft. We show in Figure 4.4-12 the counting rates for a selected number of fixed electron energy levels (for the MATE instrument) plotted vs the peak charging level. As expected, no sensational relationship can be found. It is obvious that the high energy electron flux *alone* is not a major physical parameter for determining the charging level of Freja. If we instead divide the flux (count rate) with the cold plasma density, as Frooninckx and Sojka (1992) did, a somewhat better (still bad) relation appears. However, a rather good relationship is obtained near the peak energy (around 4.3 keV) if we also divide the flux with the flux at the lowest energy channel (794 eV, Figure 4.4-13). This low-energy flux is well below the break-even energy for secondary electrons emitted from the surface, and the larger this flux is the lower charging level we expect. A high energy electron flux level is indeed needed, but it seems that other physical parameters, such as the thermal plasma density (and the return current from this plasma to the spacecraft) and the low energy electron flux (which produce many secondary electrons) determines the charging level to a great extent as well. A somewhat better dependence therefore is seen in Figure 4.4-13. Thus the following relationship seems to roughly hold:

$$Q \propto \left(\frac{\Phi_{peak}}{\Phi_{low} \cdot n_e} \right)^{1.5}$$

where Q is the charging level attained, n_e, the thermal plasma density, Φ_{peak}, the electron flux at the inverted-V peak energy, and Φ_{low}, the electron flux at low energies (e.g. around a few hundred eV).

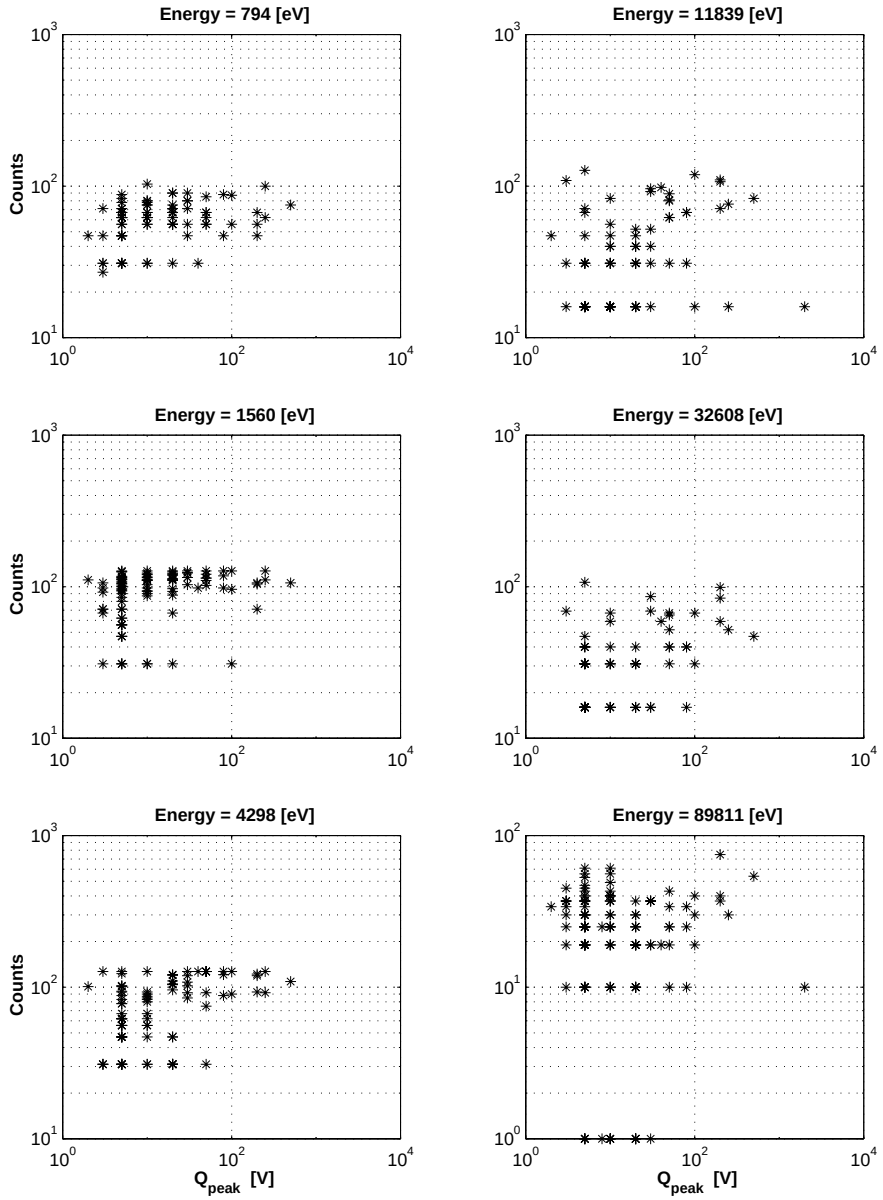

Figure 4.4-12: The count rate (flux) for a selected number of fixed electron energy levels (from MATE) plotted vs the peak charging level.

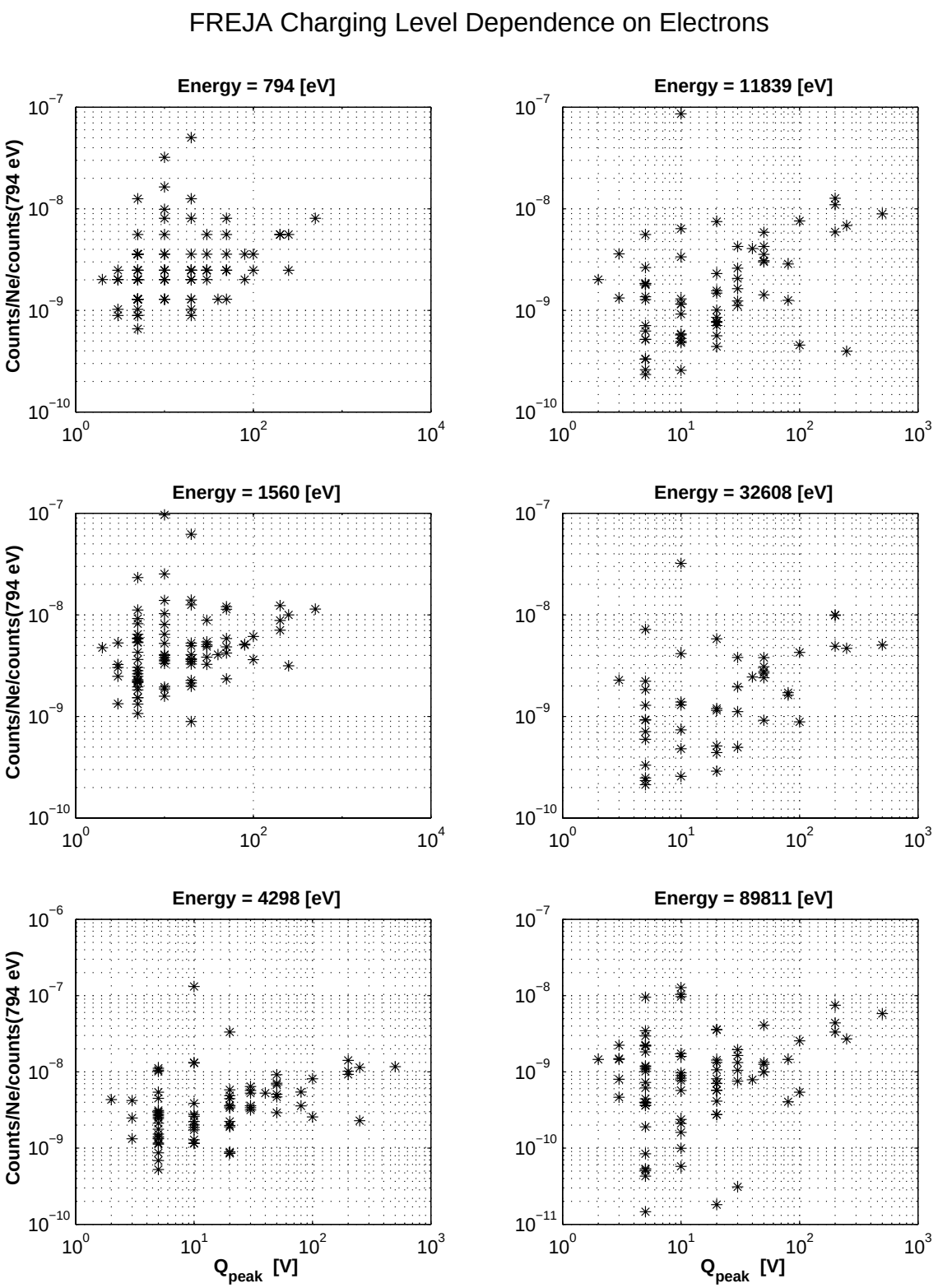

Figure 4.4-13: The magic formula. The low energy electron flux is an inhibiting charging factor, since it produces relatively large amounts of neutralising secondary electrons. The larger the density, the harder it is to charge a spacecraft because of increasing the neutralising thermal ion current. Above a certain threshold energy, the flux near the inverted-V energy peak carry a net negative charge to the spacecraft (less backscattered and secondary electrons). There is a good relationship near the inverted-V peak energy (first column, bottom panel).

4.4.7. Variation with altitude and magnetic field strength

The distribution of Freja charging events with altitude is displayed in Figure 4.4-14. The normalised altitude occurrence of charging events (panel b, although "noisy") seems to be rather evenly distributed. Perhaps there is an increasing trend for increasing altitude, but this trend is within the possible errors.

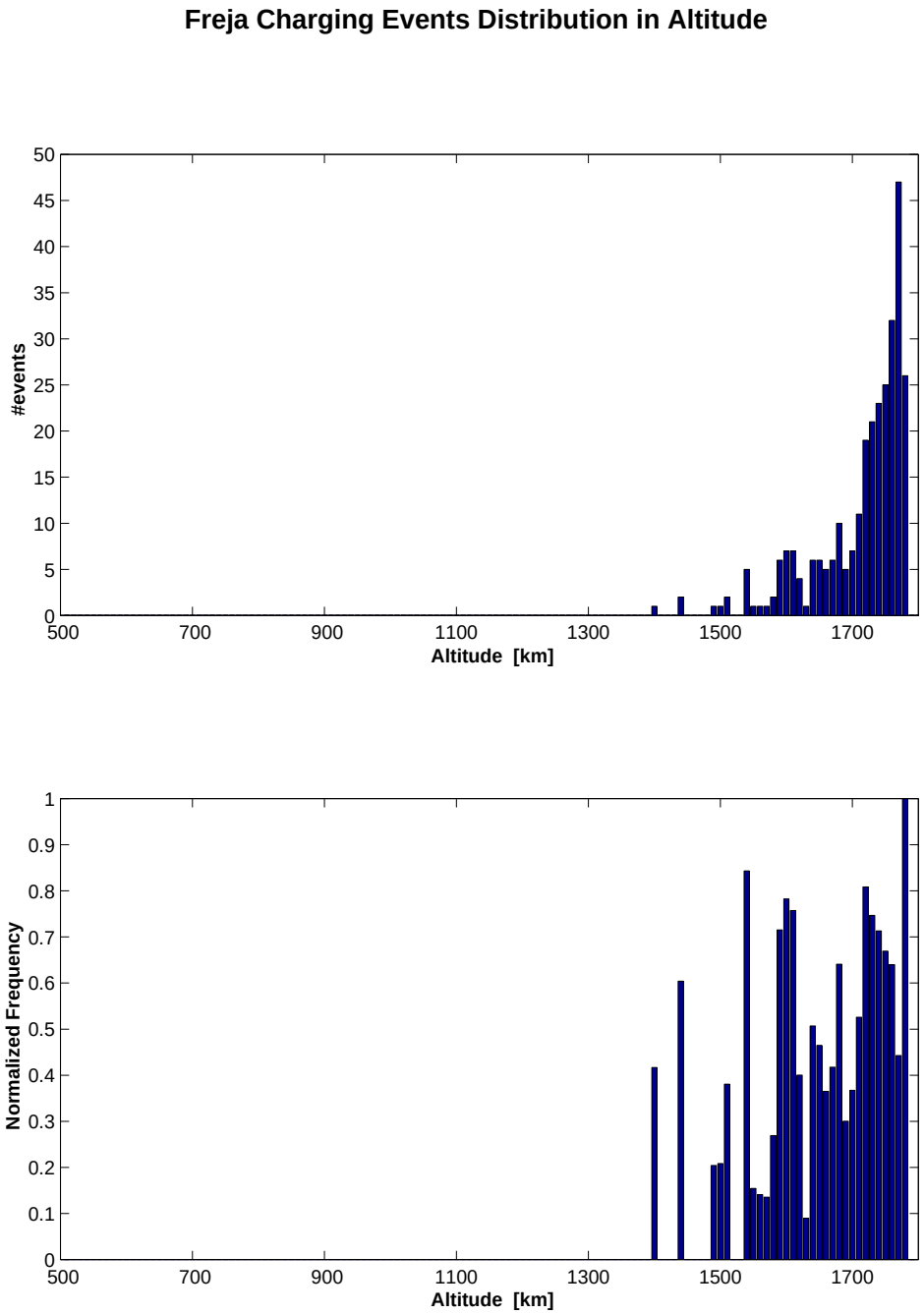

Figure 4.4-14: Variation in altitude.

In low Earth orbit, the geomagnetic field **B** is strong enough that secondary electrons and photoelectrons emitted from the spacceraft surface have an average gyroradius

smaller than typical dimensions of a spacecraft. For Freja conditions these dimensions are comparable. This implies that escape of such electrons may be inhibited on surfaces nearly parallell with **B**, which in turn may affect the current balance of the spacecraft and make high-voltage charging more likely (Laframboise, 1988). The effect of the Freja orientation with respect to the magnetic field direction was therefore investigated. Figure 4.4-15 displays the dependence of the Freja spin axis angle to the magnetic field direction. There is an apparent increase of charging events at smaller magnetic field angles (panel b). However, this is just a latitude effect. Figure 4.4-16 further shows that no obvious dependence exists between charging level and magnetic field direction in the Freja dataset. We conclude that the magnetic field orientation was not a major factor for charging of the Freja satellite.

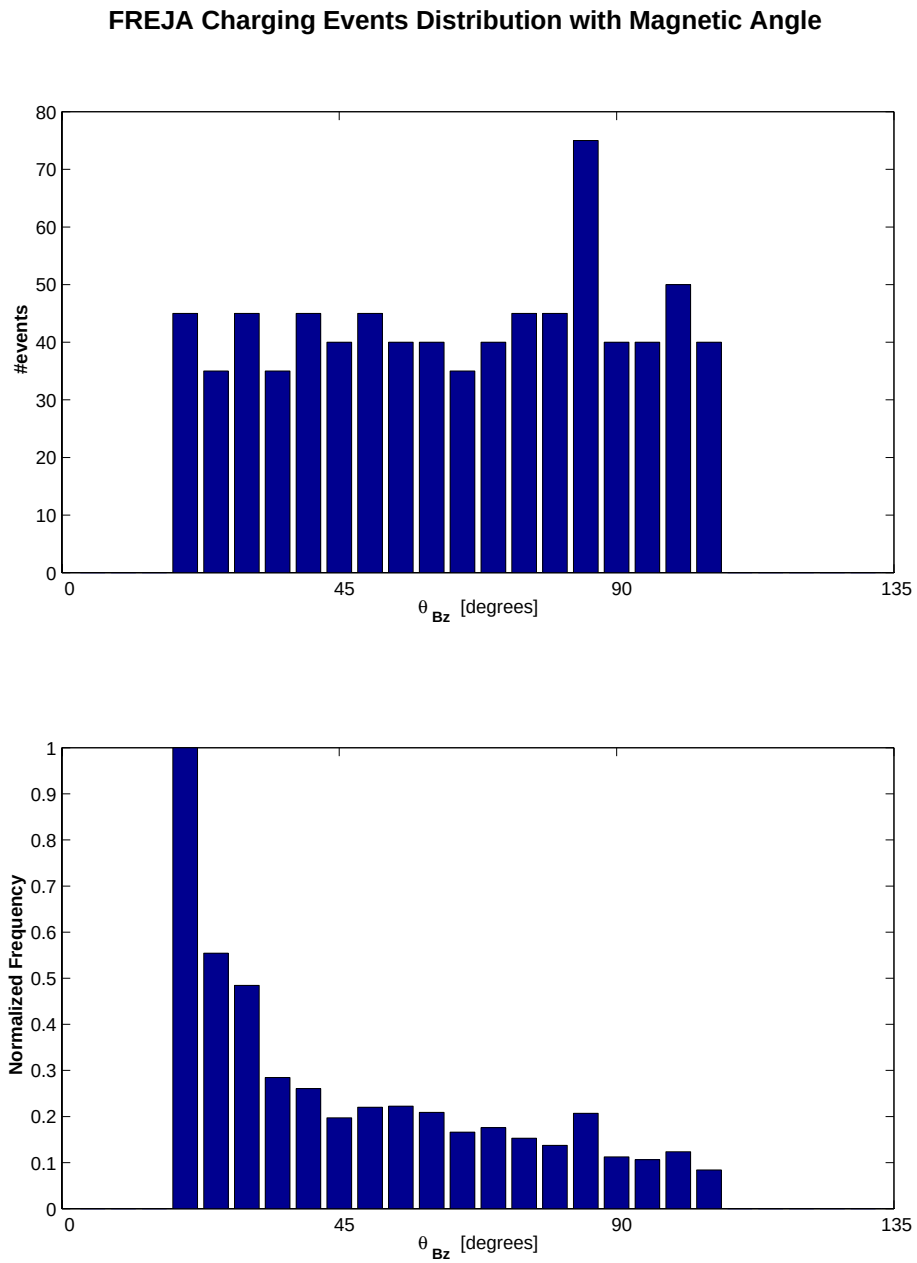

Figure 4.4-15: Dependence of Freja's orientation with magnetic field direction. The apparent increase toward smaller angles is unfortunately only a latitude effect.

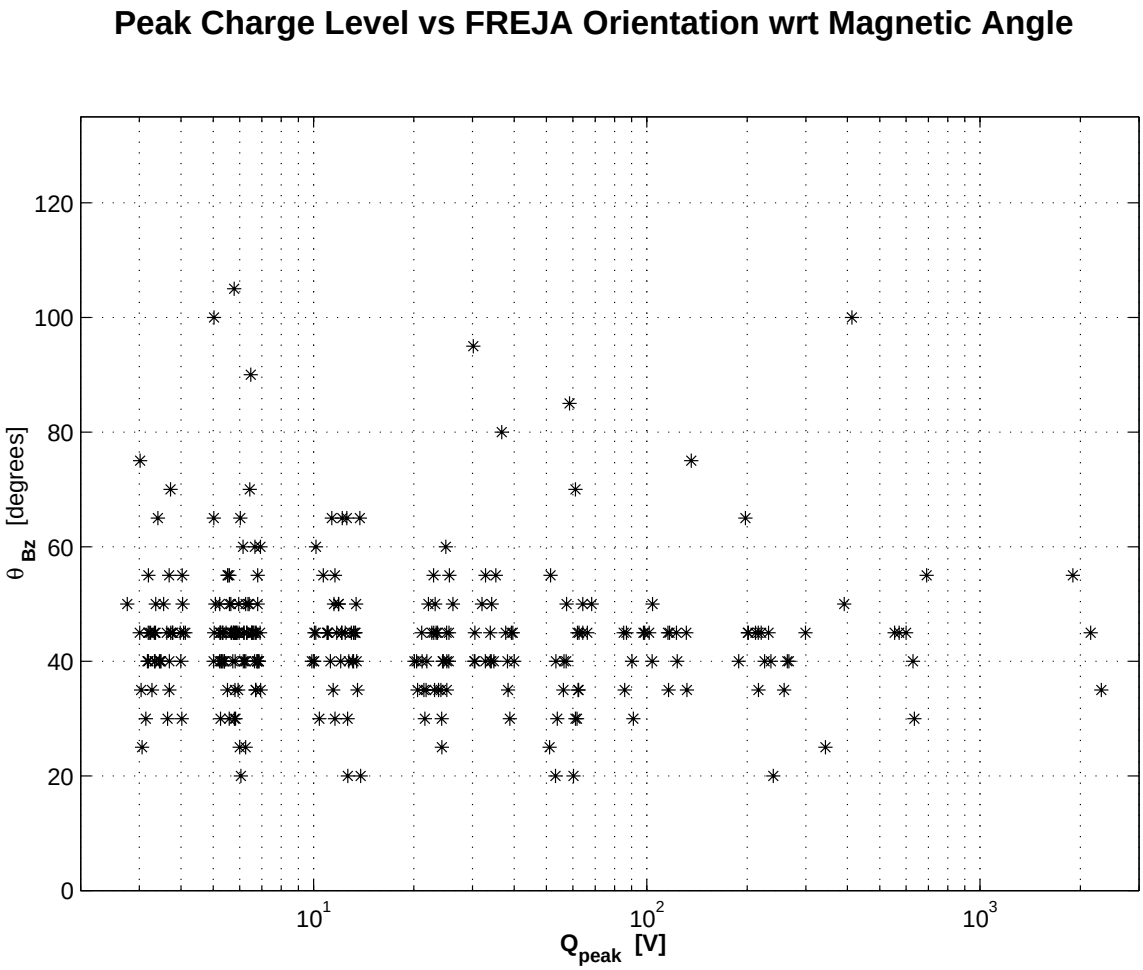

Figure 4.4-16: Dependence of charging level with geomagnetic field direction.

4.4.8. Conclusions regarding to Freja charging statistics

By far the most common type of charging detected on the Freja satellite occurred during high-latitude auroral inverted-V events when extreme fluxes of high energy (5–80 keV or more) hit the spacecraft. Usually the cold ambient plasma density was low ($<1\times10^9$ m^{-3}) during the events, and a majority of them occurred during eclipse. All charging events can be classified in four different types:

- Charging by energetic electrons during eclipse
- Charging by energetic electrons during sunlight and terminator conditions
- Low level charging variations due to sunset/sunrise.
- Low level charging probably due to an increased bulk electron temperature.

The last two types of charging usually remained to levels below the threshold we have chosen for this statistical study, and therefore only few such events were included.

Based on the data sampled on 291 orbits we can draw the following conclusions:

- Most charging events did not reach charging levels in excess of 10 V (negative). Only a handful of the events reached charging levels around –2000 V.

- The duration of the charging events were mostly shorter than one minute. Only very few lasted several minutes even though Freja had an orbit that passed almost tangentially along the auroral oval. This fact reflects the passage time over so called inverted-V structures within the auroral region (i.e. bursty events of precipitating high energy electrons). Thus, when the source for charging disappears, the charging disappears simultaneously. This is confirmed by the results from the event study (section 4.3 above).
- All charging events occurred only above Corrected Geomagnetic Latitudes of 60° with a frequency peak centred above the auroral zone.
- The geomagnetic activity as measured by Kp needs to be larger than 2+ for charging events to be probable and the probability increases for larger Kp.
- Typical inverted-V electron differential fluxes are 10^6 to 10^8 $(cm^2\text{-s-str-keV})^{-1}$. Examples of worst case electron spectra were presented in section 4.3. However, the ambient plasma density, sunlight conditions and the energy of the inverted-V peak affect the charging levels more dramatically. Also, electrons at energies around a few hundred eV, for which the surface secondary yield is the largest, appear to inhibit negative charging.
- No Freja charging events occurred for thermal plasma densities above $2 \cdot 10^9$ m^{-3}. DMSP had a threshold value of 10^{10} m^{-3}. The larger density increases the neutralising thermal ion return current to the spacecraft.
- The electron spectra show low flux levels below about 1 keV, and larger flux levels above a few keV. The spectra seem to have two populations, one with peak energies of a few keV, and one high energy tail between 10–100 keV.
- Most charging events occurred during the absence of photoemission from the Freja spacecraft (i.e. in eclipse), and enhanced negative charging levels were obtained during sunlight only during very active auroral conditions (Kp > 2–3).
- No charging events occurred during the summer months, while a maximum of occurrence appeared in the winter months. This is probably due to the combined effect of increased eclipse time and the expected lower thermal plasma density in the absence of photo-ionisation and the upward diffusion at lower altitudes.
- Most charging occurred in the MLT interval 18 pm – 03 am.
- No obvious relationship was detected regarding the orientation of the Freja spin axis with respect to the geomagnetic field direction even though the electron gyroradius of the photoelectrons and secondary electron emission from the spacecraft surface and the dimensions of Freja are comparable.

It is worrisome that an electromagnetically clean spacecraft where the designers have made special effort to provide conductive surfaces still gains charging levels of several thousand volts negative during auroral active conditions. The main surface material on Freja was ITOC, which has a cross-over energy of about 2.5–3 keV, above where the secondary yield falls below 1. The second largest surface type was covered by thermal blankets with a slightly larger secondary yield crossover energy of just below 4 keV. The spectral characteristics of a typical auroral inverted-V events with

insignificant low-energy fluxes (< 1 keV) and large fluxes of high energy electrons (often isotropically distributed in pitch-angle) make these events particularly effective in producing high charging levels on *any spacecraft* where the secondary yield crossover energy for the surface material is a few keV. Highly conductive surface materials are needed to avoid differential charging problems among different surfaces on a spacecraft, but if a total charging of a polar spaccraft shall be avoided, then the surface materials need have secondary yield crossover energies of at least 20–30 keV, which seems impractical.

The gyroradii at Freja/DMSP altitudes for around 2 eV secondary electrons are 0.1–0.4 m, which is a significant fraction of the size of Freja. Even so, only very few of these electrons will return to Freja through gyromotion, depending on orientation with respect to the Earth's magnetic field direction (Laframboise, 1988). For a larger spacecraft a larger fraction of these secondaries will return to the spacecraft surface, and a larger spececraft will thus likely gain even higher charging levels. The same argument is true with regard to sunlight conditions, when large amounts of photoelectrons are emitted from the surface. A smaller spacecraft will not see the photoelectrons return as easily as a larger spacecraft, and the larger spacecraft is therefore more easily charged.

We make the conclusion that high level surface charging will continue to occur on spacecraft in PEO, and that it will require serious engineering efforts to produce surface materials with large secondary yields for incident electron energies in excess of tens of keV but which are still conductive. Of course, indirect methods to reduce charging levels exist, like expelling a cold rather dense plasma around the spacecraft, but such methods instead tend to increase the contamination and differential charging problems. Problems which will affect the performances of scientific instruments onboard these spacecraft.

4.5. Numerical modelling of Freja charging observations

In this section we discuss the modelling of Freja charging events using the numerical spacecraft charging codes SUCHGR and POLAR. As explained above the Freja instrumentation makes it possible to experimentally study bulk charging of the spacecraft, and this is what is modelled here. Differential charging as such is not a chief consideration in this work as no observational Freja input exist, but some effects of local electrostatic perturbations are investigated.

From discussion in sections 4.3. and 4.4. it is clear that voltage levels below the expected floating potential, as based on the thermal plasma characteristics, often are observed on Freja. It was also shown that the spacecraft potential in these cases is closely correlated to electron precipitation above some keV. In thissection we attempt to model these results using SUCHGR and POLAR, briefly presented in subsection 4.5.1. Our approach is that of an "un-prejudiced best-effort": we first describe the spacecraft (4.5.2) and its surface materials, then model it (4.5.3) and its environment (4.5.4) as accurate as possible, and finally use this as input to POLAR, the code developed to deal with

auroral charging phenomena in low-Earth orbit. For the simulations (4.5.5), we use POLAR version 1.3.7, kindly provided by David Cooke of the US Air Force Research Laboratory. We find that POLAR used by us in this way does not reproduce the observed charging levels, although variation of material or simulation parameters sometimes get us close to observed voltages. Possible reasons for the discrepancies are discussed, and we conclude this study with a summary and recommendations for further investigations and software development in subsection 4.5.6.

4.5.1. Modelling spacecraft charging

4.5.1.1. Spacecraft charging codes

Several software tools for modelling spacecraft surface charging exist. Most well known and commercially available is the NASA Charging and Analysis Program, NASCAP, developed in the USA in 1980s. For the study of charging effects on satellites in polar orbits, the code POLAR was developed from NASCAP in the late 1980s. POLAR has additional capabilities to model the auroral electron precipitation, which is the essential source of spacecraft charging on polar orbits. In Russia, the ECO-M and COULOMB codes have be developed (e.g., Danilov et al., 1998; Krupkinov et al., 1992). Common to these and most other spacecraft charging codes is that they use quasi-analytical models for some parts of the calculations, for example for the wake structure, rather than doing a complete particle-in-cell simulation or numerical solution of the Vlasov-Poisson equations for the spacecraft-plasma system. There are 2D particle-in-cell for charging studies codes (e.g. Usui et al., 1993) and 3D codes are under development, but at present only the semi-phenomenological codes mentioned above are widely available and applicable in practical situations.

POLAR has previously been applied, e.g., to the SPEAR-1 rocket (Katz et al., 1989), the CHARGE-2 rocket payload (Mandell et al., 1989), and to the DMSP series spacecraft (Cooke et al., 1989). For modelling of Freja charging events, typically at around 1500 km altitude in the auroral zone, POLAR was chosen as the most appropriate tool presently available, although NASCAP was used as well in some preliminary work (Svensson, 1997). We have also used the program SUCHGR which is distributed with the POLAR code. SUCHGR is a simplified code modelling the spacecraft as a homogeneous sphere, while POLAR allows detailed modelling of the spacecraft. POLAR and SUCHGR are described in detail in the POLAR User's Manual (Lilley et al., 1989, hereafter refered to as PUM). In the context of the present study it is necessary to have some knowledge of what POLAR can do and what it cannot, as this clearly is important for understanding the results of the simulations of the Freja charging events.

4.5.1.2. Currents collected from the plasma

The currents flowing to an isolated body in a plasma depend on the potential of the surface with respect to the surrounding plasma. Under all conditions, the body will attain a potential V such that the total current I is zero. The presence of non-conductive materials, which may give local charging to parts of the spacecraft, or biased parts like scientific instruments for particle collection, may perturb the electrostatic field around the spacecraft. Denoting the equilibirum potentials of surfaces k by V_k the spacecraft boundary to space will be such that the total current is zero

$$\sum_{k=1}^{n} I_k(V_1, V_2, ..., V_n) = 0 \quad . \tag{4.5.1}$$

This is the fundamental equation of spacecraft charging. For simple models like a homogeneously conductive spherical spacecraft of uniform surface it may sometimes be possible to give closed-form expressions for *I(V)*, although the presence of shielding and particularly wake effects make the problem hard to solve (see Al´pert, 1983). The code SUCHGR uses this simple model. For a uniformly conductive spacecraft, results based on such simplifications may often be very good, particularly if the Debye length is large compared to spacecraft dimensions. In other cases, where a spacecraft with many different surfaces and a complicated geometry is to be considered or wake effects are important, more elaborate calculations are needed. Codes like NASCAP and POLAR divide the satellite into a set of surfaces, each satisfying a current balance equation similar to (4.5.1), where I and V are vectors describing the currents and potential for each surface. In general, the current to any surface depends not only on its own potential but also on the potentials of the adjacent surfaces and the spacecraft bulk, as these potentials will influence the particle motion in the plasma and the current flow on the spacecraft.

For modelling a spacecraft-plasma interaction problem with negative charging, POLAR typically starts from user-supplied input on the spacecraft geometry and materials, the plasma parameters and initial potential of the spacecraft. An initial wake structure is determined using geometric shadowing of the spacecraft or a neutral flow approximation. An initial sheath edge is fixed, and using these boundary conditions Poisson's equation for the potential is solved. The motions of test ions are then tracked through the field, and the currents they carry to the spacecraft surfaces are calculated. The currents and densities due to the repelled electrons are calculated using the Boltzmann relation. The response of the spacecraft surfaces to the incoming particle flux is calculated, resulting in a new potential distribution on the spacecraft. This is then used as a new boundary condition for Poisson's equation, which is solved with the ion density found from the tracking process and Boltzmann distributed thermal electrons providing the charge density. Contributions to the charge density from high-energy electrons, secondary electrons, photoelectrons and backscattered particles are not modelled.

If the plasma is sufficiently tenuous, the electric fields encountered by the particles can be determined from the boundary conditions without reference to other particles in the plasma. In this limit where the Debye length is much larger than the spacecraft size, fields will also decay with distance so slowly that the current is

independent of the detailed structure of the field. This is known as the orbital motion limit or OML, for which useful analytical results exist (Mott-Smith and Langmuir, 1926; Medicus, 1962). At the other extreme, in a plasma so dense that the Debye length is much smaller than the spacecraft size, a sheath may form and shield off potentials so effectively all particles that enter the sheath are absorbed. Also for this limit, the sheath limit, some exact results exist (Al´pert, 1983). In between the extreme levels we have a situation which we may call the space charge limited current collection, which is where the scheme described in the preceeding paragraph is needed.

Evidently, the space charge limited case is more complicated to handle than OML. However, one may note that outside the sheath edge, OML conditions always apply. If detailed tracking of particle orbits is needed, this has to be done only inside the sheath. This is utilised in POLAR, which switches from OML relations to detailed particle tracking at a presumed well-defined sheath edge, defined by default as $|\Phi| = 0.47\, KT_e / e$. POLAR also has the option of using OML theory only and skip detailed particle tracking. Finally there is a hybrid of the two built into POLAR, where the OML calculation is done for finding the distribution of currents on different parts of the spacecraft, whereafter the total current to the spacecraft is normalized to the sheath current. This approach significantly reduces the amount of calculations as compared to the detailed particle tracking in the sheath, but its usage is not well tested or documented (David Cooke, private communication).

In a magnetised plasma, calculating the current-voltage relation for even a simple sphere is very complicated, and few really useful closed-form results exist. In contrast to NASCAP, POLAR can model the trajectories of the attracted ions taking magnetisation into account, but the effects seen when including non-zero magnetic field in the Freja simulations are found to be small, as could be expected. The gyroradii of the attracted ions are greater than the typical spacecraft dimension (about 1 m). For the repelled electrons, an analytical OML result is valid even in a magnetised plasma, and magnetisation can thus generally be neglected for the repelled species. An exception would be the case where a magnetic field line is cut at two points by spacecraft structures, with plasma open to space in between. However, as discussed below in subsection 4.5.6, magnetisation may possibly have impact on emission of photoelectrons and secondary electrons.

4.5.1.3. Photoelectron emission

Photoelectron emission from surfaces exposed to sunlight provides an important current in the charging balance for a spacecraft in geostationary orbit or elsewhere in the tenuous magnetospheric plasma. At Freja altitudes, the photocurrent is not as important as in the GEO environment, although it acts to stabilise the spacecraft potential in sunlit conditions. The photocurrent from a surface is fairly simple to model, at least as long as magnetisation effects are neglected. For negative potentials, the photocurrent is essentially independent of the potential: all electrons escape from the surface. This may be changed by the presence of a magnetic field, which may turn some photoelectrons

back to the spacecraft even if they are energetically allowed to escape. Laframboise (1988) found that for a planar surface with an angle θ between the surface normal and the magnetic field, the current carried by emitted electrons decreases by a factor $\cos\theta$ if there is no normal electric field at the surface. If such an electric field is present, the quenching effect becomes less important, and for high voltage charging, here defined as a high value of the ratio of the *E/B* drift speed to the particle speed at emission, the effect is negligible. Still it may be important for low-level charging events. POLAR presently does not include this effect.

Another effect suppressing the photocurrent is the formation of electrostatic barriers due to different voltages on different surfaces on the spacecraft, as illustrated in Figure 4.5-1. Local potential minima may form in space outside a surface, turning back photoelectrons to the surface. POLAR 1.3.7. includes a simple model of this phenomenon (see subsection 4.5.6), known to be important in charging in geostationary orbit conditions (Purvis, 1983) where the plasma density is low.

The electrostatic field may also return emitted particles to other points on the spacecraft than they were emitted from. These photoelectrons should be accounted for in the current balance also for the surface where they end up. This phenomenon is incompletely modelled in POLAR 1.3.7. (see subsection 4.5.6).

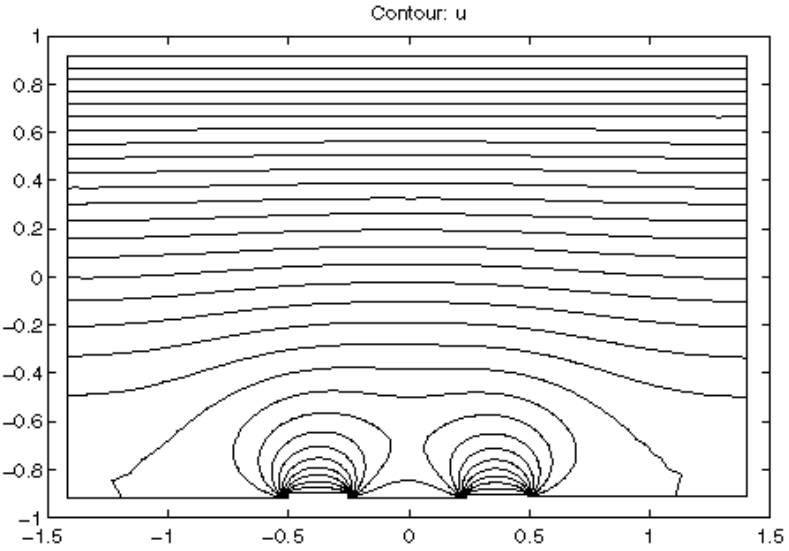

Figure 4.5-1. A numerical solution of the two-dimensional Laplace equation above a surface at 20 V with two small segments at 30 V. Equipotential lines with 2 V separation are shown. The potential is put to zero at the upper boundary, and the horizontal electric field is zero on the right and left boundaries. The formation of a local potential maximum of a few volts in space between and above the two small plates at 30 V is evident. Such a potential can form a barrier for particles expelled from the surface between the two small plates with energy below the magnitude of the potential barrier.

4.5.1.4. Secondary electron emission

When an electron or ion hits a surface, one or several other electrons may be emitted from the material, usually at fairly low energy (a few eV). The number of electrons emitted for each incoming particle is known as the yield *Y*. For incoming electrons, *Y* strongly depends on their energy *E*. The yield curve *Y*(*E*) is obviously zero for zero energy and also zero for infinite energy (as very high energies give very limited possibility of interaction), so there must be at least one maximum in between. Experimentally, most materials are found to have one maximum in the yield curve, at a few hundred eV (compare Figure 4.5-3, below). The maximum value of *Y* may well exceed one: for aluminium, the peak yield is 0.97, while it is around 3 for teflon. Thus secondary electron emission may be very important to the current balance for a spacecraft. A corollary is that simulations and calculations of spacecraft potential will be sensitive to errors in the model used for describing the secondary emission.

POLAR includes the NASCAP algorithms for calculation of secondary currents. The inputs needed are material properties and spectra of incoming primary particles. All materials known to NASCAP are included in POLAR, and for this study a number of other material specifications provided by ESTEC have also been used. As is the case with photoelectrons, POLAR looks at the secondary electrons only as a term in the current balance: they are not tracked out in space and do not contribute to the calculated charge density in the plasma. The treatment of current suppression due to potential barriers is similar to the that applied to photoelectrons.

4.5.1.5. Charging dynamics

Dynamic effects may enter the spacecraft-plasma interaction on two levels. The first and simplest level is when the boundary conditions in the plasma or for the spacecraft change so slowly that the sheath appears constant to the particle on a time scale it traverses the sheath. Dynamic effects on this time scale can be treated by introducing a displacement current in equation (4.5.1), thus requiring knowledge of the relevant capacitances. This can be a complicated task, as unless all parts on the spacecraft are conductors in contact with each other, there will be internal capacitances within the spacecraft. The spacecraft-plasma interaction may in this situation be modelled as a sequence of quasi-steady states, which is the approach taken by NASCAP and POLAR. The internal capacitances between various parts of the spacecraft must be explicitly provided by the user, while external capacitances to the plasma are modelled by the code.

The second and more advanced level for treating dynamical situations would be to consider not only quasi-steady states but the real dynamics of the plasma itself, down to Debye length and plasma oscillation scales in space and time. This would allow the modelling of wave generation and other time-dependent plasma phenomena, but would

require a full plasma simulation of the interaction, which would be very costly in terms of computer power.

Correct treatment of charging dynamics including internal capacitances may be very important when studying the formation of differential charging on a spacecraft, which eventually may lead to an arcing discharge. Our main interest is the final equilibrium state of the overall satellite potential configuration, and we therefore do not attempt to model the charging dynamics. In particular, no attempt to estimate internal capacitances has been made. For numerical reasons, a short timestep has to be used in the simulations, but we do not attempt to interpret the timescale we use as necessarily corresponding to the real charging timescale. One may note, however, that the charging timescale for Freja is observed to be short. Figure 4.3-2 indicates that the variations of the spacecraft potential, as mapped by the low energy cutoff in the ion spectra, occurs on a timescale of a few seconds, which is confirmed by investigations of individual ion spectra with a 2.8 second time resolution.

4.5.2. Modelling the Freja spacecraft

4.5.2.1. General Freja design

Freja is a sun-pointing spacecraft with solar panels placed on a flat circular surface. The overall diameter is 2.2 m (Figure 4.5-2). The solar panel platform constitutes the "upper" deck or platform. The "lower" deck is connected to the upper via a central aluminium tube. Radially from this tube four support webs are mounted between the decks. The lower deck is 1.2 m in diametre. The distance between the two decks is 0.44 m.

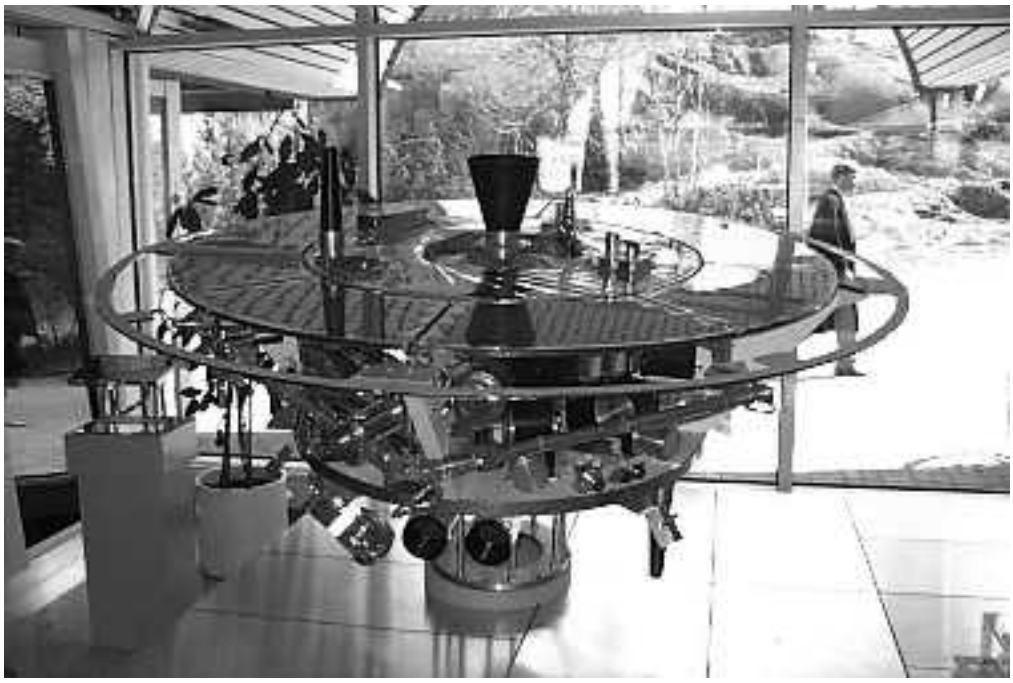

Figure 4.5-2. The Freja mockup at the entrance hall of the Swedish Space Corporation in Solna, showing the essential features of the spacecraft. The flight model has the instrument bays covered by thermal blankets.

In the central tube two solid powered motors, used to lift the the spacecraft into its final orbit, are mounted: one facing "upwards", one facing "downwards". Each motor has a nozzle made of composite material. The conductive properties of these nozzles, which are dielectrics on ground, are not well known, but a carbonisation effect during their use is assumed to make at least their inner surface conductive. We have in this study represented them by the conductive material CFPR (see next section) and a variation of this material with very low conductivity. The space between the decks is partitioned by the support webs into four distinct compartments known as instrument bays, where the different booms, scientific instruments and other system units are mounted.

An important design goal was to have as much as possible of the outer surface electrically conductive in order to cancel electrical charges induced by the plasma environment and prohibit differential charging. It is not possible to achieve a 100% coverage of the surface with conductive material, as insulating material must be used for certain purposes, such as insulating an electrostatic probe from the satellite. The total area of exposed insulators on Freja is about 0.38 m^2 (including engine nozzles) which may be compared to the thermal blanket exposed area of about 5.5 m^2.

The basic structure of the spacecraft is made of aluminium. Structure elements extending outside blankets are painted with white conductive paint of type PCB-Z. The eight identical solar panels are each covered by solar cells of 0.19 m^2 area, giving a total solar cell area of 1.52 m^2. A transparent conductive coating of indium tin oxide (ITO) is applied to the solar panels in order to ensure conductivity.

To keep the temperature within desirable limits, and to provide a conductive outer coating, a large part of the spacecraft including most of the instrument bays are covered by Sheldahl thermal blankets of aluminised kapton with ITO coating (Sheldahl, 1985).

4.5.2.2. Freja surface materials

In order to accurately model the spacecraft, we must know the properties of its surfaces. A detailed investigation of the Freja satellite has been performed, and a materials list has been compiled. A summary of the surface materials is found in Table 4.5-1. Names of model materials for the POLAR simulations are also given in the table. These model materials are further discussed below. For purposes of spacecraft charging, the exposed insulators are of particular interest. These are listed in Table 4.5-2.

For correctly calculating the charging and discharging of dielectrics and the photocurrents and secondary currents, POLAR needs a specification of the material of each surface in the spacecraft model it uses. The principal properties we need to know for each material are the relative dielectric constant, the thickness of dielectrics, the bulk

conductivity and surface resistivity, the atomic number, parameters describing the secondary yield curves for incoming ions and electrons, the maximum photocurrent and the discharge potentials. Laboratory values of these parameters for some materials are available directly in the NASCAP and POLAR codes. Other material parameters have been supplied by ESTEC based on measurements at DERTS. For the POLAR simulations of Freja charging events, the following materials have been used to model the satellite:

ITOC Indium tin oxide (ITO) coating. The secondary electron yield for materials with this coating has in laboratory tests been found to be rather independent of the underlying bulk material. In our case, the ITOC is applied on the solar panels. Source: ESTEC

BLAN Thermal blankets of Sheldahl fabrication. Aluminized kapton with ITO coating. Source: ESTEC

ALUM Aluminium for some spacecraft structure parts, particularly interface ring. The values we use are for pure aluminium surfaces. In reality, oxidization will increase the secondary electron yield. Source: NASCAP.

PCBZ White paint assumed conductive in space, applied to most aluminium areas which otherwise would have been directly exposed. Source: ESTEC

CFRP Conductive carbon fibre material, used to model the engine nozzles and some details. Source: ESTEC

CARB This material has been constructed for simulating the behaviour of non-conductive carbon fibre. We use the parameters for CFRP above, with bulk conductivity and surface resistivity replaced by CONT values.

CONT A generic for dielectric materials having been exposed to the space environment. In laboratory tests, the secondary yield properties were found to be rather independent of which dielectric it was, so we use this for modelling of all dielectrics except carbon fibre parts. Source: ESTEC

Part	**Material**	**Model material**	**Area [m^2]**	**Comment**
Instrument bays	Thermal blanket	BLAN	2.8	Thermal blankets covering scientific instrument electronic units and system units. Some exposed detectors.
Top and bottom platforms	Thermal blanket	BLAN	2.7	
Solar panels	ITO coating	ITOC	1.65	
Central tube inner mantle	Thermal blanket	BLAN	1.1	
Support webs (four)	Painted aluminium	PCBZ	4 x 0.7	Only exposed outer parts are painted and included in the area estimate.

Interface ring	Al	ALUM	0.5	Approximated as 2D ring, r = 1100 mm, dr = 37 mm
Main engine STAR 13A body	Titanium	ALUM	0.4	Considered as mantle of cylinder r = 154 mm, h = 396 mm.
Solar cell support	Painted aluminium	PCBZ	< 1.65	Some area covered by support webs and bay blankets.
Sun sensors	ITO coating	ITOC	2 x 0.05	One on top, one on bottom platform. Approximate dimensions 0.1 x 0.1 x 0.1 m.
TM antennas	Carbon fibre	CARB	2 x 0.05	One each on top and on bottom platform. Considered as cylinder r = 50 mm, h = 340 mm. Assumed insulator in this study.
Main engine nozzle	Carbon fibre	CARB	0.3	Considered as cylinder of radius 150 mm, h = 240 mm. Assumed insulator in this study.
Bottom engine STAR 6B	Aluminium	ALUM	0.02	

Table 4.5-1. Materials of major exposed surfaces on Freja. The "model material" refers to the baseline input for POLAR simulations.

Item	**Surface area** [m^2]
External parts of equipment bay:	
LSL Coax	0.0001
Separation switch harness	0.0300
Coax switches	0.0036
Power splitter	0.0009
Coaxes	0.0144
TICS cable	0.0020
Arming plugs	0.0020
DC-magnetometer boom:	
DC probe harness	0.0023
Cable loops	0.0075
CYLP pyro	0.0018
Search Coil Magnetometer boom:	
HF pyro	0.0018
Bottom platform:	
Lower TM antenna cover	0.05
S-band antenna coax	0.0050
Kevlar retention string	0.0004
TESP cradle rubber	0.0006
TESP rubber support	0.0010
TESP cables	0.0050
TESP backshell	0.0020
TESP pyro	0.0015
TESP kevlar string	0.0004
LSL antenna base	0.0015

MATE cable	0.0045
MATE cradle support	0.0004
STAR 6B nozzle	0.0100
Top platform:	
Upper TM antenna cover	0.05
S-band antenna coax	0.0050
Kevlar retention string	0.0004
STAR 13A nozzle	0.1200
STAR 13A harness	0.0150
Solar panels:	
Brackets	0.0058
Rear side cabling	0.0110
Top side TCC	0.0180
Edge TCC	0.0285
Total area including nozzles:	**0.38**
Total area excluding nozzles:	**0.24**

Table 4.5-2. List of exposed insulators on Freja. The list also includes the engine nozzles, as the impact of a possible non-conducting layer on these is assesed in the study.

The most important feature of the materials for this study is the secondary electron emission (Figure 4.5-4). This also shows the yield curves for another conductive paint CPAI (source: NASA) and for Teflon (source: ESTEC).

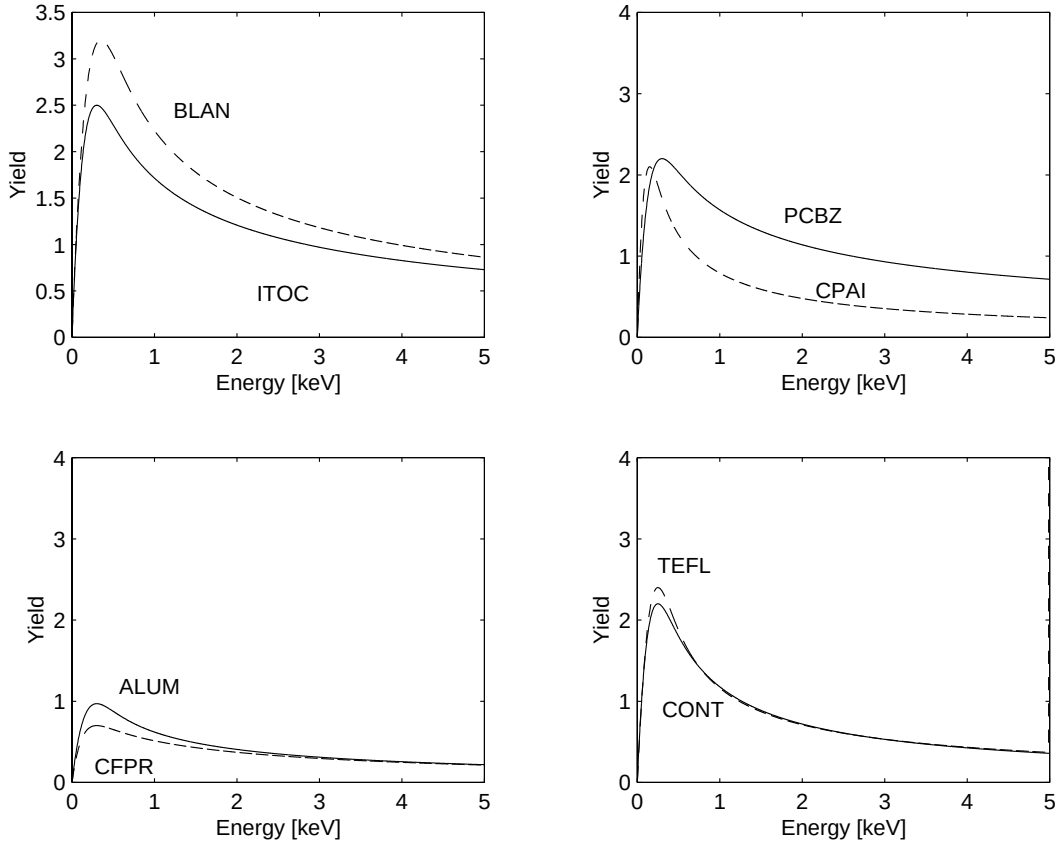

Figure 4.5-3. Secondary yield curves for materials used in the Freja model.

4.5.3 Freja models for POLAR simulations

In POLAR, a spacecraft is modelled in a fixed grid of cubical elements. Except for the additional ability of NASCAP to model one-dimensional structures (i.e., booms) as well as the two-dimensional (rectangular plates and slanted triangular surfaces) and three-dimensional (cuboids, octagons, wedges etc) objects possible to model in POLAR, the two programs are similar in terms of spacecraft definition. For a detailed description of how to model a spacecraft in POLAR, see PUM sections 6.10–6.14.

In order to test the effects of geometric details in the simulation software, spacecraft models on three levels of sofistication have been used. The basic versions of these three models, known as A, B, and C in order of increasing geometric complexity, are outlined below. In the actual simulation runs, the models have been varied in terms of material definitions and slight geometrical changes in order to estimate the effects of such changes. The models are shown in Figures 4.5-4 – 4.5-6.

Model A is a simple definition of the spacecraft as a rectangular object of 2x1x2 grid units (Figure 4.5-4). This very simple model is used (a) for testing the plasma environment models on a simple object requiring comparatively little computational effort, and (b) for comparison to the results from Model C in order to test the effects of geometrical details and small surfaces of non-conducting materials.

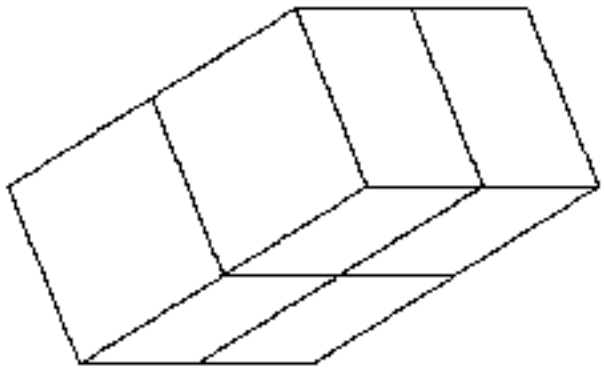

Figure 4.5-4. Geometry of Freja model A.

Model B uses a spacecraft definition grid size of 17 x 17 x 33 cells, which was the limitation of previous versions of POLAR. This leads to a grid unit length of approximately 16 cm for Freja. A version of this model was first used in preliminary runs in May 1997 (Svensson, 1997), and later for comparisons to Models A and C for some events. The model incorporates the main features of Freja (Figure 4.5-5) with some details.

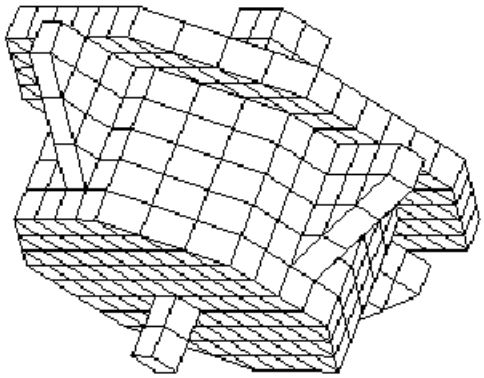

Figure 4.5-5. Geometry of Freja model B.

Model C is the most detailed, with a grid size of 10 cm, allowing additional detail (Figure 4.5-6). In particular, implications of adding small objects of insulating material are possible to study in this model. For more details of these models, see SPEE-WP120-TN, available at the SPEE www-server: http://www.geo.fmi.fi/spee/docs/

POLAR 1.3.7 allows a grid size of up to 50 x 50 x 100 points for the definition of the spacecraft. However, a maximum number of 1250 simple surfaces can be handled, which means that for any reasonably spherical or disc-like spacecraft, the full number of grid points can never be used. For Freja, with a diameter of 2.2 meter, geometrical restrictions alone would allow a resolution of less than 5 cm in grid size, but due to the need to keep the number of surface elements low, the grid resolution of 10 cm used in Model C is the smallest that can be used in practice.

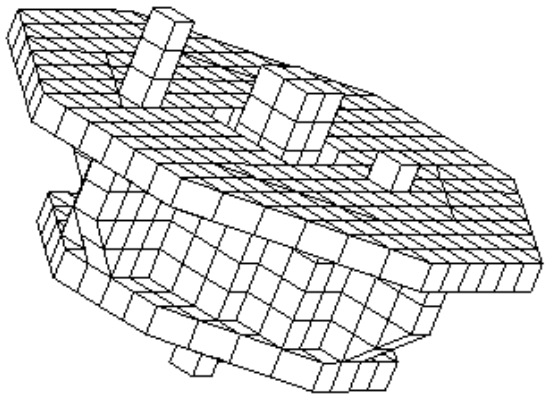

Figure 4.5-6. Geometry of Freja model C.

Figures 4.5-7 and 4.5-8 show examples of how the materials described above have been distributed on spacecraft models A and C. For model C, care has been taken to get the total area of the insulators as closely approximating the values in Table 4.5-2 as possible. For the crude model A, the dielectric surfaces are exaggerated in size. More examples can be found in SPEE-WP120-TN.

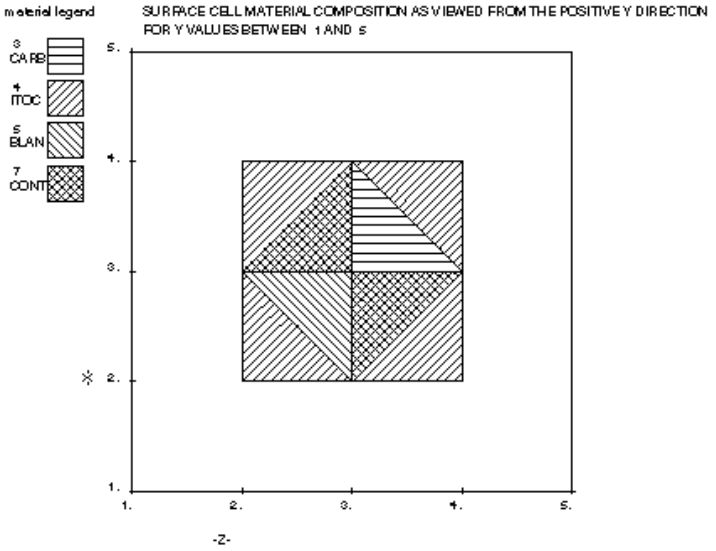

Figure 4.5-7. Distribution of materials on the upper deck and solar panels in model A.

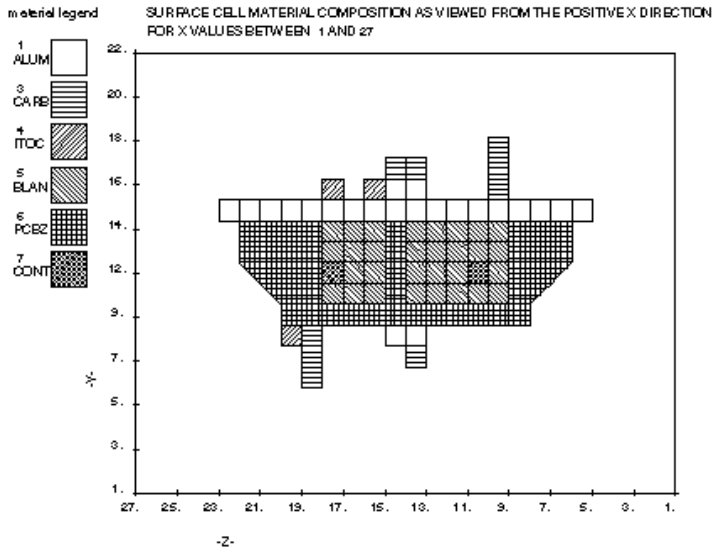

Figure 4.5-8. Distribution of materials on the sides of model C.

4.5.4. Modelling the charging environment

The spacecraft-plasma interaction depends on the actual plasma parameters. The cold plasma density and temperature define the fundamental shielding properties of the plasma and the plasma currents to the spacecraft. We also need to know the ion

composition, as the currents depend on particle dynamics. In auroral conditions, charging is caused by auroral electrons, so we must also characterise the energetic electron environment. Additional information on sunlight/eclipse conditions and magnetic fields is also sometimes required, as is the orbital speed of the spacecraft.

For the simulations presented here we have, unless otherwise stated, assumed that the only ion species present is oxygen, and that ion and electron temperatures are equal. Including a component of hydrogen, which is likely to be present in reality, has the effect of decreasing the observed charging level as the lighter hydrogen is easier for the spacecraft to collect. The spacecraft speed is always put to 7 km/s, and the magnetic field is specified at its observed value and direction. However, the effect of satellite spinning is not included, so one particular spin phase value is picked at random.

The precipitating auroral electrons are in POLAR modelled as a sum of a power law, a hot Maxwellian and a Gaussian population. The particle flux expression [unit: m^{-2} eV^{-1} $sr^{-1}s^{-1}$] is

$$\Phi(E) = AE^{-\alpha} + \frac{n}{\sqrt{2m_e}} \frac{E}{(\pi K T_2)^{3/2}} e^{-\frac{E}{KT_2}} + BEe^{-\frac{(E-E_0)^2}{\delta^2}} \qquad (4.5.2)$$

(PUM section 3.41) where A, α, C, T_2, B, E_0 and δ are free parameters that may be fitted to a measured distribution. The form of (4.5.2) is inspired by a statistical study of auroral zone electron spectra by Fontheim et al. (1982). Although not perfectly flexible, we will see below that it actually can be used to get good fits to the electron spectra encountered by Freja in the events to be studied here (e.g. Figure 4.5-9). The distribution is mapped to a surface element on the spacecraft by use of energy conservation and Liouville's theorem, and the resulting current contribution is calculated by integration over energy. The Maxwellian and Gaussian components have analytic expressions for the integration over all energies, but for the power law component finite integration limits must be supplied since the integral diverges at zero energy.

One should note that in order to find the parameters in equation (4.5.2), we cannot directly compare to the electron spectra observed in the charging events. These refer to electron energy as measured at the spacecraft, which in charging events is not the same as the electron energy of unperturbed plasma. We have therefore corrected for the observed charging level by mapping the POLAR flux expressions from the outside plasma to the spacecraft using Liouville's theorem.

Expression (4.5.2) includes no reference to angular distribution, and POLAR assumes the distribution to be isotropic. While this is rarely the actual case, a high degree if isotropy is often observed in electron distributions at Freja outside the loss cone due to the isotropising magnetic mirror effect on particles travelling from the magnetosphere down toward the ionosphere. In some situations the anisotropy of electron spectra may be an important factor for spacecraft charging processes, but this will mostly apply to spacecraft with large non-conductive parts.

Typical plasma conditions for the Freja charging events were discussed in sections 4.3. and 4.4. For the simulations here we have also used additional detailed data. For determining the parameters describing the energetic electrons, we have visually

fitted expressions of type (1) to electron spectra observed by TESP (Boehm et al., 1994) and/or MATE (Eliasson et al., 1994) electron detectors on Freja. Plasma density is inferred from the identification of plasma oscillations and Langmuir waves, in wave data from the F4 instrument (Holback et al., 1994). Observational Freja input on the electron and ion temperatures is weak, although T_e sometimes can be estimated from Langmuir probe sweeps of the F4 instrument if any reasonably interpretable sample is available close to a charging event. When no input is available, we assume 0.2 or 0.3 eV for ions and electrons alike.

4.5.5. Simulations of charging events

4.5.5.1. Event selection and characteristics

Out of the ten events studied in detail in this project, five six-second periods (a full spin revolution) were selected for detailed simulation of the spacecraft charging process using SUCHGR and POLAR. Table 4.5-3 summarizes the baseline environmental parameters, discussed in Section 4.5.4 above, used in the simulations.

Each event in Table 4.5-3 is studied during a full spin period, which is 6 seconds. The plasma density on line 5 is based on a plasma oscillation within this period. Electron and ion temperatures (lines 6 and 7) are assumptions, except for event 9 where the electron temperature has some experimental foundation. Line 8 is the electron Debye length, line 9 the oxygen-based Mach number of the plasma flow seen in the spacecraft frame of reference, and line 10 is the assumed fraction of oxygen ions. Lines 11 to 19 are parameters defined by equation (4.5.2.), based on visual fits of observed electron spectra (pcutl and pcuth are the integration cutoffs). Two examples of such fits are presented in Figures 4.5-9 and 4.5-10. Lines 20 and 21 show magnitude and direction, in the spacecraft frame of reference, of the observed magnetic field. As the satellite is spinning around the y axis in our models and we consider spin averaged quantities, the direction of B in the x-z-plane is undefined. However, the angular relation between the directions of magnetic field, direction to sun (line 23) and plasma flow direction (line 24) are fixed, and we have arbitrarily chosen a spin phase angle such that the plasma flow is in the y-z-plane in all our simulations. Line 23 is the solar intensity, defined as 0 in darkness and 1 in full sunlight. An observed value of the spacecraft potential in this six second interval, as based on ion data (Section 4.2.5), is found on line 25.

1	Event #	3	6a	6b	7	9
2	Orbit	790	1666	1666	1785	736
3	Date [yymmdd]	921205	930209	930209	930218	921201
4	UT [hhmmss]	023828	091715	091800	093148	003508
5	n_e [cm^{-3}]	125	50	30	60	125
6	T_e [eV]	0.3	0.2	0.3	0.3	2
7	T_i [eV]	0.3	0.2	0.3	0.3	0.5
8	λ_D [m]	0.4	0.5	0.7	0.5	0.9
9	M_{O+}	5.2	6.4	5.2	5.2	4.0

10	n_{O+}/n_e	1	1	1	1	1
11	n_2 [m^{-3}]	1.5e3	2.2e5	6.2e5	5.2e4	1.3e4
12	T_2 [eV]	5e3	7e2	8e3	2.9e3	4e2
13	A [m^{-2} sr^{-1} s^{-1} eV^{-1}]	3.2e12	1.9e11	7.6e14	3e12	3.1e11
14	α	1.9	1.3	2.0	1.6	1.3
15	pcutl [eV]	0.5	0.5	0.5	0.5	0.5
16	pcuth [eV]	6.5e4	1e4	2e4	2e4	6e4
17	D [m^{-2} sr^{-1} s^{-1} eV^{-1}]	1.2e5	3e4	1.3e4	1.5e3	6e4
18	E_0 [eV]	1.5e3	2e3	1.1e4	1.3e4	1.8e3
19	δ [eV]	3e3	6e3	1.5e3	8.1e4	6.5e3
20	B [μT]	26	28	28	28	27
21	B direction (x,y,z) (model B)	0.1 -0.62 -0.78	0.55 -0.83 -0.02	0.55 -0.83 -0.02	0.76 -0.63 -0.19	0.71 -0.69 -0.14
22	Solar intensity	0	0	0	1	0
23	Sun direction (x,y,z) (model B)				0.12 -0.88 -0.46	
24	Flow direction (x,y,z) (model B)	0 -0.70 0.72	0 0.26 0.97	0 0.26 0.97	0 -0.21 0.98	0 -0.06 1.00
25	Observed potential [V]	-25	-40	-1000	-160	-40

Table 4.5-3. Freja charging event parameters for modelling by SUCHGR and POLAR. The table entries are described and discussed in Section 4.5.5.1.

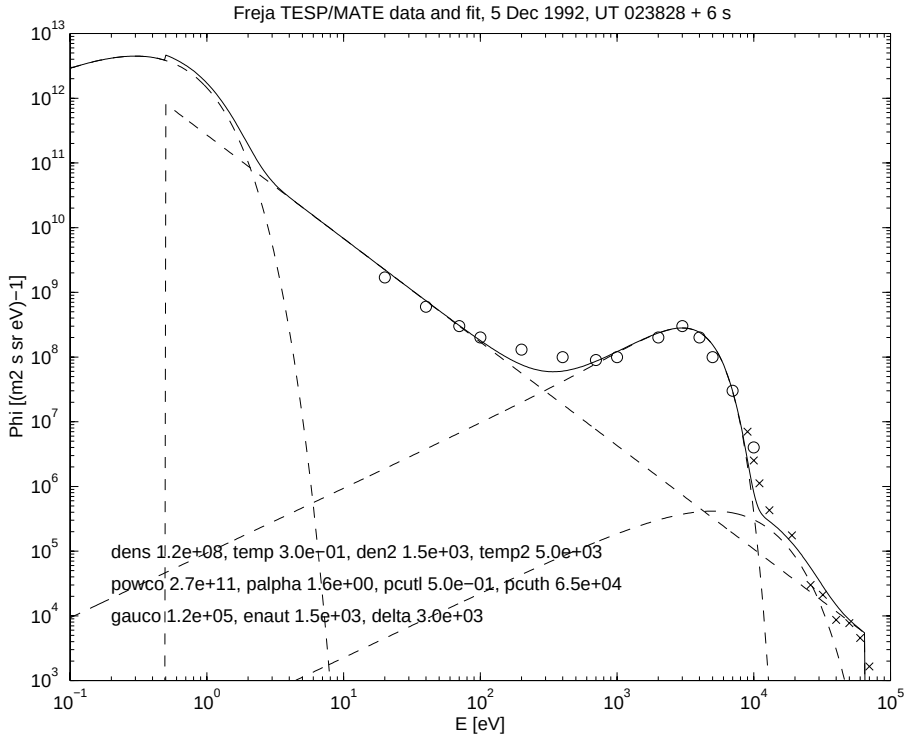

Figure 4.5-9. Spin-averaged electron spectrum for event 3 (orbit 790) based on data from the Freja TESP (o) and MATE (x) electron spectrometers, and a fit to the flux expression (2) with parameters as given in table 4.5-3.

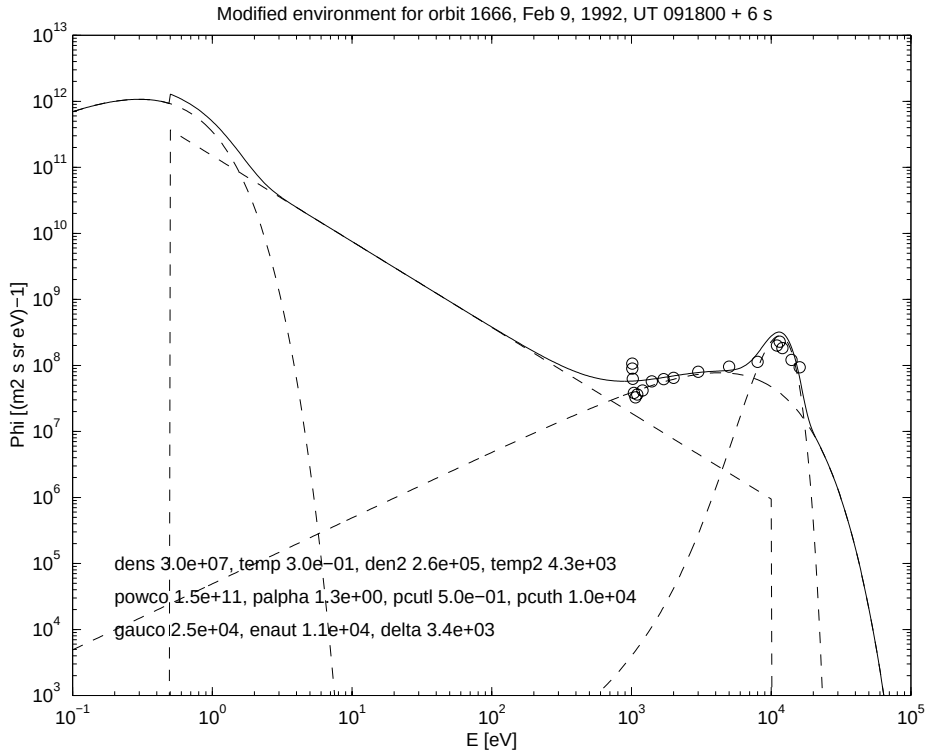

Figure 4.5-10. Spin-averaged electron spectrum for event 6b (orbit 1666) based on data from the Freja TESP (o) electron spectrometer, and a fit to the flux expression (2) with parameters as given in Table 4.5-3.

4.5.5.2. Event simulations

After having defined the spacecraft model and the plasma model, we have a well-defined problem for the SUCHGR and POLAR codes. Table 4.5-4 summarizes the results we get when using this direct approach on the problems. Some of the table entries are based on orbit limited and some on space charge limited calculations, depending on the nature of the problem. A more detailed disucssion of each case is found in SPEE-WP120-TN.

In most cases the simulations did not reproduce the observed charging levels. Only one case, event 9 using the simple model A produced high charging level, this case actually exceeding the observed level. However, when the more realistic model C was used, also here only weak charging was found. The reasons for these discrepancies are disucssed below.

Event	3	6a	6b	7	9
Highest observed voltage	-65	-1800	-1800	-500	-70
Observed voltage at modelled time	-25	-40	-1000	-160	-40
SUCHGR (ITOC)	-0.8	-0.1	-0.3	2.6	-0.6
SUCHGR (ALUM)	-7.2	-12	-72	2.9	-12
POLAR (model A)	-6.9	-5.4	-11	[-4…1]	-105
POLAR (model C)	-1.2	-18	[-40…0]	[-0.2…0.9]	-1

Table 4.5-4. Results of SUCHGR and POLAR simulations for the nominal environments defined in Table 4.5-3. Model A has 1 m grid size, model C grid size 10 cm. Table entries are potentials in volts. The brackets denote that oscillations within these limits were found when the simulation was stopped after it had become clear that charging to the observed level was not going to be reproduced even if the oscillation would damp out.

4.5.5.3. Discussion of the simulation results

There are several possible sources for the observed discrepancy between the observed charging voltages and the POLAR predictions. They may be grouped into (a) errors in the spacecraft definition, (b) errors in the plasma environment definition, (c) errors in the application of the code and (d) limitations of models used in the code. A fifth possibilility, namely pure software bugs, is considered less likely as POLAR has been extensively tested for other situations and showed to work there. We discuss each of these possibilities below.

(a) *Spacecraft definition.* For all the major materials on Freja, we have used parameters established in the laboratory. The exception are the relatively small areas of the nozzles and TM antennas, for which we have assumed material parameters as for CFRP but with very low conductivity, and the also small aluminium parts, for which we have used unoxidized aluminium as model. However, defining the carbon fibre areas as CONT or CFRP has been found to make no big effect to the simulations, and the use of pure aluminium parameters should exaggerate rather than diminish the predicted charging level as the secondary electron yield increases in the oxidization process. If something should be wrong in the material description it must be for some of the more dominating Freja surface materials. One may note that Freja charging events are seen from the very beginning of the mission, so material ageing is a less likely cause of the discrepancy. It is outside the scope of this study to experimentally or theoretically investigate the properties of the materials used. As an example one may note that if the assumed high conductivity of the PCB-Z paint should be significantly lower than thougt, this would bring a major change to the spacecraft model, making a major part of the spacecraft an effective dielectric. Another such possibility is that the ITO cover on the thermal blankets may crack and decrease conductivity. Such effects could cause build-up of large differential charging levels, which by influencing the potential distribution in plasma and hence particle orbits may cause an overalla charging of the spacecraft.

Spacecraft model problems could also be in the geometry of the spacecraft. An even more detailed model of the spacecraft may possibly give better results. We think this is less likely, as it all major parts are quite accurately modelled by model. Although we do not think it likely, it is in principle possible that some of the larger linear elements on Freja, like the magnetometer booms, could influence the potential distribution and thereby change the charging level. One further study could thus be to

construct a Freja model for NASCAP, which can handle booms. Although NASCAP cannot accurately model the auroral spectra seen by Freja, a comparison between NASCAP and POLAR results for a charging environment they both can handle could be of interest.

(b) *Plasma environment*. Several of the plasma parameter values we have used are rather uncertain. For the cold plasma, the temperatures we have used are assumed values. However, varying these within reasonable limits does not very much change the voltage predicted by POLAR. Taking event 3 as an example, runs on model C with temperature 0.1 eV and 1 eV yield spacecraft potentials of –1.3 V and –3.8 V, respectively, which are not dramatically different from the –1.2 V observed for the nominal parameters. We do not think that the cold plasma density could be a major source of error. First, the density values in these charging events are already very low for this altitude range. Second, our identification of the narrowband HF emissions on which we base our density estimates as plasma oscillations and Langmuir waves has been verified by comparison of these emissions with the Langmuir probe current in non-charging events. Third, the ion spectra in the charging events show an uplift in energy of the ram flow, not a major decrease of the ram flow intensity, which should be the case if the density dropped drastically.

The high-energy electrons are well measured by the TESP and MATE detectors, who have been tested in numerous studies (e.g. Boehm et al., 1994; Eliasson et al., 1994). In the region of overlapping energy the two detectors give very similar shapes of spectra with intensities within factor of two from each other. However, we should note a few possibly important uncertainties. First, in the events studied, no truly field-aligned electron spectra have been obtained. The pitch-angle coverage of the detectors depended on the spacecraft attitude. The perpendicular direction is always covered, but pitch angles below 20^{o} were not covered in any of our cases. Table 4.5-5 summarizes the pitch angles of the spectra used, and the observed anisotropies. In some cases, there is no sign of anisotropy in the pitch angle range covered (events 7 and 9), while others may show such anisotropies, in particular for the energy range around 1 keV, which has important impact on the secondary electron production. For the modelling, the 90^{o} spectra have been given more attention, as in an averaging process to find the omnidirectional flux, the directional fluxes will be weighted by the sine of the pitch angle. However, we should note that there in principle may be energetic electrons at near-parallel or near-antiparallel pitch angles which we do not measure. This cannot be checked within the Freja events used here. An extended study could search for Freja charging events with better pitch angle coverage, or use another data set with more complete pitch angle coverage most of the time. Even so, the only way to include them in a POLAR 1.3.7 simulation would be to use pitch-angle averaged spectra.

Event	**Available P/A** [^{o}]	**Anisotropy**	**Used P/A** [^{o}]

3	68, 69, 84, 100	Peak value (3 keV) factor 2 higher at 68^o than at 90^o.	68
6a	33, 34, 90, 103	Peak value slightly higher at 90^o. Flux at 1 keV factor 4 higher at 90^o and 103^o than at 33^o and 34^o.	90
6b	32, 33, 90, 104	Peak isotropic. Factor 2 higher flux at 1 keV (uncorrected) than at 32^o and 33^o.	Average
7	22, 23, 90, 103	Isotropic	-
9	44, 46, 88, 93	Isotropic	-

Table 4.5-5. Observed anisotropies in the spectra used for the specification of the nominal electron environments for the modelled charging events. All energies are as observed at the detector without any charging correction.

(c) *Application of POLAR.* The POLAR code is a complex numerical package with several options on the use of physical and numerical models and of numerical parameters. A straightforward application of default settings of the code fore several of these parameters could lead to unphysical results. A good example is the choice of the grid size. For the Freja applications in plasmas of low density, the real sheath size may easily extend outside the chosen simulation box edge. In that case, the sheath predicted by the code would be too small, the ion currents underestimated, and the magnitude of the charging level overestimated. While this is easy to detect, a more subtle effect is that even though the sheath boundary is well inside the simulation box, the boundary condition that the potential is zero one grid unit outside the simulation box could cause errors in the potential determination, and thereby in other parameters like the sheath location an in the prediction of barrier potentials.

While care has been taken to find an minimise such sources of error, investigating all aspects of the POLAR code is a formidable task beyond the scope of this study. However, the results presented here are based on extensive trial-and-error investigations and studies of parts of the code.

At least in one of the simulation cases (6a) the initial condition on potential was very important for the final outcome. This raises the question whether the time history of charging should be modelled as well. This could, in principle, be done with POLAR 1.3.7 but would, in practice, require an effort that was not possible with the available resources for this study.

(d) *Code limitations.* POLAR has previously been used to simulate DMSP charging events, where higher plasma density was reported. The low plasma density in the Freja events makes sheath sizes large, which is a practical problem in a code using the fixed-grid-resolution strategy of POLAR, leading to unreasonable simulation times. The simulations of our study required run times from one hour (model A) to a few days (model C) in a relatively fast workstation. Nevertheless, simulations performed using

NASCAP as well as POLAR for a –80 V charging event (Svensson, 1997) indicated that the sheath size limitation of POLAR cannot explain the discrepancies between simulations and observations, as NASCAP was not more succesful in the case studied.

In addition, three of the five events studied here, and most of all observed Freja charging events, consider spacecraft potentials less than –50 V, while the driver for the development of POLAR and other charging codes is the study of higher levels of charging, where potentially harmful effects in terms of arcing and discharging may set in if differential voltages appear. However, the biggest discrepancies between simulation and observations was seen to be in the highest charging level events.

In the following section, we discuss some physical phenomena that may need a refined treatment in the code in order to model the Freja charging.

4.5.5.4 Suppression of secondary current and photocurrent

It was above that a direct best-effort approach to POLAR modelling of the Freja charging events did not reproduce the observed charging levels. Possible causes for this discrepancy related to spacecraft and plasma modelling and code handling were discussed above. Assuming no such errors exist, what physical effects could cause the observed discrepancy?

The main problem for getting the observed charging level in a POLAR simulation is that the secondary currents, and for the sunlit event 7 the photocurrent, must be suppressed. From studies of spacecraft in geostationary orbit, it is well known that one way of efficiently doing so is the build-up of barrier potentials related to differential charging (e.g., Purvis, 1983). On Freja, such a scheme has its problems as the area of insulators is fairly small. On the other hand, the secondary yield of the carbon fibre elements (nozzle, TM antenna domes) are so low that they possibly may charge differentially to very high voltages. Indeed the freja simulations showsome development of differential charging. It is therefore of interest to accurately model the suppression of secondaries and photoelectrons by barrier potentials.

The POLAR 1.3.7. algorithm for modelling this is rather simplistic. If the secondary current or photocurrent emitted by a surface is I_0 and the normal electric field E_n on the surface is such that the emitted electrons are attracted back to the surface, POLAR assumes that the actually escaping current is

$$I_{\mathrm{esc}} = \frac{I_0}{1 - \Phi / U_0} \tag{4.5.3}$$

where $\Phi = 2 E_n D$, D is the grid cell size and U_0 = 1 V. Figure 4.5-11 shows a comparison between this model and the suppression resulting if assuming Boltzmann distributed electrons emitted along the surface normal into a purely normal electric field with potential barrier height equal to F. Temperatures 1.5 eV and 3 eV are used, approximately describing photoelectrons and secondary electrons, respectively. It is seen that for small barrier potentials, up to some 3 V, the current suppression of photoelectrons is more pronounced by POLAR than by the Boltzmann model. For secondaries, the corresponding limit value is about 9 V.

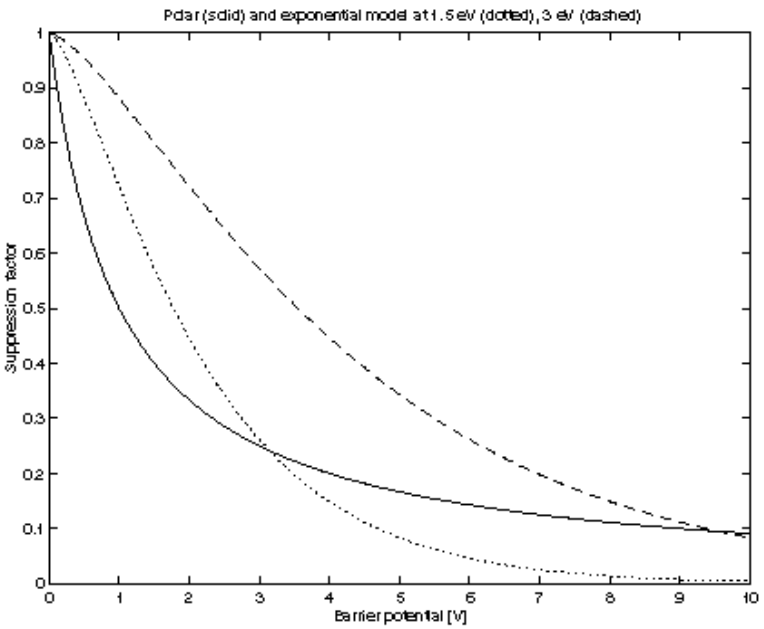

Figure 4.5-11. Comparison between the POLAR algorithm for suppression of photoelectrons and secondary electrons (solid curve) to a Boltzmann (dashed 3 eV, dotted 1.5 eV) with normal emission direction.

Neither the POLAR nor the Boltzmann algorithm takes higher-dimensional effects into account. For an infinite surface with a potential above it only depending on the coordinate along the surface normal, current limitation will be much more severe than modelled above if elctrons are emitted at all angles to the surface. On the other hand, the appearance of electric fields with a component perpendicular to the surface normal above the surface on a geometrically complex spacecraft will allow some particles escape above other surfaces than those they were emitted from. Some particles will also hit the spacecraft at other surface elements that they were emitted from, a phenomenon called hopping. POLAR has a hopping model, unfortunately not supported in POLAR 1.3.7. This effect is therefore not included in the Freja simulations.

One may note that hopping and barrier formation are most effective in low density plasmas. In the charging situations previously studied with POLAR, densities have been higher and these effects therefore less unimportant (David Cooke, private communication). It may therefore be fair to say that the POLAR algorithms are not operationally validated for the Freja environment. In order to treat hopping secondaries and barrier suppression correctly on a geometrically complex spacecraft, numerical integration of test particle orbits in the self-consistently determined potential distribution around the spacecraft would be desirable.

Another means of achieving suppression of emitted electrons from a spacecraft surface may be by the ambient magnetic field turning them back to the spacecraft. This

effect has been studied by Laframboise (1988) for infinite planes and for various strengths of the normal electric field at the surface. To estimate the maximum importance of this effect, we have integrated Laframboise's fitted expression for the current suppression as a function of angle between surface normal and magnetic field over a sphere. The result should give some average value roughly applicable to a spherical spacecraft as long as its radius is much larger than the gyroradius (the infinite plane assumption). The lower normal electric field, the more pronounced the effect will be. As an upper limit of the importance of the effect, we assumed Freja to be a sphere of radius 0.7 m with a vacuum (Coulomb) electric field around it. The results are tabulated in Table 4.5-6, showing that the effect possibly may be of some importance for the low-level charging events but certainly not for the charging to hundreds of volts, particularly as the real electric field will be stronger than the vacuum field, thereby diminishing the importance of this effect. However, for low-charging or floating potential calculations its impact on the photoelectrons may be of interest.

Event	**Iesc/I0**
3	0.85
6a	0.90
6b	1.00
7	0.98
9	0.90

Table 4.5-6. Lower bound on ratio of escaping to emitted secondary current (or photocurrent in the case of event 7) calculated by averaging the result of Laframboise (1988) over the surface of a sphere of radius 0.7 m assuming Coulomb electric field at the surface.

4.5.6. Conclusions of the charging study

A list of materials for the Freja satellite has been compiled. Properties for these materials are known from laboratory experiments, except for some details like engine nozzles and TM antenna domes whose properties are not well known. Models of Freja at different resolution have been prepared, and five Freja events were studied in detail to provide information on the plasma environment in the charging events. The models of spacecraft and plasma were used as inputs to simulations using the POLAR code. It was found vital to compensate the impact of the charging level of the spacecraft on the electron detectors when modelling the charging events for POLAR. The observed levels of charging were usually not reproduced by the code, although there were a few exceptions. For some events, the discrepancy is very large. Variations in cold plasma density and temperature within reasonable limits cannot explain the discrepancy. It is possible that high energy electrons at pitch angles not covered by the detectors could be responsible: however, the inverted-V precipitation spectra which accompany the charging events are usually quite isotropic except in the loss cone. The Freja model is quite detailed and should not be a cause of the discrepancy, although erroneous material parameters for some of the applied surface materials would be a problem if present. The numerical parameters for the code have been varied in numerous runs, and we do not believe unsuitable instructions to the code is a major error source, although this is hard to rule out using the POLAR documentation. Some physical processes not, or insufficiently, treated by POLAR may be the suppression of photocurrent and secondary electron current by potential barriers, hopping to other surfaces and, but only for the lowest charging voltages, the magnetic field, and effects of the charging history of the spacecraft.

When POLAR arrived in the late 1980s, it represented a major breakthrough in the study of charging effects in low Earth orbit in the auroral zone by its ability to self-consistently model a spacecraft sheath, include wake effects and magnetisation, and its facilities for modelling auroral electron spectra. Applications of POLAR have mainly concerned objects large compared to Debye length, which have shown that POLAR works well in this domain. The Freja situation, with the density so low that the Debye length is on the order of the spacecraft dimension, is something of a new application. If it is desirable to model this situation, we recommend that the Freja charging events are studied further as an input to code development. The Freja spacecraft and environment models used in this study are available for that purpose.

For the low-density plasmas studied here, the size of the sheath and the boundary condition that the potential should be zero at the simulation box edges sometimes are problems, as they neccesitate very large grids and thereby causes the calculation time to grow unpractically large. The possibility of employing some adaptive-grid algorithm at least outside the sheath should be considered, reducing the necessary grid resolution in this area and thus saving computational time without jeopardizing the physical accuracy.

The POLAR tools for keeping track of electrostatic barrier formation and currents hopping between surface elements may be insufficient for the Freja case, where these features are of higher importance than in the denser plasmas studied in previous POLAR applications.

For low-level charging events and floating-potential calculations, the inclusion of a magnetic limitation algorithm for the secondary current and photoelectron current could be of some importance. Such an algorithm should be fairly straightforward to implement, using the interpolation formula of Laframboise (1988). If only the ability of the code to model high-level charging events (100 V or more in magnitude) is interesting, this effect may be neglected.

5. SPACECRAFT ANOMALY FORECAST SYSTEM

This Chapter describes studies on forecasting of satellite anomalies in geostationary orbit based on local, non-local, and heterogeneous input data. The anomaly data are from the Meteosat-3 and Tele-X satellites. Meteosat-3 had an onboard particle monitor whereas Tele-X did not.

5.1. The geostationary plasma environment

To understand the occurrence of satellite anomalies at geostationary orbits (GEO) some basic knowledge of the plasma environment at GEO is needed. These orbits are circular at the geocentric distance of 6.6 R_E with low inclination; they are often referred to as geosynchronous orbits although the concept of geosynchronism is a wider concept. The plasma environment is controlled by the magnetic field configuration determined by the internal dipole field and external currents in the magnetosphere and the spacecraft move through variable plasma conditions. The temporal variation of the solar wind influences the magnetosphere and the plasma characteristics at GEO. During magnetic storms the trapped particle belts inside GEO can grow in size and intensity, and more dense populations of particles (high energies) connected to the radiation belts will reach beyond the GEO and modify the spacecraft environment. The increase of particles in the radiation belts and the ring current comes mainly from the magnetosphere tail. Near and inside the GEO orbit electrons from the tail move eastward on trapped paths around the Earth whereas high-energy protons move eastward. Particles that become trapped in the Earth's nearly dipolar magnetic field form a net westward ring current.

The main contributions to the ring current are particles in the keV energy range. The radiation belts consist mainly of particles with higher energies. The particles in the inner radiation belt are in stable trapped orbits, which implies that there is no obvious entry or sink for the inner radiation belt. The source is usually assumed to be galactic or anomalous cosmic rays (GCR or ACR). Since the loss rate is low the number density can grow to significant levels. As ACRs typically are only singly- or doubly-ionised they can reach lower parts of the radiation belt and play a significant role there compared to the more numerous GCR (Klecker, 1996). The decay of the radiation belts is slow and mainly caused by pitch angle diffusion and charge exchange with neutral particles.

During quiet times the geostationary orbit is always inside the magnetopause, but during severe magnetic storms the dayside magnetopause may move inside GEO. The plasma environment a spacecraft experiences depends on the local time. Because the majority of injections occur from the tail, the morning hours usually have bursty flows of electrons. At other local times the injected particles have been smeared out to lower concentration due to the adiabatic motion, energy filter effects and particle losses at the dayside magnetopause. High-energy electrons have the highest density in the noon sector due to the adiabatic motion and the compressed dayside magnetic fields. The typical plasma sheet electron temperature at GEO distance is 1 keV but during high

geomagnetic activity the temperature can increase to 10 keV. A typical time for flux levels to build up in the magnetosphere is 80 hours (Rodgers, 1991).

The angle between the Earth's magnetic dipole axis and the rotation axis is ≈11°. The geostationary orbit is in the plane of the Earth's rotation. Since the Earth is orbiting the Sun and the Earth's rotation axis is tilted with respect to the ecliptic plane, the geostationary orbit is in the Earth-Sun plane twice a year, during the equinoxes. The rest of the year the orbit is tilted compared to the Sun-Earth line. The solar activity follows an 11-year cycle. A 27-day periodicity in magnetic storms originates from the solar rotation. The 27-day rotation can clearly be seen in the high speed solar wind streamers during the declining phase of the solar cycle.

The main charging component on the spacecraft in geostationary orbit is electrons since they are more mobile than ions (Rodgers, 1991). The geostationary orbit passes through the outer radiation belts with trapped electrons in the energy range 1 to 10 MeV. The electrons do not usually interact directly with electronic components because a modest amount of shielding (approximately 2 mm Al) is enough to stop the majority of them, although their accumulated dose can eventually cause significant component degradation. Electrons above 30 keV cause a large number of secondary particles, which in their turn can charge parts inside the spacecraft and cause deep-dielectric charging. Frederickson (1980) found that bulk charge in dielectrics required at least a week to decay and possibly much longer. Hence the effect of many bursts of energetic electrons can add up and cause problems on the spacecraft.

The time scale of charging depends on the capacitance of the surface as well as the magnitude of the charging current (Rodgers, 1991). In geostationary orbit, time scales for the charging of surfaces are in the order of seconds. The differential charging of the largest surfaces relative to each other may take from seconds to hours. Since periods of disturbed plasma likely to cause intense charging usually have time scales of minutes, equilibrium is not always reached. During eclipses, when of course photoelectron emission can not occur, the SEM-1 on Meteosat-2 frequently observed differential charging which caused potential differences of around -600 V in one hour. They disappeared minutes after the eclipse had ended. In GEO the eclipse orbits and shadowing of different surfaces are the most common cause to changes in the spacecraft potential.

5.2. Spacecraft anomaly forecasting using local environment data

5.2.1 Local environmental data

Local environmental data would always be very useful in analysis of spacecraft anomalies. The optimal case would be a scientific satellite equipped with several detectors, such as Freja discussed in the previous chapter. However, most satellites do not carry any environment monitors or just have some very simple detectors.

The USAF Defense Meteorological Satellite Program (DMSP) spacecraft carry space environmental sensors). At present the three sensors are: a space plasma monitor (SSIES-2), an auroral particle sensor (SSJ/4), and a magnetometer (SSM) (see http://www.ngdc.noaa.gov/dmsp/descriptions/dmsp_sensors.html). The data are used to make space weather spacification and forecasts at the 55th Space Weather Squadron, Falcon AFB Colorado, to determine causes of satellite malfunctions as well as to provide warnings to satellite controllers and users when hazardous environmental conditions that could adversely affect satellite operations exist. The SSJ/4 instrument is designed to measure the flux of charged particles precipitating into the atmosphere. It consists of four electrostatic analysers for the energy range 30 eV to 30 keV. The topside ionospheric plasma monitor (SSIES) measures the thermal plasma. The sensors are tailored for the sun-synchronous orbit altitude of 840 km. The SSIES, SSIES2 and SSIES3 system contain an ion retarding potential analyser, an ion drift meter, a total ion trap and a spherical electron sensor. The SSIES3 also contains a plasma plate on the ion array for measuring the ionospheric electrons. In addition to the sensors for collection environmental data the three systems contain a sensor, SENPOT, measuring the electric potential between the plasma and the spacecraft. The sensor part of SENPOT is a section of the ion sensor aperture plane, which is electrically isolated from the spacecraft by 100 Mohms. The ion sensors are Faraday cups measuring thermal ions and Langmuir probes measure thermal electrons.

The Space Test Program at the Space and Missile Center (USA) together with Phillips Laboratory Geophysics Laboratory have developed the Compact Environmental Anomaly Sensor (CEASE) to monitor the environment. The instrument is designed to provide alerts when anomalies are expected to be caused by surface charging, deep dielectric charging, SEU or radiation dose effects. The instrument stores data up to 72 hours, which can be transmitted down at request. The TSX-5 satellite is expected to be the first flight for CEASE. It is also planned for STRV-1C.

The Japanese Engineering Test Satellite-VI (ETS-VI), launched in August 1994, was equipped with a set of instruments to measure space environment effects (Goka et al., 1996a,b). The set of instruments called Technical Data Acquisition Equipment (TEDA), included a heavy ion telescope, dosimeter, magnetometer, single event upset monitor, total dose monitor, solar cell radiation damage monitor, contamination monitor, and electrostatic potential monitor.

On the Space Technology Research Vehicle (STRV-1B), launched in 1994 a Radiation Environment Monitor (REM) (Bühler et al., 1994) was flown to detect electrons and protons in a GTO orbit. REM was also flown 1994 in LEO on the space station MIR. The instrument was designed at the Paul Scherrer Institute (PSI) together with ESA. It has two Si detectors under shielding domes and detects electrons >1 MeV and protons >30 MeV (Bühler et al., 1996 a, b). The GTO passes through the most severe parts of the proton and electron radiation belts. The proton dose variation showed some variation with active solar periods, as well as a general solar-cycle-related trend. An increasing trend in proton doses was suggested to be consistent with the anti-correlation expected for protons. The electron environment was found to be very dynamic. During

disturbed periods the radiation belts correlate well with solar rotation and a clear seasonal pattern was seen. When a high-speed stream arrived, the energetic flux first showed a dropout and then an increase of the flux. For more information on REM results see, e.g., Daly (1998), Bühler et al., (1997), Bühler et al. (1998).

An improved version of REM is the Standard Radiation Environment Monitor (SREM) (Vuilleumier, 1997) which is developed and manufactured by Oerlikon-Contraves Space in co-operation with the Paul Scherrer Institute (PSI) under an ESA contract. The first SREM model is schedule for flight 1999 on STRV-1C and later on ESA satellites such as Integral and Rosetta. The instrument is calibrated with protons up to 600 MeV and electrons 5 MeV. One difference compared with the REM is that the problem with contamination of electrons in the high-energy proton channels is removed by a telescope configuration (Bühler et al., 1996a). The particle detectors measure electrons (0.3– 6 MeV) and ions (8 –300 MeV) in fifteen energy bands. The instrument has two alarms for high/low dose rates, dead-time correction for alarm, detection of SEE, total radiation dosimeter, and a large memory. SREM is contained in a box with the size 10 x 12 x 22 cm, weight • 2.5 kg, and power consumption < 2 W.

An integrated environmental monitoring system is developed for several commercial satellites, e.g., on Martin Marietta spacecraft (Bogorad et al., 1995) and Lockheed Martin Astrospace (Intelsat VIII/VIIIA) (Ozkul et al., 1996). The system contains two sensors, a Surface Charge Monitor consisting of a 2 x 2 inch plate, where the potential difference is measured and a Dosimeter/Internal Charge Monitor. The surface charge monitor is designed to respond to electrons with energies from 5 to 20 keV. On INTELSAT VII/VIIIA two sets of plates are included, one looking away from Earth and the other towards north or south. The dosimeter/internal charge monitor consists of radiation sensitive p-FET integrated dosimeter devices with different thickness of the shielding. The p-FET device is sensitive to electrons with energies from 200 keV to 6 MeV but does not provide particle species or energy discrimination. The main components of the dosimeters are designed, manufactured and tested at the Center for Space Microelectronics Technology, Jet Propulsion Laboratory, California Institute of Technology. The total weight of the instrument is less than 0.5 kg and the power consumption about 0.5 W.

5.2.2. Anomalies on Meteosat series satellites

The first Meteosat satellite, Meteosat-1, was launched in November 1977. The satellite was a spin-stabilised meteorological satellite with the main payload consisting of a scanning radiometer. The satellite experienced several anomalies. At the same time Meteosat-2 was being designed and the first investigation of Meteosat-1 anomalies was made already after one year (Hoge and Leverington, 1979). A clear correlation between anomalies and the spring equinox and a weaker correlation with the autumn equinox were seen for four different satellites: Skynet, Meteosat-1, Symphonies-A and B. Correlation with local time, solar direction, or eclipses could not be established. A clear correlation between anomalies on Meteosat-1 and the geomagnetic indices two days

before the detected anomaly was seen. The two day delay was also indicated in the Skynet data. A ground test of the engineering model was set up for investigation of the space environmental effects on Meteosat-1.

On Meteosat-1 about 80% of the outer surface of the satellite was not conductive, e.g., solar cell cover glass, second surface mirrors, and black paint. Large metallic surfaces of the thermal shields were not grounded because no cost-effective solution existed at that time. The grounding was a multipoint grounding system. Current injection tests did not give any failures during a five-week test period. Thermal shield test of irradiation was performed but the discharges were smaller than expected and seemed to have no impact on the satellite. The result from an electron irradiation test (Hoge and Leverington, 1979; Hoge, 1980; and Hoge, 1982) showed that virtually all isolated surfaces on Meteosat were subject to arc discharges every second or so but the energy was too low to cause any damage on-board. The test was set up to simulate typical substorm conditions.

The Meteosat-1 spacecraft charging investigation led to the recommendation for Meteosat-2 to ground the shield, to improve some critical interfaces, and to incorporate charging monitors. The charging monitors on Meteosat-2 consisted of an electron analyzer, SSJ3, built at Emmanuel College, Boston, USA, and an electrostatic discharge monitor EEM-1 built at ESA/ESTEC. The SSJ3 had an energy range of 50 eV – 20 keV in a low and a high energy channel

The Meteosat-2, with the improved design, was launched in June 1981. Meteosat-2 also encountered anomalous status changes (Hoge, 1982). During the first year a clear correlation of Meteosat-2 flux measurements and the Marecs-A satellite anomalies was seen. Most of the Marecs-A anomalies occurred when the spacecraft passed through the plasma sheet. The monitors onboard Meteosat-2 confirmed that the presence of spacecraft charging did not perturb the Meteosat-2 functions, and therefore the interest of looking at more energetic radiation was raised. From the Meteosat-2 satellite the rapid degradation of the solar array indicated the presence of high energy particles but it did not correlate with the anomalies. Coates et al. (1991) studied almost six years of anomaly data from Meteosat-2 and found that the anomalies did not fit the pattern for surface charging effects. They suggested deep-dielectric charging as the most likely explanation.

Hoge (1982) concluded that the improvements of the design of Meteosat-2 were effective although the monitored data did not agree with the hypothesis for the charging mechanism which was used to introduce these modifications. Other types of environmental effects or onboard generated interference may have been the cause of the remaining Meteosat-2 arcing anomalies. A spectrum of monitors for future launches was recommended. For Meteosat-3 a new environmental monitoring instrument SEM-2 was used to measure higher energies. The SEM-2 was built at the Mullard Space Science Laboratory, UK under an ESA/ESTEC contract.

An assessment study (Frezet et al., 1989) was made on GEO satellites, one of which was Meteosat-2. It used the NASCAP and MATCHG codes to investigate electrostatic charging, especially for the radiometer cavity on Meteosat-2. Due to the

seasonal dependence the code was run for different solar aspect angles. The simulation lasted 15 minutes. Less charging was found at solstice conditions than at equinoxes because of the larger sunlit area. The study recommended avoiding floating metalisation and high-resistivity material. The differential charging was reduced considerably when all conductors were grounded. Further improvements were seen when insulation black paint was made conductive and the Teflon was replaced by the lower-resistivity Kapton. With this the charging of the cavity was almost removed. In the result of the test a seasonal dependence was observed but a good correlation between severe plasma events and the observed Meteosat anomalies was lacking. This indicated that at least part of the problem was caused by "deep-dielectric charging" induced by high-energy electrons.

5.2.3. Meteosat-3 anomalies

Meteosat-3 was launched on 15 June 1988, to become one of ESA's geostationary satellites in the meteorological satellite series. The satellite was operated by Eumetsat and was moved several times (see Table 5.1).

From	**To**	**Position**
Launch 15 June 1988	June 1989	0°E
June 1989	January 1990	50°W
January 1990	April 1990	0°E
April 1990	November 1990	5°W
July 1991		50°W
late 1992		75°W
April 1993		72.8°W
February 1995	November 1995	70°W, inclined

Table 5.1. Meteosat 3 position

The anomaly set covers the time period from 21 June 1988 to 20 October 1995. The environment monitor SEM-2 was operated during the same time period except for a few months. Meteosat-3 had several types of anomalies. In Table 5.2 the anomalies are presented in 18 different categories. Most anomalies were related to the radiometer, about 70% of all anomalies. The total number of anomalies during the operational lifetime was 724.

In Figure 5.1 all anomalies from Meteosat-3 are plotted versus the local time and time of year. It shows that more anomalies occurred in the late evening/early morning sector (00-09 LT) than during the rest of the day. This has also been seen in earlier studies (Rodgers, 1991; Wilkinson, 1994; Vampola, 1994; Wrenn and Sims, 1993). The increase of anomalies is usually attributed to the injection and drift of electrons into this local time sector.

The radiometer anomalies have a peak in the midnight–morning sector (Figure 5.2), but most other anomalies are spread evenly in local time. This and earlier results (Grystad, 1997) suggest that the radiometer anomalies may have a different cause. The battery charger anomalies are clearly correlated with equinox. The image line anomalies

occur late in the mission and could be due to aging or be more susceptible to cosmic rays. The rest of the anomalies are evenly spread over the year and local times. The effect of the special conditions during equinox is clear on most types of anomalies.

Code	**Description**	**Count**
1	Radiometer stops	295
2	Radiometer position jump	84
3	Radiometer position jump and stop	127
4	Other radiometer anomalies	3
5	Battery charger 1 anomaly	7
6	Battery charger 2 anomaly	49
7	Battery charger 1 and/or 2 off	14
8	Battery charger rate anomaly	4
9	Digital multiplexer 1 off / 2 on	8
10	Corrupted/lost image lines	67
11	Command decoder anomaly	3
12	Temperature reading anomaly	14
13	SIC anomaly	29
14	EDA bias jump, SIC lid jump, rad gain	5
15	VIS 2 gain jump	2
16	Regulator loop voltage anomaly	2
17	Spurious memory reconfiguration	2
18	Other anomalies	9

Table 5.2. The codes of Meteosat-3 anomalies

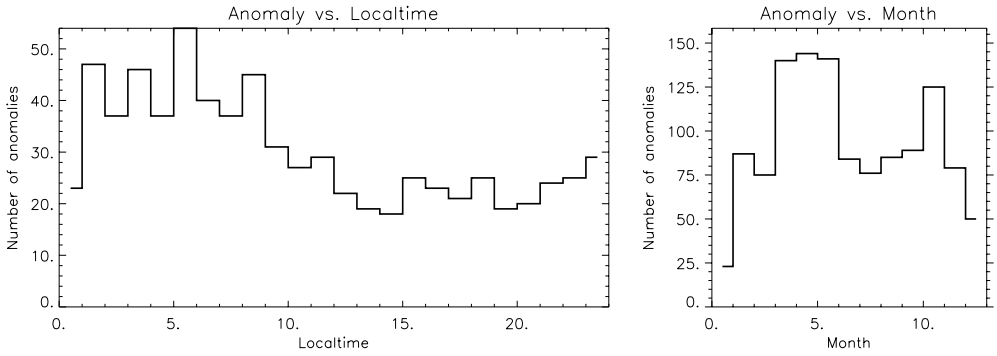

Fig 5.1. Meteosat-3 anomalies vs. the local time and month, respectively.

The solar cycle dependence (Figure 5.3) has to be carefully analysed because the operational period of the satellite covered less than one solar cycle, starting during solar maximum (1989) and continued into solar minimum. Ageing effects can make the spacecraft more susceptible to the environment. If the effect is mainly due to solar activity causing variation of plasma characteristics in the magnetosphere, the number of anomalies would be highest at the beginning of the mission. The effects solar proton events or GCRs and ACRs should give a different solar cycle dependence with more events during solar minimum. The ageing of the spacecraft is expected to increase the number of anomalies with time, although for some cases the ageing can cause anomalies to disappear. In this study we cannot separate the ageing effect from the solar cycle effect.

(a)

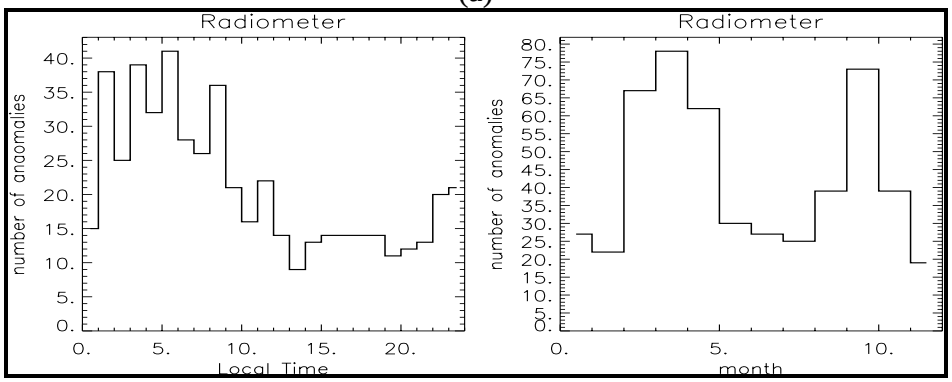

(b)

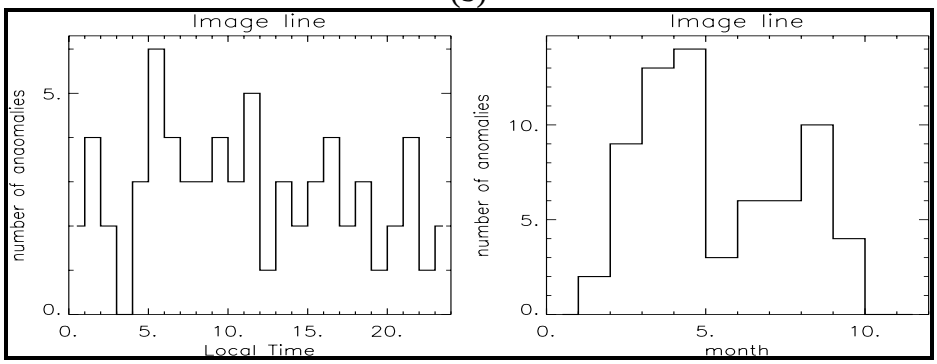

(c)

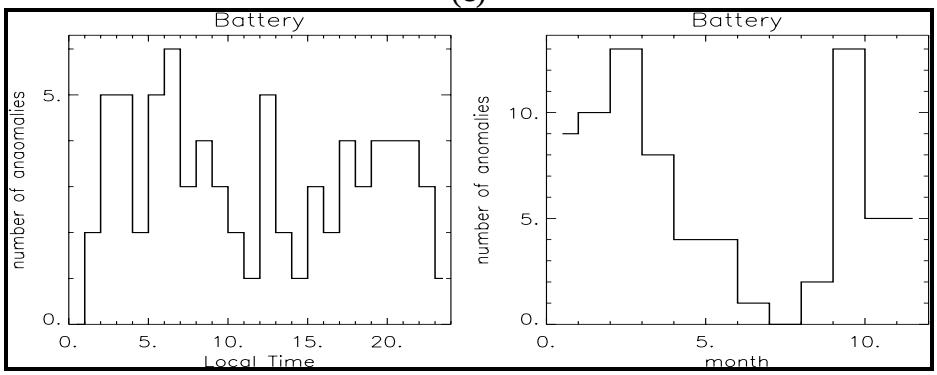

Figure 5.2. Different anomalies plotted vs. local time and month. The different figures show; a) Radiometer anomalies (code 1, 2, 3, 4) ;b) Image line anomalies (code 10) and; c) Battery anomalies (code 5, 6, 7, 8). The codes refer to Tabel 5.2.

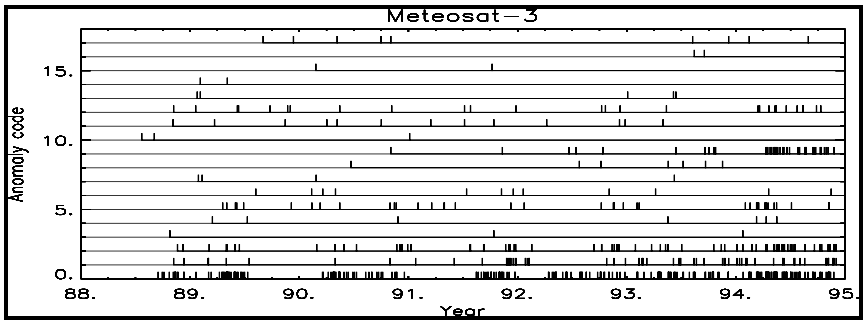

Figure 5.3. The different anomalies as function of time.

5.2.4. Earlier studies on Meteosat-3 anomalies

Rodgers (1991) studied 166 anomalies of the Meteosat-3 (also called Meteosat P2) from the radiometer together with primarily the low-resolution data from SEM-2. A clear correlation was seen between some of the anomalies and the electron flux. A statistical study showed that for a typical anomaly the flux levels had been built up during the preceding 80 hours. Anomalies correlated with the highest flux occurrence mainly at 3-9 local time (LT). Anomalies correlating with low fluxes and longer build-up times occur at 15-24 LT. Both seem to be more correlated with the high energy range on SEM-2 and indicate that deep-dielectric charging is the most likely cause. Different energy ranges and their relative importance were compared using a time window around the anomaly and an average level (not time dependent). No correlation was found with incident angle for low-resolution data but for high resolution some dependency of theta was discovered. Earlier studies showed that anomalies have a strong seasonal dependence. This suggested that eclipse periods are important. The equinox coincides with the sun shining directly into the radiometer cavity, and this should reduce the surface charging effect but would not effect the deep-dielectric charging effect. Rodgers (1991) concluded that the anomalies might have different causes but are probably due to deep-dielectric charging. The morning anomalies seemed to be triggered by a high flux of particles while evening anomalies had a long accumulation phase, over 8 days without a peak in the fluxes.

Rodgers et al. (1997) continued the study of Meteosat anomalies with the full seven-year anomaly data set (total 725 anomalies) together with the SEM-2 data. The detailed investigation was only on the radiometer anomalies (486 anomalies). They found that the highest energy channel was correlated with anomalies with high fluxes at the time of the anomaly. The 5-9 LT anomalies are mostly correlated with the high-energy channel. These were again suggested to result from deep-dielectric charging, and 16 of 121 anomalies in 5-9 LT occurred in the same 3-hour bin as the previous anomaly. The other, especially 17-21 LT, anomalies occurred after long build-up times and with relatively low fluxes at the time of the anomaly.

López Honrubia and Hilgers (1997) ivestigated pattern classification techniques for Meteosat anomaly data analysis. They used 40 anomalies over 5 years from Meteosat-3, 4, and 5 (they are known as the Meteosat P2, launched 1988, the Meteosat Operational Satellites MOP-1, mid 1989, and MOP-2, February 1994, respectively) together with high energy (>2 MeV) electron measurements from the US series of Geostationary Operational Environmental Satellites (GOES). The data set was divided into two classes “anomaly”- “non-anomaly”. The analysis was made with a Learning Vector Quantization (LVQ) network. The data set contained 2000 input vectors, 40 of which were associated with anomaly days. The input data consisted of an N-day window with N days of the mean daily flux; the window did not use information from the same day as the anomaly to make the analysis to be a forecast. The output was 1 if there was an anomaly the following day, -1 if there was an anomaly within the window N before or after and otherwise 0 (the cases with -1 were not analysed). Although

limited by the small amount of anomaly data, the technique gave evidence for correlation of this type anomaly with MeV electron data measured by GOES and for time dependent effects.

Grystad (1997) applied a similar technique as López Honrubia and Hilgers (1997) to analuse the same data as Rogers et al. (1997). Both a Bayesian linear classifier and an LVQ were used on the Meteosat -3 anomaly set and on the on-board SEM-2 instrument. The highest energy channels showed slightly different characteristics with a maximum at 4 days. The main conclusions, although still preliminary, were that the lower energy range correlates when only average flux over the latest day is considered, while for higher energies the best window length is longer.

5.2.5. Forecasting Meteosat-3 anomalies using neural networks and local data

The space environment monitor on Meteosat-3, SEM-2, covered the energy range 42.9–300 keV with the time resolution 8–10 minutes (Rodgers, 1991) The SEM-2 has a low mass (2.5 kg), power (1.8 W), and telemetry rate (1.9 bits/s). It is a solid-state detector which uses the stop length to estimate the energy. The highest energy bin includes all high-energy particles, also those which do not stop in the detector (energies above 300 keV). The energy range was selected to look for deep-dielectric charging effects. It was based on an array of five surface barrier detector-collimator systems and was built by the Los Alamos National Laboratory and calibrated by the Mullard Space Science Laboratory. The detectors were arranged in a fan shape with each detector at a different angle to the spacecraft spin axis to give five polar angle bins. The field of view of each detector was 5 degrees. Azimuthal information was obtained by the spacecraft spin. The spin axis was aligned with the Earth's north-south axis.

An anisotropy index was derived from a two-dimensional array of fluxes at each polar and azimuthal angle, summed over all energy bins. This index is calculated by fitting spherical harmonics to the data (Rodgers, 1991 and references therein). Zero second-order anisotropy index corresponds to an isotropic distribution. Negative index corresponds to an equatorially enhanced or “pancake” distribution which is frequently seen near local midnight. Most electrons in this energy range have come from the tail in this sector. The axis of symmetry of the distribution is found in the same fitting process and is expressed in terms of its polar (θ) and azimuthal angle (ϕ). Since the electrons are expected to be controlled by the magnetic field, the axis of symmetry is an indicator of the magnetic field direction although the sign and strength of the magnetic field are unknown.

The data files were stored in two sets with the resolution 8–10 min and 30 min, respectively. Only the 30 minute resolution data were used. The archive SEM-2 data files contain: flux (summed over ϕ and θ) as function of energy, flux (summed over energy and ϕ) as function of θ, flux (summed over energy and θ) as function of ϕ, flux (summed over energy) as function of ϕ and θ, total flux (summed over energy), spectral index (γ), second-order anisotropy index α, and the polar (θ) and azimuthal (ϕ) angles

defining the axis of symmetry, Kp (the planetary magnetospheric activity index) and the status of the on-board memory SEU monitor.

At the beginning of the mission there were more sporadic electron fluxes (solar maximum), while at the end (solar minimum) more regular changes took place corresponding to the 27-day rotation of the Sun. There was a variation between the daily average fluxes but no clear changes of the mean flux between solar minimum and maximum. The variation during one day was larger than the day-to-day variation.

5.2.6. Anomaly data set

About 724 anomalies occurred during the almost 7 year mission of Meteosat-3. The anomalies often occurred after a period of high electron fluxes. The difference between a time period preceding a non-anomaly and a period preceding an anomaly was less than the normal daily variation (one orbit) of the electron fluxes.

A data set containing electron fluxes with a time resolution of two hours was created. During the lifetime of the Meteosat-3 satellite there were six longer (• 1) periods when SEM-2 was not operated. This implies that the data set has to be treated as seven separate time series. A few small gaps (• 4) were replaced with a linear integration from the surrounding points. The total number of two-hour-data are approximately 27500.

The forecast is based on electron fluxes as input to a neural network. The network predicts if an anomaly will occur or not (output). The desired output was set to zero (0) if no anomaly occurred within a time window and to one (1) if an anomaly occurred. The time window is selected to give a warning to a spacecraft operator as early as possible without giving too many false alarms.

Statistically, one anomaly occurred every fifth day. Therefore the time window was set to predict anomalies within 24 hours. Since the data set has a resolution of two hours this leads to one anomaly giving 12 rows of warnings in the data file. If two anomalies occur within 24 hours the number of warnings (rows with value 1) will be less than 24. Consequently, the forecast success for warnings and anomalies can be different. The total number of warnings is approximately 5200, i.e. for 19% of the total number of 2-hour-steps.

The two-hour time-series is created to keep as much information as possible from the SEM-2 measurements. For each of the five energy bins four flux values are calculated and saved in a file; the 2 hour mean flux, the maximum flux during the 2 hours, the minimum flux during the 2 hours, and an average flux from the previous 72 hours (3 days). 72 hours was selected because it is longer than a day (to average out daily variations) and less than the 80 hours of some magnetospheric storm effects. Three files with different data combinations were produced, one using all five energy bins plus information of the spectral shape (spectral index, anisotropy index, θ and ϕ), giving 24 columns for each 2-hour step (data combination called "_all"). The other combinations used only the three highest energies or the three lowest energies, giving 12 columns for

each 2-hour step (called "_high" and "_low"). All data combinations contain the logarithm of the flux to make the data set more linear.

In order to limit the number of dimensions (inputs), a principal component analysis (PCA) was performed on all three data combinations creating new data sets containing only three dimensions. The PCA gives the eigenvalues for the data set and selects the largest as the first component, the second largest variance as the second component, etc. If only the three largest components are used this will be a transformation from 24 dimensions (the data combination _all) down to three. In this case the first principal component was associated with the average, minimum, and maximum flux for all energy bins. The second principal component was associated with the running mean for all energy bins, and the third component is more of a mixture.

The data combination files (_all, _low, and _high) now contain three columns with information on the fluxes for each time step (row). In order to predict anomalies with a neural network, an input file is built with information on the magnitude of the components and the dynamics of the electron fluxes preceding the forecast. The preceding time of the forecast is selected to be a window, with a time length up to several days. If all data (with 2 hour resolution) for a selected time window are used to predict the anomaly there will be a large number of inputs. Table 5.4 shows some of the data combinations. For the combination pa3, the magnitudes at the time of the forecast are used together with the values 12 points before (i.e., 24 hours before) plus the values 24 points before. This leads to a time window of 48 hours containing three points each with 3 components, thus 9 inputs.

ref. name	**point resolution**	**number of PCA used**	**total number of columns**	**length of time window (h)**	
pa2	3	3	9	24	
pa3	12	3	9	48	
pa4	3+12	6	18	48	points at 0, 4, 7, 10, 12, and 48
pa5	3	4	12	20	
pa6	6	6	18	54	
pa7	12	6	18	144	

Table 5.4. All different combinations for the PCA file used in this report. pa3 is described in the text.

After low-pass filtering, a frequency analysis was made on three different time windows. The three selected time windows were 32, 64 and 128 points. The result is referred to as wa32, wa64, and wa128. A wavelet transformation (Kumar and Foufoula-Georgiou, 1997) into 15 components was used. The wavelet transformation can better reproduce the dynamics of short time series than the Fourier technique.

The neural networks used in the study are ordinary back propagation networks of different sizes. The output of the back propagation network is a real number. This implies that a threshold must to be selected to distinguish when the net is predicting an anomaly or not. The threshold is chosen so that the success of predicting non-anomaly

is equal to the ratio between anomalies and non-anomaly, i.e. the threshold is set to give a success rate of non-anomalies to about 80% or better.

The input to the neural network is a combination of magnitudes, dynamics (wa32, wa64 and wa128) and performed on different data combinations: _all, _high, and _low. A data file containing the inputs and the desired outputs (1 if anomaly occurs within a 24 hour time window, else 0). From the created file (approximately 27500 points or rows) all rows associated with anomaly warnings (1) and twice the number of rows associated with no anomalies (0), are selected randomly to train and test the network. The training of the neural network is made with 2/3 of the data set and the test with 1/3. Normalization of the data is made using commercial network software (Neural Ware).

Table 5.5 shows some of the results using different configuration of the network and inputs. The first column is a reference number of the row. Second column, top row gives information about the data combination (the definitions are described in the text above). The bottom row of the second column indicates the level to separate the anomalies into two different cases, file fiI and fiII. The "net" indicates how many inputs and outputs used for the case and "PE" is the size of the back propagation net. Last three columns show the results from different trained network, trained with _all, fiI and fiII anomalies. For all three cases are 2/3 of the data used as a training set and 1/3 as the test. The last two files (fiI and fiII) were created using "level" in the second column. Anomalies following within 24 hours after a high value of the largest principal component (i.e. high electron fluxes) is in fiI, and the rest of the anomalies in fiII. The selected non-anomaly cases are randomly selected. In this way one network is trained to predict anomalies associated with high electron fluxes and the another network to find other causes. The "level" is set so the anomalies associated with high energy fluxes are approximately 20% of the total anomalies.

The results of the different tests in Table 5.5 are presented as the success (in percentages) of predicting the anomalies (top) and the non-anomalies (bottom) in each box. Since the output of a back propagation net is real number, the threshold for each individual test is chosen so that the non-anomaly success rate is close or higher than 80%. Since only thresholds of 0.3, 0.4 , 0.5 and 0.6 were used and only one of the results is presented in the table, a comparison between different runs in the table can be difficult.

The cases presented below are only a few of the many combinations that were tested. For more details, see WP-210-TN at http://www.geo.fmi.fi/spee/docs/

Intensities

Only the electron fluxes at the time of forecast, 24 and 48 hours before the forecast are used to train the network given in row 1 (Table 5.5 data file, pa3). The network was designed for 12 inputs, 1 output, 5 neurons in the first layer and 2 neurons in the second layer. The training of the network was made with 2/3 of the data. When tested on the unseen Meteosat-3 data (1/3), the warnings (for anomaly) were predicted correctly to 41% when 88% of the non-anomalies were correctly predicted. When testing the trained

network with the full time series, the result was almost the same (40% and 88%, respectively). For the anomaly warnings, 33% of the cases were unseen and for the non-anomaly cases 66%.

Using the same set-up and training the network with only anomalies associated with the high-energy fluxes (fiI), these anomalies are predicted with the accuracy 94% (both for warnings and non-anomalies). When testing the full data set this trained network is almost as good as from the network trained with all anomalies (if the non-anomalies are predicted with 94% accuracy the anomaly warnings are predicted with 26%).

	Traning file	**All**		**fiI**		**fiII**	
	Test file	**test**	**me**	**test**	**me**	**test**	**me**
	File comb.						
1	pa3 _all	41	40	94	26	25	32
	level.96 net9+1 PE6+2	88	88	94	94	88	91
2	pa7 _all	47	50	92	32	36	42
	level.95 net18+1 PE9+3	79	79	92	88	88	80
3	pa7 _low	46		88		27	
	level.96 net18+1 PE9+3	81		87		82	
4	pa7 _high	48		89		43	
	level.93 net18+1 PE9+3	79		91		83	
5	wa64 _all	40	39	71	34	30	33
	level.96 net15+1 PE8+2	77	79	82	83	82	83
6	pa7 wa128 _all	52	38	92	32	37	39
	level.95 net33+1 PE10+6	76	87	91	89	79	80
7	pa2 wa32	53	54	93	36	39	42
	level.95 net24+1 PE8+4	76	76	91	88	76	80
8	pa6 wa64 _all	51	40	90	40	43	42
	level.95 net33+1 PE10+4	78	88	91	84	77	77

Table 5.5. Some of the results from different neural networks. Three different training files were used for each file combination. Two different test files were used, the test file with the unseen data and the full time series of Meteosat-3 with all anomalies.

The last example in row 1 is a network trained with anomalies not directly correlated with high electron fluxes (fiII). This network is not as successful, and mainly the anomalies associated with high fluxes are predicted. When comparing the output from these networks as function of time for the full time series (with all anomalies), the network trained with fiI is easiest to analyse. The output from fiII is hardest to use, the difference between the lowest and the highest output value is small. This leads to results that are very sensitive to the selection of threshold. A small change in the threshold gives a completely different result in the forecast.

Different combinations of values from Table 5.4 have been tested, one of them is row 2 in Table 5.5. Independently of the selection, the result is more or less the same.

Dynamics

The influence of the dynamics of the electron fluxes is tested separately in row 5. All three window lengths are tested (wa32, wa64 and wa128) with the same result. The forecast success is lower than in the previous case. When compared with row 1 and 2 the best result is for the network trained with fiII.

Combination

Combinations of values from Table 5.4 and the dynamics of the electron fluxes were also made, a few of them can be seen in rows 6-8. Independently of how the combinations were made the result was not improved compared to using only intensities. When the threshold was selected to predict 80% of the non-anomalies, the warnings were predicted with a success of 40–45%. Since the anomalies are more frequent at times with high electron fluxes the actual forecast rate of anomalies is 50–55%.

Energy interval

Information from all energy bins was used. In row 2–4 three different cases using full energy range, lower or upper range are presented. The results indicate that during events with high electron flux, all energy ranges are affected. There is no difference between the three energy ranges in the tests.

Anomaly types

The success of predicting the different types of anomalies was investigated, using one or a few of the same type. It was not possible to see if any of the anomaly types was easier to predict than the others (result not shown). The difference in some of the results can be attributed to bad statistics (too few cases).

Local times

The different local time sectors were also investigated. The warnings were indicated with the local time sector an anomaly occurred in. The predicted anomalies are predominant in the morning sector (2–10 LT) and the anomalies not predicted are evenly distributed.

5.2.7. Summary

The predicted anomalies are associated with high fluxes of electrons in the energy range 43–300 keV. Tests of different energy ranges, different types of anomalies, different combinations of data inputs and comparing different local times have been made. The anomalies on Meteosat-3 were predicted with a back propagation network. If the threshold was set to predict times without anomalies with a accuracy of 80% the warnings can

be given with 40–45% accuracy (this is 50–55% of the anomalies) using on-board electron measurements.

5.3. Spacecraft anomaly forecasting using non-local environment data

In this section we study the anomaly forecasting using non-local data. In addition to the Meteosat-3 data we use anomaly data from the Swedish satellite Tele-X.

5.3.1. Tele-X

Tele-X was a broadcasting satellite owned by Nordiska Satelliteaktiebolaget, NSAB. It was launched on 2 April 1989 into a geostationary orbit at 5°E. Anomalies were registered from the 2 April 1989 (launch) until the end of the mission in 1998. The satellite is a 3-axis stabilised platform with a solar array span of 19 m. The payload mass is 170 kg.

The environment conditions considered for the design of Tele-X were: ground handling tests, launcher environment, vibrations and electromagnetic radiation, space radiation, sun incidence angles and eclipses. The considered radiation elements were: electrons trapped in the van Allen belts, low energy protons, high energy protons from solar flares and cosmic rays.

The calculated radiation dose for different parts was estimated to a maximum value of $1x10^7$ rad for sensitive equipment. Externally mounted equipment could be exposed to $5x10^7$ rad.

Code	Description	Count
1	CMU1 reset	132
2	CMU2 reset	13
3	CMU1 and CMU2 both reset	8
4	Closure of LV31/41	16
5	Closure of LV32/42	3
6	Spontaneous heater boost	2
7	OBC1 stop	14
8	OBC2 stop	2
9	OBC1/ISE1 data transfer failure	1
10	OBC2/ISE2 data transfer failure	1

Table 5.6. Anomalies on Tele-X

During the period from 2 April 1989 to 26 October 1996 192 anomalies were reported (Table 5.6). Most anomalies occurred in the Command Manager Unit (CMU) causing the command counter to reset to zero (codes 1–3). Some anomalies were causing a latch valve to spontaneously close (code 4–5). Two anomalies caused a heater to spontaneously heat to higher temperatures than intended (code 6). The on-board computer (OBC) “hanged” (code 7, 8) during the satellite lifetime, and finally contact has been lost between the OBC and the Interface Safety Electronics (ISE) (code 9–10).

The days when anomalies occurred on Meteosat-3 and Tele-X are shown in Figure 5.4, for 724 anomalies on Meteosat-3 and 192 anomalies on Tele-X. From 21 June 1988 to 20 October 1996 there were 53 days with anomalies on both Meteosat-3

and Tele-X. While only considering the anomalies (on Meteosat-3) included in the training set, from 880621–961020, there were 33 days with anomalies on both Meteosat-3 and Tele-X. There were 26 days in total when anomalies did not occur on Tele-X but did occur on Meteosat-3. Here the anomalies on Meteosat-3 refer to the 613 anomalies used in the neural network study that focused on non-local data.

In addition, there were 81 data intervals of non-anomalies on Tele-X where anomalies on Meteosat-3 occurred during the last 4 days of the 10 days non-anomaly intervals for Tele-X. This means that 81 non-anomalies on Tele-X were associated with anomalies on Meteosat-3 with the time difference not longer than 4 days. Following the same procedure, but only comparing with the anomalies included in the training set, we obtain that the number of such non-anomalies on Tele-X is 69.

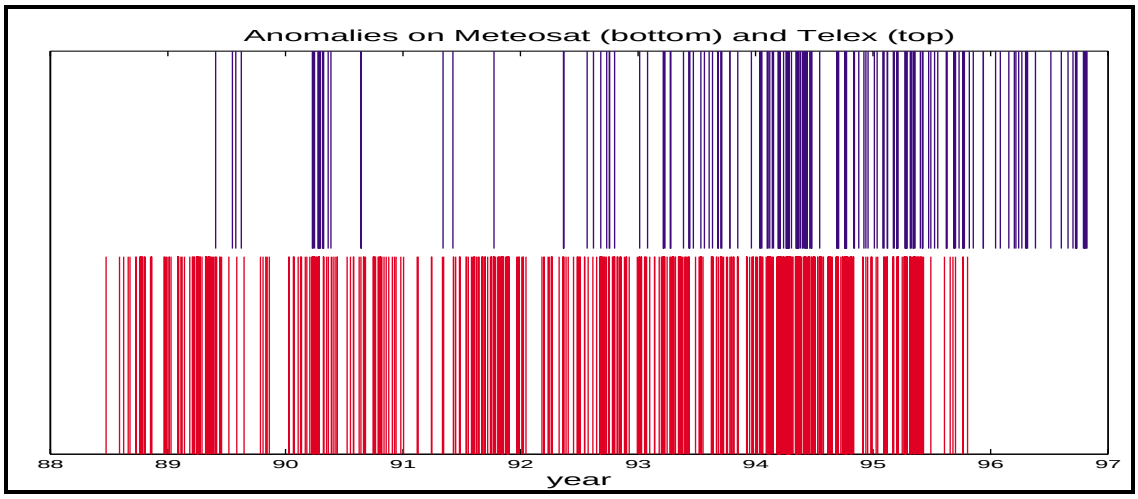

Figure 5.4. Occurrence of anomalies on Meteosat-3 and Telex-X during 880621-961020. The anomalies on Meteosat-3 are displayed on the lower panel and those on Tele-X are displayed on the upper panel.

5.3.2. Non-local environment data sets

5.3.2.1 Satellite environment data

The environment data used in this study are energetic electron flux (>2 MeV) data, from NOAA GOES space environment monitor CD-ROM. Data are from the measurements by GOES-6, GOES-7, and GOES-8. The original data are 5-minute averages. The selected data cover the period 1988–1996 because the anomaly data being investigated are from 1988–1995 on Meteosat-3 and from 1991–1996 on Tele-X. A data interval is defined to be qualified for the study if the data gaps inside the interval are less than 2 hours. After data interpolation, we averaged the data to hourly and daily resolution.

We obtain 613 data intervals qualified for the study of the 724 anomalies on Meteosat-3. Each interval is a period of 15 days and the 15th day is the day when an anomaly occurred on Meteosat-3. Likewise, we obtain 167 intervals qualified for the study of

the 192 anomalies on Tele-X. Each interval also covers the period of 15 days and the 15th day is the day when an anomaly occurred on Tele-X.

A non-anomaly interval is defined as follows: if there were no anomalies on Meteosat-3 only or Tele-X only within an interval of 10 days, then the interval is selected as a non-anomaly interval. Based on this criterion, 420 (368+52) non-anomaly intervals have been found for Meteosat-3 while 140 non-anomalies are found for Tele-X, each interval with a period of 10 days and the 10th day preceding a day with no anomaly.

5.3.2.2. Geomagnetic activity data

The geomagnetic indices Kp and Dst are also used as input parameters in this study. Kp is the mean standardized K-index from 13 geomagnetic observatories between 44° and 60° northern or southern geomagnetic latitude. Dst was originally devised to describe ring current variations during the International Geophysical Year (IGY). The present Dst index is calculated from hourly H component observations at 4 low-latitude observatories. Although Kp and Dst data are continuous with no gaps, in order to use them in combination with energetic electron flux data, only the same data intervals as those of electron flux will be used for the study.

5.3.3. Forecasting anomalies using neural networks

5.3.3.1. Training, validation, and test data

Input data are the daily averaged energetic electron flux and Dst as well as the daily sum of Kp. The data of Dst, Kp and the logarithm of electron flux are normalized to the interval [–1, 1].

Training is made on 70% of the events (including anomalies and non-anomalies) on Meteosat-3 only. Neural networks are validated on the remaining 30% of Meteosat-3 events and the tested on the Tele-X data. The validation set is used to determine where the training should be terminated. The minimal validating error means that the optimal generalisation capability of neural networks has been found and that the networks can be generalised by a test set.

The training set consists of 454 anomalies and 279 non-anomalies on Meteosat-3. The validation set consists of 159 anomalies and 131 non-anomalies on Meteosat-3. The test set consists of 167 anomalies and 140 non-anomalies on Tele-X.

5.3.3.2. Time-delay neural network and learning vector quantization network

A time-delay neural network (TDNN) is a supervised learning feed-forward back-propagation network with a time delay line in the input layer. Learning Vector Quantization (LVQ) is a classification network, which assigns vectors to one of several classes. An LVQ network contains a Kohonen layer which learns and performs the classification. The input layer contains one neuron for each input parameter, the output layer contains

one neuron for each class. LVQ network is a combination of supervised and un-supervised learning networks. The classes are predefined and we have a body of labelled sample data; each sample input vector is tagged with its correct class. This is the sense of being supervised. "Un-supervision" in LVQ comes from its way of weight updating.

5.3.3.3. Forecasts using time-delay neural network

Input Kp

With Kp as input, the forecast results are summarized in Table 5.7, and are shown in Figures 5.5 (a)–(f) in terms of different time delay lines in the input layer and different number of network hidden neurons.

The quantities in Table 5.7 are specified in the following way: τ is the length of a time delay line. S is the number of hidden neurons. R_{te} is the total rate of forecast for anomalies and non-anomalies on Meteosat-3. R_{te1} is the rate of forecast for anomalies on Meteosat-3. R_{te2} is the rate of forecast for non-anomalies on Meteosat-3. R_{tlx} is the rate of forecast for anomalies and non-anomalies on Tele-X. R_{tlx1} is the rate of forecast for anomalies on Tele-X. R_{tlx2} is the rate of forecast for non-anomalies on Tele-X. R_{tr} is the training rate of forecast for anomalies and non-anomalies on Meteosat-3. R_{tr1} is the training rate of forecast for anomalies on Meteosat-3. R_{tr2} is the training rate of forecast for non-anomalies on Meteosat-3. These quantities are also applied in the following tables.

Take one of the best results for 8 days time window as an example. For anomalies on Meteosat-3, Kp can predict 78% correctly while for non-anomalies Kp can predict 80% correctly. The total forecast rate is 79%. For events on Tele-X, Kp gives the total forecast rate 64% where 78% is for anomalies and 46% for non-anomalies.

The low forecast rate for non-anomalies on Tele-X is mainly due to the definition of non-anomalies based only on one satellite. Several non-anomalies on Tele-X were selected during the data intervals where anomalies did occur on Meteosat-3. Most of these data intervals have been used to train the networks. If the networks learn most information encoded in the training set, the networks will give forecast of anomalies in response to these data intervals as the input. Therefore, the low forecast rate on non-anomalies on Tele-X is expected and is due to the definition of non-anomalies.

As the time delay line varies from 4 to 10 days and the number of network hidden neurons varies from 4 to 20, the total forecast rate varies between 71% and 79% for events on Meteosat-3 and between 62% and 68% for Tele-X. An 8-day time delay line gives slightly better accuracy than the others using Kp as the input parameter.

In summary, the forecast rate varies 71–80% for anomalies and 65–80% for non-anomalies on Meteosat-3. For Tele-X, the forecast rate varies 77–84% for anomalies and 40–51% for non-anomalies.

$\tau(days)$	S	R_{te}	R_{te1}	R_{te2}	R_{tlx}	R_{tlx1}	R_{tlx2}	R_{tr}	R_{tr1}	R_{tr2}
4	4	0.723	0.786	0.652	0.664	0.826	0.471	0.750	0.815	0.645
4	8	0.730	0.767	0.688	0.681	0.844	0.486	0.735	0.811	0.613
4	12	0.723	0.780	0.660	0.671	0.832	0.479	0.742	0.815	0.624
4	16	0.743	0.761	0.723	0.681	0.820	0.514	0.731	0.795	0.627
4	20	0.740	0.799	0.674	0.658	0.826	0.457	0.744	0.826	0.609
6	4	0.710	0.748	0.667	0.638	0.814	0.429	0.756	0.815	0.659
6	8	0.713	0.761	0.660	0.645	0.844	0.407	0.759	0.828	0.645
6	12	0.733	0.748	0.716	0.664	0.808	0.493	0.759	0.795	0.699
6	16	0.720	0.774	0.660	0.638	0.814	0.429	0.748	0.819	0.631
6	20	0.700	0.742	0.652	0.632	0.826	0.400	0.763	0.837	0.642
8	4	0.750	0.774	0.723	0.648	0.784	0.486	0.754	0.811	0.663
8	8	0.790	0.780	0.801	0.635	0.784	0.457	0.753	0.813	0.656
8	12	0.763	0.767	0.759	0.638	0.778	0.471	0.769	0.822	0.685
8	16	0.773	0.792	0.752	0.642	0.796	0.457	0.765	0.833	0.656
8	20	0.757	0.774	0.738	0.622	0.802	0.407	0.763	0.841	0.634
10	4	0.733	0.686	0.787	0.606	0.743	0.443	0.783	0.852	0.670
10	8	0.743	0.711	0.780	0.638	0.772	0.479	0.768	0.830	0.667
10	12	0.750	0.717	0.787	0.625	0.772	0.450	0.769	0.837	0.659
10	16	0.747	0.736	0.759	0.635	0.814	0.421	0.767	0.852	0.627
10	20	0.767	0.748	0.787	0.619	0.766	0.443	0.771	0.833	0.670

Table 5.7. One day ahead forecast of spacecraft anomalies from Kp (TDNN)

(a)

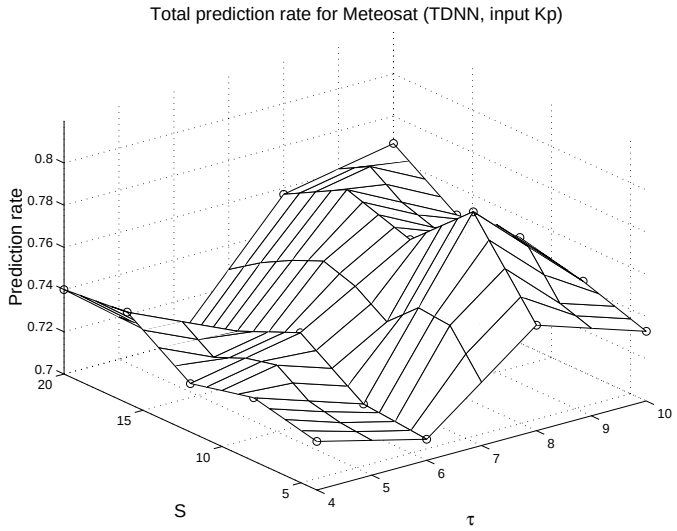
Total prediction rate for Meteosat (TDNN, input Kp)
Prediction rate
0.8
0.78
0.76
0.74
0.72
0.7
20
15
10
5
S
4
5
6
7
8
9
10
τ

(b)

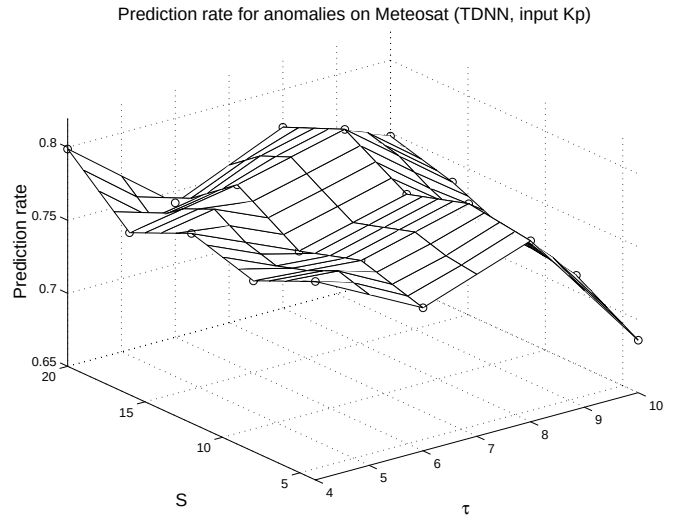
Prediction rate for anomalies on Meteosat (TDNN, input Kp)
Prediction rate
0.8
0.75
0.7
0.65
20
15
10
5
S
4
5
6
7
8
9
10
τ

(c)

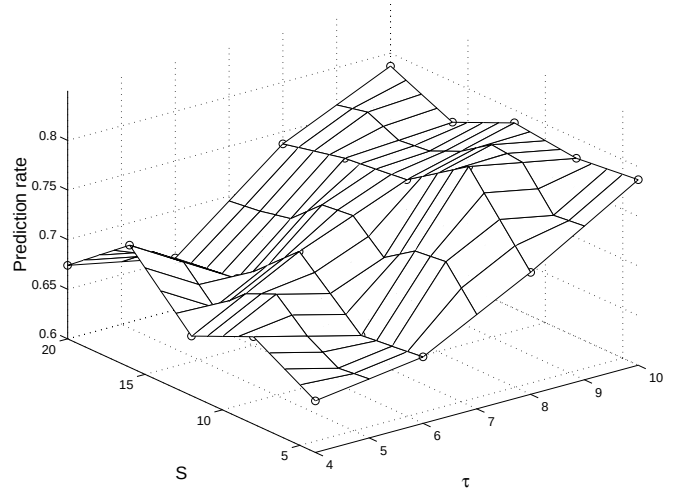
Prediction rate for non-anomalies on Meteosat (TDNN, input Kp)
Prediction rate
0.8
0.75
0.7
0.65
0.6
20
15
10
5
S
4
5
6
7
8
9
10
τ

(d)

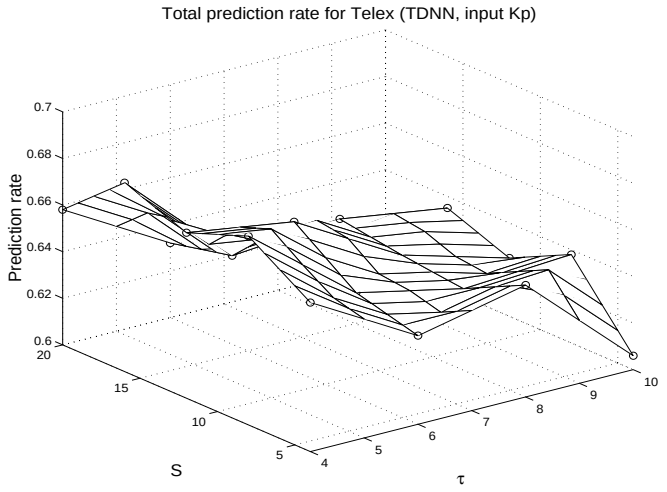

(e)

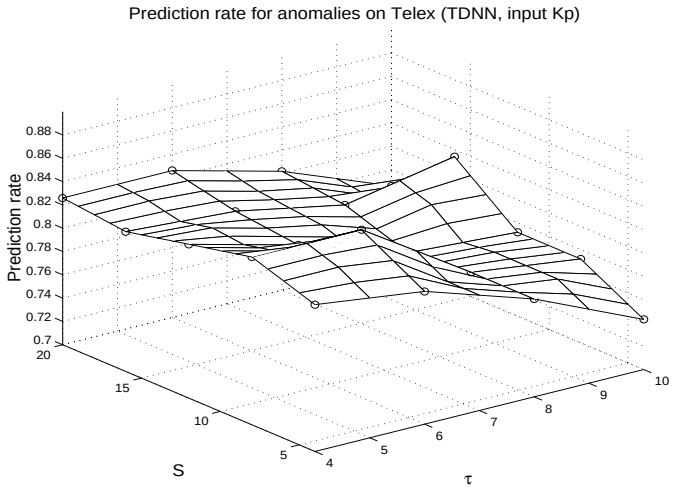

(f)

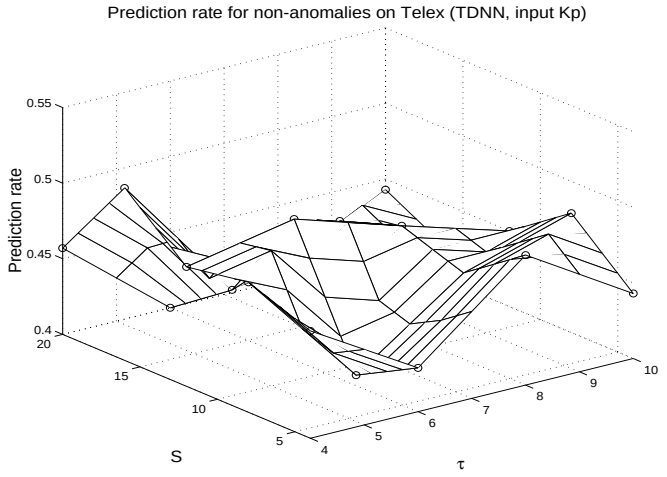

Figure 5.5. Accuracy of 1 day ahead forecast from the input Kp using TDNN in terms of the network architecture (i.e., the time delay line and the number of hidden neurons). (a-c) Total forecast rate, forecast rate for anomalies,and non-anomalies on Meteosat-3, respectively; (d-f) The same for Tele-X

Input Dst

The forecast results are given in Table 5.8 and Figures 5.6 (a)-(f) using Dst as the input parameter. When the delay line length is 8 days, the total forecast rate is 73% for events on Meteosat-3, the forecast rate is 77% for anomalies and 67% for non-anomalies on Meteosat-3. The total forecast rate is 65% for events on Tele-X, the forecast rate is 81% for anomalies and 44% for non-anomalies on Tele-X. A 10- or 8-day delay line results in similar forecast accuracy.

The total forecast accuracy is rather stable in terms of time delay line and number of hidden neurons with Dst as input. The total forecast rate varies 69–73% for events on Meteosat-3 while the total forecast rate varies between 62–66%.

The forecast rate varies 70–80% for anomalies and 56–72% for non-anomalies on Meteosat-3. For Tele-X, the forecast rate varies 77–84% for anomalies and 41–46% for non-anomalies.

Input electron flux (E > 2 Mev)

For the electron flux as the input parameter we summarize the forecast results in Table 5.9 and Figures 5.7 (a)-(f) in terms of the time delay line and the number of the network hidden neurons.

As can be seen from Table 5.9, the total forecast rate varies between 52% and 62% for the events (included in the validation set) on Meteosat-3, the forecast rate is in the range 57–86 % for anomalies on Meteosat-3 and in the range 33–53 % for non-anomalies on Meteosat-3. For Tele-X, the total forecast rate ranges from 61% to 67%, the forecast rate ranges from 74% to 93% for anomalies and from 32% to 49% for non-anomalies.

The energetic electron flux tends to predict anomalies much more accuartely than to predict non-anomalies. It might well imply that if energetic electron flux is high, then anomalies will probably occur and that if energetic electron flux is low, it is still possible to have an anomalies which is caused by some other factors, e.g. low energy electron flux. When we look at training error, it can be found that training accuracy (above 80%) for anomalies is much higher than that (37% to 62%) for non-anomalies. We can see from the training that the energetic electron flux is not able to well predict non-anomalies.

In contrast, when the input is Kp and Dst, respectively, during training the training accuracy ranges between 61% and 70% for the input Kp and ranges between 64% and 72% for the input Dst.

$\tau(days)$	S	R_{te}	R_{te1}	R_{te2}	R_{tlx}	R_{tlx1}	R_{tlx2}	R_{tr}	R_{tr1}	R_{tr2}
4	4	0.687	0.799	0.560	0.651	0.844	0.421	0.759	0.826	0.649
4	8	0.693	0.792	0.582	0.651	0.844	0.421	0.757	0.826	0.645
4	12	0.700	0.774	0.617	0.661	0.832	0.457	0.749	0.804	0.659
4	16	0.693	0.792	0.582	0.661	0.844	0.443	0.754	0.819	0.649
4	20	0.690	0.786	0.582	0.651	0.844	0.421	0.761	0.828	0.652
6	4	0.707	0.748	0.660	0.635	0.814	0.421	0.769	0.833	0.667
6	8	0.707	0.748	0.660	0.622	0.802	0.407	0.761	0.830	0.649
6	12	0.707	0.748	0.660	0.625	0.802	0.414	0.764	0.833	0.652
6	16	0.713	0.704	0.723	0.625	0.772	0.450	0.760	0.782	0.724
6	20	0.700	0.730	0.667	0.622	0.790	0.421	0.756	0.815	0.659
8	4	0.720	0.786	0.645	0.651	0.826	0.443	0.772	0.835	0.670
8	8	0.710	0.723	0.695	0.635	0.796	0.443	0.759	0.811	0.674
8	12	0.723	0.780	0.660	0.648	0.832	0.429	0.765	0.828	0.663
8	16	0.727	0.774	0.674	0.645	0.814	0.443	0.768	0.824	0.677
8	20	0.713	0.748	0.674	0.642	0.820	0.429	0.763	0.826	0.659
10	4	0.733	0.748	0.716	0.642	0.808	0.443	0.772	0.828	0.681
10	8	0.730	0.774	0.681	0.658	0.832	0.450	0.778	0.844	0.670
10	12	0.727	0.742	0.709	0.645	0.820	0.436	0.779	0.839	0.681
10	16	0.730	0.761	0.695	0.648	0.826	0.436	0.775	0.844	0.663
10	20	0.720	0.767	0.667	0.655	0.832	0.443	0.778	0.844	0.670

Table 5.8. One day ahead forecast of spacecraft anomalies from Dst (TDNN)

(a)

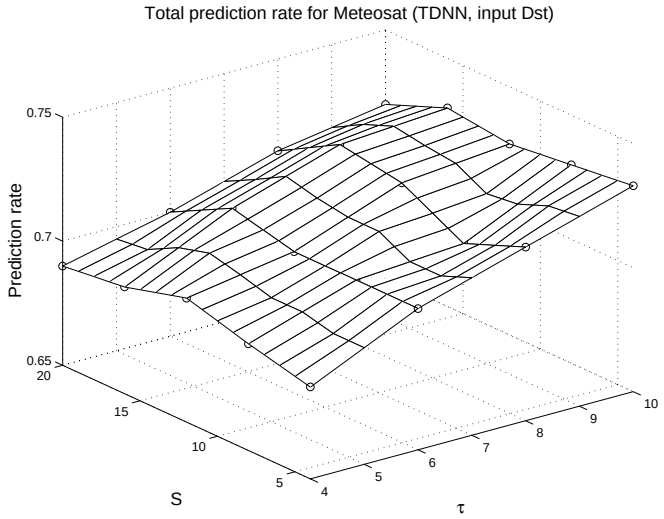
Total prediction rate for Meteosat (TDNN, input Dst)
Prediction rate
0.75
0.7
0.65
20
15
10
5
S
4
5
6
7
8
9
10
τ

(b)

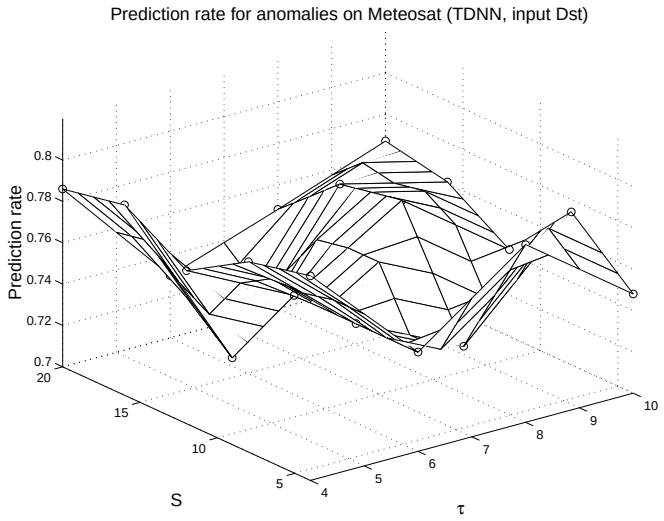
Prediction rate for anomalies on Meteosat (TDNN, input Dst)
Prediction rate
0.8
0.78
0.76
0.74
0.72
0.7
20
15
10
5
S
4
5
6
7
8
9
10
τ

(c)

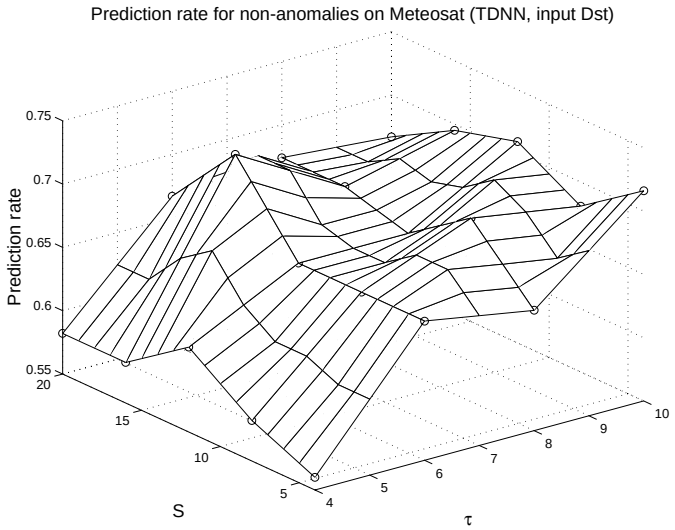
Prediction rate for non-anomalies on Meteosat (TDNN, input Dst)
Prediction rate
0.75
0.7
0.65
0.6
0.55
20
15
10
5
S
4
5
6
7
8
9
10
τ

(d)

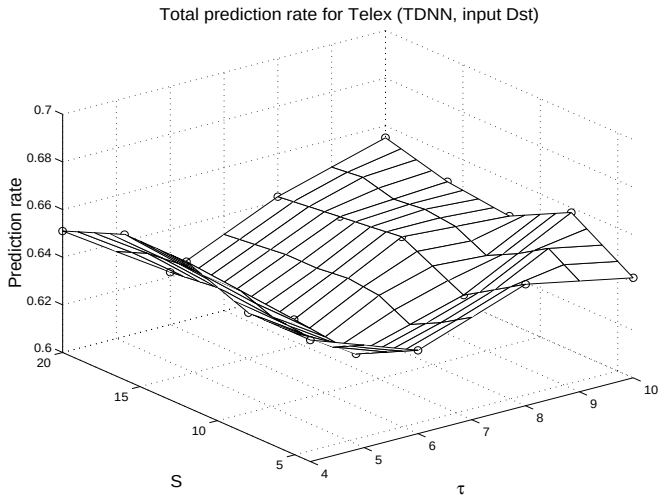

(e)

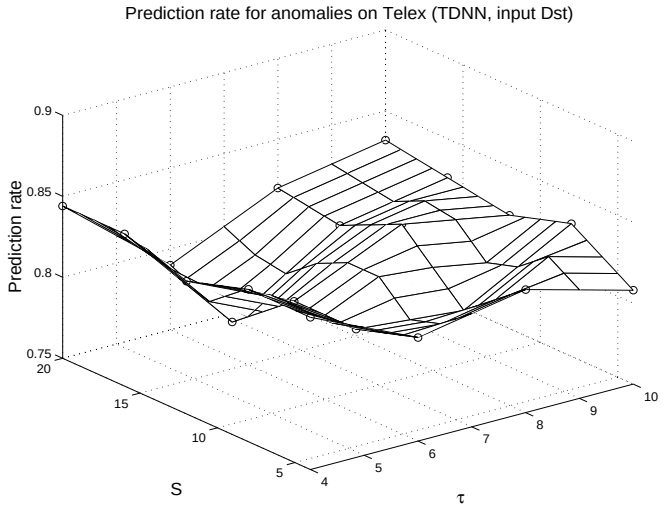

(f)

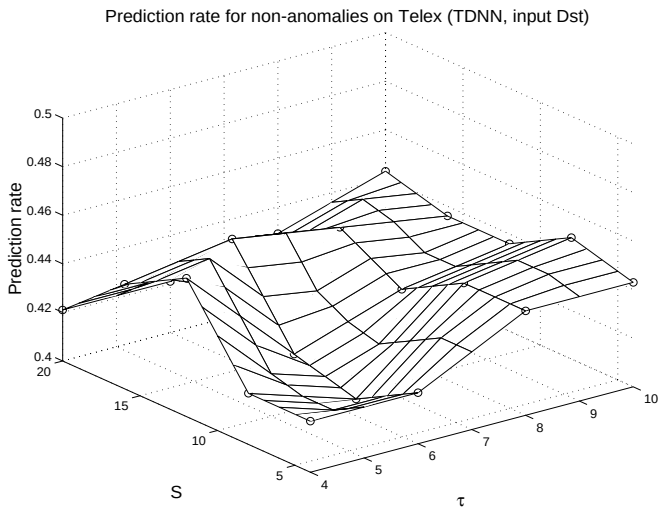

Figure 5.6. Same as Figure 5.5 but using Dst as input.

$\tau(days)$	S	R_{te}	R_{te1}	R_{te2}	R_{tlx}	R_{tlx1}	R_{tlx2}	R_{tr}	R_{tr1}	R_{tr2}
4	4	0.587	0.761	0.390	0.648	0.868	0.386	0.675	0.813	0.452
4	8	0.620	0.862	0.348	0.674	0.934	0.364	0.673	0.861	0.366
4	12	0.613	0.836	0.362	0.648	0.886	0.364	0.681	0.850	0.405
4	16	0.593	0.811	0.348	0.648	0.892	0.357	0.674	0.848	0.391
4	20	0.593	0.704	0.468	0.642	0.772	0.486	0.643	0.696	0.556
6	4	0.577	0.736	0.397	0.642	0.868	0.371	0.692	0.830	0.466
6	8	0.587	0.761	0.390	0.622	0.862	0.336	0.679	0.824	0.444
6	12	0.580	0.792	0.340	0.625	0.880	0.321	0.670	0.835	0.401
6	16	0.540	0.623	0.447	0.642	0.826	0.421	0.675	0.760	0.538
6	20	0.540	0.723	0.333	0.651	0.880	0.379	0.682	0.835	0.434
8	4	0.583	0.780	0.362	0.651	0.862	0.400	0.690	0.848	0.434
8	8	0.547	0.635	0.447	0.635	0.796	0.443	0.696	0.778	0.563
8	12	0.573	0.723	0.404	0.629	0.832	0.386	0.696	0.837	0.466
8	16	0.563	0.673	0.440	0.635	0.826	0.407	0.707	0.835	0.498
8	20	0.573	0.717	0.411	0.619	0.826	0.371	0.709	0.846	0.487
10	4	0.560	0.667	0.440	0.651	0.820	0.450	0.704	0.815	0.523
10	8	0.563	0.679	0.433	0.629	0.832	0.386	0.697	0.846	0.455
10	12	0.553	0.610	0.489	0.629	0.820	0.400	0.737	0.833	0.581
10	16	0.520	0.629	0.397	0.609	0.802	0.379	0.722	0.837	0.534
10	20	0.550	0.572	0.525	0.609	0.743	0.450	0.744	0.822	0.616

Table 5.9. One day ahead forecast of spacecraft anomalies from electron flux (TDNN)

(a)

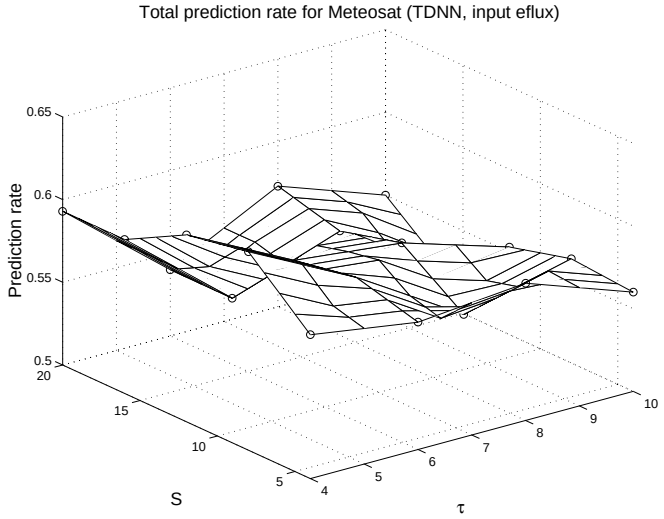
Total prediction rate for Meteosat (TDNN, input eflux)
Prediction rate
0.65
0.6
0.55
0.5
20
15
10
5
S
4
5
6
7
8
9
10
τ

(b)

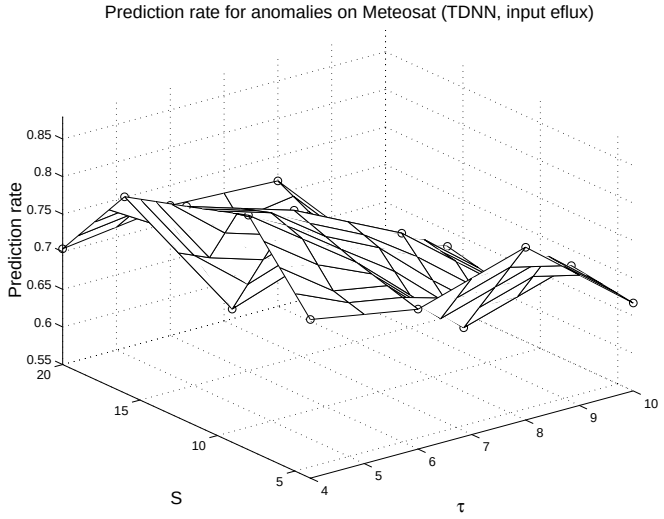
Prediction rate for anomalies on Meteosat (TDNN, input eflux)
Prediction rate
0.85
0.8
0.75
0.7
0.65
0.6
0.55
20
15
10
5
S
4
5
6
7
8
9
10
τ

(c)

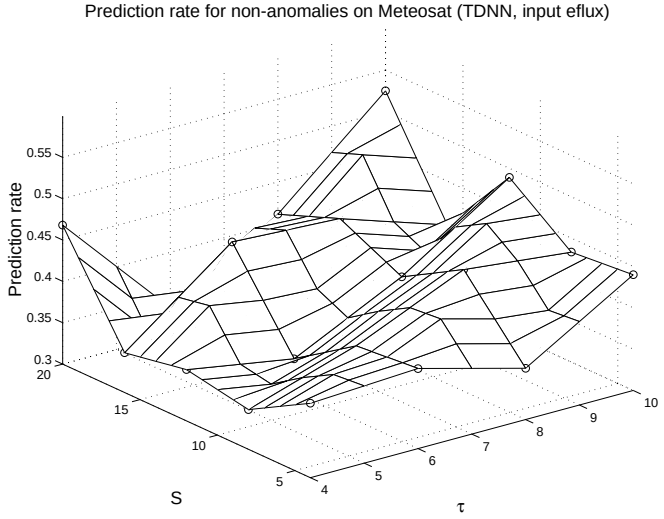
Prediction rate for non-anomalies on Meteosat (TDNN, input eflux)
Prediction rate
0.55
0.5
0.45
0.4
0.35
0.3
20
15
10
5
S
4
5
6
7
8
9
10
τ

(d)

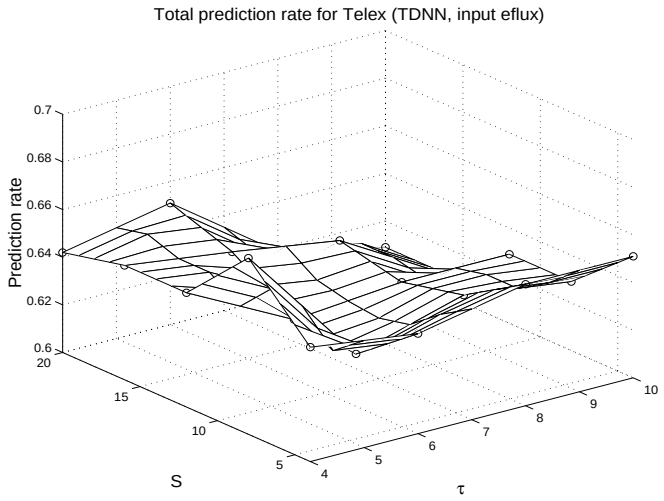

(e)

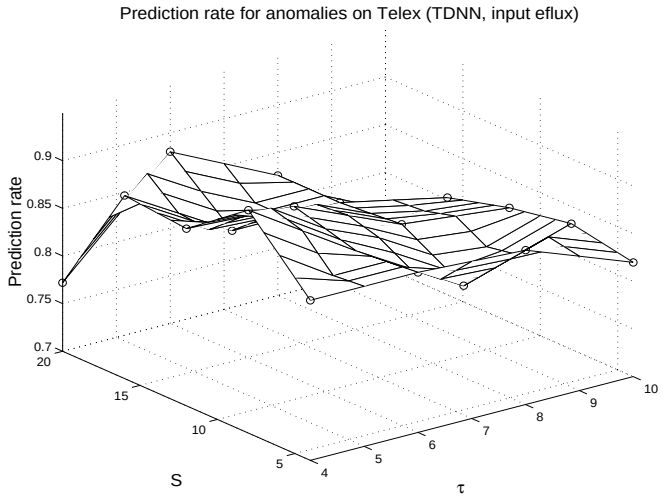

(f)

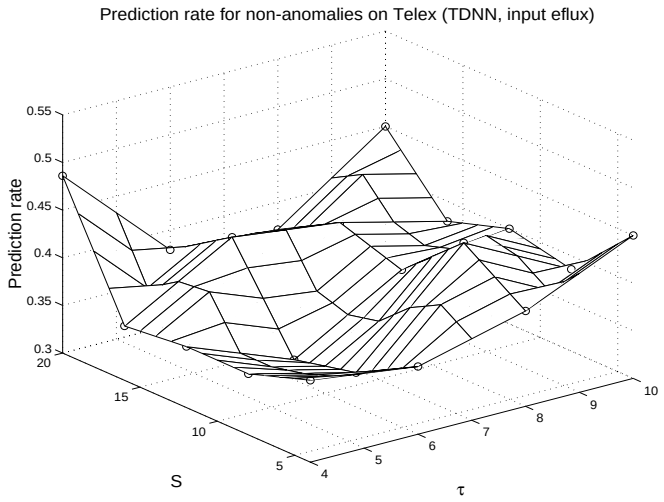

Figure 5.7. Same as Figure 5.5 but using energetic electron flux (E > 2 Mev) as input.

5.3.3.4. Forecasts using learning vector quantization network

We have used two network classes (TDNN and LVQN) and found that they give similar forecast accuracy. Therefore, we mainly focus on TDNN. In order for a comparison, we present the results as the input is Kp and energetic electron flux.

Input Kp

The forecast results are given in Table 5.10. Comparing Table 5.8 and Table 5.10 we see that the two network classes give similar accuracy.

$\tau(days)$	S	R_{te}	R_{te1}	R_{te2}	R_{tlx}	R_{tlx1}	R_{tlx2}	R_{tr}	R_{tr1}	R_{tr2}
4	6	0.730	0.805	0.645	0.671	0.814	0.500	0.722	0.782	0.624
4	10	0.717	0.723	0.709	0.658	0.707	0.600	0.697	0.716	0.667
4	14	0.733	0.742	0.723	0.664	0.766	0.543	0.726	0.749	0.688
4	18	0.740	0.736	0.745	0.687	0.772	0.586	0.727	0.736	0.713
6	6	0.710	0.723	0.695	0.655	0.778	0.507	0.689	0.729	0.624
6	10	0.727	0.723	0.730	0.648	0.725	0.557	0.724	0.742	0.695
6	14	0.743	0.736	0.752	0.674	0.784	0.543	0.718	0.744	0.674
6	18	0.740	0.730	0.752	0.661	0.784	0.514	0.738	0.771	0.685
8	6	0.767	0.755	0.780	0.638	0.796	0.450	0.746	0.793	0.670
8	10	0.790	0.761	0.823	0.635	0.778	0.464	0.739	0.791	0.656
8	14	0.807	0.792	0.823	0.645	0.820	0.436	0.759	0.813	0.670
8	18	0.797	0.748	0.851	0.671	0.772	0.550	0.741	0.775	0.685
10	6	0.777	0.736	0.823	0.612	0.766	0.429	0.718	0.780	0.616
10	10	0.763	0.667	0.872	0.645	0.743	0.529	0.741	0.769	0.695
10	14	0.777	0.698	0.865	0.642	0.731	0.536	0.737	0.758	0.703
10	18	0.813	0.742	0.894	0.655	0.737	0.557	0.763	0.797	0.706

Table 5.10. One day ahead forecast of spacecraft anomalies from Kp (LVQNN)

Input electron flux (E > 2 Mev)

With electron flux as the input, the results are given in Table 5.11. The accuracy is slightly lower than that using TDNN.

5.3.4. Discussion

With Kp as the input parameter, the accuracy is as high as 80% at the best. With Dst as the input parameter, the accuracy is slightly lower than that in the case of Kp as input. This 3-hour planetary index Kp was introduced by Bartels (1949) and is designed to measure solar particle radiation by its magnetic effects. Kp is derived from the standard-

ized K-index from 13 geomagnetic observatories between 44 degrees and 60 degrees northern or southern geomagnetic latitude. Dst was originally devised by Sugiura (1964) to describe ring current variations during the International Geophysical Year (IGY). The present Dst index is calculated hourly from the H component recorded at 4 low-latitude magnetic observatories. All of these observatories are about equally spaced in longitude (i.e. evenly distributed in local time) and at low latitudes, 20°-30° away from the dipole equator where both auroral- and equatorial-electrojet effects are minimal. Therefore, Kp is a more global indicator of geomagnetic activity than Dst. The forecast accuracy obtained with Kp or Dst as the input parameter is reasonable in comparison. The reason that Kp is the best candidate for predicting anomalies and non-anomalies of satellites is not only the accuracy but also its availability in real-time. The estimated Kp is available in real-time (http://www.sel.noaa.gov/planetary_k.html).

τ(days)	S	R_{ie}	R_{ie1}	R_{ie2}	R_{ii}	R_{iie}	R_{iie2}	R_{ii}	R_{ii1}	R_{ii2}
6	6	0.5[illegible]3	0.651	0.[illegible]18	0.615	0.760	0.507	0.611	0.696	0.[illegible]80
6	10	0.513	0.604	0.[illegible]11	0.[illegible]34	0.[illegible]78	0.6[illegible]4	0.628	0.69[illegible]	0.[illegible]34
6	14	0.537	0.629	0.[illegible]73	0.678	0.772	0.561	0.628	0.705	0.502
6	18	0.52[illegible]	0.[illegible]72	0.[illegible]3	0.[illegible]11	0.760	0.[illegible]64	0.6[illegible]6	0.731	0.[illegible]34
8	6	0.583	0.792	0.348	0.618	0.832	0.[illegible]29	0.622	0.7[illegible]7	0.[illegible]19
8	10	0.537	0.597	0.[illegible]18	0.657	0.751	0.607	0.608	0.680	0.573
8	14	0.527	0.623	0.[illegible]18	0.67[illegible]	0.781	0.513	0.632	0.707	0.509
8	18	0.550	0.[illegible]72	0.525	0.651	0.760	0.586	0.640	0.676	0.581

Table 5.11. One day ahead forecast of spacecraft anomalies from eflux (LVQNN)

Dst is not available in real-time. But we can accurately predict Dst 1-2 hours ahead with the real-time solar wind input from WIND or ACE satellite (Wu, 1997; Wu et al., 1998). Hence we can have real-time forecast of Dst which can be used for the study of satellite anomalies.

With the energetic electron flux as the input, the forecast accuracy is relatively lower, mainly due to the lower accuracy of non-anomalies. We argue that the reasons are twofold. One is the energetic electron flux (E > 2 Mev) is not the only factor causing anomalies on satellites, for example if the anomalies is caused by surface charging. The lower energy electron flux could be an important factor causing anomalies due to, e.g., surface charging. In other words, if energetic electron flux was high, there would be

anomalies occurring on satellites. However, if energetic electron flux was low, the possibility for an anomaly to occur still exists (due to low energy electron flux).

To completely describe how satellite anomalies are caused by electron flux, we will need electron flux data with energy from low (the order of keV) to high (the order of MeV). This will be able to give a better forecast accuracy.

The definition of non-anomalies is based only on one satellite. If we train the neural networks on one satellite and test on the same satellite, the accuracy will not be affected much since the distribution of local conditions on the satellite in the training set and in the test set will not be much different. But if we train on events on one satellite and test on events on the other. The error will originate from the different local conditions and local environments on different satellites. Since this study is focused on using nonlocal space environment data, it has been presumed that the local conditions and local environments are the same on different satellites, although this is not a good approximation in reality.

To reduce the error caused by different local conditions and local environments, we have to have a definition of non-anomalies as strict as possible by taking into account as many satellites as possible. It means that the definition of non-anomalies is satellite-independent. This will give a better forecast accuracy for non-anomalies and for anomalies as well. However, another problem will be raised. That is, we do not know how accurately our neural network models can generalise from one satellite to another. Therefore, while combining nonlocal data with local data as input, this problem might be solved to a large extent.

The training was on Meteosat with the threshold of 0.5. For the results given in Tables 5.7-5.9, the threshold for an output (of TDNN) to be an anomaly or a non-anomaly is 0.5. The specific criterion is that, if the value of the TDNN output is in the range (0.5 1.5), then the output gives an anomaly forecast and if the value of the TDNN output is in the range (-0.5 0.5) then the output gives a non-anomaly forecast. The local conditions of Tele-X are different from Meteosat. We can expect when how neural network models will not generalise well from one satellite to another since the definition of non-anomalies is satellite-dependent. To have a better generalisation from one satellite (Meteosat) to another (Tele-X), we try to find a new threshold value for a network output to determine if the output is an anomaly or a non-anomaly for Tele-X. We investigate whether or not the threshold value is satellite-dependent. In other words, we examine if such a threshold value exists that forecast accuracy for anomalies and for non-anomalies is very close to each other as the case for Meteosat with the threshold of 0.5. Nonetheless, it should be noted that the total forecast rate will be unchanged.

For forecasts on Tele-X, as we can see from Tables 5.7–5.9, the forecast accuracy for non-anomalies is much lower than for anomalies. Therefore we vary the value of threshold for 2 neural network models (for input Kp and 8-day time window) respectively with 8 and 16 hidden neurons. We obtain the forecast results for Tele-X in Table 5.12 and Figure 5.8. As seen from Figure 5.8, we have found a new threshold value which can give better accuracy of non-anomalies at the expense of accuracy for anomalies. This threshold value is 0.63, giving forecast rate of about 65 percent for both

anomalies and non-anomalies. The two different models give almost the same value of threshold. Anomaly or non-anomaly forecast accuracy varies with the threshold value in the same way for the two network models. In order to confirm the threshold of 0.63 is valid in all cases, we need to do some more investigations. However, at least it indicates that the difference of local conditions of different satellites might be described by the value of the threshold.

$\tau(days)$	S	Threshold	R_{tlx}	R_{tlx1}	R_{tlx2}
8	8	0.40	0.635	0.898	0.300
8	8	0.50	0.635	0.784	0.457
8	8	0.55	0.635	0.743	0.529
8	8	0.60	0.635	0.701	0.586
8	8	0.65	0.635	0.653	0.707
8	8	0.70	0.635	0.599	0.771
8	16	0.40	0.642	0.880	0.307
8	16	0.50	0.642	0.796	0.457
8	16	0.55	0.642	0.760	0.529
8	16	0.60	0.642	0.701	0.600
8	16	0.65	0.642	0.635	0.700
8	16	0.70	0.642	0.581	0.764

Table 5.12. One day ahead forecast accuracy on Tele-X from Kp (TDNN) vs threshold value.

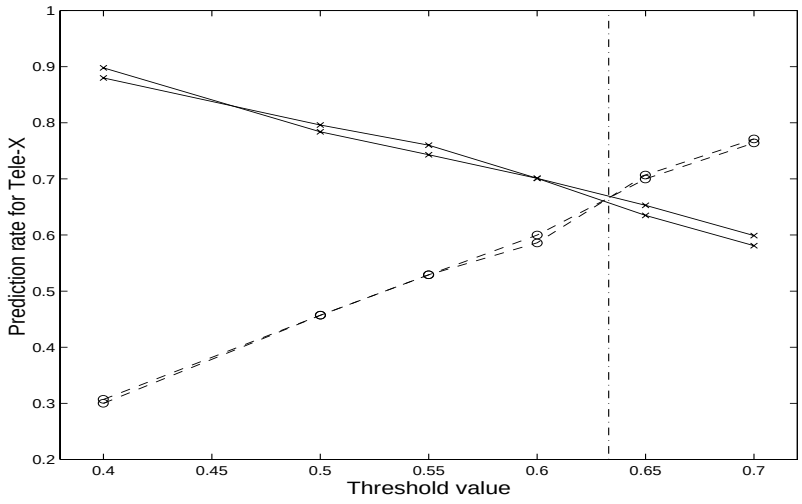

Figure 5.8. The forecast accuracy for Tele-X versus the threshold value. The solid line represents the forecast for anomalies on Tele-X and the dashed line represents the forecast for non-anomalies on Tele-X.

5.4.Spacecraft anomaly forecasting using heterogeneous environment data

In the previous sections anomaly forecasting using local and non-local data were analyzed separately. In both studies the environmental data were used to predict anomalies on GEO spacecraft.

5.4.1. Heterogeneous data

The data files for predicting spacecraft anomalies in Section 5.2.6. were expanded to be used with a heterogeneous data set. The Kp- and Dst-indices were included with 2-hour resolution (the Kp index is normally given as a three-hour index) to comply with the rest of the data set. The anomalies from both the Tele-X satellite and Meteosat-3 were used.

5.4.2 Test of different combinations

Table 5.13 shows the result of some of the trained networks. The first column shows the number of the row, the second how the data set is combined and the last four columns indicate on which data set the back propagation net has been trained; Meteosat-3, Tele-X, the fiI (described in Section 5.2.6.) and fiII. For each trained net 2/3 of the anomalies are used to train the net and 1/3 to test the net. The result for each tested net is shown in the column marked test. Since the non-anomalies are much more common, each net is tested with the full time sequence of Meteosat-3 (me) and Tele-X data (te). Note the order between me and te is reversed for the network trained with Tele-X anomalies in the Table. The results for the different tests are presented as the success (in percentages) of predicting the anomalies (top) and the non-anomalies (bottom) in each box. Since the output of a back propagation net is a real number the threshold for each individual test is chosen so that the non-anomaly success rate is close to or higher than 80%. Only the thresholds of 0.3, 0.4 , 0.5 and 0.6 were used.

Electron fluxes

In rows 1 and 2 the data are selected in a similar way as in Section 5.2.6. The result for the network trained with all Meteosat-3 anomalies, only the anomalies associated with high fluxes (fiI) and the anomalies not in fiI (fiII) is the same as in Section 5.2.6. The network is also trained to predict Tele-X anomalies. The success rate for the Tele-X anomalies is higher than for Meteosat-3. If the non-anomalies are to be 87% correctly predicted, the Tele-X anomalies are predicted to 60%.

When the full time series of Meteosat-3 is used as a test file on the network trained with Tele-X anomalies, the result is almost equally good as if the full time series of Meteosat-3 is tested on a network trained with Meteosat-3 (row 1 high lighted). This was also true the other way around using the full time series of Tele-X (not shown).

	Training file	**Meteosat**		**Tele-X**			**fiI Meteosat-3**			**fiII Meteosat-3**		
	Test file	**test**	**me**	**test**	**te**	**me**	**test**	**me**	**te**	**test**	**me**	**te**
	File comb.											
1	pa3 _all	41	**40**	60	54	**39**	94	26	38	50	59	72
	level.96 net12+1 PE6+2	88	**88**	87	86	**89**	94	94	92	72	73	70
2	wa64 _all	40	39	44	43	37	71	34	37	30	33	33
	level.96 net15+1 PE8+2	77	79	77	77	79	82	83	81	82	83	80
3	Kp 10x12 (_all)	43	42	50	49	49	85	23	30	31	33	34
	level.96 net10+1 PE5+2	89	88	89	88	82	94	96	94	87	88	85
4	Dst 10x12 (_all)	53	35	62	61	48	88	24	30	14	15	16
	level.96 net10+1 PE5+2	77	89	78	78	81	94	95	92	94	94	93
5	pa3 dst 3x24 _all	54	41	68	51	34	96	22	31	38	41	48
	level.96 net12+1 PE6+2	80	89	82	89	91	95	96	94	82	84	80
6	pa3 kp 3x24 _all	55	53	67	53	36	92	24	34	47	49	55
	level.96 net12+1 PE6+2	81	81	79	88	91	96	96	94	75	76	73
7	pa3 wa64 kp+dst 10x12 _all	**47**	49	**64**	67	40	92	21	28	38	40	44
	level.96 net44+1 PE20+10	**87**	87	**86**	85	87	98	96	94	85	86	82
8	pa3 month(1/2 year) _all	47	47	60	71	52	88	41	59	37	36	38
	level.95 net10+1 PE5+2	80	79	88	76	80	94	82	83	79	81	80
9	pa3 year _all	47	41	63	75	51	86	42	55	45	49	45
	level.95 net10+1 PE5+2	80	81	87	78	82	93	84	85	76	79	87
10	pa3 hour _all	50	51	54	66	46	95	42	61	32	33	40
	level.95 net10+1 PE5+2	79	81	89	78	80	85	82	82	82	85	83
11	pa3 4x18Kp+Dst hh mm yy	57	51	69	79	37	**96**	**46**	**63**	54	50	41
	level.95 net20+1 PE5+2	78	83	85	78	88	**88**	**81**	**80**	74	74	82
12	pa3 4x18Kp+Dst hh mm yy	57	50	70	82	41	97	46	63	55		51
	level.95 net20+1 PE10+4	78	84	85	79	87	88	81	80	74		82
13	1 output=Meteosat+Tele-X	62	63				76	58		38	62	
	All the rest as test 11	79	80				85	81		87	79	
14	as test 11 + time since last	52	53				95	43		48	43	
	meteosat anomaly	81	80				89	83		77	78	
	level.95 net18+1 PE5+2											

Table 5.13. Forecast result of anomalies on Meteosat-3 and the Tele-X satellites. Different data sets and back propagation nets have been used. The numbers show the success rate in percentages for anomalies (top value in each box) and non anomalies (lower value in each box). See text for further details.

Kp index

In Section 5.3. the Kp-index was used to predict anomalies on the satellite. In this test we created the data set slightly differently in order to combine the Kp index to the dataset created in Section 5.2.6. In row 3 ten values of the Kp-index have been used as

input to the neural network. The 10 values were a combination of data at the time of forecast and then 9 previous Kp values spread out with 12 hour time steps between each other. In row 3 this is indicated as Kp 10x12. Comparing row 3 with row 1 the success for the different tests is equal, the electron fluxes from the Meteosat-3 satellite is as good as the Kp-index. This is not surprising since the Kp-index shows the level of geomagnetic activity (Wrenn and Sims, 1993).

Forecasts using electron fluxes from Meteosat-3 (row 1) had a higher success rate for Tele-X than for Meteosat-3. In the case using Kp to predict anomalies the success rate between the two satellites is more equal.

Dst index

In the same way as for Kp, the Dst was tested (row 4). In this test, as in Section 5.3, Dst is not as good to predict anomalies as Kp.

Combination

In rows 5 - 7 the electron fluxes measured on the Meteosat-3 are combined with the Kp- and Dst-indices with different resolution. Different combinations of local and non-local data are made. The improvement between row 1-4 and row 7 (high lighted) is approximately 5 %.

Time of year

The frequency of anomaly occurrence as function of; time of year, time in solar cycle, and the local time were studied for both Meteosat-3 and Tele-X. In row 8 the year has been devided into two parts centered around equinox, giving a 6 month period. The input to the net is the electron flux from pa3 (see Table 5.4) and the month. The information of the time of the year does not improve the result. The peaks at equinox are already in the electron flux data. Explicit information of the time of year is thus not needed.

Time in solar cycle

The phase of the solar cycle was used ranging year 1988 (0) to the end of the Meteosat-3 mission (7). When the net trained (row 9) on Tele-X anomalies, it was trained only for times from year 4 and higher. When the Meteosat-3 data are tested with the full seven years of data, the first years of data will not be predicted. This indicates that unless the information of the full solar cycle exists, one shall be careful to introduce the explicit information of the phase in the solar cycle. Row 9 shows Meteosat-3 result using only the same time period as the Tele-X satellite.

Universal time

Local time is difficult to use since the two satellites are not at the same location and Meteosat-3 was moved to different positions during its lifetime. For this reason the UT time was used instead (row 10). The spacecraft are not far away from each other. Again

the difference of anomaly occurrence with respect to the local time is already in the information of the electron flux.

Information on latest anomaly

Another test (row 14) was made to see if information about the last anomaly occurrence improves the forecast result. Wrenn and Sims (1993) suggested that for deep-dielectric charging the successive switching is some 30 hours. This means that the satellite needs time after a discharge to build up a new potential. The test did not give any improvement in forecast success of the Meteosat-3 anomalies. Possible explanation for the result may be that there are few anomalies that are close in time to each other, giving rise to bad statistics when using all anomalies.

Combine all

In row 11 and 12 a larger combination of inputs is used. The improvement is not significant. Figure 5.9 shows the results of the four different nets from row 11. The time period in the figure is the time when both satellites were operational. Four curves in four different panels are shown; from bottom Meteosat-3, Tele-X, fiI and fiII data used to train the net. At the top the desired output for Meteosat-3 (lower) and the Tele-X (higher) are indicated by squared lines.

Combination of Meteosat-3 and Tele-X

In row 13 the input to the network is the same as in row 11 but the desired output is a combination of Meteosat-3 and Tele-X, one (1) if one of the two satellites has an anomaly within 24 hour otherwise zero (0). The result is not much different from the previously trained networks. The difference is mainly due to the fact that more anomalies exist in the data set. The anomalies that were previously not predicted are still not predicted.

5.4.3 Summary

The anomaly warnings on Meteosat-3 and Tele-X are predicted using different inputs. When the non-anomalies are predicted with approximately 80% accuracy, the success rates for anomalies are 60% and 70% respectevly. This is better than only using the local electron data or one of the indices, Kp or Dst.

Using these data for forecast the clearest output signal is given when the neural net is trained with only warnings associated with high fluxes. If one allows the success to predict the non-anomalies to 80% the warnings can be predicted to 47% (this is about 57% of the total anomalies) for the net trained on the high fluxes. The net trained with the anomalies associated to high fluxes gives the output that is easiest to use for an operator. The net trained on anomalies not associated with high fluxes is better to predict the start of a period of high fluxes.

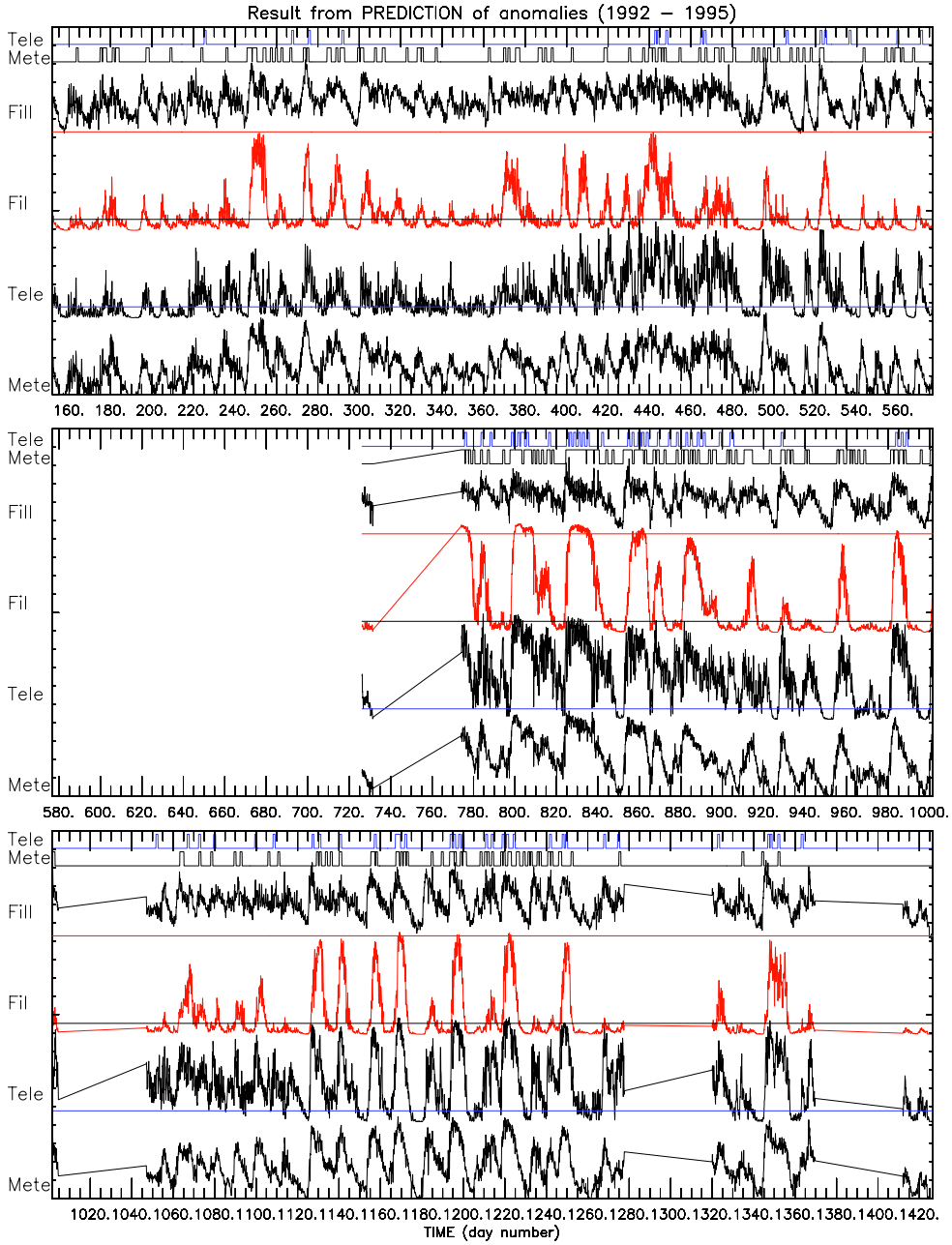

Figure 5.9 The result from the different networks (row 11). The time series covers 1992 to 1995. There were time gaps when the SEM-2 was not operated. From bottom is the output result from the net trained with; Meteosat-3 , Tele-X, fiI and fiII. At the top are the anomalies from Meteosat-3 and Tele-X represented as a squared line. The square lines are 12 points (one day) and the anomaly occurred at the end of the block.

5.5 Discussion of anomaly forecasting

It seems feasible to construct an automatic system producing warnings based on information on energetic electron fluxes, possibly combined with near-real-time information on geomagnetic or solar activity. A warning can be given about 24 hours ahead of the time for increased risk of anomalies. Environment monitors should always be included on-board spacecraft; Not only to give possibilities to predict times with higher risk for damage of components or system failures but also to provide data together with instruments on other spacecraft that can help us to better understand the space environment. Long time series will be needed to separate long-term effects from variations on shorter time-scales. This type of investigation can be compared to the importance to have long time series of ground temperature measurements to understand the climate changes on the Earth.

The neural network could only find the anomalies that are associated with intense energetic electron fluxes. Three measurements of the fluxes preceding the forecast seems to be enough for the forecast.

Wrenn (1995) and Wrenn and Sims (1996) analyzed anomalies on the satellite DRA δ together with electron fluxes from GOES (>2 MeV) and Meteosat-3 (>0.2 MeV), from March 1991 to March 1994. The anomalies on DRA δ were similar to the Meteosat and Tele-X anomalies. There was a clear relation between the anomalies on DRA δ and high electron fluxes observed for several days preceding the event. The electron fluxes from GOES and Meteosat-3 were used to calculate the fluence behind a thin foil (equivalent to a <1.5 mm Al). At the time of the anomalies the satellite had been exposed to a fluence above 10^{11} MeV cm^{-2}. This is enough to cause deep dielectric charging on the spacecraft. The local time of the anomalies, 6–12, also support this conclusion.

The results from Section 5.2 show that the anomalies on Meteosat-3 were associated with high fluxes at energies above 40 keV, indicating that many anomalies are caused by deep dielectric charging. There are also reasons to believe that the flux of electrons below 43 keV is increased, therefore deep dielectric charging is not necessarily the only possible cause. Also surface charging can cause some of the anomalies.

The deep dielectric charging is usually reported to occur in the sector 6–12 local time. The surface charging occurs mainly 22–08 local time. As concluded in Section 5.2. the anomalies that are not predicted are evenly distributed. The peak of the predicted anomalies occurs at 2–10 local time. In this sector both surface charging and deep-dielectric charging can take place. The local time pattern for surface charging during active periods was different (Wrenn and Sims, 1993). At quiet times, the anomalies are evenly distributed in local time. Non-predicted anomalies are randomly distributed (Table 5.14 rightmost column), indicating that cosmic rays might be a possible cause for these anomalies.

For Meteosat-3 the number of anomalies increased with time. The reason that the same result was obtained when the net was tested with different time periods may be

that during the early days the high fluxes of electrons were not so frequent or of long duration and therefore less anomalies occurred. Deep-dielectric charging seems to be more commonly occuring during solar minimum. It would be interesting to study data from a satellite launched during solar minimum and covering a solar maximum to compare the solar cycle effects with the ageing.

local time	12 point warning	predicted	not predicted	1 point warning	predicted	not predicted
22-24	489	93	**396**	51	17	**34**
0-2	435	91	344	50	18	32
2-4	**551**	**259**	292	**64**	**44**	**20**
4-6	556	195	361	61	35	26
6-8	509	148	361	60	30	30
8-10	526	184	342	62	30	32
10-12	393	83	310	44	12	32
12-14	336	**67**	269	34	**6**	28
14-16	**327**	82	**245**	**33**	12	21
16-18	342	68	274	37	9	28
18-20	348	80	268	35	7	28
20-22	367	81	286	39	11	28
average value	432	119	312	48	19	28

Table 5.14. Local time results from the analysis in Section 5.2. The threshold was set to 0.5. Therefore the success rate of the non-anomalies is not optimised to 80%, but higher. This gives the success rate of warnings only to approximately 30%. This table is only shown to identify the tendency of the forecast

5.5.1 Improved space environment monitors

In this study 50–60 % of the anomalies on Meteosat-3 and Tele-X have been predicted and associated with high electron fluxes. The possible cause of these high-energy particles is deep dielectric charging, but all of the predicted anomalies do not necessary have to be due to that. Electrons of low energies (below 30 keV) were not investigated and therefore anomalies caused by surface charging can have been missed. SEUs cannot easily be monitored and the percentages of anomalies due to SEUs is not established.

This study has used all anomalies that were available. When a new satellite is launched several anomalies occur which the operators have to understand. When they understand the behaviour of the satellite, only more pronounced anomalies that have an impact to the mission are reported. We recommend that all anomalies, also those without any impact on the mission, should be reported in order to understand the environmental influence on each spacecraft. Wrenn (1995) concluded “Comparison between ANIK and DRA δ might suggest that the higher the threshold, the fewer the

discharges, but that when one does occur it will be larger and much more damaging; the chance of this happening increases with mission duration."

Futher studies on anomalies associated with electron fluxes measured on spacecraft should take into account that:

- the time resolution has to be better than one day
- the number of input parameters should be kept low by pre-processing the data
- the natural variability of fluxes that a spacecraft encounters in orbit around the Earth can disturb the models so that the number of false alarms becomes high
- the analyzed data set must be big enough due to the large variability of the environment and in the cause of anomalies
- the model should be tested with a "real" time-series of data.

The SREM instrument contains three particle detectors with high energy resolution, an internal dosimeter, and internal temperature measurement. This study shows that a high energy resolution of a space monitor is not needed. With an onboard monitor short time effects can be automatically used to give a warning. For post-event analyses and for onboard autonomous systems higher time resolution is preferred.

The SEU rates have mainly been monitored in LEO, and hence mainly the SAA and auroral oval effects are included. For an environmental monitor onboard a GEO spacecraft the long term variation of high energy particles are of interest. A long term investigation of SEUs on many spacecraft in GEO will give knowledge of the variations of cosmic rays and solar proton events. Since the Earth's magnetic field acts as a shield for cosmic rays, SEU detectors will be interesting to analyze. A SEU monitor is more or less a memory chip that holds a pattern in its memory cells. A computer continuously checks how many bit filps have occurred during the integration time and then resets the pattern. The memory cells that are selected for this type of monitor should be SEU sensitive but latchup resistant.

An environmental monitor for commercial satellites could also use the concept of Bogorad et al. (1995); a dosimeter measuring energetic particles from about 80 keV for internal charging and one or several detectors measuring the surface charging (can either be a dosimeter in the energy range about 1-30 keV or a plate detector). Measurements of the surface charge can, however give the information to late. The dosimeter measure accumulated total dose and might not have the temporal resolution needed for good forecast possibilities. In this study the influence of the electron above 2 MeV was not strong but we still believe that it is important to cover this energy range. In addition a sensitive memory chip to monitor the SEU rate is recommended. The impact of protons is not studied, but a dosimeter measuring the high-energy protons might help improving the understanding of the processes causing anomalies and to develop improved space weather monitors.

An environmental monitor must be able to survive the whole mission, although ground-based data can be used after the first part of the mission when the sensitivity to energetic particles is known. It is also shown that a fairly good forecast can be made

using data from another spacecraft. There will, however, in the future also be other needs for a good knowledge about the space weather. A set of space weather monitors can therefore play a very important role, in the same sense as meteorological instantaneous and long time series data are for the climatology today. Also the knowledge about the space "climate" will be essential when more space based tools are being used and more manned spacecraft are being launched. The weight and power consumption of an environmental monitor must be kept low.

5.5.2. Satellite anomaly index

If a spacecraft operator will use an index that predicts anomalies, it must be easy to use and reliable. A satellite can have no or numerous anomalies. Therefore the index needs to be flexible so the operator can adjust it after learning how the satellite behaves.

The forecast model can give a warning about 24 hours or less before the anomaly. The model is developed to correctly predict the non-anomalies with at least 80%. Using the energy flux directly is not recommended because the output of the model gives an index fluctuating between high and low almost at every point and the normal daily variation is clearly seen. The model that is easiest to read and have the largest difference between low and high is the model trained with anomalies associated with high fluxes. Therefore a satellite index we recommend indicates the presence of high fluxes in GEO. This index can be used on several spacecraft simultaneously.

The index can be used to find about 46% and 63% of the desired warnings, respectively. When the index is low, it is correct to 87% and 96%. The anomalies that the model does not predict are probably caused by other effects than high electron fluxes, i.e. this index is not built to predict them. The 23-24% of the time when the model have a high index it is to 36% to 22% true. If this is not accurate enough the threshold can be selected differently.

On the tested satellites the model predicted up to 70% of the anomalies. The model gives no warnings 75% of the time. Depending on the satellite sensitivity and selected threshold value, when the model gives a warning 22 to 36 % of the times is it correct.

5.6. Conclusions

All spacecraft are effected by the space environment, the difference is the threshold for the different interactions. The spacecraft designers must build the spacecraft to minimise the impact taking the available resources into account.

Operating the spacecraft tells the operator how each individual satellite behaves. After launch, the satellites often encounter many different anomalies both environmentally induced and others. When the satellite's behaviour is established, also harmless anomalies can be useful for further studies.

From the different forecast models one is selected as a good satellite index to warn satellite operators for time with high anomaly risk due to high fluxes of electrons. The forecast model warns if anomaly will occur within 24 hours. 75% of the time the model predicts low activity and low risk for anomalies. When the model warns for a high anomaly risk within 24 hours, it is 22–36% correct depending on the spacecraft sensitivity.

High energy resolution is not needed for an environmental monitor capable of doing good forecasts. An environmental monitor can be a dosimeter, measuring in the energy interval between 40 keV and 10 MeV. The low-energy electrons (below 20 keV) were not studied here, but the low energies should be covered by an environment monitor to give a better understanding of spacecraft charging. SEU effects are also of interest but have mainly been studied in low Earth orbit.

Many satellites are equipped with environmental monitors to monitor the local environment. The instruments provide both information to the operator but also can be designed to warn autonomously. Many of the new monitors are still not tested in space.

Kp and Dst are good candidates for predicting anomalies and non-anomalies on GEO spacecraft, while electron flux (E > 2 Mev) is good for predicting anomalies and less good to predict non-anomalies.

Time-delay neural network and learning vector quantization network are well suited for the forecasting task. Both networks give similar forecast accuracy. Nevertheless, time-delay neural network gives a more stable performance than does learning vector quantization network.

With Kp as the input, using daily averaged data, the total forecast rate is about 80% at highest for events on Meteosat-3, the corresponding forecast rate for anomalies is 78% and for non-anomalies is 80%. And the total forecast rate is 64% for events on Tele-X, the forecast rate is 78% for anomalies and is 46% for non-anomalies. With Dst as the input, the total forecast rate is 73% at highest for events on Meteosat-3, the corresponding forecast rate for anomalies is 75% and for non-anomalies is 72%. And the total forecast rate is 64% for events on Tele-X, the forecast rate is 81% for anomalies and is 44% for non-anomalies. With electron flux (E > 2 MeV) as the input, the total forecast rate is 62% at highest for events on Meteosat-3, the corresponding forecast rate for anomalies is 86% and for non-anomalies is 35%. And the total forecast rate is 67% for events on Tele-X, the forecast rate is 93% for anomalies and is 36% for non-anomalies.

In order to describe the different local conditions in space environment for Meteosat and Tele-X, we investigated how the threshold value affects the forecast accuracy for anomalies and non-anomalies, for a given total forecast rate. By examining two trained neural network models, we have found a new threshold value for Tele-X which can give better accuracy of non-anomalies at the expense of accuracy for anomalies. In addition, the two network models show a similar variation of forecast accuracy with the threshold value. This indicates that the threshold value might be satellite-dependent and be associated with satellite local conditions (including local space environment, satellite design and materials, etc).

6. GLOBAL SPACE WEATHER MODELLING

6.1. What is space weather modelling?

Improved modelling is essential both for engineering solutions to avoid space weather damage and for all types of forecasting: Whether analysing space environment conditions that led to a space weather event or making a forecast, we need models which can use the relatively sparse observations as input and produce a reliable global map of charged particles and electromagnetic fields in the geospace region of interest.

A "grand unified" model encompassing the Sun, the solar wind, the magnetosphere, the ionosphere, and the atmosphere, is probably beyond our horizons. However, for all these regions we already now have a large number of different models, the most advanced of which also address the coupling between adjacent domains.

Longer-term (more than ~1 hour) forecasting requires good models for the solar activity. Forecasts extending to 1–2 days utilise models of generation and of solar flares and coronal mass ejections, their propagation through the interplanetary medium, and their interaction with the magnetosphere. The solar wind-magnetosphere interaction is one of the key issues in the magnetospheric dynamics and simultaneously one of the most difficult problems in STP. In order to protect technological systems against space weather events, warning systems and models of trapped radiation during enhanced magnetospheric activity are needed. Theoretical and/or empirical models are needed in advance for spacecraft design and mission planning, whereas operational purposes require models running in real time utilising real-time data input. Modelling of the electromagnetic coupling to the auroral ionosphere is needed for avoiding communication problems and for warning of the induced current effects on the ground systems. Coupling to the neutral atmosphere is an important issue, as enhanced energetic particle precipitation during solar activity heats the atmosphere, leading to order of magnitude increase of atmospheric drag, which may cause problems for low-altitude satellites or for the re-entry of manned spacecraft. Furthermore, recent studies have shown that the energetic particles precipitating in the Earth's upper atmosphere may change the atmospheric chemistry and thus influence the ozone content shielding the Earth's surface from UV radiation. Many of these effects are also functions of the long-term variability in the Sun, the 11-year (or actually 22-year) solar cycle, thus belonging both to the realm of space climatology and space weather.

In order to assess the risk to either space-borne or ground-based technologies, we need models for the effects of ground-induced current loops in power grids or gas pipe lines, models for determining how the spacecraft electronics are harmed by energetic particles, and models for assessing how the spacecraft charging affects the satellite subsystems. All these models are important tools for both the technical design and operational use.

As discussed below, there are separate models for these and many other space weather purposes. In many cases they have been developed from purely scientific motivation and will require considerable effort to be made operational. Other models have

been developed for specific space environment problems for engineering use. The natural goal, a more integrated effort of combining various models, has to be approached in a stepwise manner, as all partial models still require development and many of them are and will remain incompatible with each other.

6.2. Current space weather modelling capabilities

Space weather has its origin in the variable activity of the Sun. The consequences of the solar activity propagate from the solar surface, through the interplanetary medium to the Earth orbit, interacting with the magnetosphere, the ionosphere, and the upper atmosphere. There are hundreds of models to address various aspects of this chain. Most of these models are developed for purely scientific purposes, and often it has been more important to study and illustrate the fundamental physical processes than to attempt to reproduce the processes with such a detail accuracy as is necessary in operative space weather applications. It is both impossible and not very useful to consider all models in detail here. Instead we pay the main emphasis to those which are deemed to be closest to be useful to cope quantitatively with the problems discussed in Chapter 3.

6.2.1. Models for solar activity

The solar activity is the driver of space weather. Thus it is important to be able to predict the violent eruptions such as coronal mass ejections (CME) and solar flares, as well as solar energetic particle events (SEPE). In the longer, climatological, time scales the modelling of the 11-year sunspot cycle (or 22-year magnetic cycle) is of considerable interest, but we do not discuss these aspects further.

From the modelling point of view CMEs, flares, and SEPEs are closely related to each other because the acceleration of energetic protons to several tens of MeV is associated with CMEs and/or X-ray flares, although the details are not yet fully understood. From the forecasting and warning viewpoint these phenomena are different due to the very different time scales in which they reach the Earth orbit. For example, a 50-MeV proton can move along the magnetic flux tube from the Sun to 1 AU in 25 min whereas the plasma and magnetic clouds of a CME reach the Earth in 3-4 days. Thus a warning time for SEPEs from a flare observation is very short and there is a need to predict the events that can produce SEPEs. The direct effects of CMEs are mostly due to their strong perturbation of the magnetosphere and there is ample time to take protective measures once a CME heading toward the Earth is observed. A major problem here is that we cannot yet reliably predict whether an observed CME will hit the Earth or not, and how geoeffective it will be, until it is observed, e.g., at L1 from where the CME moves to the magnetopause in about 1 hour. From the first effects at the magnetopause it takes some tens of minutes more before the damaging effects have propagated to the various regions of the geospace.

6.2.1.1. Solar proton models

For interplanetary missions the most important long-term hazard is posed by the accumulative effect, the fluence, of SEPEs. At present the most widely used statistical model of solar proton fluence is the JPL-91 model (Feynman et al., 1993). It predicts, on a probabilistic basis, fluences at integral energies of 1, 4, 10, 30, and 60 MeV, for mission lengths of 1 to 7 years. The selection of the confidence level is a critical issue. If one wants to have high, say 90%, confidence that the dose will not exceed a given level the model gives for a 5-year mission about 2 order of higher fluence than if only 50% confidence level is required (cf. Gabriel et al., 1996).

In order to be able to predict individual SEPEs the generation of CMEs and X-ray flares and the associated particle acceleration have to be understood much better than today. So far, there are no first-principle physics-based simulation models that would yield useful predictions. Work is underway in application of neuro-fuzzy techniques to use long-duration X-ray flares as input and predict the SEPEs one hour in advance (cf. Gabriel et al., 1996). Note further that there are no models to describe the duration of SEPEs, which is another parameter of interest for spacecraft engineering.

A new ESTEC contract, called SEDAT, was initiated in 1998. One of its goals is a further development of the solar proton models.

6.2.1.2. Modelling of CMEs and flares

A CME carries some 10^{12}–10^{13} kg mass away from the Sun. Nevertheless, they were basically unknown (unobserved) until early 1970s. Before it was commonly held that the flares are the most geoeffective form of the solar activity. Even after the observations it took quite a long time before the wide STP community, beyond those actively involved in the CME research, fully realised the importance of the CMEs. A landmark paper was Gosling (1993). Presently SOHO is producing unprecedented data of CMEs, examples of which are available on WWW: http://sohowww.nascom.nasa.gov/

Physics-based models of CMEs are still in their infancy. A recommendable and up-to-date collection of papers is the AGU Geophysical Monograph, 99 "Coronal Mass Ejections" (1997). The book provides an extensive review of the current observational, theoretical, and modelling status of CMEs. Present-day models are directed toward the understanding of the production of CMEs in general terms and have not yet been transformed toward space weather applications. However, strong efforts toward this goal are underway. Linker and Mikic (1997) discussed the possibilities of accurate MHD modelling of the corona to 1 AU and demonstrated their ability to determine the current sheet crossings of Ulysses during its first perihelion pass from the south to the north. (Note that the perihelion of Ulysses is beyond 1 AU!) Furthermore, there is a clear and increasing awareness of the importance of the goal toward application oriented CME models (e.g., NSWP Implementation Plan; Luhmann, 1997).

Although our understanding of CMEs is still behind our knowledge of the magnetosphere, the situation from the forecasting and warning point of view is not hopeless.

It is, in fact, possible to make meaningful forecasts and warnings of CME-driven effects in geospace without understanding the origin of CMEs themselves. For practical purposes it will be sufficient to detect an approaching CME after it has left the Sun and base the predictions on this information. Predictions of the effects are still quite uncertain because only a fraction of CMEs hit the Earth and only about 1 of 6 CMEs hitting the Earth produce major geomagnetic storms (e.g., Gosling, 1997).

It is clear that the SOHO mission already has turned a new page in this part of space weather modelling and forecasting (for first SOHO results, see Solar Physics, vol 175, part 2, 1997). The January 1997 CME was the first major event heading toward the Earth predicted on basis of SOHO observations. The warning was neglected, e.g., by NOAA/SEC. Now SEC continuously checks SOHO quick-look data as a part of their forecasting activity. There have also been false alarms from SOHO. As noted above, only some CMEs hitting the Earth have sufficient momentum and favourable geoeffective magnetic field orientation to lead to major storms. At this preliminary stage false alarms have to be accepted but on the long run too many false alarms will turn against the development of space weather warnings.

In SOHO European scientists have an opportunity to undertake leading activities in the modelling of the origins of space weather. The present activities could and should be enhanced. An important point is to increase the awareness of space weather among the solar physics community. If this awareness had been at a higher level in mid 1980s, SOHO would carry at least a simple plasma and magnetic field monitoring package to probe the local IMF and plasma conditions.

6.2.2. Models for solar wind properties

Modelling of the solar corona and the solar wind are closely tied to each other. A key issue is the shape of the interplanetary current sheet and the magnetic spiral which determine whether or not an energetic particle burst from the surface of the Sun can propagate along the magnetic flux tube to a given location, e.g., to the surface of the Moon where a future astronaut may be outside the protection of the lunar base. Another important issue is the shape of the solar wind current sheet and the location of sector boundaries. So far these have usually been modelled by the source surface models (e.g., Wang and Sheeley, 1992) but the discussion by Linker and Mikic (1997) indicates that MHD models are soon to become the standard.

There is also a need for more detailed solar wind models closer to the Earth. A particularly useful solar wind monitoring point is the L1 that is 1.5 million km from the Earth. The advantages of this point are its stability and about 1-hour warning time. Disadvantages are the problems of deducing the three-dimensional structure of the local solar wind from single-point observations. Interplanetary shock fronts may have very variable orientation and the local direction of the magnetic flux tube may be quite different from the average. These make the mapping from L1 to the Earth a formidable task (e.g., Ridley et al., 1998). For the model development it would be highly desirable to have more spacecraft closer to the Earth, e.g., on a 30-40 R_E orbit. The IMP-8 satel-

lite has made, since its launch in 1973, an exceptional service exceeding all expectations, but it is bound to cease functioning some time quite soon. For space weather it is most unfortunate that the STP community has not been able to persuade any space organisation to take the responsibility for continuous near-Earth solar wind monitoring. Because exact information of upstream conditions will be needed also in future scientific studies, the continuation of IMP-8-type observations is essential for science as well as for space weather applications.

Modelling of solar wind propagation from L1 to the terrestrial magnetopause requires more fine-tuned approach than is possible for the modelling of the entire corona. Most of the present flow models involving the planetary bow shock are based on the magnetogasdynamic model by Spreiter and Stahara (1980). With detailed enough input it gives sufficient description for the flow up to the magnetopause. However, dealing with the magnetopause and the transfer of solar wind plasma and magnetic field requires a more extensive approach with massive solar-wind magnetosphere interaction models discussed in the next section.

6.2.3. Models for solar wind - magnetosphere interaction

Different magnetospheric domains are coupled to each other and models describing some specific region are not independent of physics of the surrounding regions. This section deals with empirical models describing the magnetopause and the magnetospheric magnetic field and the large-scale MHD approach to magnetospheric dynamics. Section 6.2.4. discusses models whose goal is to model the inner magnetosphere including radiation belts and geostationary orbit.

6.2.3.1. Empirical models for magnetospheric configuration

The boundary separating the shocked solar wind plasma in the magnetosheath and the region dominated by the terrestrial magnetosphere is the magnetopause. Its subsolar point it is typically at the distance of 10 R_E whereas in the nightside tail the boundary is identifiable at distances of several hundred R_E. During exceptionally strong solar wind dynamic pressure the dayside magnetopause may become compressed inside geostationary orbit (6.6 R_E) as happened during the January 1997 CME event. There are several empirical models for the bow shock and magnetopause (e.g., Slavin and Holzer, 1981). A recent well-documented model based on fresh data is that of Shue et al. (1997). The model has a simple functional form and two adjustable parameters, the stand-off distance in the solar direction and the tail flaring. It has been applied, e.g., to the above mentioned CME event of January 1997.
See: http://www-istp.gsfc.nasa.gov/istp/cloud_jan97/event.html.

In recent years, several empirical magnetic field models for the magnetospheric field have been developed, which are based on both magnetospheric magnetic field measurements and mathematical modelling of the extra-terrestrial current systems (e.g., Tsyganenko, 1990; 1995; Hilmer and Voigt, 1995). The external fields are superposed

to a description of the geomagnetic field, which is usually described by the regularly updated IGRF model. These purely statistical models utilise the vast database of magnetic field values accumulated over the years, parameterised by indices describing the level of geomagnetic activity (Kp, Dst, AE). Time-evolving models developed for post-event analysis utilise, in addition, the field measurements taken at the time of the event to adjust the statistical model to best describe the actual field configuration (Pulkkinen et al., 1992).

Statistical models are already widely used both by the scientific and by the space weather communities, for example, the Hilmer-Voigt model is used in the MSFM (see section 6.2.4.1. below). The models are continuously updated to account for more complex processes in the magnetosphere, for example, the most recent version of the Tsyganenko models (Tsyganenko, 1997) can account for the configuration changes during magnetospheric substorms. However, as the magnetospheric dynamics depends on both the solar wind conditions and the previous history of the magnetosphere, and the present models use only the present values as input, they are not very reliable predictors of the magnetospheric state.

The time-evolving event-oriented models utilise all available information of a particular event to determine the large-scale magnetospheric configuration. The input for these models are various indicators of the magnetospheric state, such as the auroral boundary, or the measured magnetic field values. Through an iterative process, a best-fit configuration is arrived at. The models have been developed and used in scientific problems, but they can be further developed to produce real-time global maps if implemented together with real-time magnetospheric observations.

6.2.3.2. Three-dimensional MHD simulations

Fully three-dimensional magnetohydrodynamic models, which include the solar wind, the magnetosphere, and the ionosphere, have been developed for scientific use by a number of groups. These models involve heavy numerical computing requiring supercomputer capabilities including parallel processing if real-time running is needed. Probably the best known of the models, that are also closest to implementation for operational use, although not necessarily scientifically or numerically the most advanced ones, are those developed at the University of Maryland (see Mobarry et al., 1996) and at the University of California at Los Angeles (there is no published record of the model itself, for a recent application, see Raeder et al., 1997). At UCLA there is also another MHD model (see Walker et al., 1993), but Raeder's model is which people usually refer to in space weather context. In Europe there is only one advanced model at the Finnish Meteorological Institute (Janhunen, 1996) but also it is developed for scientific use only. Furthermore, the group at CETP, France, is doing basic research on MHD simulations. In summary, the field is in a state of continuous evolution and the state of art is not a static concept. Several groups are developing their models further and they do not publish the details of their models too early, if at all.

Global MHD models accept solar wind density, velocity, and interplanetary magnetic field as input parameters. From these time series, they predict the dynamic response of the magnetosphere-ionosphere system. The inner boundary of the magnetosphere is typically set to somewhat above 3 R_E and physical quantities are mapped along field lines to a two-dimensional ionospheric surface. The details of how the ionosphere is included vary from one model to another.

These models replicate the global response of the magnetosphere to increased solar wind energy input deduced from observations: energy loading followed by an explosive energy release into magnetospheric particle energy, into the ionosphere, and out from the magnetosphere in the form of a plasmoid. However, the timing of these events is critically dependent on various model parameters, e.g., diffusion, which are not uniquely determined from the underlying physics.

The problems related with the MHD simulations are mostly concerned with the inner magnetosphere and the thin current sheets. The model boundary at 3.5 R_E and the inherently non-MHD processes dominant in the inner magnetosphere prohibit the proper description of the plasmasphere, the ring current region, and the radiation belts. Note, however, that the numerical inaccuracies are, in most cases, still more severe than those introduced by the MHD approximations. It is not always understood that the MHD equations are structurally much more complicated than the corresponding Euler equations of neutral gas. Furthermore, the coupling with the ionosphere is as yet poorly understood, and only crudely modelled in the simulation codes. Thin current layers, on the other hand, require dense grid spacing. The increase of grid points in 3D simulations costs both memory and computing time. E.g., increasing the resolution by a factor of 10 in all directions requires that the time stepping is also made 10 times more frequent. In total this means a factor of 10000, which is the difference between 1 s and 3 hr in computing time. It is possible to define a different grid spacing in different parts of the magnetosphere, putting the best resolution where it is mostly needed (e.g., Janhunen, 1996). This adaptation should also be made dynamic; e.g., to follow the moving magnetopause or tail current sheet but the efficiency of this method has not yet been thoroughly tested in a supercomputer environment. However, this will soon be routine in the most advanced models (P. Janhunen, private communication, 1998).

6.2.4. Models for the inner magnetosphere

Models describing particle fluxes in the inner magnetosphere, say inside 10 R_E, are of specific interest to spacecraft engineers and operators. Because the global MHD simulations often are computationally too heavy to determine the electric and magnetic fields needed to calculate the energetic particle trajectories and they cannot yet treat the inner magnetosphere properly, these models take another approach. The underlying fields are determined using statistical magnetic and electric fields and the particle orbits are calculated from these. The evaluation of complete particle distributions is numerically demanding and problems arise particularly during exceptional conditions when the fields

deviate from the statistical models. At the same time, these exceptional conditions are often the most important from space weather viewpoint.

6.2.4.1. Magnetospheric Specification and Forecast Model (MSFM)

Of the large-scale physical models, the MSFM is and advanced approach toward an operational space weather model. It is an update of a series of earlier models capable of following particle drifts through the inner magnetosphere in model electric and magnetic fields. It is being developed for operational use by the US Air Force. Its predecessor, the MSM (Magnetospheric Specification Model), has been installed also at NOAA/SEC and is used in daily space weather services. The most up-to-date easily available document of MSFM is the WWW-document by Freeman et al. (1995). A recent example of its use in scientific analysis is Lambour et al. (1997).

The MSFM is designed to specify fluxes of electrons in the energy range responsible for spacecraft charging, ~100 eV to ~100 keV, and also H^+ and O^+ fluxes in the same energy range. The model output gives electron and ion fluxes in the inner and middle magnetosphere, fluxes of electrons precipitating into the ionosphere, ionospheric electric fields, and magnetic-field mapping information. As a secondary parameter it furthermore gives daily average of more than 2-MeV electrons.

The major advancement of the MSFM over the earlier models is the complexity of the electric and magnetic field models and its capability to run in real time. The primary input parameters for the model are the Kp-index, the Dst-index, the polar cap potential drop, the auroral boundary index, the solar wind density and speed, which define the magnetopause stand-off distance, and the IMF, which is used to select the appropriate convection pattern in the polar cap. These parameters determine the used magnetic and electric field models. Secondary input parameters include precipitating particle flux and polar cap potential profile from the operational DMSP satellites and the sum of Kp, which is an indicator of the longer-term activity level. The model can operate with reduced sets of input parameters, particularly, it can be run using Kp alone. The MSFM also includes neural network algorithms that predict the input parameters empirically from solar-wind measurements, which gives the code some capability for short-term space weather forecasting.

The MSFM follows particle drifts through the magnetosphere using slowly time-varying electric and magnetic field models while keeping track of energetic particle loss by charge exchange and electron precipitation into the ionosphere. The magnetic field model is based on the model by Hilmer and Voigt (1995). The field values for various conditions are tabulated and the field configuration is updated every 15 minutes. The magnetospheric electric field is determined by specifying the electrostatic potential in the ionosphere (Heppner and Maynard, 1987; Rich and Maynard, 1989) and mapping this field along magnetic field lines into the magnetosphere. The electric field is also updated every 15 minutes. The model assumes an isotropic particle distribution, which is maintained by pitch-angle scattering mechanisms that do not change particle energy.

Data-based algorithms are used to specify the initial particle fluxes and the fluxes at the model boundaries. A simplified flow-chart of the model is given in Figure 6.1.

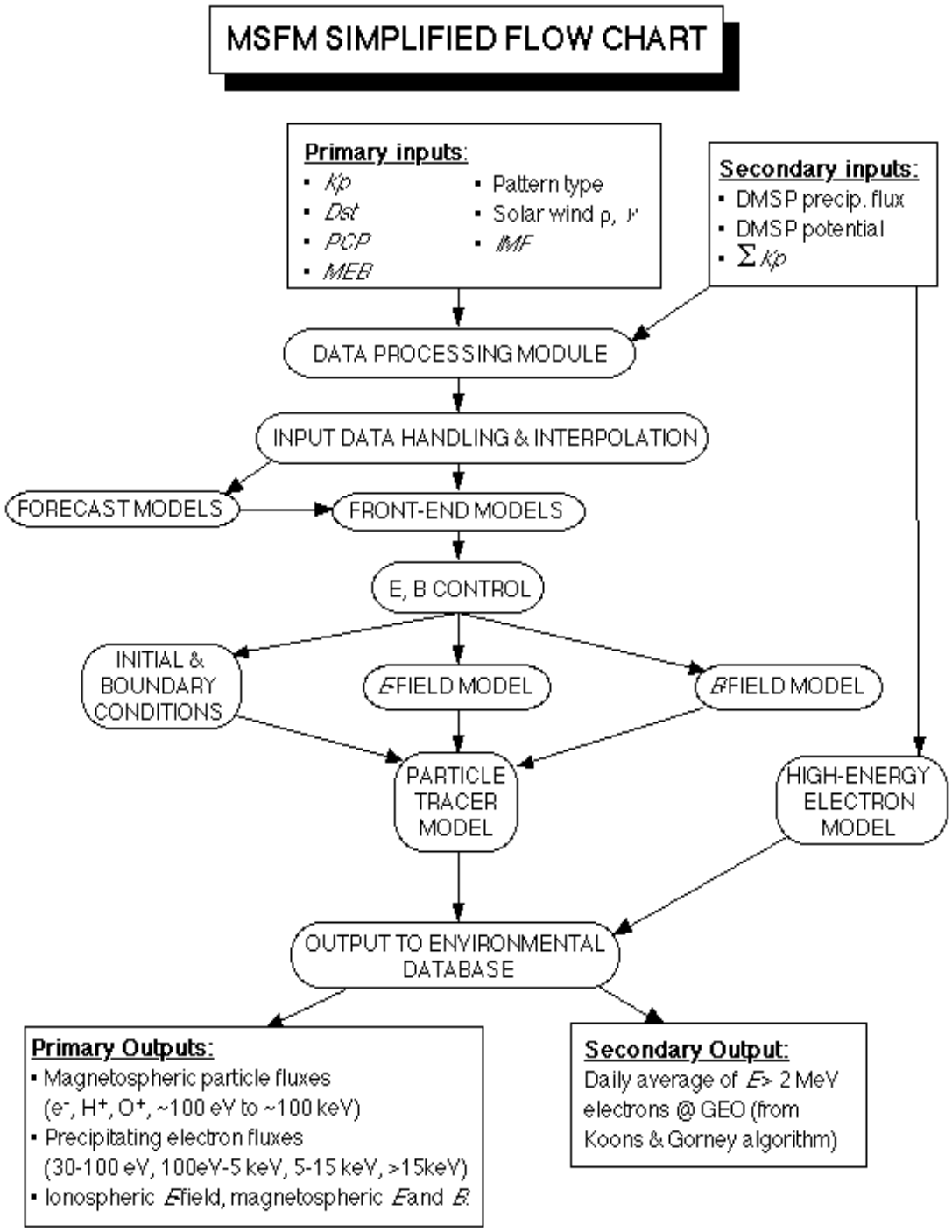

Figure 6.1. Flow chart of MSFM

Extensive tests have shown that the MSFM successfully represents most major electron flux enhancements observed at geostationary orbit. Flux dropouts, often preceding the flux enhancements, are predicted with less confidence, especially the dropouts near dawn meridian are often missed.

6.2.4.2. Salammbô

In Europe there is no effort comparable to MSFM. Many elements of it have been used in scientific analysis also by European scientists, such as the Heppner-Maynard convection models.

We comment here one important European model, Salammbô of CERT-ONERA in France (Bourdarie et al., 1996, 1997). The model solves the diffusion and convection equations in the inner magnetosphere assuming a dipole magnetic field and simple convection and corotation electric fields (Volland, 1973). Its recent version (Bourdarie et al., 1997) allows for an eccentric dipole and thus has three spatial dimensions, and energy as the fourth dimension. The model computes the particle fluxes from convection-diffusion equations.

The Salammbô model has some attractive features: (1) It calculates the particles from realistic diffusion equations, including the most important diffusion mechanisms: wave-particle and neutral atmosphere interactions. Because the model equations are physics-based, it is straightforward to include the diffusion coefficients according to the best available physics understanding. (2) The model is well-documented in open scientific literature, which makes it easier to discuss than, e.g., MSFM (3) The model has different level of versions (3D, 4D); in some engineering applications the magnetic local time dimension may not be needed and the model can be run much faster.

More problematic from the operational viewpoint is that in order to produce realistic results Salammbô requires input from several other models in addition to the background electric and magnetic fields, especially, the correct description of the upper ionosphere and atmosphere is essential. Furthermore, the outer boundary conditions as well as more complex background fields require further investigation. However, it would be interesting to do a point-by-point comparison of the respective pros and cons between MSFM and Salammbô. Salammbô could be the starting point for a European inner magnetosphere model that might be able to compete with the MSFM.

6.2.4.3. Radiation belt models

The details of energisation of the very high-energy radiation belt particles in conjunction with large magnetospheric disturbances are as yet poorly understood. Statistically, it is known that the energetic particles appear as a response to high-speed solar wind streams, but the acceleration mechanisms are not yet known. Thus, further work is required before the onset of these particle flux enhancements can be modelled and predicted.

The static NASA radiation belt models (AE8 for electrons and AP8 for protons; see Vette, 1991) which were developed mainly in the 1960s have been extensively used in the past spacecraft design and post-event analysis. These models are public domain and available from the NSSDC. Recent measurements have, however, shown that the radiation belts are extremely dynamic, and vary significantly over relatively short periods of time. In addition, there are important interactions between the inner belt and the

atmosphere, leading to slow changes. Therefore, several efforts toward more dynamic radiation belt models and standards are presently underway. In Europe, especially the Belgian Institute of Space Aeronomy (BIRA/IASB) in Brussels has been active in this field. To co-ordinate the international efforts, COSPAR has accepted a resolution calling for the creation of a new task group to develop new standards for radiation belt models.

BIRA/IASB has led a series of ESTEC Contracts on Trapped Radiation Environment Model Development (TREND, TREND-2, see Lemaire et al., 1995, and TREND-3). These studies have utilised the AE8 and AP8 models and the UNIRAD software developed at ESTEC. An important part of the TREND studies was the incorporation of the Russian radiation belt modelling effort at the Institute for Nuclear Physics (INP) of the Moscow State University based on the NASA models and data from the Soviet and Russian spacecraft missions.

The applications of these developments are included in the Space Environment Information System (SPENVIS, also developed under an ESTEC Contract). SPENVIS is a WWW-server (http://www.spenvis.oma.be/) which can be used to generate a spacecraft trajectory or a co-ordinate grid and then to calculate, for example:

- the geomagnetic coordinates B (magnetic field) and L
- trapped proton and electron fluxes and solar proton fluences
- radiation doses
- damage equivalent fluxes for Si and GaAs solar panels
- linear energy transfer (LET) spectra and single event upsets
- trapped proton flux anisotropy
- atmospheric and ionospheric densities and temperatures
- atomic oxygen erosion depths
- spacecraft charging

Magnetic field line tracing is implemented, as well as the generation of world maps and altitude dependence plots of the magnetic field and the current models of the neutral atmosphere and the ionosphere. The server is continuously updated.

As part of the US Air Force Space Radiation Effects Program, the CRRES satellite examined the inner magnetosphere radiation belts for 14 months in 1990–1991 (Gussenhoven et al., 1996). The models created with the CRRES data are attempts to define the dynamical variations that occurred over the satellite lifetime, and are averages of data over time periods considered appropriate to the variations. All these models are pertinent to the solar maximum conditions. Five different models have been compiled: CRRESRAD calculates expected satellite dose accumulation behind aluminium hemispherical shielding for different thicknesses, orbits, and geomagnetic conditions; CRRESPRO calculates proton omnidirectional fluences; PROSPEC gives proton differential fluxes; CRRESELE provides the outer zone electron omnidirectional fluence; and CHIME calculates the differential energy flux for all stable elements over the energy range relevant for major cosmic ray sources. These empirical models handle time-dependence in a purely statistical way since the processes governing short-term variations are non-adiabatic.

6.2.5. Ionospheric models

The International Reference Ionosphere (IRI) is an empirical standard model of the ionosphere. It has been produced and updated as an international project sponsored by COSPAR and URSI since the late 1960s. It is based on all available data sources. For given location, time and date, IRI describes electron density, electron temperature, ion temperature, and ion composition in the altitude range from 50 km to 2000 km, and also the electron content. It provides monthly averages in the non-auroral ionosphere for magnetically quiet conditions. The major data sources are the world-wide network of ionosondes, the powerful incoherent scatter radars, the ISIS and Alouette topside sounders, and in situ instruments on several satellites and rockets. IRI is updated yearly during special IRI Workshops. Several extensions are planned, including models for the ion drift, description of the auroral and polar ionosphere, and consideration of magnetic storm effects. The model is available at NSSDC:
http://nssdc.gsfc.nasa.gov/space/model/ionos/iri.html

Modelling of the dynamics of the auroral region and polar cap ionosphere is a more difficult task. Several models have been developed that use multiple ground-based and space-based observations of the ionospheric dynamics to produce global maps of the ionospheric parameters.

At present the most widely used statistical model of ionospheric plasma convection, based on DE 2 observations, is that of Heppner and Maynard (1987). It organises the ionospheric convection as a function of Kp and IMF direction. It is available for collaborative scientific purposes and does not require large computational resources. The Heppner-Maynard convection patterns are used as input in the MSFM.

More detailed models utilising more data systems have been produced for scientific purposes. One of them is the AMIE (Assimilative Magnetosphere Ionosphere Electrodynamics) model that uses data from ground-based magnetometers, radars, as well as particle and electric field measurements and auroral images from low earth-orbiting satellites (for a recent reference, see, Lu et al., 1996). These data are assimilated to produce maps of the ionospheric potential patterns, the global magnetic disturbances, and the global conductivity patterns. AMIE is a scientific tool that requires a considerable effort for any single event analysis. As such the model appears to be too heavy for operational space weather applications.

Using a wide enough ionospheric radar network the ionospheric convection pattern is possible to determine in nearly real-time. Applied Physics Laboratory of the Johns Hopkins University has started providing such convection maps in the WWW:
http://sd-www.jhuapl.edu/RADAR/radar/convection/index.html
The convection patterns are derived from the SuperDARN (Dual Auroral Radar Network) system which at present consists of three pairs of coherent HF radars in the northern hemisphere located at Saskatoon (Canada), Kapuskasing (Canada), Goose Bay (Canada), Stokkseyri (Iceland), Pykkvibaer (Iceland), and Hankasalmi (Finland) and three stations in the southern hemisphere. The method how the convection patterns are calculated is presented in Ruohoniemi and Greenwald (1996). Now the network covers

about 120• of the northern hemisphere polar region and it is planned to expand further. This WWW server illustrates the power of real-time data transfer to a centre that has resources to compute useful products.

6.2.6. Atmospheric models

Atmospheric models have several different roles in space weather modelling: (1) They form an important boundary condition for radiation belt and inner magnetosphere models. (2) The increased atmospheric temperature during space weather disturbances is to be considered during launch and re-entry phase of spaceflight. (3) The long-term effects of space weather and space climatology have long-term consequences in the climate of the Earth.

Several national and international organisations have established committees for the development of atmospheric reference models of which the most widely used model is the COSPAR International Reference Atmosphere (CIRA), an effort that started in 1961 with the publication of CIRA-61. Its third generation is CIRA-86. In 1970s in situ measurements of atmospheric parameters by mass spectrometers and ground-based incoherent scatter radars observations of thermospheric temperature were combined to establish the Mass Spectrometer Incoherent Scatter (MSIS) models: MSIS-77, -83, -86. The CIRA and MSIS groups joined forces in 1986 and MSIS-86 became the upper part of CIRA-86. The MSISE model describes the neutral temperature and densities in the Earth's atmosphere from ground to thermospheric heights. MSISE-90 is essentially a revised MSIS-86 model taking into account data derived from space shuttle flights and more recent incoherent scatter results. Also these models are available at NSSDC through WWW: http://nssdc.gsfc.nasa.gov/space/model/atmos/

The atmospheric drag on spacecraft depends both on particle precipitation during magnetospheric storm activity but also on the solar cycle dependent UV ionisation. The average neutral density at 400 km increases by about a factor of 10 from solar minimum to solar maximum. This can decrease the lifetime of a spacecraft at an initial altitude of 400 km from 4 years at solar minimum to 6 months during solar maximum (for discussion, see Hastings and Garrett, 1996).

The energetic particle precipitation during magnetospheric storms and substorms has consequences to the atmospheric physics and chemistry. The particle-induced ionisation leads to dissociation of the tightly bound N_2 molecules and to the formation of the reactive nitrogen compounds NO and NO_2. These compounds are transported downward from the region they were formed especially during the polar night when photodissociation of NO is weak. In the lower mesosphere and upper stratosphere, the particle-produced NO participates in a catalytic cycle leading to destruction of ozone.

6.2.7. Predictions based on non-linear and AI methods

There are a large number of models that are designed to predict some well-defined parameters of the solar-terrestrial system based on various mathematical methods such as

non-linear ARMA (auto-regressive moving average, e.g., Vassiliadis et al., 1995) models or neural networks. Two well-studied examples are the auroral electrojet indices (AL or AE) and the storm-time index Dst that is an approximate measure of the strength of the ring current.

These models do not involve dynamical equations governing the solar-terrestrial physics but are based on the repetitive structure of the observed parameters, which of course displays the underlying physics. This way of predicting is sometimes considered inferior and less physical but from the application point of view the only thing that matters is whether a reliable prediction is available in time to react. The great advantage of the non-linear filtering and neural network models is that they are fast to compute and for short prediction periods they are today still more accurate than a derivation of the same parameters from the massive simulation models. E.g., non-linear ARMA models driven by solar wind input can forecast the AL index. As described by Vassiliadis et al. (1995) the AL index can be predicted from the solar wind input very accurately afterwards for up to several hours. Here the term "prediction" is sometimes misinterpreted as advance prediction, whereas it really means the ability to reproduce the index from a given initial value and continuous solar wind input for several hours. For this prediction of the AL-index from the WIND spacecraft data or from a single-point polar cap index and see the WWW-page:
http://lepgst.gsfc.nasa.gov/people/vassiliadis/htmls/alprediction.html

There are, however, strong limitations for long-term in advance prediction. For example, the AE index starts to respond to the changes in the solar wind within about half an hour. Takalo et al. (1994) showed that there is an inherent time-scale in the AE index of about 2 hours after which the self-affinity properties of the index change. This change is related to the autocorrelation time of AE and may be interpreted so that the index loses its memory in about two hours and there is not much hope to forecast AE further than 2 hours from any external input without actually simulating the physics of the currents giving rise to the index.

Because the Dst index describes a physical system whose temporal variation is slower, its autocorrelation time is also longer allowing for longer prediction times. Using neural network techniques Wu and Lundstedt (1997) have successfully predicted the Dst index some 3-5 hours ahead from solar wind data. However, when the forecasting time exceeds 1-2 hours the method cannot any more reproduce the initial phase of a magnetic storm because it appears soon after the shock hitting the magnetosphere, however the main phase, i.e., the main negative excursion of the Dst index can be forecasted reasonably well up to several hours in advance. Thus if real-time input solar wind and IMF data are readily available, techniques for reliable forecasting of magnetic storms already exist.

6.2.8. Transforming research models to operational products

Except for certain statistical models (e.g., JPL-91, AE8, AP8) the models discussed above have been designed primarily for scientific purposes. This implies that in many

cases the models have features that are not desirable for operational space weather products, e.g.

- the model may require unreasonable computing resources (time, power)
- only few specialists may be able run the model and/or interpret its output
- the codes may be poorly documented (if at all)
- only basic equations are published but not the details, e.g., how to avoid numerical problems
- needed input data are only rarely available or require long time to collect
- the model may emphasise general physical features at the expense of detail accuracy
- an operational model must be able to run using what input is available whereas scientific modelling is often based on choosing "best events", based, e.g., on particularly favourable satellite configuration and/or exceptionally interesting case.

Some of the models to be developed to operational space weather models are developed under classified contracts (e.g., MSFM). Their basic principles have been published but the details are not generally available. Every physics-based numerical model contains complicated procedures to deal with numerical problems or computing efficiency, which have required considerable amount of work by the modellers. This makes the conversion of these models to user-friendly tools quite difficult.

Before it is possible to estimate how much effort a development of a good modelling tool would require several questions are to be answered. For example

- Should the model be able to propagate the state of the system or just assimilate certain amount of data to produce a static pattern?
- What will be the requirements for computing resources and modelling speed?
- Does the model require best possible optimisation?
- How complicated boundary conditions are to be used (e.g., radiation belt-atmosphere interaction)?
- Must the model be portable (perhaps even to massively parallel environment, e.g., in the case of MHD-models)?
- Is high-level real-time visualisation required?

According to modelling specialists it is relatively easy to write even a very complicated model, e.g., a global 3D MHD simulation. The problems arise when the model has to be made efficient, stable and reliable. For example, in development of MHD codes, most effort goes to finding efficient and stable solutions for numerical problems, administrating variable grid sizes, using variable time steps, etc. The easiest way of solving many such problems would be to make the grid simply finer, but as noted above, decreasing the grid spacing in 3D by a factor of ten, requires 10 times more time steps as well, resulting in 10000 times increased demand for computing.

Not all space weather research models are suitable for transformation to operational use. Before the effort is started the candidate models must be carefully studied

addressing not only their scientific merits but also such features that may affect their use in practice. For example, will the required input data be available and can the model be coded in an effective way? The Rapid Prototyping Center of NOAA/SEC is an attempt to solve these questions. Whatever the future European approach to space weather modelling will be, continuous model evaluation activity should be a part of it. This would not only save time from unnecessary attempts to take unsuitable models into use but also increase the expertise among those who will be responsible for this work.

6.3. Physics requirements

Space weather modelling and forecasting cannot be better than our ability to understand the underlying physics. To some extent the modern artificial intelligence (or pattern recognition) methods such as neural networks seem to make miracles. However, that is not true. That a neural network produces a correct prediction for the Dst index a few hours in advance is just an expression of the empirical fact that the solar wind drives the magnetospheric activity. The mathematical tool is much more efficient to rigorously identify and categorise details in the solar wind driver and to correlate them with the magnetospheric output than a human being but there is no miracle involved.

6.3.1. Limits of the AI approach

The non-linear filtering methods and neural networks can still be refined to a much higher level of sophistication than today, especially in the field of specification. However, there are natural limits in their applicability to forecasting. It is not possible to make reliable predictions further in advance than the underlying physical system permits. The analysis by Takalo et al. (1994) indicates that the limit for the AE index from any direct solar wind driver would be about 2 hours. For the Dst index the possible advance prediction time is somewhat longer, but does not extend to days.

Forecasting AE or Dst alone may not be sufficient for practical space weather applications but the predicted indices may be very useful input to dynamical models. For example, Dst is an input parameter to the MSFM. Calculation of the actual Dst requires magnetometer data and finite time. Thus it is useful to get a reliably predicted Dst in advance to speed up the actual dynamic modelling.

One of the important aspects of the studies of the global magnetospheric dynamics based on the structural properties of the activity indices has been the possibility that the magnetosphere is a low-dimensional chaotic system. Whether it really is such, is still an issue of open debate. If it is, the system is sensitive for small errors in initial data which is not good for long-term prediction but at the same time the low-dimensionality means that the system can be described by a relatively small number of free parameters which is good for development of physically meaningful models that may in future lead to reduced dynamical model execution times.

6.3.2. Limits of dynamical modelling

All plasma physics-based models of the solar-terrestrial system are approximations to the actual physical environment. Space weather taking place in (nearly) collisionless plasma systems is fundamentally different from the ordinary weather in collision-dominated Maxwellian gases. Both systems have their physical challenges, but they are for a large part different. In dilute non-collisional plasma the dominating interaction is determined by the long-range but weak Coulomb and Lorentz forces. It is impossible to make global modelling based on this level of description and we have to go through a long chain of approximations to end up with fluid descriptions like MHD. Even then we arrive at numerical computation schemes where the numerics is still a more severe problem than the hidden approximations behind the dynamical equations. Going beyond the MHD approach is needed at various levels. For example, the present 3D global magnetospheric MHD models include a non-MHD ionosphere in the calculation scheme. The interface to the inner magnetosphere, on the other hand, is as yet an unsolved problem. In the future the diffusion coefficients at magnetospheric boundaries may be computed using more detailed plasma description in those regions.

Models such as MSFM and Salammbô represent a quite different approach to the global modelling with different physics limitations. They are based on various different pieces of physics knowledge of the magnetospheric system. They rely heavily on empirical models of the magnetospheric magnetic field, the polar region electric potential pattern, and interfacing upper atmospheric models. Several critical assumptions are made and the goodness of the models depends on the goodness of these assumptions. For a magnetospheric scientist it is clear that our understanding of the system is not quite sufficient yet but this understanding cannot be required from an operational space weather forecaster.

6.3.3. Required advances in physics understanding

We lack sufficient physics understanding on two important fronts. There are large voids in our knowledge of critical physics phenomena concerning, e.g., the solar origins of space weather, details of solar-wind magnetosphere interactions, or particle acceleration in the magnetosphere. Our physical models often give satisfactory answers to average and moderately disturbed conditions. In space weather we are much more interested in extreme phenomena, in hurricanes instead of afternoon showers, to use an atmospheric weather analogue. The second class of difficulties is related to the complexities in mathematical and numerical problems. It would be a mistake just to wait for better and faster computers to solve the problems. Advances are also required in mathematical and numerical aspects of space plasma physics.

Instead of going too deep into the details we list some of the physics requirements essential for improved space weather modelling:

- understanding the release of CMEs and onset of an X-ray flares on the surface of the Sun with associated SEPE production

- determination of the solar wind structure within 1 AU from limited data
- extreme solar wind-magnetosphere interaction, especially associated to CMEs
- details of storm development and storm-substorm relationships
- acceleration to high-energies in the magnetosphere

These and related problems are challenges to the STP community illustrating the viewpoint that space weather can be a great motivation for continuous efforts in basic research. These are problems that must be attacked by the scientists being aware of the long-term possibilities for applications, but not too constrained by short-term requirements to be able to provide full-tested models too quickly.

6.4 Practical aspects for improvement of space weather modelling

6.4.1. Testing

Regardless whether we want to improve the physics-based, empirical, or artificial intelligence methods of space weather modelling we encounter several practical problems to be solved. It is not sufficient to look just for more sophisticated physical models or ingenious mathematical and numerical schemes to solve the physical model equations but the models are to be continuously put to rigorous tests against observations. Furthermore, the models need the best possible observational input. For post-analysis and model development it is acceptable that collecting of observational data takes time but for real-time specification, warning, or forecasting activities the data inflow must be continuous and reliable.

The current ISTP programme period with its great armada of spacecraft extending from L1 to various parts of the magnetosphere is producing an unprecedented complex of data to be used in tests of space weather models, or models that might be made to space weather models. The STP community is already doing this work, but more interaction with the S/C engineering and user communities is necessary. There hardly will soon be another period when the total state of the magnetosphere at the time of satellite anomalies can be determined as completely as now.

6.4.2. Data acquisition and transfer

Data acquisition is one of the areas where the space weather activities are clearly inferior to the atmospheric weather services, and will remain so. The weather centres continuously receive real-time observations of several parameters world-wide, including continuous global satellite coverage. For space weather the input comes from a small number of space-borne and ground-based observatories and only a fraction of all collected data is in such a format that it can be readily fed into the models.

The rapid development of the internet has considerably improved the access to various data sets. More and more groups are making their data products available in this

way. For scientific analysis this is one of the most important steps forward, in a sense comparable to the advent of digital computers. For operational space weather needs this positive development may hide the fact that these data sets are not always in well-defined formats, the availability may vary depending on how much resources the principal investigator happens to have available for this service, etc. Operational space weather services need guaranteed and rapid transfer of the key data they use. To improve this is an obvious task to organisations like ESA. Binding commitments between the data provider and the service centre are necessary, as are rapid data transfer procedures.

6.4.3. Human resources

As is clear from previous sections, the physical system to be mastered in space weather modelling is very complicated and as yet poorly understood. The research in solar-terrestrial physics progresses continuously toward a better understanding and its results are consequently transferable to the space weather modelling applications. Documentation of models and early conversion to practical applications can be made by scientists but the final products must be produced by professional programmers. Thus, in order to improve the space weather modelling at higher pace than the improvements coming as side-products of the basic research, significant investments in the human resources are necessary. These investments must be made both in the field of fundamental STP research and in the space weather service community for practical model development. The present situation where many STP scientists turn their attention to space weather in order to avoid threatening cuts in basic research is not satisfactory. Without a living STP community there is little hope for practical improvements in space weather either.

6.4.4. Modelling tools

Although many parts of the space weather modelling can be facilitated using modern work stations, it is important to realise that any significant space weather service requires substantial computer resources both for data acquisition and storage, and running the physics-based models. The front-line magnetospheric MHD models require efficient supercomputers, and yet they cannot use ideal grid sizes and time steps for resolving the dynamics to meet the quality requirements of time constraints of forecasting or real time specification. Dedicated space weather centres must have access to state-of-the-art supercomputers; it is quite another question how many such centres are needed worldwide. More than one is a conservative estimate to allow for competition and flexibility.

6.5. Requirements for modelling tools

This section describes a hypothetical space weather modelling tool. Up to now, no such modelling tool has been developed in Europe. There are several physical research models for different parts of the solar-terrestrial system, which are in scientific use. Inte-

gration of these to an operational modelling tool, with near-real-time input from space, has been done under a U.S. Air Force contract at Rice University (the MSFM model), but that model is not available for outside users.

6.5.1. Assumptions for the software

The software will use observational data from the Sun, the solar wind, and different regions of the magnetosphere as input. It will use an integrated set of numerical models to give user-dependent relevant parameters at a given time and place in pre-defined regions of the magnetosphere.

The primary uses of the software are in

(1) (post-)analysing spacecraft anomalies after they have been identified.

(2) predicting conditions hazardous for spacecraft

The software can also be used in the design phase of new spacecraft for predicting statistical occurrence of different conditions during spacecraft lifetime, and thus setting constraints for spacecraft design.

The benefits of such a modelling tool are many. At present, spacecraft anomalies cannot be predicted better than as probabilities over an extended period of time. These estimates are either based on data from previous missions, or statistical behaviour of the solar-terrestrial system. With a modelling tool, physical conditions along spacecraft orbit during its lifetime can be estimated with better accuracy.

For operational spacecraft, the modelling tool allows for forecasts of hazardous conditions. By avoiding critical operations when hazardous conditions are predicted, this may save from anomalous effects harming the spacecraft, and at best save the spacecraft from being lost.

When an anomaly has occurred, the modelling tool allows for a detailed post-analysis of the event. At present, there are no models that would give the external physical conditions at the time of an anomaly, and one has to rely on on-board measurements of external conditions. Since the on-board instrumentation for measuring external conditions typically gives few parameters only, if such instruments exist at all, one cannot conclude with confidence what has caused the observed anomaly. With the modelling tool, the post-analysis can be based on more data, which helps in the design of future spacecraft.

The modelling tool also allows for estimating occurrence probabilities of the most hazardous ("worst case") conditions, e.g., in terms of radiation from different sources, and thus vulnerable parts of hardware can be designed according to either maximum, mean, or optimum conditions, whichever is considered most appropriate.

Different users have different needs for the output in terms of access times, required parameters, and user interface. Even if only specifying the two different uses mentioned above, the User and Software Requirements differ. Thus we shall deal with these two uses separately.

The final product shall include, for both user groups,

1 a distributed system for collecting data from observation sites in space as well as on the ground,
2 software for converting these input into a form to be used by the modelling tool,
3 the (physics-based) state-of-the-art simulation model, used for the interpolation/ extrapolation of, and forecasting from, the observational data, and
4 a dedicated user interface for each user group, giving output with an accuracy and in a format best suitable for different uses.

Item 1) is an essential requirement for making the modelling tool. However, it is not an integral part of the system. Instead, organisations responsible for collecting the data shall also be responsible for delivering verified data as input to the modelling tool. Item 2) shall include interpolation routines, both in space and time, to adjust the input data in the format used by the modelling tool. This software shall be called the modelling tool data front end hereinafter. Item 3) includes the most critical software of the modelling tool. It will be called the modelling tool core in this document. Item 4) is the user interface software.

6.5.2. General description of the model

6.5.2.1. Product perspective

Predictive models, using linear/non-linear ARMA or neural network approaches, are able to forecast geomagnetic activity parameters both in the short-term and asymptotically. These models might thus be used for operational forecasting of increased probability of hazardous events. However, they do not fulfil the requirements of prediction of physical conditions at a given place, or of the possibility for post-analysis. For these requirements, a physics-based model is needed.

Essential parts of the physics-based modelling tool include:

- *Solar and solar wind monitors*. The model accuracy relies on continuous monitoring of the conditions in the Sun and the solar wind. Without adequate coverage of observations, no model will have the desired accuracy. Solar and/or solar wind monitors are also needed for predictive models.
- *Model for solar wind behaviour*. Disturbances originated in the Sun propagate to the magnetosphere with the solar wind, and thus a model of the solar wind is necessary. For modelling of solar energetic particle events, this is extremely important, since the particles enter the near-Earth environment in a time scale of the order of 20 minutes, after they have been ejected from the surface of the Sun.
- *Model for solar wind - magnetosphere interaction*. The magnetosphere is a complicated system of different temporal and spatial scales, demanding careful connection of different models, such as
  - model for the large scale behaviour of the magnetosphere,

- empirical models for magnetospheric configuration,
- models for the trapped energetic particle environment,
- ionospheric models, and
- atmospheric models.

The present state of the availability and maturity of different models for operational use was discussed in section 6.2. above.

6.5.2.2. Quality requirements

Probably the most important item that has to improve in space weather forecasting is the quality of the products. At present there are no generally accepted standards (metrics) for the quality control of the warnings and forecasts, and it is quite difficult to define them given the present level of physical understanding. In the Implementation Plan of the US NSWP the current capabilities vs. requirements were presented as Table 6.1:

	Warning	Nowcast	Forecast	Post-analysis
Solar/Interplanetary	fair/poor	fair/poor	fair/poor	fair
Magnetosphere	poor	fair/poor	poor	fair/poor
Ionosphere	poor	fair/poor	poor	fair
Neutral Atmosphere	poor	fair/poor	poor	fair/poor

Table 6.1. Current capabilities for various levels of space weather service according to the US NSWP. The grading scale is poor, fair, good.

This analysis is based on requirements formulated by the US Air Force and the pessimistic result of the analysis may partly be due to specific military requirements, or the need to stress the urgency of increased resources for the model development and related basic research.

NOAA/SEC monitors the level of their next-day forecasts for M and X flares, solar proton events, 10.7 cm radio flux, a local (Fredericksburg) A-index, and the planetary Ap index (see, http://www.sel.noaa.gov/forecast_verification/). A useful quality parameter is the so-called skill as a comparison of the actual forecast with respect to a given reference method of the events: If the skill is positive, the forecast is better than the reference estimate, if it is negative the forecast is worse. During last few years the skill of the above mentioned predictions, as compared to sample climatology, has varied from a quarter to another, but not infrequently most of the parameters show negative skill (e.g., July-September 1997). It is an obvious requirement that one-day forecasts based on actual observations should do better than climatological statistics.

Another interesting statistical result provided by NOAA/SEC is the success of pseudo Ap storm forecasts, defined by the Ap level higher than 30, over the Solar Cycle 22 (July 1986-March 1997). Of 432 of Ap storms only 164 were correctly forecasted and there were 234 false alarms.

6.5.2.3. User characteristics

Two different groups of users of the software have been identified. These are:

1. Study engineers or scientists, and design engineers
2. Satellite operators

These groups have somewhat different needs for the software, and will thus be dealt with separately.

Study engineers and/or scientist work on post-analysis of observed anomalies on spacecraft, that shall be called events in this document. This group will use the Modelling Tool to reconstruct the conditions in the space environment in the vicinity of the spacecraft at the time of an observed anomaly. These users have scientific education, often at doctoral level. Thus the actual physical conditions in the environment of the spacecraft, at the time of the anomaly, are of interest. It is assumed to be up to the users to make their conclusions from the physical data given by the modelling tool. These kind of studies usually take up to a few weeks, and thus the accuracy of the modelling is more critical than a fast response time. Since these users use the tool only occasionally, the interface shall be user-friendly and self-explaining.

Design engineers may use the modelling tool for predicting statistical occurrence of different conditions (e.g., certain levels of radiation) along spacecraft orbit during its lifetime. Precise conditions at a given time and location are not necessarily required, since statistical ('typical') data are to be used as input. Design engineers are professionals in spacecraft design, but not necessarily in space physics. The results of the modelling tool thus have to be translated into occurrence probabilities of radiation doses and other relevant parameters to be defined with the users. The design groups do not use the tool routinely after constraints have been fixed, and thus the user interface has to be user-friendly and easy to familiarise with.

Satellite operators are people working on daily on-line operation of spacecraft, including orbit control, communications and maintenance of the satellite. These users work in a real-time environment. They must make decisions of action immediately, and thus need a reliable software tool with a user-friendly, satellite-specific user interface. These people are responsible for taking care of any action for recovery after an anomaly on the spacecraft has been observed. The people in this group usually have a technical background for operating the spacecraft. Users in this group are not assumed to know the cause and effect relationships between different conditions and the spacecraft in detail, but to be concerned about the kind of anomaly that could be expected.

6.5.2.4. General constraints

In general, the modelling tool has to be

1. Fault-tolerant in terms of input data and run-time instabilities in the physics-based model.

   Bad or missing input data shall not cause the running of the modelling tool to stop, nor shall ill-posed physical conditions cause program error. However,

these situations have to be clearly indicated to the user, so that the user knows that the results have to be interpreted with proper care.

2. Flexible in terms of input.
   Input data available from any part of the magnetosphere, on ground, or from the solar wind, shall be possible to include in the input data set used by the tool. An obvious example is data from spacecraft, whose instrumentation and positions are variable. If conflicts between data from different sources exist, the modelling tool shall indicate such occasions. Also, any input data *not* available shall be allowed to be omitted. The modelling tool shall adapt to existing data, and not be critically dependent on single observation.
3. User-friendly.
   The modelling tool shall have a dedicated user interface for each identified group of users, and, for operational use, for each satellite.
4. Reliable in terms of quality of output.
   As already stated in item (2) above, missing or probably erroneous input data shall be indicated as lowering the quality of the output, so that no false conclusions of the cause of an anomaly are made, and no over-design or too small margins will result for design of future spacecraft (user group 1), and no false recommendations for actions to be taken are made (user group 2). Obviously the quality of the output depends on the quality of the data, and a measure of the reliability of the output data shall be given for all users.

Partly these requirements are for the physical models, partly for the modelling tool and its implementation on a computer system. Again, the two are intimately interrelated.

6.5.2.5. Assumptions and dependencies

It is assumed that when the modelling tool is developed, there exist

1. sufficient amount of observational sites in the critical regions of the solar-terrestrial system to provide necessary input data for the modelling tool, and a coordinated system for collection of that data for modelling
2. sufficiently accurate physics models of the solar-terrestrial interaction

- powerful enough computers to perform the desired calculations in the required response time (group 1), or in the lead time needed for forecasting (group 2).

6.5.2.6. Operational environment

The modelling tool will run in a distributed net of computers, with different tasks in different phases of the modelling in the most appropriate hardware and location. The observations are verified and pre-processed at the organisation responsible for the observation in (near) real-time. The data is then transferred through a network (e.g. internet or a dedicated link) to the modelling centre.

The physics-based model, used for post-analysis, requires (today) super computer class hardware, and thus has to be run in a computer centre having that facility. For ensuring the smooth operation of the modelling tool, dedicated professionals both for computer operation and result verification and interpretation are needed.

For predictive models that can be run on fast workstations, the actual modelling software can be run either at the modelling centre, or at the end user's organisation. In each case, the verification, selection and integration of input data for the modelling tool is to be done at the modelling centre. When predictive models become real physics-based forecasting models, they will pose more severe environmental constraints, such as massive parallel processing (MSP). However, such models are beyond the scope of this discussion.

The parameters and format of the output depend on the needs of the end user, and the User Interface part of the modelling tool will be run locally in the workstation of the end user. The results from the physical (or predictive) model are distributed through a data network to the users for post-processing.

The modelling tool core shall include the different physics models discussed in section 6.5.2.1, and thus the most natural choice is to distribute the responsibility of development work of the modelling tool to institutions where expertise and resources are available. However, for practical reasons, the final product (core modelling tool) shall be integrated to one place.

6.5.3. On modelling tool software requirements

The model is assumed above to be built on various model elements that have been developed more or less independently. In the development of the modelling tool, the integration of different models to the tool has to be studied and negotiated with each group separately. The fact is that some of the building blocks and, especially, their interrelationships pose such physics and numerical mathematics problems that are difficult to completely hand over to professional programmers.

The software ('modelling tool') serves as a tool to predict space environment conditions that are hazardous for operational spacecraft. It consists of functional blocks, responsible for acquisition, verification and preparation of data ('data front end'), 'core modelling tool' software, including the physics based models that calculate the required output parameters from the input parameters, and the user interface software, dedicated for each user group.

The modelling tool is a system of independent, interacting software, and of manual phases of work (data verification) in a distributed environment. The data collection and verification are done by the organisation responsible for operating the instrumentation. The input data are fed to the data front end of the modelling tool. This software converts the data to a format understood by the modelling tool, and performs, e.g., necessary interpolation routines.

After verification and preparation the data are fed to the core modelling tool. The selection of the structure of the modelling tool is a trade-off between possibility to

upgrade with more recent (advanced) partial models and computational efficiency. A completely modular program cannot be optimised to the same level as a model where the computational algorithms are selected according to the functional forms of the models used.

Specifically, the following requirements apply to the modules of the core modelling tool:

- The modelling tool shall include a (dynamic) magnetic field model, run with (near-real-time) physical parameters.
- The modelling tool shall include an electric field model, including electric fields emerging from time-variation of the magnetic fields, to be combined with the output of the magnetic field model, for particle drift calculations.
- The modelling tool shall include models for particle sources (either model or data base) and loss of particles.

The modelling tool core passes its output to the dedicated output software. Output software shall depend on the User group, and whether interactive or batch processing is used.

The block diagram of the modelling tool is shown in Figure 6.2, and a more detailed description of the magnetosphere-ionosphere (core) model in Figure 6.3.

6.5.4. Building blocks of the tool

Magnetic field model

Alternatives for choosing a magnetic field model for the modelling tool are numerous. The most simple models are the *dipole and eccentric dipole models*. These are static models, describing the non-variable component of the Earth's internal field. The advantage of these models is that they have a clear analytic form. As a consequence, analytic manipulation of the equations governing particle behaviour in combined magnetic and electric fields may substantially speed up numerical calculations. The major disadvantage is the small region of applicability of the (eccentric) dipole magnetic field. The magnetospheric magnetic field deviates from the dipole field already at the distance of the geostationary orbit, especially close to the noon-midnight meridian. Thus these models do not describe the true magnetic field very well. Also closer to the Earth, to correctly describe high energy particle precipitation to low altitudes above the South Atlantic Anomaly, a more advanced model has to be used.

The next in order of increasing complexity is the International Geomagnetic Reference Field (IGRF). This model includes higher harmonics of the internal field, and it is also updated regularly, thus following the slow variations of the internal field. However, as the (eccentric) dipole field model, the applicability of this model is also limited to close distances from the Earth, up to roughly 5 Earth Radii on the equator.

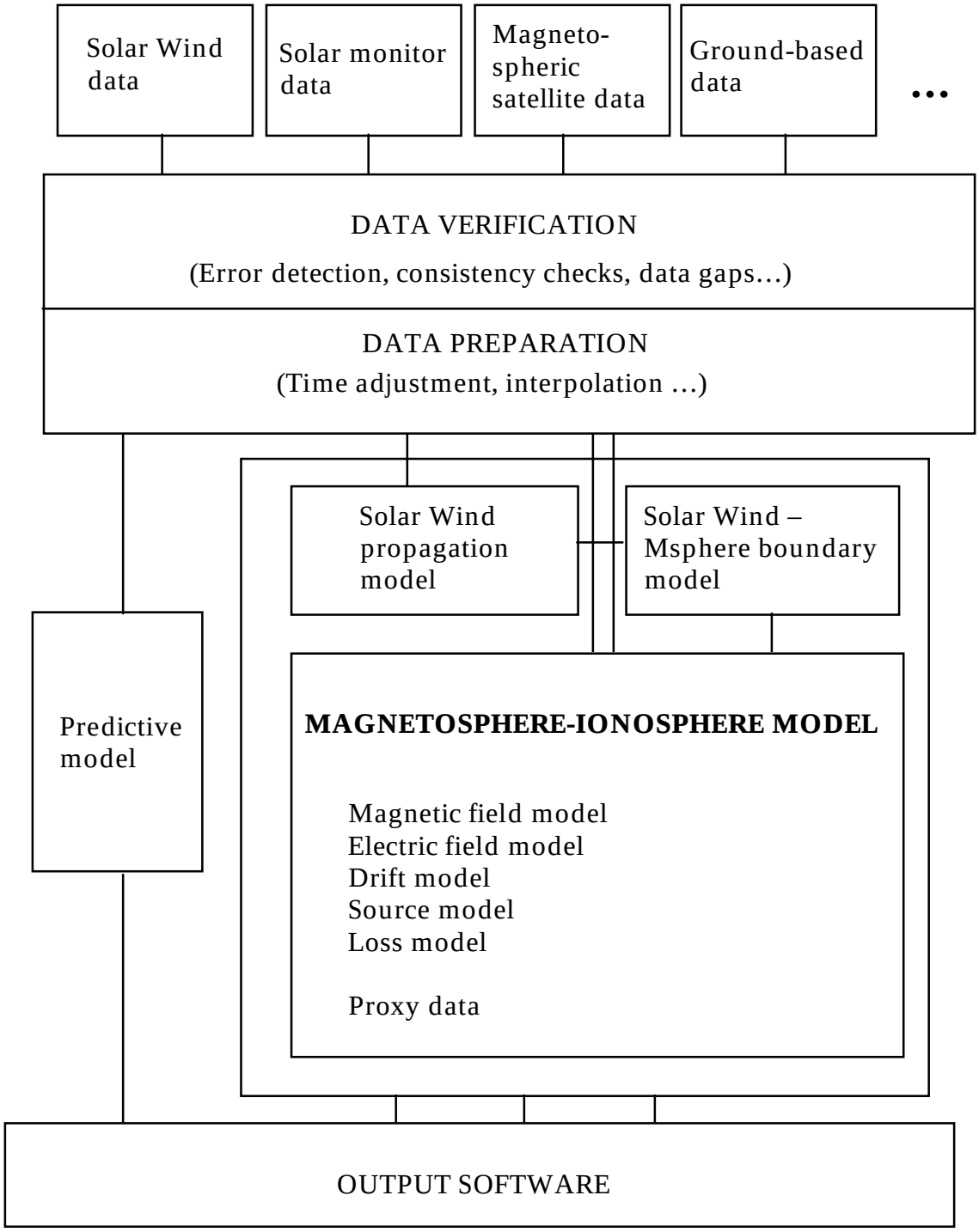

Figure 6.2. Block diagram of the modelling tool.

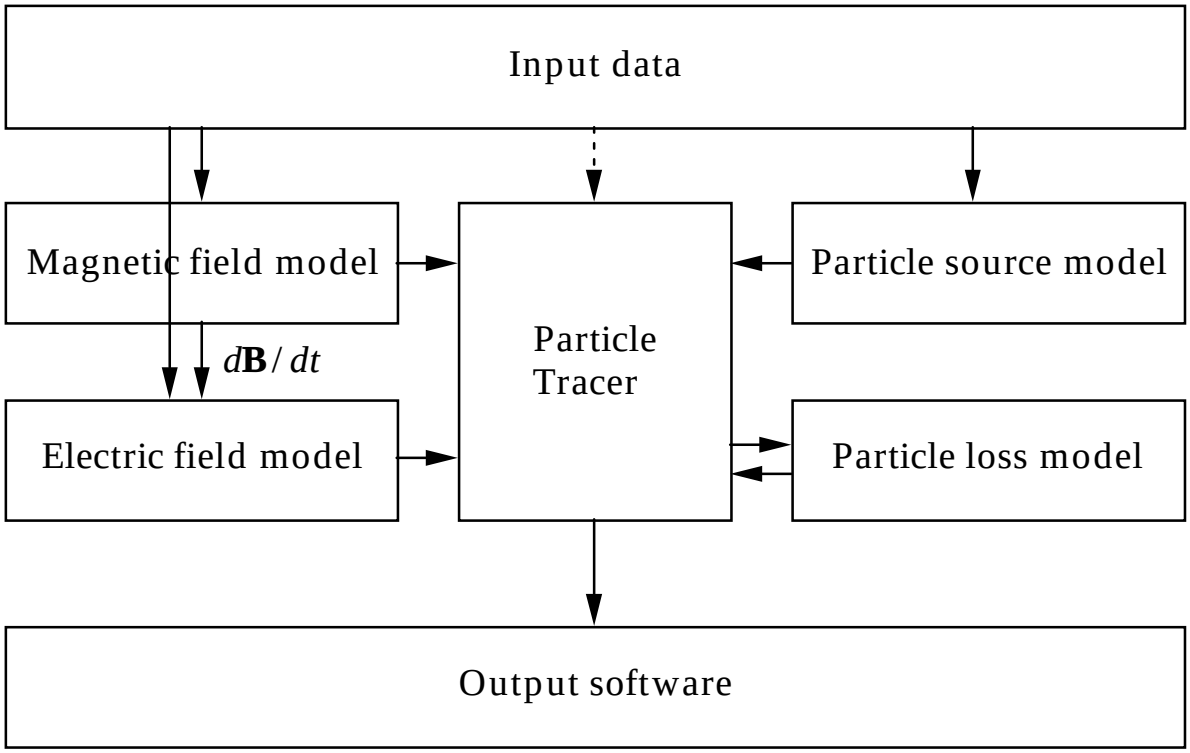

Figure 6.3. Block diagram of the magnetosphere-ionosphere model (modelling tool core) of Figure 6.2.

The magnetic field model by Hilmer and Voigt (Hilmer and Voigt, 1995), which is used in MSFM, combines the dipole magnetic field of the Earth with magnetospheric field components caused by electric currents in different parts of the magnetosphere: the equatorial ring current, the cross-tail current, and the Chapman-Ferraro current at the magnetopause. Using these source fields, the model computes the total field configuration. The input parameters of the model to set the magnitude, location, and extent of the source current systems are:

1 *The dipole tilt angle*, i.e., the angle between the axis perpendicular to the Sun-Earth direction, pointing to the north. Positive values correspond to the northern hemisphere being tilted towards the Sun.

2 *The magnetopause stand-off distance*. This parameter is used to set the size of the magnetosphere by adjusting the strength of the Chapman-Ferraro currents. The magnetopause stand-off distance can be approximated by calculating the pressure balance between the solar wind dynamic pressure and the magnetic pressure of the terrestrial dipole field. Alternatively, a more advanced model, such as Shue et al. (1997) can be used for calculating the stand-off distance from solar wind parameters.

3 *The geomagnetic index Dst*, describing the magnitude of the ring current.

4 *The midnight equatorward boundary of the diffuse aurora*. This parameter is used to indicate the degree of stretching of the magnetotail magnetic field. The midnight equatorward boundary is a rough indicator of the radius of the auroral oval, which is a measure of magnetic flux in the magnetotail. In practice, this parameter is used to define where the tail current sheet must be positioned so

that the inner edge footpoint maps to the right latitude in the ionosphere. This parameter is to be inferred either from ground-based observations, or satellite measurements of precipitating particles in the midnight sector.

In the practical implementation of the MSFM, the model magnetic field values have been pre-calculated and tabulated in the computational grid of the model, for a range of parameters, to save computing time.

The main advantage of the Hilmer-Voigt model is that the input parameters are directly measurable, and thus adjust the magnetic field to the prevailing conditions, with several parameters that can be verified. The region where the model can be used, well covers the inner magnetosphere, up to nearly subsolar point towards the Sun, and down to approximately 30 R_E towards the tail.

The different versions of the Tsyganenko magnetic field models (Tsyganenko, 1987; 1989; 1995; 1997) are widely in use among the scientific community. They are all available on the WWW, and due to the large number of users, they have been thoroughly tested, and the strengths and weaknesses of the models are well known.

For a modelling tool, the main weakness of the Tsyganenko models is that they only use global parameter(s), typically magnetic activity, and in the later versions also solar wind parameters to adjust the magnetic field configuration. Also, like all statistical models, the models have been averaged over large amount of events, and thus extreme configurations are not reproduced.

The basic principle of the Tsyganenko models is very similar to the Hilmer-Voigt model: the magnetic field in the magnetosphere is calculated from electric currents inside and at the boundaries of the magnetosphere. The approach in the Tsyganenko models is to use vector potentials to describe the currents and magnetic fields. This approach ensures that the magnetic field remains divergence-free.

The input parameters for the two most recent versions are, in addition to the point in space where the magnetic field is to be calculated:

- Tsyganenko 1989: Magnetic activity index Kp, and either geodipole tilt angle or date and time
- Tsyganenko 199X: Magnetic activity index Dst, Solar Wind pressure, IMF By and Bz, and either geodipole tilt angle, or date and time.

The user may also choose whether to use the dipole or IGRF internal magnetic field model. The output of the models is a three component magnetic field vector

Electric field model

For the selection of the electric field model for the modelling tool there are essentially two alternative approaches:

(1) Specifying the electric field in the equatorial plane of the magnetosphere, and using mapping along magnetic field lines for the rest of the modelling region, or

(2) specifying the electric field in the high-latitude ionosphere, and using mapping towards the equatorial plane for calculating the electric field in other parts of the model.

Approach (1) has been used in the Salammbô model (6.2.4.2), whereas the latter option (2) has been used in the MSFM model. Both approaches exclude the effects of inductive electric fields, which are important in the dynamics of particles.

The choice is not obvious. The motivation for using the equatorial electric field in Salammbô is that the model used (Volland-Stern-model, Volland, 1973; Stern, 1975) has a simple analytical form that can easily be implemented in the code, and analytic manipulation is straightforward. On the other hand, the Volland-Stern model is very much simplified, and does not correctly account for small-scale structures of equatorial electric field, nor the region between the corotation-dominated electric field (up to 5 R_E) and the convection-dominated electric field (tailward of 10 R_E).

In the MSFM model, the Heppner-Maynard model (Heppner and Maynard, 1987; Rich and Maynard, 1989) is used. It specifies the ionospheric potential pattern at latitude above 60 degrees (thus excluding innermost part of the magnetosphere, inside 4 R_E). The Heppner-Maynard-Rich (HMR) model uses spherical harmonics in magnetic local time and latitude, to describe the variation of the potential pattern, as a function of IMF. For southward IMF, also explicit variability with geomagnetic activity is included. In the MSFM model, the HMR model was modified to accept the Polar Cap potential drop as an extra input parameter. The HMR model is available from its authors.

Neither of the approaches discussed above include time variation of the electric field, nor inductive electric fields due to magnetic field variation. The modelling tool shall be able to model transient effects like Storm Sudden Commencements (SSC), that cause rapid heating of plasmaspheric plasma to keV and even MeV energies, and auroral substorms, that cause flux dropouts and energetic particle injections at geostationary orbit. Both phenomena are, according to present knowledge, due to inductive electric fields (electric fields caused by time variation of the magnetic field, $\partial \mathbf{B}/\partial t$). Those variations are not included in the present magnetic field models (with the exception of some research models).

Particle energisation in the inner magnetosphere due to an SSC was successfully modelled by Hudson et al. (1997), who used magnetic and electric fields obtained from a 3D MHD simulation of an SSC event. The applied azimuthal electric field produces first inward and then outward acceleration of particles, causing acceleration and deceleration, respectively, due to conservation of the first magnetic invariant in an increasing and then decreasing magnetic field.

The Salammbô model originally used the dipole magnetic field and the Volland-Stern electric field model. In later versions, the Volland-Stern electric field model has been modified to also include time variation of the convection electric field (Bourdarie et al., 1997). With this modification, and adding a new low-energy (8 keV) particle source at the near-Earth magnetotail (9 R_E), injection features during strong magnetic activity were modelled. The latest version (Bourdarie et al., 1998) also uses a ring current term (Tsyganenko and Usmanov, 1982) and Mead-Williams (Mead, 1964; Williams and Mead, 1965) model for magnetotail currents. With time-varying magnetotail current location flux dropouts observed at geostationary orbit during substorm expan-

sion phase were modelled. In this model, the injection front of Bourdarie et al. (1997; see above) was not included.

On the other hand, to reproduce the flux dropouts, only minor modifications to the magnetic field are needed, since the geostationary orbit is located in a region, where particle orbits are sensitive to even small changes in the magnetic field (P. Toivanen, private communication, 1998). The recent studies by Toivanen et al. (1999) also show that even moderate changes in the magnetic field, when translated to induced electric field, cause substantial variations in particle distributions during substorm cycles. Thus a model neglecting these terms clearly is not sufficient, if high accuracy is desired.

Particle drift model

Particles in combined magnetic and electric fields drift across the magnetic field, in addition to their rapid gyration around the magnetic field line and their motion along the magnetic field (e.g., Northrop, 1963). These drifts depend on the strength, temporal variation, and spatial gradients of the fields. In addition to these relatively slow drift motions, the particles may also experience acceleration by electric fields parallel to the magnetic field, as well as acceleration by wave electric fields.

In large-scale modelling the fast gyromotion around magnetic field direction is neglected resulting in equations governing the motion of the particle gyrocenter (i.e., the large-scale drifts). The lowest-order drift is the electric drift $\mathbf{E} \times \mathbf{B} / B^2$ which is the same for all charged particles. Slow time variation of the electric field introduces a polarisation drift term that separates electrons and positive charges leading to a polarisation current. Spatial gradients in the magnetic field introduce gradient and curvature drifts. In the nearly dipolar field around the Earth, the gradient and curvature drifts of electrons are eastward and of ions westward. The net current is thus westward.

Particle tracer

There are practically two ways of performing the drift calculations. One is to use the Hamiltonian formalism, as in Salammbô. One does not solve the equations of motion (given above) explicitly, but uses instead the adiabatic invariants in the Hamiltonian equations of motion, and solves the Fokker-Planck (diffusion) equation for the time evolution of the distribution function. Knowing the relation between the distribution function and particle flux, one can then calculate the corresponding measurable parameters from the distribution function.

This approach is effective when the magnetic and electric field configurations have (simple) analytic forms (like a dipolar magnetic field, and Volland-Stern electric field), leading to well-defined and well-behaved adiabatic invariants. In more complicated magnetic field geometries (like any non-dipolar magnetospheric field), the same analytic expressions are not valid, and the calculations become very time-consuming.

Another approach is to use a set of "test particles", which may represent an ensemble of particles with given energies and pitch angles at a given place, and follow their drift paths with integration of the equations of motion in time. At the same time the electric and magnetic fields are updated according to their time evolution (measured

or modelled) during the event. This approach is used in the MSFM model, and, e.g., in the drift modelling by Toivanen et al. (1999). Special care has to be taken to ensure that the integration scheme conserves the constants of motion: In the case of a model that is not self-consistent, this has to be regularly checked.

In the Toivanen et al. model particle orbits averaged over one bounce period (time which it takes for a particle to travel from the equator to one mirror point above the ionosphere, to the other mirror point, and back to equator). Thus the smallest time step is the highest energy electron bounce period. The ions drift a substantial distance in the azimuthal direction during one bounce period, and this approach is not accurate to compute ion drifts. Also, the bounce-averaged formalism does not allow for exact energisation of particles (due to electric drifts) during the bounce period: only upper and lower limits are available. Diffusion due to wave electric fields and/or pitch angle scattering are straightforward to implement.

Particle heating due to plasma waves

In addition to drifting in the magnetic and electric field, particles also gain energy by being heated by interactions with plasma waves. Good models for the existence or heating efficiency of plasma waves in different parts of the magnetosphere do not exist. The results shown by the Salammbô group are calculated using a diffusion coefficient, based on simple assumptions of azimuthally constant heating region at the outer edge of the plasmasphere. The values for the diffusion coefficient were calculated using results from Lyons et al. (1972) and Thorne et al. (1973). The results show general agreement with data, but these values are only applicable for this very limited region, and for other parts of the magnetosphere similar models do not exist.

Boundary conditions: Particle sources

There are a number of statistical models for the particle environment in different parts of the magnetosphere. Probably the best modelled regions are the radiation belts, for which the NASA radiation belt models (AE8 for electrons and AP8 for protons, see Vette, 1991), models developed under ESTEC Contracts (TREND, TREND-2, see Lemaire et al., 1995, and TREND-3), and data from the CRRES spacecraft (Gussenhoven et al., 1996) are available.

For other important source regions of plasma in the magnetosphere, the availability of models is not as good. An important reservoir of plasma is the plasmasphere. Plasmaspheric models have been developed, and the average properties at the equator are relatively well known (e.g., Carpenter and Anderson, 1992: an empirical model for equatorial electron density). Lambour et al. (1997) used a modified version of MSFM to model the behaviour of the plasmasphere following storm sudden commencements, with the Carpenter and Anderson model as an initial condition.

The plasma sheet is an important source of particles, especially during magnetically active periods. However, there are no useful models for the plasma sheet. The most coherent set studies of plasma sheet properties, based on measurement on board the AMPTE/IRM spacecraft, was summarised by Baumjohann (1993).

The ionosphere is another important source of magnetospheric plasma. However, its role is more of filling the reservoirs of the plasma sheet and plasmasphere, of lesser importance for this study.

It is important to keep in mind that variations of, e.g., energetic electron flux, from statistical values can be as high as several orders of magnitude during disturbed conditions. Thus, as a conclusion, the only really reliable boundary condition in a source region is an in situ measurement.

Boundary conditions: Particle loss model

In the first order approximation, particles are lost either through precipitation to the ionosphere/ neutral atmosphere, charge exchange, or by drifting to dayside and lost to non-closed orbits.

The precipitation to ionosphere can, in the simplest approach, be modelled through removing particles that have their magnetic mirror points below a given altitude. This is equivalent to assuming a completely absorbing ionosphere. A more accurate model, using an exosphere neutral gas model, and friction model to describe the interaction of energetic particles with neutrals, has been successfully implemented in the Salammbô model (see Beutier et al., 1995)

The efficiency of charge exchange as a loss process depends on neutral (hydrogen) density, and the details of the charge exchange process. Energetic Neutral Atom (ENA) production through charge exchange is generally accepted to be an important mechanism for ring current energy dissipation, and modelling of ENA production during magnetic storms has been presented (e.g., Roelof et al., 1985; Roelof, 1987). However, even if steps towards modelling the microscale interactions and their relation to ENA production have been taken, the models are not mature to be used in an operational model.

Energetic particle loss by drift is automatically included in a complete drift model: When particles drift to non-closed orbits, they are lost from the model.

6.5.5. Resource estimates

Computer resources

The modelling tool, if based on a particle drift model approach, sets high requirements on computing power. Memory resources are not extensive (on a 3D particle drift code one has 12 variables / test particle), but the computations take a long time. The Toivanen et al. (1999) particle drift code used the Tsyganenko 1989 magnetic field, with modifications corresponding to the time-varying magnetic field during substorms, and inductive electric fields calculated from the variation of magnetic field. For modelling of one orbital period of the CRRES satellite (approximately 11 hours of real time) by backward calculation of particle drifts from the substorm onset to the measurement during previous orbit, takes approximately 16 hours of computer time on a fast workstation/server machine (P. K. Toivanen, private communication, 1998).

Most of the time is spent on the tracing of the magnetic field lines of the model, and the more complicated the model is, the slower calculation. It is estimated that tracing the field lines of the Tsyganenko 1996 model takes approximately 10 times more time than tracing the T89 model (N. A. Tsyganenko, private communication, 1998). The tracing part of the code cannot be vectorised, and thus not much better performance is expected on a vector processor.

Manpower resources

Present research models have been developed gradually, as research projects, during several years, and are in continuous development. In general, approximately one third of the development project consists of planning, one third actual programming, and one third tests and, finally, "production" runs. For research models, each "production" run of the model can be considered as one more test.

The effort needed for developing a physics-based model of the dynamics of the magnetosphere is extremely difficult to estimate. However, to give an idea of the order of magnitude of the work needed, we give three sample cases:

The development of the 3D MHD model by Janhunen (1996) was started in 1995, and the model (now in third generation) is still in continuous development. The model today consists of about 35000 lines of code (in C++), including visualisation. Recently almost 95 % of the development work of the code has been directed towards computational efficiency.

Another example, the drift model by Toivanen (1995) was originally developed in one year by one person. That version of the model did not include the time-varying magnetic field, nor the inductive part of the electric field, which both are essential for a complete description of the dynamics. Finding a workable solution for the implementation of these two physical phenomena into an efficient computer code, coding, and testing, took then almost two years (Toivanen et al., 1999).

The first results of the Salammbô model were published in 1995 (Beutier et al., 1995). Since then, the model has been gradually developed, and still, after 3 years from the first results, modifications are made to make the accuracy better (in terms of both qualitative and quantitative agreement with observations). Updating the model with some of the Tsyganenko magnetic fields has also been considered, but not implemented.

The research modelling projects typically are, or at least include, work directed towards doctoral thesis, and thus one could argue that the persons working on the model development perhaps are not the most skilled professionals, neither in physics, nor in computational mathematics. We would not, however, draw this conclusion. Fact is, that there are no better specialists on those fields, and the support by the research groups is enough to guarantee continuation of work. Of course, one can benefit a lot if there is support from specialists available, when needed, but we do not think that would speed up the progress by a factor of two.

Thus one could think that writing a simulation model software is a work of a year or two for a small group of engineers and physicists. It *is* in principle quite straightforward to translate the basic physics equations to a numerical computer code,

but to make the model give physical (and even quantitatively correct) results in an acceptable computing time, quite a lot of technical problems have to be solved. This is analogous to building an instrument for space measurements: The basic design is quite straightforward, but to take into account the limitations of mass, power, and telemetry, and still get useful results, one has to work a long time. Usually the problems are solved in an iterative manner (by trial and error) and finding the right solutions to the problems requires a lot of thinking. In conclusion: A computer engineer, even if highly skilled, cannot translate the physics equations to an efficient working model without help from physicists, who know the problem, and maybe skilled mathematicians, specialised in computational mathematics. In an ideal situation, of course, some of these properties are combined in one person.

6.6. Space weather information server

As a part of this project a public WWW server has been developed. It contains

- Links to other space weather servers
- Description of the existing European space weather resources on WWW
- Access to data bases necessary for estimation of satellite anomaly risks
- Technical notes and other documentation of the present study

The address of the server is: http://www.geo.fmi.fi/spee

6.6.1. Links to space weather servers

There are hundreds of space weather-related WWW-servers world-wide. The focus of this server is on operational pages, i.e., modelling and forecasting aspects are underlined. Concerning "purely" scientific servers on ionospheric and magnetospheric physics, we have focused emphasis on European sites, which are also described in more detail within the server itself. The level of space weather pages varies significantly. Some sites provide exact and detailed information, while others are quite short. We have excluded links that contain only little relevant material, or which only reproduce information given on original servers.

The SPEE link lists cover the following topics:

- Case studies

  Most of the events selected here are contributed by several research teams. These presentations are mainly of quick-look type, i.e. contain data and some modelling results. Detailed (and refereed) results should still be read from traditional journals.

- Data

  These are pages with near real time data of the Sun, solar wind, magnetosphere, ionosphere, and geomagnetic field. Additionally, some links to large data ar-

chives of older data are included. There are also a huge number of smaller data collections of various projects available on WWW. They are not listed here, but they can be searched for by starting from the link collection page.

- Forecasts

  Space weather forecasts mainly concern with the geomagnetic activity of the next few days. Many of them also contain near real time data.

- General information

  A collection of servers providing space weather information on diverse levels mainly for professionals, but some educational servers are specially written for the large audience. Many of these sites are also included in other topic lists.

- Ground effects

  Some servers contain descriptions on space weather effects on ground technology (mainly power systems) or climate.

- Link collections

  These links points to servers containing extensive lists of solar-terrestrial information. This page is a starting point to find links that are not included on the SPEE server.

- Model development

  Most modelling work presented here deals with the magnetosphere without a direct aim to space weather forecasting. However, these are necessary models for understanding basic physics. Many of them could be developed or already are useful for forecasting or post-analysis too.

- Radio propagation

  A number of links are available which are specifically tailored for radio amateurs. Information is based on solar-terrestrial data obtained from data servers.

- Software

  Some space weather related programs or program packages are described on WWW. So far, interactive use is quite limited.

- Spacecraft environment

  These pages deal mostly with spacecraft charging.

For a convenient access to near real time solar-terrestrial quick-look data plots and forecasts, there are two separate shortcut link collections. Additionally, there is a simple form for key word searches from an ASCII list of space weather servers.

6.6.2. Spacecraft charging databases

The server contains the data base analysed under the present project and discussed further in Chapter 4 above.

6.6.3. Technical remarks

The structure of the server has been kept simple to allow for a convenient and fast use by all widely known browsers. HTML files are compatible with the 3.0 version.

The link list pages are created by a Perl script reading as input an ASCII file, which lists space weather servers and associated key words in a simple format. This allows for an easy and flexible maintenance of the server list. The same ASCII file is used by the search tool, also written in Perl. Access to the internal pages has been restricted by the standard method of .htaccess files.

The space weather WWW servers are as uncontrolled as anything in the WWW. New relevant pages appear regularly, others change their URL, and some of the pages are left there although their content becomes obsolete. Thus there is need for continuous updating of the pages. This requires a regular checking of links (e.g. once a month), as well as active searching for new sites.

6.7. Assessment of specific European capabilities for space weather activities

It is not straightforward to give a full picture of European capabilities in the field of space weather. The meaning of the very concept of space weather is still rather unclear and different interest groups use it differently to seek support to their own activities. Most of the space weather modelling discussed above has started before the whole term was coined. The spacecraft engineers may prefer to talk about space environment modelling and there has been some reluctance to accept the American term by the European STP community as well. During the present project the meaning of space weather was brought up in several discussions and a small questionnaire was sent to some key European players. We briefly summarise here the main results of this questionnaire.

6.7.1. Relationship between space weather and STP science.

While some of the proponent of the US NSWP have voiced an opinion that STP and space weather are (nearly) the same thing, in Europe the claim that there is, or should be, a distinction between STP and space weather seems to be more popular: STP is basic research, the results of which may be converted to space weather products and services whereas space weather is more application-oriented concept which can stimulate and challenge STP but should not direct the STP research. It is important to realise that development in space weather monitoring and prediction capabilities must be driven by users, not by the model developers. It is not possible to develop successful products by creating artificial needs. For example spacecraft constructors want solutions to their immediate problems, not ten-year research programme. Thus it is essential to have a vital basic STP research living in harmony with the application-oriented space weather

6.7.2. Volume of European space weather activities.

The European resources are scattered. ESTEC possesses considerable experience with various aspects of space environment modelling. The recent contract studies in space environment modelling (TREND-1, -2, -3, SPENVIS, SPEE, SEDAT) have been successful in fostering further contacts between groups having relevant competence. Of active groups we can mention RAL, MSSL, AEA Culham, and DERA in the UK, CERT-ONERA in France, IASB in Belgium, NDRE in Norway, IRF (Kiruna, Uppsala, Lund) in Sweden and FMI in Finland.

6.7.3. Strengths and weaknesses in Europe.

There seems to be wide consensus that the European STP science is on a very high level. With SOHO ESA has gained a leadership in one of the key areas of space weather, the Sun.

When it comes to weaknesses in Europe it is useful to compare with the US space weather community. First, the European resources are scattered and there is no clear structure on which to base co-operation. Second, in Europe there is much less cross-fertilisation between the science and application communities than there is in the US. This lack of communication is a particularly serious problem in the field such as space weather where the problems deal with complicated and very expensive technological systems whereas the origin of the problems is in very complicated physics.

6.7.4. Awareness of products

Understanding of a space weather product varies from the science community to the spacecraft engineers. While the science community often sees the models as products they can provide to the applications community, the user of space weather may be interested in the output of the models only. This also reflects the missing dialogue between science and engineering mentioned above.

For the product development the question, who are the users, is a problem. In order to develop products their users should be identified and in order to find users there should be products to offer to them.

6.7.5. Engineering solutions vs. forecasting

It has been asked whether space weather activities should lead to engineering solutions to get rid of the problems once for all, or should we go toward ordinary weather service-type of activity with forecasting and warning. The most reasonable answer is that both are needed. The immediate engineering solutions are necessary but solving the space weather-related problems totally by mission design may become too expensive. There are also hazards that cannot be avoided by engineering, e.g., launch conditions, re-entry to the atmosphere, EVA.

The STP community sees the forecasting development perhaps more challenging than provision of average radiation doses based on long-term statistics to the spacecraft engineers. Also the spacecraft operators would like to know when they should avoid complicated manoeuvres of their spacecraft, especially when the spacecraft become old and more susceptible for anomalies. In the middle between design analysis and forecasting is the specification (nowcasting) which is particularly helpful when something has happened and it is important to know why. As a conclusion there is a continuous need to develop better models for spacecraft engineers but also the forecasting and warning need to be improved.

6.7.6. European autonomy

One of the main motivation for founding of ESA was the establishment of autonomous European space programme. This is an important overall political goal but the degree of autonomy may still vary in various fields of space activities. Concerning the autonomy in space weather the European opinions on autonomy vary from the request for full autonomy to comments that there is no more such a thing as European autonomy. It is clear that space weather is something very global and, for example, proper monitoring of space weather cannot be done by Europeans alone. The strongest space weather activity is in the US and the NSWP will further strengthen their position. Good co-operation with the Americans is probably the most reasonable way to proceed. However, without strong own activity Europe cannot be a credible collaborator.

6.7.7. How Europe should organise the space weather activity?

To this question all kinds of answers are given, extending from "do nothing" to "establish a full-scale European space weather centre". Three alternative levels of engagements are discussed in section 6.8.2. below.

6.7.8. Where to put the European efforts?

Also here the opinions vary much and reflect the background of each individual. Those who work with data bases, see them as the most urgent task, models are the most precious to the modellers. It is clear that engineers need engineering models whereas forecasters need simulation models and input data. A balanced programme should respond to all these interests.

6.7.9. Where are the future markets?

Perhaps the greatest surprise of our investigation of European opinions was that the manned space flight was expected to be the most important market of space weather products in future. This is understandable in the sense that if an astronaut will be killed or seriously harmed by a space weather event, this will get much stronger media re-

sponse than the loss of Telstar 401 in 1997. However, it is likely that for long time to come the most active users will be the spacecraft engineers and spacecraft operators, including the launch and re-entry operations.

6.8. Recommendations for rationalised development of space weather activity in Europe

This item should probably be analysed starting from the question what to do. However, we live in Europe where interests and resources are scattered, and the question who should take the lead to formulate a rationalised approach to space weather becomes urgent. This actually happened also in the US where the formulation of the NSWP took first several years of inter-agency negotiations and politicking before the coherent strategy was possible to formulate.

6.8.1. Who should take the lead?

When asking this question we have received three main answers: ESA, EU, and a consortium of national institutions. We have also been asked the reverse: Do we have to engage to this at all, would it be enough that we co-operate with Americans? This is of course a legitimate question, but irrelevant to the goals of this study.

A fact is that the European Union is not very active in practical space activities. It is very difficult to see how EU could take the lead in this rapidly growing and very up-to-date area. EU can support, e.g., networks of national groups in space weather-related research. This actually is a recommendable route to take for groups seeking funding in space weather research.

The national institutions interested in space weather form, in any case, the basis of any European space weather activity. None of them, nor any ESA country alone, is expected to be able to support an independent full-scale space weather activity. More limited, localised space weather centres are, on the other hand, quite possible, and would be very valuable as parts of an international space weather system. There are embryos of such, e.g., the Solar-Terrestrial Laboratory of the Swedish Institute of Space Physics in Lund and the ISES Regional Warning Centres, of which the Western Europe RWC is located in Meudon. Furthermore, groups such as MSSL, BIRA/IASB, DERA, ONERA-CERT, IRF, FMI, TOS-EMA, and many others, already have activities which could contribute significantly to a European space weather network.

However, as one respondent to our questionnaire answered: Europeans have difficulties to agree upon anything. Thus it may well be that the only way of organising a rationalised European space weather activity is to have an authoritative organisation to supervise the development. For this we have ESA and space weather can be argued to be a classic example of Agency responsibility. At present ESA's engagement in space weather is in the technological front. They have good expertise on the design of spacecraft and space environment effects (SEE). TOS-EMA at ESTEC has resources for in-

ternal activities and controls some amount of funds within TRP for limited studies, such as this particular contract, TREND, SPENVIS, or SEDAT. The present space weather funding is a negligible part of the total annual R&D budget of ESA (• 40 MECU).

To speed up the process of creating an European space weather agenda the STP community can be very helpful. In the US the NSWP was very much a response to the pressure from the science community and it seems that this pressure is increasing in Europe as well. Note, however, that in the US space sciences and engineering have a tradition of cross-fertilisation which is much weaker in Europe, and furthermore, the military sector is much more active in the US. In Europe a particularly authoritative body is the ESA Science Programme. We thus recommend that:

1. ESA Science Programme should take space weather on its agenda.

2. Form a formal Science/Technology Interdisciplinary Space Weather Programme that reports to SPC/SSWG and IPC.

At the beginning this does not require large funds and could be realised, e.g., by some increase of TRP funding and matching the activity with Science Programme. The scientific supervision could be defined as a part of the SSWG, or a small ad-hoc working group could be formed to define the ESA Space Weather activities. This group should involve the present expertise at ESTEC and the future activities should be closely coordinated with the more technologically oriented projects of ESTEC. It is of crucial importance, however, that ESA will make a long-term commitment to its involvement in space weather.

6.8.2. Possible level of concerted European approach

We also suggest that three different levels of European space weather activity should be carefully considered.

1) European Data and Model Centre (EDMC)
2) European Data, Model, and Specification Centre (EDMSC)
3) European Space Weather Centre (ESWC)

For simplicity, we call these units here “Centres” although the final solution may be a decentralised structure.

This is a hierarchical sequence: Levels 2) and 3) cannot do without having data and models, and if a centre is able to forecast, it can provide environment specifications and nowcasting as well. Thus the rapid flow of reliable data is basis of everything. At present this is the worst bottle-neck.

1) European Data and Model Centre (EDMC)

The mission of EDMC should be twofold. It should create links to all relevant data for space weather services and be able to provide up-to-date data services to engineers, op-

erators, and scientists. It should also collect available models and have sufficient expertise to work for conversion of these models toward operational applications, resembling the "rapid prototyping" of NOAA/SEC. It is likely that models having significant operational capability will be protected by patents. A natural task for the EDMC would be to take care of the necessary agreements concerning the user rights and in this way also guard the interests of the patent holders.

This operation could be started with a staff of 10-20 persons equally divided between data and model specialists. For evaluation of the models sufficient scientific expertise is necessary.

The centre would not need to be centralised. It needs a head-quarter but it could be distributed provided that the nodes of a distributed system are strong enough for efficient operation. Both centralised and distributed systems have their advantages and problems. A distributed system could more easily get local support and the whole system could be more extensive. On the other hand, this approach requires binding commitments from all parties to guarantee efficient communication and most likely increased interface costs. A recommendable compromise would be a central EDMC with local affiliations responsible for products within their local expertise. This solution would probably provide the best outcome for least initial cost to the organisation(s) supporting EDMC.

It should be noted that TOS-EMA already now has activities toward this direction through some of their own activities and contracts such as TREND, SPENVIS, and SPEE.

2) European Data, Model, and Specification Centre (EDMSC)

This centre should do everything EDMC would and, in addition, provide post-analysis and nowcasting services to customers. EDMSC needs everything there is in an EDMC and scientific and technical staff for analysis and nowcasting. Here a centralised core where the most critical work is performed is likely to be the most efficient solution. Also the staff must be sufficient, at least 20-30 persons.

3) European Space Weather Centre (ESWC)

This would be a logical third stage based on items 1) and 2) above. It may not be a realistic near-time goal in Europe and will require a thorough market and cost-benefit analysis. Even without such analysis it looks reasonable that it should be realised in close collaboration with other organisations, particularly NOAA/SEC and ISES. In addition to approach 2) the ESWC needs 24-hour operations, fast communication lines, and extensive supercomputer resources. A minimum staff of 50 persons is required.

Our third recommendation is that:

3. ESA should initiate work to establish a European Space Weather Data and Model Centre (either centralised or distributed with a central core). This Centre should have as its goal to become a European Data, Model, and Specification Centre, and it should look for a workable solution for a full-scale European Space Weather Centre.

6.9. Suggestions for space weather studies making use of European S/C data

At the end of this report we list here a number of suggestions where ESA could and should be active without necessarily having to invest large funds.

1. Use of SOHO in studies of the origins of space weather on the Sun is strongly encouraged. This applies particularly to instruments observing the solar disc and the corona. Especially, development of models to forecast the CMEs and SEPEs should have a high priority.
2. A concrete study to be initiated is investigation how to determine whether a CME will be geoeffective and lead to specific hazardous conditions, or not.
3. Establish a space weather interdisciplinary position in the SOHO team.
4. Space weather issues should be introduced to the agenda of the Cluster mission. While Cluster will not provide direct observations of particles harming spacecraft, it is expected to make significant contributions to the understanding of energy and mass transfer from the solar wind to the magnetosphere. Also here either an interdisciplinary scientist or working group should be established.
5. A goal to include radiation environment monitors (REM, or more advanced devices) in nearly all European spacecraft, commercial and scientific alike, should be pursued.
6. Data from the radiation environment monitors developed at ESTEC must be efficiently exploited.
7. Attempts to make more satellite anomaly data available for studies should be made.
8. Make maximum use of the ISTP programme period to understand satellite anomalies and charging events.

Furthermore, in future ESA should seek means for helping to secure continuous solar wind monitoring in the future. The STP fraction of the SSWG has tried to persuade this, e.g., in the context of medium scale missions. However, this kind of routine monitoring missions cannot in practise compete with more glorious missions being proposed.

7. CONCLUSIONS

Need to understand space environment effects has existed since the first space flights some 40 years ago and even longer if we include the effects on the ground. These 40 years have contributed a wealth of knowledge on the space environment effects and we have learned much how the harmful consequences can be avoided, or at least minimised. However, the space environment remains hazardous. The society is more and more dependent on space technology, the human presence in space is expected to increase, and at the same time there is a tendency toward smaller and more vulnerable electronic components. All these facts underline the need for intensified efforts toward better understanding of the space environment and its effects on technological systems, and toward better warning and forecasting methods.

During last few years the new concept of Space Weather has entered into the scene of space environmental effects and solar-terrestrial physics. While the concept can be argued to be just a new package of old goods, it has had a positive influence making more people aware of the unifying views of the different disciplines. For example, in Europe the communication between the space science community and spacecraft engineering and operations has not been very good. Under the realm of space weather we have a new forum for science and applications communities to meet each other. Space weather is an application-oriented discipline which, at the same time, provides great intellectual challenges to the scientists. On the other hand, the future space weather products need significant scientific expertise to be developed, especially when we come to the question of real forecasting of space weather conditions.

The project summarised in this document was conducted by scientists having expertise in solar-terrestrial physics, spacecraft charging, neural networks, modelling, simulations, etc. However, we certainly hope that the results of this project are useful also for the applications community.

7.1. Charging of Freja

The basic principles of spacecraft charging are well-known but the actual occurrence and severeness of charging events are not known in detail. In this particular study the low-altitude charging events were investigated using the data base of the Freja satellite. While the spacecraft was successfully designed to be electromagnetically clean and highly conductive, it, nevertheless, experienced charging when it crossed a region of intense auroral electron precipitation. To become charged the spacecraft required very low ambient plasma density of 2×10^9 m^{-3} which was about five times smaller than the corresponding threshold for the DMSP satellite. But when the spacecraft became charged, it sometimes reached very large negative potentials, more than –2000 V, under the most intense electron precipitation in the 10-keV energy range. Most, but not all, charging events took place in eclipse and all charging events took place during winter

months. From the observed data it can be considered as proven that the auroral electrons of several keV energies are a source of concern for polar orbiting spacecraft.

Several of the Freja charging events were modelled using the POLAR charging code. Even after a very careful modelling of the spacecraft shape and surface materials as well as the observed electron spectra it was impossible to reach the observed charging levels, especially the highest charging levels showed to be beyond the capability of the model to reproduce. Nevertheless, this study gives useful hints for further development of the POLAR code. It must be noted that POLAR was originally designed for studies of the DMSP series satellites in a lower orbit (about 800 km) and, consequently, higher ambient plasma density.

7.2. Satellite anomaly forecasting

The satellite anomalies on GEO were analysed using anomaly data bases from the European meteorological satellite Meteosat-3 and the Swedish telecommunication satellite Tele-X.

Meteosat-3 carried an instrument for local observations of electrons in the range 43–300 keV. These observations were used to study how well neural networks could be trained to predict observed satellite anomalies. After treating the particle data with principal component analysis the networks were found to train well. Requesting that non-existence of anomalies during next 24 hours had to be predicted at least at 80% accuracy about 50% of anomalies were possible to predict based on the local input data.

Tele-X, as most GEO satellites, did not carry instruments to study the local space weather conditions. Both Meteosat-3 and Tele-X anomalies were studied using non-local data including energetic particles (E > 2 MeV) from geostationary GOES-6, GOES-7, and GOES-8 spacecraft and ground-based magnetic activity indices Kp and Dst. In this study several variations of neural networks were tested. It was found that the best predictions were obtained using the Kp index, the best predictions for Meteosat reaching about 80% for both anomalies and non-anomalies. The Dst showed to be a less successful predictor. The non-local electron data was not found as useful, especially due to its less accuracy to predict non-anomalies.

Both local and non-local input data were combined in a study to search for a satellite anomaly index. It was found that by combining the non-local and local observations reasonably good anomaly indices can be constructed. However, the index used by satellite operators could be adjusted for each satellite individually, reflecting the fact that anomalies of each spacecraft are caused by a particular combination of environmental characteristics, which can be highly hardware dependent. In addition to local measurements of high-energy electrons, simple lower-energy detectors in the 0–10-keV range are required.

7.3. Space weather modelling

The European solar-terrestrial physics community has strong scientific competence in the fields relevant to space weather modelling and forecasting. On the technological side Europe has good expertise in modelling of the effects of space environment. However, the cross-fertilisation between scientists and engineers is much weaker in Europe than in the US.

In the field of space weather modelling Europe has already established impressive activities in the modelling of energetic particles and their effects in the ring current and radiation belt regions of the inner magnetosphere. Also in the field of applying modern analysis methods, such as neural networks, Europeans are at high international level. Furthermore, the Solar and Heliospheric observatory (SOHO) provides good possibilities for European scientists to take a leading position in the studies of the solar origins of space weather. Joining the European expertise in global magnetospheric dynamics, it is quite feasible that competitive global magnetohydro-dynamics (MHD)-based modelling activity could be initiated in Europe.

A specific weakness in Europe is that the resources are scattered and it is unlikely that any single group or country could form a significant independent space weather activity. It is suggested that the ESA Science Programme should take space weather on its agenda, a formal Science/Technology Interdisciplinary Space Weather Programme which should report to SPC/SSWG and IPC should be initiated, and ESA should initiate work to establish a European Space Weather Data and Model Centre (either centralised or distributed with a central core). This Centre should have as its goal to become a European Data, Model, and Specification Centre, and it should look for a workable solution for a full-scale European Space Weather Centre.

7.4. WWW space weather server

The World Wide Web provides an excellent tool to gather up-to-date information. The web is, however, an uncontrolled organism where the information is continuously updated and it requires some expertise to find the most relevant information sources. The WWW server developed in this project is designed to help in this process. We recommend that the readers use this tool in their studies of space weather its interaction with spacecraft. Once more, the address of the server is:

http://www.geo.fmi.fi/spee

This server contains the public documentation summarised in this report and useful links to space weather servers all over the world.

8. REFERENCES

Al´pert, Ya. L., Gurevich, A. V., and Pitaevskii, L. P., *Space physics with artificial satellites.* Consultants Bureau, Washington D.C., 1965.

Al´pert, Ya. L., *The near-Earth and interplanetary plasma, volume 2: Plasma flow, plasma waves and oscillations.* Cambridge University Press, Cambridge 1983.

Anderson, P. C., and H. C. Koons, Spacecraft charging on a low-altitude spacecraft in an aurora, J. of Spacecraft and rockets, 33, 734, 1996.

André, Mats (editor): *The Freja Scientific Satellite*. IRF Scientific Report 214, Swedish Institute of Space Physics, Kiruna 1993.

Anselmo, J.C., Solar storm eyed as a satellite killer. Aviation week and Space Technology, January 27, 1997.

Baker, D. N., Solar wind - magnetosphere drivers of space weather, J. Atmos. Terr. Phys., 58, 1509, 1996.

Baker, D.N., J.H. Allen, R.D. Belian, J.B. Blake, S.G. Kanekal, B. Klecker, R.P. Lepping, X. Li, R.A. Mewaldt, K. Ogilvie, T. Onsager, G.D. Reeves, G. Rostoker, R.B. Sheldon, H.J. Singer, H.E. Spence and N. Turner, An assessment of space environmental conditions during the recent Anik E1 spacecraft operation failure, ISTP Newsletter, Vol 6, No. 2. June 1996.

Bartels, J., The standardized index, Ks, and the planetary index. Kp, IATME Bull. 12b, 97, IUGG Pub. Office, Paris, 1949.

Baumjohann, W., The near-Earth plasma sheet: An AMPTE/IRM perspective, Space Sci. Rev., 64, 141-163, 1993.

Beutier, T., D. Boscher, and M. France, Salammbô: A three-dimensional simulation of the proton radiation belt, J. Geophys. Res., 100, 17181, 1995.

Blake J. B., D. N. Baker, N. Turner, K. W. Ogilvie, and R. P. Lepping, Correlation of changes in the outer-zone relativistic electron population with upstream solar wind and magnetic field measurements, Geophys. Res. Lett., 24, 927–929, 1997.

Boehm, M., G. Paschmann, J. Clemmons, H. Höfner, R. Frenzel, M. Ertl, G. Haerendel, P. Hill, H. Lauche, L. Eliasson and R. Lundin, The TESP electron spectrometer and correlator (F7) on Freja. *Space Sci. Rev., 70,* 509-540, 1994.

Bogorad A., C. Bowman, A. Dennis, J. Beck, D. Lang, R. Herschitz, M. Buehler, B. Blaes, and D. Martin, Integrated environmental monitoring system for spacecraft, JPL Technical Report. (http://www.jpl.nasa.gov/techreport/1995/95-0846.rfr.html)

Bourdarie, S., D. Boscher, T. Beutier, J.-A. Sauvaud, and M. Blanc, Magnetic storm modeling in the Earth's electron belt by the Salammbô code, J. Geophys. Res., 101, 27171–27176, 1996.

Bourdarie, S., D. Boscher, T. Beutier, J.-A. Sauvaud, and M. Blanc, Electron and proton radiation belt dynamical simulations during storm periods: A new asymmetric convection-diffusion model, J. Geophys. Res., 102, 17541–17552, 1997.

Bourdarie, S., D. Boscher, and A. Vacaresse, A radiation belt model based on convection-diffusion theory including a time dependent magnetic field, Ann. Geophys., 16, Supplement III, C852, 1998.

Bühler P., S. Ljungfelt, A. Mchedlishvili, N. Schlumpf, A. Zehnder, L. Adams, E. Daly, and R. Nickson, REM, first year in space, 1994. (http://www1.psi.ch/www_lap_hn/ASTR_REM_JB94.HTML)

Bühler P., L. Desorger, A. Zehnder, L. Adams, and E. Daly, Monitoring of the radiation belts with the raditation environment monitor REM, Radiation Belts: Models and Standards. Geophysical Monographs 97, Amearican Geophysical Union, 1996a.

Bühler P., A. Zehnder, L. Desorgher, W. Hajdas, E. Daly, and L. Adams, Simple instruments for continuous measurements of trapped particles, in Proceedings from "Environment Modelling for Space-based Applications", ESTEC, Noordwijk, NL, 18-20 September 1996b.

Bühler P., A. Zehnder, L. Desorgher, W. Hajdas, E. Daly, and L. Adams, Measurements of the radiation belts from MIR and STRV 1994–1997 http://www.estec.esa.nl/wmwww/wma/jan97/ieee97.html

Bühler P., A. Zehnder, L. Desorgher, W. Hajdas, E. Daly, Observations of radiation-belt energetic electrons with REM, 1998. http://www.estec.esa.nl/wmwww/wma/rem/sctc98/index.htm

Carlson, M., The Langmuir probes on Freja, IRF Uppsala internal report, 1994.

Carpenter, D.L., and R.R. Anderson, An ISEE/whistler model of equatorial electron density in the magnetosphere, J. Geophys. Res., 97, 1097, 1992.

Coates, A.J. , A.D. Johnstone, D.J. Rodgers, and G.L. Wrenn, Quest for the source of Meteosat anomalies, Proc. Spacecraft Charging Technology Conference 1989, Naval Postgraduate School, 120-146, 1991.

Cooke, D. L., M. Tautz, and J. Lilley, Polar code simulation of DMSP satellite auroral charging, paper presented at the AiAA meeting, Reno, Nevada, January 11, 1989.

Crooker, N., J.-A. Joselyn, and J. Feynman (editors), Coronal Mass Ejections, Geophysical Monograph 99, American Geophysical Union, Washington, DC, 1997.

Daly, E. J., F. van Leeuwen, H. D. R. Evans, and M. A. C. Perryman, Radiation belt transient solar-magnetosphere effects on Hipparcos radiation background, IEEE Tans. Nuc. Sci., NS41, 1994.

Daly, E., REM, 1998, http://www.estec.esa.nl/wmwww/wma/rem/

Danilov, V., G. Drolshagen, V. M. Dvoryashin, A. M. Kramarenko, P. Pita Leira, V. S. Sokolov, and Yu. V. Vasilyev, Numerical simulation of high-voltage charging at high altitudes: comaprison of NASCAP and ECO-M, Presentation at *The 6th Spacecraft Charging conference,* US Air Force Research Laboratory, Nov. 2-6, 1998.

Davidson, W. F., The magnetic storm of March 24, 1940 – Effects in the power system, Edison Electric Institute Bulletin, July, 1940, p. 365.

DeForest, S. E., Spacecraft charging at synchronous orbit, J. Geophys. Res., 77, 651, 1972.

Eliasson, L., O. Norberg, R. Lundin, K. Lundin, S. Olsen, H. Borg, M. André, H. Koskinen, P. Riihelä, M. Boehm and B. Whalen, The Freja hot plasma experiment - instrument and first results.*Space Sci. Rev., 70,* 563-576, 1994.

Feynman, J., G. Spitale, J. Wang, and S. B. Gabriel, J. Geophys. Res., 98, 13281-13294, 1993.

Fontheim, E. G., K. Stasiewicz, M. O. Chandler, R. S. B Ong and T. Gombosi, Statistical study of precipitating electrons, *J. Geophys. Res., 87,* 3469-3480, 1982.

Frederickson, A.R. Radiation induced dielectric charging, in “Space Systems and their interactions with the Earth's space environment,“ Eds. Garett and Pile, Vol 71, 386-412, AIAA, Washington DC, 1980.

Freeman, J., R. Wolf, R. Spiro, B. Hausman, B. Bales, D. Brown, K. Costello, R. Hilmer, R. Lambour, A. Nagai, and J. Bishop, The Magnetospheric Specification and Forecast Model (updated Oct. 1995). (Retrievable from: http://rigel.rice.edu/~ding/msfm95/msfm.html)

Freja magnetic field experiment team, Magnetic field experiment on the Freja satellite. *Space Sci. Rev., 70,* 465-482, 1994.

Frezet, M., E.J. Daly, J.P. Granger and J. Hamelin, Assessment of electrostatic charging of satellites in the geostationary enevironment. ESA Journal Vol 13, 89-116, 1989.

Frooninckx, T. B., and J. J. Sojka, Solar Cycle Dependence of Spacecraft Charging in Low Earth Orbit, J. Geophys. Res., 97, 2985, 1992.

Gabriel, S. B., J. Feynman, and G. Spitale, Solar energetic particle events: Statistical modelling and prediction, in Environmental Modelling for Space-based Applications, ESA SP-392, pp. 59–64, 1996.

Garrett, H. B., The Charging of Spacecraft Surfaces, Rev. Geophys. Space Phys., 19, 577, 1981.

Garret, H. B., and A. C. Whittesley, Spacecraft charging, an update, AIAA 96-0143, American Institute of Aeronautics and Astronautics, Washington, 1996.

Goddard Space Flight Center, Orbital anomalies in Goddard spacecraft for CY 1993, System reliability and safety office, code 302, Greenbelt MD 20771, 1994. (http://arioch.gsfc.nasa.gov/302/oags.htm)

Goka T., H. Matsumoto, T. Fukuda, and S. Takagi, Space environment and effect measurements from ETS-VI satellite, in Proceedings from "Environment Modelling for Space-based Applications," ESTEC, Noordwijk, NL, pp. 18-20, 1996a.

Goka T., H. Matsumoto, T. Fukuda, and S. Takagi, Measurements of radiation belt particles with ETS-6 onboard dosimeter, in Radiation Belts: Models and Standards, Geophysical Monograph, 97, eds. Lemaire, Heyndericksm and Baker, AGU, pp. 251–254, 1996b.

Gosling, J. T., The solar flare myth, J. Geophys. Res., 98, 18937, 1993.

Gosling, J. T., Coronal mass ejections: An overview, in Coronal Mass Ejections, AGU monograph, 99, N. Crooker, J. A. Joselyn, J. Feynman (eds.), pp. 9-16, 1997.

Grystad, D., Meteosat operational anomalies correlation with the space environment, Design project report ESTEC, 1997.

Gussenhoven, M. S., D. A. Hardy, F. Rich, and W. J. Burke, and H.-C. Yeh, High-Level Spacecraft Charging in the Low-Altitude Polar Auroral Environment, J. Geophys. Res. 90, 11009, 1985.

Gussenhoven, M. S., E. G. Mullen, and D. H. Brautigam, Phillips Laboratory Space Physics Division radiation models, in Radiation Belts Models and Standards, edited by J. F. Lemaire, D. Heynderickx, and D. N. Baker, Geophysical Monograph 97, AGU, Washington, DC, 1996, p. 93.

Hastings, D. E., A review of plasma interactions with spacecraft in low Earth orbit, J. Geophys. Res., 100, 14457, 1995.

Hastings, D, and H. Garret, Spacecraft-environment interactions, Cambridge University press, Cambridge, 1996.

Heppner, J. P., and N. C. Maynard, Empirical high-latitude electric field models, J. Geophys. Res., 92, 4467-4489, 1987.

Hilmer, R. V., and G.-H. Voigt, A magnetospheric magnetic field model with flexible internal current systems driven by independent physical parameters, J. Geophys. Res., 100, 5613, 1995.

Hoge, D., and D. Leverington, Investigation of electrostatic discharge phenomena on the Meteosat spacecraft, ESA Journal Vol. 3, 101-113, 1979.

Hoge, D.G., Meteosat spacecraft charging investigation, ESA N82-14265, 1980.

Hoge, D.G., Results of Meteosat-F2 spacecraft charging monitors. in Proceedings of an International Symposium on Spacecraft Materials in space, ESA SP-178, 1982.

Holback, B., S.-E. Jansson, L. Åhlén, G. Lundgren, L. Lyngdal, S. Powell, and A. Meyer, The Freja wave and plasma density experiment. *Space Sci. Rev.*, *70*, 577-592, 1994.

Hudson, M.K., S.R. Elkington, J.G. Lyon, V.A. Marchenko, I. Roth, M. Temerin, J.B. Blake, M.S. Gussenhoven, and J.R. Wygant, Simulation of radiation belt formation during storm sudden commencements, J. Geophys. Res., 102, 14087-14102, 1997.

James, B. F., O. W. Norton, and M. B. Alexander, The natural space environment: Effects on spacecraft, NASA Ref. Pub. 1350, 2, 1994.

Janhunen, P., GUMICS-3 – A global ionosphere-magentosphere coupling simulation with high ionospheric resolution, in Environmental Modelling for Space-based Applications, ESA SP-392, pp. 233–239, 1996.

Kalweit, C., Review of the status of spacecraft-charging studies, ESA Journal, Vol 5, 75, 1981.

Katz, I., G. A. Jongeward, V. A. Davis, M. J. Mandell, R. A. Kuharski, J. R. Lilley, Jr., W. J. Raitt, D. L. Cooke, R. B. Torbert, G. Larson and D. Rau, Structure of the bipolar plasma sheath generated by SPEAR-1, *J. Geophys. Res.*, 94, 1450-1458, 1989.

Klecker, B., Energetic particle environment in near-Earth orbit, Adv. Space Res., 17, (2)37-(2)45, 1996.

Krupnikov, K. K., V. N. Mileev, L. S. Novikov, and g. v. Babkin, Mathematical modelling of high altitude spacecraft charging, In *Proceedings of the International Conference on Problems of Spacecraft / Environment Interactions,* Edited by G. Drolshagen, 167–175, Novosibirskm Russia, 1992.

Kumar, P., and E. Foufoula-Georgiou, Wavelet analysis for geophysical applications. Rev. of Geophys., 35, 385-412, 1997.

Laframboise, J. G., Calculation of Escape Currents of Electrons Emitted from Negatively Charged Spacecraft Surfaces in a Magnetic Field, J. Geophys. Res., 93, 1933, 1988.

Lambour, R. L., L. A. Weiss, R. C. Elphic, and M. F. Thomsen, Global modeling of the plasmasphere following storm sudden commencements, J. Geophys. Res., 102, 24351–24368, 1997.

Lanzerotti, L.J., C. Berglia, D.W. Maurer, G.K. Johnson III, and C.G. Maclennan, Studies of spacecraft charging on a geosynchronous telecommunications satellite, in Proceeding of the 1996 COSPAR conference.

Lauriente, M., and Vampola, A. L., Spacecraft anomalies due to radiation environment in space NASDA/JAERI 2nd International Workshop on Radiation Effects of Semiconductor Devices for Space Applications, March 21, 1996, Tokyo, Japan (http://envnet.gsfc.nasa.gov/Papers/Reno98.html)

Leach, R. D., and M. B. Alexander, Failures and anomalies attributed to spacecraft charging, NASA Reference Publication 1375, 1995.

Lemaire, J., A. D. Johnstone, D. Heynderickx, D. J. Rodgers, S. Szita, and V. Pierrard, Trapped Radiation Environment Model Development, TREND-2 Final Report, Aeronomica Acta, Institut d'Aeronomie Spatiale de Belgique, Bruxelles, 1995.

Leung, P., A. C. Whittlesey, H. B. Garret, and P. A. Robinson Jr., Environment-induced electrostatic discharges as the cause of Voyager 1 power-on resets, J. Spacecraft, 23, 3, 1986.

Lilley, John R., David L. Cooke, Gary A. Jongeward and Ira Katz, *POLAR User's Manual*. Technical report GL-TR-89-0307, Geophysics Laboratory, Air Force Systems Command, Hanscom AFB, Mass. 1989.

Linker, J. A., and Z. Mikic, Extending coronal models to Earth orbit, in Coronal Mass Ejections, AGU monograph, 99, N. Crooker, J. A. Joselyn, J. Feynman (eds.), pp. 269-277, 1997.

López Honrubia, F.J., and A. Hilgers, Some correlation techniques for environmentally induced anomalies analysis. J. Spacecraft and Rocket, 670-674, 1997.

Lu, G., B. A. Emery, A. S. Rodger, M. Lester, J. R. Taylor, D. S. Evans, J. M. Ruohoniemi, W. F. Denig, O. de la Beaujardiere, R. A. Frahm, J. D. Winningham, and D. L. Chenette, High-latitude ionospheric electrodynamics as determined by the

assimilative mapping of ionospheric electrodynamics procedure for the conjunctive SUNDIAL/ATLAS 1/GEM period of March 28-29, 1992, J. Geophys. Res., 101, 26697, 1996.

Luhmann, J., CMEs and Space Weather, in Coronal Mass Ejections, AGU monograph, 99, N. Crooker, J. A. Joselyn, J. Feynman (eds.), pp. 291-299, 1997.

Lundin, R., G. Haerendel, and S. Grahn, .Eds., The Freja Mission, Space Science Reviews, 70, Nos. 3-4, 405-602, 1994.

Lyons, L.R., R.M. Thorne, and C.F. Kennel, Pitch-angle diffusion of radiation belt electrons within the plasmasphere, J. Geophys. Res., 77, 3455, 1972.

Mandell, M. J., J. R. Lilley, Jr., and I. Katz, Computer modelling of current collection by the Charge-2 mother payload. In *Polar Code Validation*, technical report GL-TR-89-0276, US Air Force Geophysics Laboratory, 1989.

Mead, G. D., Deformation of the geomagnetic field by the solar wind, J. Geophys. Res., 69, 1181, 1964.

Medicus, G., Spherical Langmuir probe in drifting and accelerated Maxwellian distributions. *J. Appl. Phys., 33*, 3094-3100, 1962.

Mobarry, C. M., J. A. Fedder, and J. G. Lyon, Equatorial plasma convection from global simulations of the Earth's magnetosphere, J. Geophys. Res., 101, 7859, 1996.

Mott-Smith, H. M., and I. Langmuir, The theory of collectors in gaseous discharges, *Phys. Rev., 28*, 727-763, 1926.

Mullen, E. G., M. S. Gussenhoven, D. A. Hardy, T. A. Aggson, B. G. Ledley, and E. Whipple, SCATHA Survey of High-Level Spacecraft Charging in Sunlight, J. Geophys. Res., 91, 1474, 1986.

Northrop, T.G., The adiabatic motion of charged particles, John Wiley & Sons, New York, 1963.

NSWP: *The National Space Weather Program, Implementation Plan*, Office of Federal Coordinator for Meteorological Services and Supporting Research, FCM-P31-1997, Washington, D.C, January 1997.

Olsen, R. C., A Threshold Effect for Spacecraft Charging, J. Geophys. Res., 88, 493, 1983.

Ozkul A., F. Scali, D. Liu, and C. Bowman, Design and operational charecteristics of electrostatic charge measurement onboars Intelsat VIII & VIII-A communication satellites, Abstract ESA Symposium on Environmental Modeling for Space based Applications, 1996.
(http://www.estec.esa.nl/CONFANNOUN/96a09/Abstracts/abstract60)

Prescott, G. B., History, Theory, and Practice of the Electric Telegraph, Boston: Ticknor and Fields, 1860.

Pulkkinen, T. I., D. N. Baker, R. J. Pellinen, J. Büchner, H. E. J. Koskinen, R. E. Lopez, R. L. Dyson, and L. A. Frank, Particle scattering and current sheet stability in the geomagnetic tail during the substorm growth phase, J. Geophys. Res., 97, 19283–19297, 1992.

PUM, *Polar User´s Manual*, see Liley et al. (1989)

Purvis, C. K., The role of potential barrier formation in spacecraft charging. In *Spacecraft/Plasma Interactions*, ESA SP-198, 115-126, European Space Agency, 1983.

Raeder, J., J. Berchem, M. Ashour-Abdalla, L. A. Frank, W. R. Paterson, K. L. Ackerson, S. Kokubun, T. Yamamoto, and J. A. Slavin, Boundary layer formation in the magnetotail: Geotail observations and comparisons with a global MHD simulation, Geophys. Res. Lett., 24, 951–954, 1997.

Remez, J. W., and H. C. McLeod, Goddard Space Flight Center, Oribital anomalies in Goddard spacecraft for calender year 1995, NASA technical paper, 1996.

(http://arioch.gsfc.nasa.gov./302/oags.htm)
Rich, F. J., and N. C. Maynard, Consequences of using simple analytical functions for the high-latitude convection electric field, J. Geophys. Res., 94, 3687–3701, 1989.
Ridley, A. J., G. Lu, C. R. Clauer, and V. O. Papitashvili, A statistical study of the ionospheric convection response to changing interplanetary magnetic field conditions using the assimilative mapping of ionospheric electrodynamics technique, J. Geophys. Res., 103, 4023-4039, 1998.
Robinson, P., W. Lee, R. Aguero, and S. Gabriel, Anomalies due to single event usets, J. Spacecraft and Rockets, 31, Marc-April, 1994.
Rodgers, D.J., Correlation of METOSAT-3 anomalies with data from the spacecraft enviromnent monitor, Internal ESTEC working paper, no.1620, 1991
Rodgers, D.J., E.J. Daly, A.J., Coates, and A.D. Johnstone, Correltation of METOSAT-3 anomalies with data from the space environment monitor, J Spacecraft and Rockets, 1997
Roelof, E. C., Energetic neutral atom image of a storm-time ring current, Geophys. Res. Lett., 14, 652–655, 1987.
Roelof, E.C., D.G. Mitchell, and D.J. Williams, Energetic neutral atoms (E ~ 50 keV) from the ring current: IMP 7/8 and ISEE 1, J. Geophys. Res., 90, 10991 - 11008, 1985.
Rosen, A., Spacecraft charging by magnetospheric plasmas, American Institute of Aeronautics and Astronautics, Washington DC, 1976.
Ruohoniemi, J. M., and R. A. Greenwald, Statistical Patterns of high-latitude convection obtained from Goose Bay HF radar observations, J. Geophys. Res., 101, 21743-21763, 1996.
Selding, P. B., Matra puzzled over Spanish satellite failure, Space News, January, 1998.
Shaw, R. R., J. E. Nanevicz, and R. C. Adamo, Observations of electrical discharges caused by differential satellite charging, in *Spacecraft Charging by Magnetospheric Plasmas*, Prog. Astronaut. Aeronaut., ed. A. Rosen, AIAA Press, New York, 47, 61-76, 1976.
Sheldahl, *Thermal control material & metalized films: part number listing and general specifications.* Sheldahl corporation, Northfield, MN, 1985.
Shue, J.–H., J. K. Chao, H. C. Fu, C. T. Russell, P. Song, K. K. Khurana, and H. J. Singer, A new functional form to study the solar wind control of the magnetopause size and shape, J. Geophys. Res., 102, 9497–9511, 1997.
Slavin, J. A., and R. E. Holzer, Solar wind flow about terrestrial planets 1. Modeling bow shock position and shape, J. Geophys. Res., 86, 11401–11418, 1981.
Solar Physics, Vol 175, Part 2, 1997.
Spreiter, J. R., and S. S. Stahara, A new predictive model for determining solar wind-terrestrial planet interactions, J. Geophys. Res., 85, 6769–6777, 1980.
Stern, D., A model of the terrestrial electric field, Eos Trans. AGU, 55, 403, 1975.
Stevens, N. J., and M. R. Jones, Comparison of Auroral Charging Predictions to DMSP Data, AIAA 95-0370, 33rd Aerospace Sciences Meeting and Exhibit, January 9-12, 1995.
Sugiura, M., Hourly values of equatorial Dst for the IGY, Ann. Int. Geophys. Year, 35, 1964.
Svensson, Ulrika, *Simulation of Spacecraft Charging in the Aurora: A Case Study*. ESTEC Working Paper 1943, ESTEC, Noordwijk 1997.
Takalo, J., J. Timonen, and H. Koskinen, Properties of AE data and bicolored noise, J. Geophys. Res., 99, 13239–13249, 1994.
Thorne, R.M., E.J. Smith, R.K. Burton, and R.E. Holzer, Plasmaspheric hiss, J. Geophys. Res., 78, 1581, 1973.

Toivanen, P.K., Drift modelling of dynamical magnetospheric processes, *Geophysical Publications,* Finnish Meteorological Institute, Helsinki, Finland, 1995.

Toivanen, P.K., T.I. Pulkkinen, R.H.W. Friedel, G.D. Reeves, A. Korth, C. Mouikis, and H.E.J. Koskinen, Time-dependent modelling of particles and electromagnetic fields during the substorm growth phase: anisotropy of energetic electrons, J. Geophys. Res., In press, 1999.

Tribble, Alan C., *The Space Environment.* Princeton University Press, Princeton, N.J., 1995.

Tsyganenko, N.A., and A.V. Usmanov, Determination of the magnetospheric current system parameters and development of experimental geomagnetic field models based on data from IMP and HEOS satellites, Planet. Space Sci., 30, 985-998, 1982.

Tsyganenko, N.A., Global quantitative models of the geomagnetic field in the cislunar magnetosphere for different disturbance levels, Planet. Space Sci., 35, 1347-1358, 1987.

Tsyganenko, N.A., A magnetospheric magnetic field model with a warped tail current sheet, Planet. Space Sci., 37, 5-20, 1989.

Tsyganenko, N. A., Quantitative models of the magnetospheric magnetic field: Methods and results, Space Sci. Rev., 54, 75, 1990.

Tsyganenko, N. A., Modeling of the Earth's magnetospheric field confined within a realistic magnetopause, J. Geophys. Res., 100, 5599–5612, 1995.

Tsyganenko, N. A., An empirical model of the substorm current wedge, J. Geophys. Res., 102, 19935–19941, 1997.

Usui, H., H. Matsumoto, and Y. Omura, Plasma response to high potential satellite in electrodynamic tether system, J. Geophys. Res., 98, 1531–1544, 1993.

Vampola, A.L., Analysis of enviromentally induced spacecraft anomalies, J. Spacecraft and Rockets, Vol 31, March-April, 1994

Vassiliadis, D., A. J. Klimas, D. N. Baker, and D. A. Roberts, A description of the solar wind-magnetosphere coupling based on nonlinear filters, J. Geophys. Res., 100, 3495–3512, 1995.

Vette, J. L., The NASA/National Space Science Data Center Trapped Radiation Environment Model Program (1964-1991), NSSDC/WDC-A-R&S 91-29, 1991.

Violet, M. D., and A. R. Frederickson, Spacecraft anomalies on the CRRES satellite correlated with the environment and insulator samples, IEEE Tans. On Nuclear Science, 40 (6), 1512, 1993.

Volland, H., A semiempirical model of large-scale magnetospheric electric fields, J. Geophys. Res., 78, 171–180, 1973.

Vuilleumier P., Standard radiation environment monitor (SREM) requirements specification, ESA Ref.: SREM/RS/002 Issue 8, 1997.

Walker, R. J., T. Ogino, J. Raeder, and M. Ashour-Abdalla, A global magnetohydrodynamic simulation of the magnetosphere when the interplanetary magnetic field is southward: The onset of magnetotail reconnection, J. Geophys. Res., 98, 17235, 1993.

Walker, R. J., and M. Ashour-Abdalla, The magnetosphere in the machine: Large-scale theoretical models of the magnetosphere, in: US National Report 1991--1994, Contributions in Space Sciences, AGU, Washington, D.C., p. 639, 1995.

Wang, Y.-M., and N. R. Sheeley, Jr., On potential field models of the solar corona, Astrophys. J., 392, 310–319, 1992.

Walter, B. T., Goddard Space Flight Center, Orbital anomalies in Goddard spacecraft for calender year 1994, NASA technical paper 3636, 1995. (http://arioch.gsfc.nasa.gov/302/oags.htm)

Wilkinson, D.C., National Oceanic and Atmospheric Administration's spacecraft anomaly data base and examples of solar activity affecting spacecraft, J. Spacecraft and Rockets , Vol 31, March-April, 1994.

Williams, D. J., and G. D., Mead, 1965, Nightside magnetosphere configuration as obtained from trapped electrons at 1100 kilometers, J. Geophys. Res., 70, 3017, 1965.

Wrenn G. L., Conclusive evidence for internal dielectrical charging anomalies on geosynchronous communications spacecraft, J. Spacecraft and Rockets, 32 (3), 1995.

Wrenn, G. L., and R. J. Smith, The ESD threat to GEO satellites: Empirical models for observed effects due to both surface and internal charging, in Environmental Modelling for Space-based Applications, ESA SP-392, pp. 121–124, 1996.

Wrenn, G.L. and A.J. Sims, Surface charging on spacecraft in geosyncronous orbit, in "The Behavior of Systems in the Space Enviroment," Eds. R. N. DeWitt et al., Kluwer Academic Publ., Netherlands, 491-511, 1993.

Wu, J.-G., Space Weather Physics: Dynamic Neural Network Studies of Solar Wind-Magnetosphere Coupling, Ph.D thesis, LUNFD6/(NFAS-1016)/1-136/1997, Lund University, Sweden, 1997.

Wu, J.-G., and H. Lundstedt, Geomagnetic storm predictions from solar wind data with the use of dynamic networks, J. Geophys. Res., 102, 14255–14268, 1997.

Wu, J.-G., H. Lundstedt, P. Wintoft, and T.R. Detman, Neural network models predicting the magnetospheric response to the 1997 January halo-CME event, Geophys. Res. Lett., 25, 3031–3034, 1998.